1994

A Study of the Radiative Properties of Agglomerated Flame Particulates Using Light Scattering.

Demetris Theodosios Venizelos
Louisiana State University and Agricultural & Mechanical College

A STUDY OF THE RADIATIVE PROPERTIES OF AGGLOMERATED FLAME PARTICULATES USING LIGHT SCATTERING

A Dissertation

Submitted to Graduate Faculty of the
Louisiana State University and
Agricultural and Mechanical College
in partial fulfillment of the
requirements for the degree of
Doctor of Philosophy

in

The Department of Mechanical Engineering

by
Demetris Theodosios Venizelos
B.S.M.E., Louisiana State University, 1987
M.S.M.E., Louisiana State University, 1989
December 1994

ACKNOWLEDGMENTS

I would like to thank my advisor Professor Tryfon Charalampopoulos for his guidance, encouragement, and support during this study. I would also like to thank Professor Vic Cundy and the members of my advisory committee for their valuable input.

Special acknowledgment goes to Dr. Charles Herd, Dr. Barry Stagg, Dr. Jim Watson, and their team, at the Operations and Technology Center of the Columbian Chemicals Company, for their generous contribution to this study by performing the transmission electron microscope automated image analysis of the soot samples.

I would also like to thank my friends and co-workers Dr. Barry Stagg, Mr. Pradipta Panigrahi, Mr. Wujiang Lou, and Mr. Glenn Waguespack for their assistance and useful discussions on the subject. I would especially like to thank my good friend Dr. David Hahn for his enthusiastic support that gave me strength to keep going when times got tough.

I want to especially thank my uncle, Professor Symeon Symeonides, and his wife Haroula, (my parents away from home) who stood by me in sickness and in health, and gave me material and moral support throughout my college studies.

Finally, I thank the three most important people in my life, my wife Gloria, and my parents Theodosios and Evdokia, who have given me their unconditional love, material and moral support, understanding, and encouragement to continue my studies. Their

sacrifices made it possible for me to finish my graduate studies. To them, I dedicate this dissertation.

TABLE OF CONTENTS

ACKNOWLEDGEMENTS ii

ABSTRACT vi

CHAPTER 1 INTRODUCTION AND LITERATURE REVIEW 1

CHAPTER 2 CLASSICAL LIGHT SCATTERING 12
2.1 Classical Light Scattering by Spheres 12
2.1.1 Scattering by a Single Homogeneous Sphere 12
2.1.2 Rayleigh Theory 20
2.1.3 Scattering by Monodispersed and Polydispersed Systems of Particles 21
2.1.4 Dissymmetry 28
2.2 Scattering by Agglomerates 32

CHAPTER 3 COMPUTATIONS AND SENSITIVITY ANALYSIS 41
3.1 Computer Program Optimization 41
3.2 Agglomerate Simulations and Sensitivity Analysis 57

CHAPTER 4 EXPERIMENTAL FACILITY / FLAME CHARACTERIZATION 89
4.1 Flat Flame Burner 89
4.2 Light Scattering Facility 93
4.3 Premixed Flame Parameters 96
4.4 Optical Path Length and Flame Temperature 97
4.5 Flame Velocity Measurements 101
4.6 Calibration of the Scattering Signal 109
4.7 Testing of the Light Scattering Facility 115
4.8 Particle Sampling 115

CHAPTER 5 EXPERIMENTAL RESULTS AND DISCUSSION 119
5.1 Extinction Cross Section Measurements 119
5.2 Differential Scattering Cross Section Measurements 121
5.3 Measurements of Dissymmetry Ratios R_{VV} and R_{HH} 124
5.4 Depolarization Ratio Measurements 128
5.5 Agglomerate Model Analysis 131

5.6 Transmission Electron Microscopy Results 138

CHAPTER 6 CONCLUSIONS AND RECOMMENDATIONS 151
6.1 Summary and Conclusions 151
6.2 Recommendations for Future Work 157

REFERENCES 159

APPENDIX A STRAIGHT CHAIN AND CLUSTER AGGLOMERATE RESULTS 169

APPENDIX B AGGLOMERATE ANALYSIS RESULTS 202

APPENDIX C COMPUTER PROGRAMS 215

VITA 261

ABSTRACT

The *in-situ* optical technique of inferring the soot agglomerate structural and optical properties from the measurements of the extinction cross section, the differential scattering cross section, the dissymmetry ratios in both planes of polarization, and the depolarization ratio, was investigated in detail by this study. A sensitivity analysis of the technique revealed that the dissymmetry ratios are insensitive to both the real and imaginary part of the refractive index. The ratio of the differential scattering to extinction cross sections was also found to be a weak function of the imaginary part of the refractive index. The sensitivity analysis results indicate that the technique is not suitable for inferring accurately the optical properties of the soot agglomerates. Therefore, a known value for the particle refractive index should be used in the agglomerate analysis to infer the morphology of the soot agglomerates. Experimental measurements of the above described quantities from a laminar premixed propane/oxygen flat flame, of fuel equivalence ratio of 2.1, were used with the appropriate agglomerate model to infer the structural agglomerate parameters. Soot samples were also extracted from the flame by using thermophoretic and sampling probes. It was found that the agglomerate model analysis of the measured scattering and extinction quantities (for four different soot refractive index values), underpredicts the degree of agglomeration of the soot particles. A quantitative analysis of the agglomerate morphology of the soot samples extracted with the sampling probe, indicates a self-preserved distribution of the primary particle sizes and

the number of primary particles per agglomerate with increasing flame residence time of the agglomerate. A qualitative analysis of the electron microscopy results, of the soot samples extracted with the thermophoretic sampling probe, suggests that the degree of agglomeration is a function of flame residence time, and that the primary particle sizes in the agglomerates are fairly monosized.

CHAPTER 1

INTRODUCTION AND LITERATURE REVIEW

Particulate soot is formed during the incomplete combustion of carbonaceous fuels. The presence of soot in combustion systems can be beneficial or detrimental depending on the application. The radiative heat transfer of soot-laden flames can be enhanced because of the high emissivities of soot. This may be an advantage in applications such as boilers and furnaces where it is desirable to maximize the radiative heat transfer rates. Mass production of soot, or carbon blacks, finds widespread applications in the rubber and plastics industry. In this case, knowledge of the size and morphology of the carbon black plays a very important role in the better quality control of the properties of the final products. However, in other applications, such as internal combustion and jet engines, the presence of soot can cause overheating of the combustion chambers and reduction of engine efficiency and engine life. Furthermore, soot emissions are a considerable source of particulate air pollution. Soot particles can remain suspended in the atmosphere for prolonged periods of time because of their small size and can absorb carcinogenic materials. The future holds more problems for the engineer if heavily sooting alternative fuels, such as coal derived fuels, are to be used.

Knowledge of the morphology and physical properties of soot particles, namely size and shape, is of great importance in applications ranging from radiative heat transfer prediction to soot emission control. Studies undertaken by a number of researchers over the years lead to the development of several particle sizing techniques. Before discussing the different techniques used for studying the morphology of soot particles, it would be helpful to present briefly the principles of soot formation and soot growth in hydrocarbon flames.

The first step in soot formation is nucleation. Nucleation can be described as the process by which soot inception occurs through transformation from a molecular system to a particulate system. Despite the extensive research on soot inception and nucleation, this subject is not completely understood. One of the proposed nucleation mechanisms is the growth process from polycylic aromatic hydrocarbons to higher molecular weight hydrocarbons and then to particulate soot.[1-3] Another commonly proposed nucleation scheme is the formation of ions via rapid ion-molecular kinetics and structural rearrangements. These ions contribute in the growth of larger species that serve as nuclei for the initial formation of soot.[4-6]

Once the soot particles nucleate, they begin to grow and coagulate into larger particles. Both the growth and coagulation processes may occur simultaneously. The majority of soot mass is formed by surface growth. During this heterogeneous process, hydrocarbon molecules or growth species (primarily acetylene) decompose on the particle surface and become part of the soot.[7] The above described growth process has a weak dependence on the stoichiometry of the flame and continues until the surface reactivity of soot decreases. In the early stages of soot formation (or regions nearer to the reaction zone) the dominating process is coagulation caused by the coalescent collisions between particles. Two smaller particles collide and fuse together to form a larger spherical particle. The viscosity of the soot particles eventually increases to a level at which coalescent collisions are no longer possible.[8] This particle growth mechanism explains the decrease in the particle number density and the simultaneous increase in the particle diameter during the early stages of soot formation. The shape of the soot particles at the onset of soot formation is approximately spherical and the particle size distribution can be represented by a Gaussian distribution function.[8] As the particles continue to grow, distributions tend to be weighted toward larger sizes. The zeroth order lognormal distribution, which has a skewed shape, is usually employed to better represent these size distributions.[9-10]

Aggregates of random structures are formed in the latter regions of the flame as a result of particle agglomeration. The term agglomeration is used to describe the process through which the particles stick together to form aggregates. The shape of the agglomerates can vary considerably from approximately spherical clusters to chain-like structures. Higher fuel equivalence ratios and higher fuel C/H ratios tend to enhance soot particle agglomeration. This subject is discussed in detail in a later section of this chapter.

The techniques for sizing combustion-generated particulates can be divided into two major categories: *ex-situ* and *in-situ*. In the *ex-situ* technique, the particles are usually extracted from the flame with a sampling probe or by quenching the flame with a water-cooled plate. Electron microscopy can subsequently be employed to characterize the particle size and morphology. The disadvantage of the *ex-situ* technique is that, because it intrudes the flame, it causes the morphology of the extracted soot particles to be different from that of the particles in the flame.[11]

In contrast, the optical techniques used for the *in-situ* studies of flames are non-intrusive and can be used for real time analysis. Classical light scattering and extinction techniques have been used extensively for soot particle sizing in flames.[12-30] These techniques use the measurements of the average scattering light signal as a function of the wavelength of the incident light, the scattering angle, and/or the state of polarization to determine the particle size. In these techniques the frequency of the scattered light is treated as though it were the same as that of the incident beam. The data can be reduced using the Mie theory,[31-33] which relates the scattered and absorbed light intensities to the size and optical properties of isotropic spheres. For spherical particles with a circumference smaller than the wavelength of the incident radiation, the scattering and extinction can be easily predicted by the limiting case of the Mie solution or, the Rayleigh limit. There also exist other solutions for the scattering field around other geometries, such as homogeneous infinite cylinders, prolates, and oblates. The main disadvantage of these techniques, however, is that they require knowledge of the particle refractive index

in order to yield reliable results. Since the refractive index is usually determined with an ex-situ technique, there may be uncertainties associated with the inferred particle sizes. Another drawback of these techniques is that the Mie theory assumes that the scatterers are isotropic spherical particles, an assumption that begins to break down when increased agglomeration appears in the higher positions in the flame.

Dynamic Light Scattering (DLS) or Photon Correlation Spectroscopy (PCS) is another in-situ technique frequently used for soot particle sizing in flames.[9-10,34-47] The advantage of DLS over classical light scattering is that it does not require the refractive index of the particles in the case of scattering by Rayleigh size spheres. DLS measures the frequency broadening of the scattered light caused by the diffusional motion of the particles in the scattering volume. Measurements of the power spectra densities in the frequency domain or the intensity autocorrelation function in the time domain can yield information about the translational and rotational diffusion coefficients of the particles. The particle diameter and size distribution can then be extracted from the measured power spectrum or the intensity autocorrelation functions. DLS is also limited in measurements of spherical particles or spherical clusters that possess size distributions of relatively narrow geometric widths ($\sigma < 1.45$).[42] In cases with broader size distributions, such as pulverized coal flames, multimodal sizing techniques must be incorporated in order to yield reliable information about the size parameters.[46-47] Another drawback of DLS is that the particle size range and the particle size distribution function must be known *a priori* in order to optimize the experimental conditions for these measurements. Moreover, in most cases this technique cannot provide information about the particle number densities.

As mentioned earlier, soot particle agglomeration prevails in the regions beyond the reaction zone in fuel-rich flames. Subsequently, calculations based on the Mie theory and the sphericity assumption must be carefully assessed before being implemented to predict radiative transfer properties of soot. The equivalent sphere model is often invoked in order to reduce the results of scattering/extinction measurements from agglomerates

and to infer an effective diameter. The effective diameter is that of a hypothetical sphere that displays the same scattering/extinction properties as an agglomerate. Jones[48] compared the absorption coefficients of elongated particles (prolate spheroids) to those of spherical particles and found that higher coefficients are predicted for elongated particles, leading to significant increase in the emissivity of the particles. Recognizing that an accurate account of the radiative contribution of each agglomerate shape present in the flame system can be complex, Lee and Tien[49] proposed a simple method for determining the fractions of agglomerates that possess the two limiting shapes (spheres and cylinders) based on the extinction characteristics of the particles. Charalampopoulos and Hahn[51] developed an expression for the extinction efficiencies of elongated soot particles that yield efficiencies insensitive to variations of the refractive index in the wavelength range of 0.40-15.0 μm. Mackowski et al[50] developed expressions for the extinction efficiencies of cylindrical soot particles in the wavelength range 0.50-5.0 μm.

Jones[52-54] developed a theory that describes the scattering and absorption agglomerates of Rayleigh-size primary particles and takes into account the effects arising from the multiple scattering or interaction due to the close proximity of the primary particles in the agglomerates. Jones compared the results for the scattering properties of straight chains and clusters consisting of less than ten primary particles to those of an equivalent sphere. He suggested that there is no single equivalent sphere relation that can be used to represent chains, closed packed clusters, and random clusters, and concluded that the particle assemblies must be treated as such.

Felske et al[55] used Jones' agglomerate model and developed analytical expressions that predict the vertical-vertical (VV) differential scattering cross section at 90°, the extinction cross section, and the VV dissymmetry ratio (the ratio of the scattered light in a forward direction to that scattered in the complimentary backward direction), that are valid for specific values of the particle refractive indices. Drolen and Tien[56] developed a model that accounts for all the electromagnetic interactions between all the primary

particles in a cluster. They found that the analytical results of scattering from clusters of up to 136 primary particles are similar to the equivalent solid sphere model and are in agreement with experimental data. They proposed two equivalent sphere concepts that can be used according to the specific application. The first concept uses the same refractive index of the equivalent sphere as that of the primary particles and adjusts the effective diameter. The second concept uses the largest outer dimension of the cluster as the effective diameter of the equivalent sphere and adjusts the refractive index. Kumar and Tien[57] used analytical reasoning, instead of empirical correlations based on numerical results, to show that in the Rayleigh regime there is a cube-root proportionality between the effective diameter of agglomerates and the primary particle diameter. They also presented proportionality constants for different morphologies. Purcel and Pennypacker[87] (P-P) and Iskander et al[88] (I-C-P) also proposed agglomerate models that treated the primary particles in the agglomerate as cubical cells. Their approach to the agglomerate problem basically entails the same treatment of the general electric field equation as that of Jones' solution, but different treatment of the internal electric field general equation and the approximation of the self contribution term. The Jones agglomerate solution has been corrected for the appropriate representation of the refractive index[57] and the extinction efficiency factor.[85] Ku and Shim[86] also compared the Jones solution to the P-P and I-C-P solutions, and rated it as the least accurate of the three. In addition it was stated that the Jones solution is generally unreliable because it may result in negative extinction and/or scattering efficiency factors for the densely packed agglomerate.

Recently, Lou and Charalampopoulos[90] showed that all three proposed solutions for light scattering by agglomerates, namely the Jones, P-P, and I-C-P, do not satisfy the energy conservation criterion for the extinction, absorption, and scattering efficiencies. Furthermore, Lou and Charalampopoulos[90] developed an exact form of the internal field equation for an assembly of Rayleigh size spherical particles irradiated by an electromagnetic wave. The new solution takes into account the interactions from the

neighboring particles (multiple scattering), and the self interaction term. It also, satisfies the energy conservation criterion for the extinction, absorption and scattering efficiencies. In addition, the new formulation can be reduced to the form of the equations originally developed by Jones, and to those by Purcel and Pennypacker[87] and Iskander et al,[88] as well as the two sphere analytical solution by Goedecke and O'Brien,[89] depending on how the self contribution term is approximated. The new formulation by Lou and Charalampopoulos[90] perfectly matches the analytical solution for light scattering by two Rayleigh size spheres by Goedecke and O'Brien,[89] which confirmed the validity of the new formulation and allowed verification of the new computer program developed for the calculation of the agglomerate light scattering, extinction and absorption characteristics.

After the introduction of the fractal concept and the development of the fractal theory by Mandelbrot[58-59] in the seventies, several researchers have applied the concept of fractals on aggregates using light scattering measurements. Forrest and Witten[60] were the first to discover a fractal character in smoke-particle aggregates. They studied aggregates of iron, zinc, and silicon oxides produced under different conditions (hot filament or flame). The results were obtained by manually digitizing transmission electron microscope (TEM) micrographs of the aggregates to produce a matrix of 'ones' and 'blanks' representing the presence or absence of a particle. A point well inside the structure was chosen at random and then larger and larger squares were drawn centered on that point and the number of particles in each square was counted. This analysis yielded correlation data that suggest power-law spatial dependence between the length l of the square and the number of points N within it, namely $N \propto l^{D_f}$, giving a Hausdorff fractal dimension D_f between 1.7 and 1.9. However, the relationship between the information extracted from the study of the TEM micrographs and the three dimensional agglomerates is uncertain.

Berry and Percival[61] presented a theory of the optics of smoke that includes the fractality of the soot aggregates (with $D_f = 1.78$). Using a mean field theory for clusters consisting of small primary particles as compared to the incident radiation wavelength, but

with cluster sizes that can exceed the radiation wavelength, Berry and Percival showed that multiple scattering effects are negligible for fractal dimensions $D_f < 2$ but become important for $D_f > 2$. Scattering and absorption cross-section calculations (as a function of the number density of the primary particles N_p, the fractal dimension D_f and the refractive index of the primary particle) indicate that for clusters with $D_f < 2$ the scattering per primary particle increases to a constant saturation value which exceeds that of a single particle a factor of order $(2\pi r/\lambda)^{-D_f}$. For clusters with $D_f > 2$ the scattering per primary particle increases as $N_v^{1-\frac{2}{D_f}}$. In both cases the absorption cross-section was found to be independent of D_f . Martin et al[62] studied flame-generated fumed silica aggregates dispersed in liquid solutions. Using classical light scattering and x-ray scattering measurements, they found a fractal dimension D_f of 1.84 ± 0.08, which agreed reasonably well with the micrograph analysis results by Forrest and Witten[60]. The dynamic light scattering study of the aggregates by Martin et al, indicates a power-law dependence of the Rayleigh linewidth on the momentum transfer that agrees with previous studies of solution-grown silica aggregates.

Hurd and Flower[63] also studied flame-generated fumed silica, but avoided the rather complicated sample preparation and resuspension techniques encountered in previous studies by performing *in-situ* classical and dynamic light scattering measurements. The rationale behind this approach was to preserve the structural integrity of the aggregates that are fragile and may be distorted during the *ex-situ* treatment. The fractal dimension D_f was found to be 1.49, which was smaller than the previously reported *ex-situ* and simulated D_f measurements of fumed silica. The authors speculated that the smaller D_f could have been due to electrical interactions on a local scale and to the fact that the simulations do not include the effects of rotational diffusional motion of the aggregates. Electron microscopy analysis of fumed silica showed that there is a tendency for the silica primary particles to shrink with flame residence time. This effect was attributed to possible particle ablation by thermal and chemical mechanisms.

The effects of rotational diffusion on cluster-cluster aggregation were investigated in an earlier work by Meakin[64] who used a two-dimensional off lattice cluster-cluster aggregation model that included both rotational and translational diffusion. He found that the fractal dimension D_f varies continuously from 1.40-1.45 to a limiting value of 1 as the rotational diffusion increases. Samson et al[65] studied TEM micrographs to obtain structural information of soot agglomerates generated in an acetylene coannular diffusion flame. They used stereopairs (to minimize particle overlapping) for particle counting in small clusters, and high resolution digital imaging for larger clusters. A computer simulation of a model that applies the Langevin equation to particles and clusters that undergo Brownian motion to form agglomerates was used in interpreting the experimental results. The authors considered this free molecular agglomerate growth mechanism to be most valid for small clusters formed in a flame. The fractal dimension D_f for small clusters (< 1 μm) was found to be between 1.5 - 1.6 while the computer simulation gave a value of 1.9. For larger clusters (5-12 μm) the power law exponent for the pair correlation function was found to agree with the simulated value. The exponent increases for agglomerates with dimensions larger than 12 μm. The authors concluded that experimental work on the 3-D coordinate structure of agglomerates is necessary in order to improve on the fractal description of soot agglomerates. Megaridis and Dobbins[69] studied soot extracted (with a thermophoretic probe) from a coannular ethene diffusion flame. TEM examination of the agglomerates yielded a fractal dimension D_f between 1.62 and 1.74, which is in the range reported by other investigators. The authors concluded that although the agglomerate size may vary over many orders of magnitude, the D_f and primary particle size values of flame-generated soot and fumed silica are within a narrow range, which strongly suggests a similarity of the major mechanisms that affect the particle dynamics in a variety of combustion environments.

Zhang et al[66] studied aerosolized soot agglomerates from a methane-oxygen flame using both *in-situ* optical structure factor, measurements and TEM analysis. The fractal

dimension D_f determined from the *in-situ* analysis was 1.62 ± 0.06, and from the TEM analysis was 1.72 ± 0.10. Mountain and Mulholland[67] used the Langevin dynamics technique to simulate the growth of smoke agglomerates made of 10-700 primary particles. The calculated light scattering intensity from these clusters was used to illustrate how *in-situ* light scattering/extinction measurements can be used to determine the number density, size, radius of gyration, and fractal dimension of the agglomerates. The authors advise caution in the procedure for inferring the above parameters in the cases where polydispersity of sizes exists. Moreover, the procedure requires absolute light scattering intensities that may be succeptible to significant experimental uncertainties. For a given primary particle or agglomerate size it may not be possible to perform all the scattering measurements in the visible range in order to cover both the low and high scattering wavevectors range. A comparison of simulated results between the effective sphere and agglomerate models showed that the effect of structure becomes pronounced for clusters of 30 or more primary particles. Dobbins and Megaridis[68] took into account the polydispersity effects by using a lognormal distribution of aggregate sizes in calculations of the absorption and scattering cross-sections in the vertical-vertical orientation.

Charalampopoulos and Chang[70] studied soot agglomerates formed in a premixed propane-oxygen flame using scattering/extinction and dissymmetry measurements. The data were reduced using the Mie, the Rayleigh, and the agglomerate model analysis to compare the effective particle diameters and number densities. The effective diameters from the Mie and the agglomerate analysis differed by only 1.8%. The Rayleigh analysis had underestimated the diameter by 9% and overestimated the number density by 34% at the height of 16 mm above the burner surface. The estimated fractal dimension D_f for this system was found to be 1.7.

Bonczyk and Hall[71] performed extinction and multiangle scattering measurements in an ethylene-air diffusion flame. They used the multiangle scattering measurements to determine the fractal dimension D_f and radius of gyration R_g of the soot agglomerates.

They reported a fractal dimension D_f between 1.4 and 1.55. In a later study of the same flame, Bonczyk and Hall[72] used an ultraviolet beam at 266nm derived from the frequency doubled output of a 2x Nd-YAG pulsed laser to measure the scattering from agglomerates. They reported fractal dimensions between 1.33 to 1.6 at different heights in the flame. Using extinction measurements versus wavelength (from a continuous light source), they ruled out any significant interference of polycyclic aromatic hydrocarbon ultraviolet absorptions.

As the preceding discussion shows, there are numerous approaches to the flame particulate characterization problem. Each approach has its advantages and disadvantages, depending on the assumptions and methods chosen to perform the particulate analysis. The number of unknown parameters in this type of analysis is usually larger than the available measurements. Moreover, choosing the appropriate model in interpreting the experimental results is a difficult task. The present work aims to combine a set of independent experimental measurements, complemented by the corresponding theoretical framework, in order to completely characterize flame generated particulates. Additional measurements will be used as independent checks of the results. The ultimate goal is to relate the results of the particulate morphology characterization to the radiative properties of soot-laden flames.

The next chapter presents briefly the theory of Classical Light Scattering, and Agglomerate theory. Chapter 3 undertakes a sensitivity analysis in order to determine the optimum experimental conditions for minimizing the uncertainty in the inferred parameters. Chapter 4 presents the experimental facility and the measurements taken to characterize the propane/oxygen flame used in this study. The experimental results of the measurements taken are presented in Chapter 5, along with the results of the theoretical analysis using the agglomerate model developed by Lou and Charalampopoulos.[90]

CHAPTER 2

CLASSICAL LIGHT SCATTERING

2.1 Classical Light Scattering by Spheres

2.1.1 Scattering by a Single Homogeneous Sphere

General Solution:

When a beam of light strikes a small isotropic homogeneous particle, it causes the electric charges in the particle to be set in synchronous oscillation with the oscillating electric field of the incident electromagnetic wave. The oscillating charges, or dipoles, will cause secondary electromagnetic wave emissions at the same frequency as that of the incident beam, which constitute the scattered radiation. The general solution of the scattering by a single homogeneous sphere problem was derived by Mie[31-33] in the beginning of this century. The general solution is presented following the notation of Kerker[33]. The geometry in the formulation of the problem is shown in Figure 2.1. The incident electromagnetic wave propagates in the z-direction with its electric field vector $\vec{E}$ linearly polarized along the x-axis. The vectors $\vec{B}$ and $\vec{S}$ represent the magnetic field and Poynting vectors respectively. The scattered field, at any point in space around the particle, is described by polar coordinates r, θ, and ϕ. It is customary to measure the scattering angle θ from the forward z-direction. The particle has a radius a and a complex

refractive index $\bar{m} = n - ik$. The real part (n) of the refractive index is a measure of the speed of light within the particle. The imaginary part k, signifies the amount of the incident light energy that is being absorbed by the particle. The intensity of the scattered radiation polarized in the θ and ϕ azimuths is given by[32]

$$I_\phi = I_o \frac{\lambda^2}{4\pi^2 r^2} i_1 \sin^2\phi \,, \tag{2.1}$$

and

$$I_\theta = I_o \frac{\lambda^2}{4\pi^2 r^2} i_2 \cos^2\phi \,, \tag{2.2}$$

where λ and I_o are the wavelength in *vacuo* and the intensity of the incident beam respectively, and i_1 and i_2 are the intensity scattering functions in the planes parallel and perpendicular to the plane of incidence. In the general case, i_1 and i_2 are expressed in the form of infinite series of the Mie solution as

$$i_1 = \left| \sum_{n=1}^{\infty} \frac{2n+1}{n(n+1)} \left\{ a_n \pi_n(\cos\theta) + b_n \tau_n(\cos\theta) \right\} \right|^2 , \tag{2.3}$$

and

$$i_2 = \left| \sum_{n=1}^{\infty} \frac{2n+1}{n(n+1)} \left\{ a_n \tau_n(\cos\theta) + b_n \pi_n(\cos\theta) \right\} \right|^2 . \tag{2.4}$$

The functions $\pi_n(\cos\theta)$ and $\tau_n(\cos\theta)$ are expressed in terms of the Legendre function of the first kind $P_n^1(\cos\theta)$ of argument $\cos\theta$ by the relations

$$\pi_n(\cos\theta) = \frac{P_n^1(\cos\theta)}{\sin\theta}, \tag{2.5}$$

and

$$\tau_n(\cos\theta) = \frac{d}{d\theta}(P_n^1(\cos\theta)). \tag{2.6}$$

The coefficient a_n and b_n in equations (2.3) and (2.4) are defined as

$$a_n = \frac{\Psi_n(\alpha)\Psi'_n(\beta) - m\Psi_n(\beta)\Psi'_n(\alpha)}{\zeta_n(\alpha)\Psi'_n(\beta) - m\Psi_n(\beta)\zeta'_n(\alpha)}, \tag{2.7}$$

and

$$b_n = \frac{m\Psi_n(\alpha)\Psi'_n(\beta) - \Psi_n(\beta)\Psi'_n(\alpha)}{m\zeta_n(\alpha)\Psi'_n(\beta) - \Psi_n(\beta)\zeta'_n(\alpha)}. \tag{2.8}$$

The terms Ψ_n and ζ_n in the above equations are the Ricatti-Bessel and Hankel functions respectively. The parameter α is the dimensionless size parameter, m is the refractive index relative to that of the surrounding medium $m = \bar{m}/m_o$ and $b=m\alpha$. The size parameter α is defined as

$$\alpha = \frac{2\pi m_o a}{\lambda}, \tag{2.9}$$

where a is the particle radius.

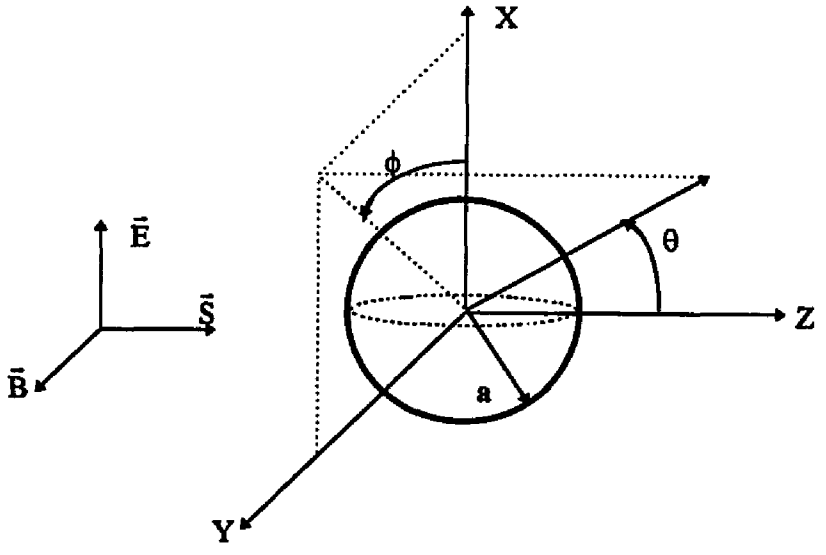

Figure 2.1 Polar coordinate system for a plane wave traveling in the positive z-axis, incident upon a homogeneous sphere of radius a.

The functions Ψ_n and ζ_n are defined[32] as

$$\Psi_n(z) = \sqrt{\frac{\pi z}{2}} J_{n+\frac{1}{2}}(z) \tag{2.10}$$

and

$$\zeta_n(z) = \sqrt{\frac{\pi z}{2}} H^2_{n+\frac{1}{2}}(z) = \Psi_n(z) + i\chi_n(z), \tag{2.11}$$

where

$$\chi_n(z) = -\sqrt{\frac{\pi z}{2}} N_{n+\frac{1}{2}}(z). \tag{2.12}$$

The terms $J_{n+\frac{1}{2}}(z)$ and $N_{n+\frac{1}{2}}(z)$ in the above equations are the half integral order Bessel and Newman functions, and $H^2_{n+\frac{1}{2}}(z)$ is the half integral order Hankel function of the second order. When the incident radiation is unpolarized, then the scattered field in any direction has intensity I_u,

$$I_u = I_o \frac{\lambda^2}{8\pi^2 r^2}(i_1 + i_2) \tag{2.13}$$

and is partially polarized with a degree of polarization P given by

$$P = \left| \frac{i_1 - i_2}{i_1 + i_2} \right|. \tag{2.14}$$

The fraction of the incident radiation scattered into a solid angle about a given direction is described by the differential scattering cross section C'_{scat} (area/steradian). The differential scattering cross section is a parameter that can be determined in a light scattering experiment where the scattered light intensity is measured by a detector positioned at a given direction. The scattering volume will subtend a solid angle when viewed from the detector. In the case where the scattering plane is the yz-plane (ϕ=90°), and the incident light is polarized perpendicularly to the scattering plane, the scattered light is also perpendicularly polarized, and the differential scattering cross section is defined as

$$C'_{VV} = \frac{\lambda^2}{4\pi^2} i_1. \tag{2.15}$$

Similarly, when the scattering plane is the xz-plane (ϕ = 0°) and the electric field is polarized parallel to the xz-plane, the scattered light is also polarized parallel to the scattering plane. In this case, the differential scattering cross section is defined by

$$C'_{HH} = \frac{\lambda^2}{4\pi^2} i_2. \tag{2.16}$$

The subscripts V and H indicate respectively the vertical (or perpendicular) and the horizontal (or parallel) states of polarization. Also, the subscript combination VV (or HH) denotes the state of polarization of the incident and scattered radiation. In the case of scattering of incident radiation polarized in the vertical or horizontal states of polarization, the differential cross sections C'_{VH} or C'_{HV} are zero. For unpolarized incident light the differential scattering cross section is given by

$$C'_{scat} = \frac{\lambda^2}{4\pi^2}(i_1 + i_2). \tag{2.17}$$

Physically, the scattering cross section represents the fraction of the incident radiation scattered in all directions, and it may be determined by integrating C'_{scat} over all solid angles.

$$C_{scat} = \int_0^{2\pi}\int_0^{\pi} C'_{scat} \sin\theta d\theta d\phi. \tag{2.18}$$

By substituting equation (2.17) into the above equation and integrating, it can be shown[32] that the total scattering cross section becomes

$$C_{scat} = \frac{\lambda^2}{2\pi}\sum_{n=1}^{\infty}(2n+1)\{|a_n|^2 + |b_n|^2\}, \tag{2.19}$$

which is valid for polarized and unpolarized incident radiation conditions.[32]

The total energy abstracted from the incident beam of intensity I_o is determined by the product $C_{ext}I_o$, where C_{ext} is the extinction cross section. For absorbing particles, the extinction cross section comprises energy abstracted by both absorption and scattering, and it is the sum of the scattering and absorption cross sections.

$$C_{ext} = C_{scat} + C_{abs}\,. \tag{2.20}$$

The extinction cross section for a spherical particle is given by

$$C_{ext} = \frac{\lambda^2}{2\pi}\sum_{n=1}^{\infty}(2n+1)\{\mathrm{Re}(a_n + b_n)\}, \tag{2.21}$$

where Re signifies the real part of the complex quantity. The corresponding efficiency factors for scattering and extinction can be determined by dividing the cross sections by the geometric cross section of the particle.

$$Q_{scat} = \frac{C_{scat}}{\pi a^2}, \tag{2.22}$$

and

$$Q_{ext} = \frac{C_{ext}}{\pi a^2}. \tag{2.23}$$

2.1.2 Rayleigh Theory

An approximate solution to the scattering by small spherical particles was developed by Rayleigh before the Mie general solution.[32] The conditions necessary for the validity of the Rayleigh solution are that both the dimensionless parameter α and the quantity $|\overline{m}\alpha|$ are much less than unity.[31-33] The differential scattering cross sections C'_{VV} and C'_{HH} and for scattering by Rayleigh particles are given by the expressions

$$C'_{VV} = \frac{\lambda^2}{4\pi^2}\alpha^6\left|\frac{\overline{m}^2-1}{\overline{m}^2+2}\right|^2, \tag{2.24}$$

and

$$C'_{HH} = C'_{VV}\cos^2\theta, \tag{2.25}$$

where λ is the wavelength in *vacuo* of the incident radiation, α is the size parameter, $\overline{m}$ is the complex refractive index of the particle, and θ is the scattering angle. The Rayleigh total scattering and absorption cross sections may be obtained by integrating the differential cross sections. The results are given as

$$C_{scat} = \frac{2\lambda^2}{3\pi}\alpha^6\left|\frac{\overline{m}^2-1}{\overline{m}^2+2}\right|^2, \tag{2.26}$$

and

$$C_{abs} = \frac{-\lambda^2}{\pi}\alpha^3\,\mathrm{Im}\left\{\frac{\overline{m}^2-1}{\overline{m}^2+2}\right\}. \tag{2.27}$$

The contribution of the scattering cross section to the extinction cross section is generally assumed to be negligible when the size parameter a is much smaller than one. As it can be seen from equations (2.26) and (2.27), the C_{scat} is proportional to the sixth power of α and, therefore, much smaller than C_{abs}, which is proportional to the third power of α.

2.1.3 Scattering by Monodispersed and Polydispersed Systems of Particles

The scattering by a particle cloud or suspension can be described by extending the single particle scattering solutions under certain conditions.[32,78] The criteria for treating the scattering from a cloud utilizing single scatterer solutions are as follows:

(i) The particle suspension must be dilute enough to avoid electrical interaction between the particles. This condition can be satisfied with particle center-to-center spacings of at least two particle diameters.[32]

(ii) There is no multiple scattering. Multiple scattering occurs when the scattered electromagnetic wave is rescattered by other particles that happen to be in its path. The problem can be alleviated with an optical mean free path that is larger than the physical dimensions of the scattering system. The homogeneous optical path length L characterizes the physical dimension of the scattering/absorbing cloud of identical particles. The optical mean free path is of the order[78] of $1/NC_{ext}$, where N is the particle number density (number of particles/volume of surrounding medium) and C_{ext} is the extinction cross section of a single particle. Therefore, the condition

of no multiple scattering can be satisfied when $1/NC_{ext} > L$, or equivalently, when the turbidity LNC_{ext} is less than unity.

(iii) There is no optical interference between waves scattered by different particles. The intensity of the scattered light from a cloud consisting of identical particles is given by[79]

$$I = I_i(\sin^2\phi_1 + \sin^2\phi_2 + ... + \sin^2\phi_n) + I_i(\cos^2\phi_1 + \cos^2\phi_2 + ... + \cos^2\phi_n),$$

where I_i is the scattered intensity from a single particle and ϕ_i is the phase of the scattered light from the i^{th} particle. It can be easily shown that the sum of the phase terms reduces to the particle number density N. The intensities can then be added directly, thus satisfying the above condition.

If all three of the above conditions are satisfied, then the extinction coefficient and differential scattering cross sections are defined as

$$K_{ext} = N\,C_{ext}, \tag{2.28}$$

and

$$K'_{pp} = NC'_{pp}, \tag{2.29}$$

where N is the particle number density, and C_{ext} and C'_{pp} are the single particle extinction and differential scattering cross sections. The subscripts pp denote the polarization state of the incident and scattered radiation. A widely used and useful quantity in light

scattering/absorption measurements is the transmission of light through a medium. For a homogeneous optical path, the spectral transmission τ_λ (the ratio of the beam intensity through the particle cloud to that of the incident beam) is related to the extinction coefficient K_{ext} by the relation

$$\tau_\lambda = \exp(-LK_{ext}), \tag{2.30}$$

where L is the optical path length through the absorbing and scattering system.

However, most particle systems possess polydispersity of sizes. In order to account for the distribution of particle sizes, the extinction and differential scattering coefficients are defined as

$$K_{ext} = N\overline{C}_{ext}, \tag{2.31}$$

and

$$K'_{pp} = N\overline{C}'_{pp}, \tag{2.32}$$

where the terms $\overline{C}_{ext}$ and $\overline{C}'_{pp}$ are the average extinction and differential scattering cross sections. The average cross sections are determined by integrating the single particle cross sections, weighted with the appropriate size distribution function P(r), over all sizes. Accordingly, $\overline{C}_{ext}$ and $\overline{C}'_{pp}$ are expressed as

$$\overline{C}_{ext} = \int_{r=0}^{\infty} C_{ext}(r)\, P(r)\, dr \quad , \tag{2.33}$$

and

$$\overline{C}'_{pp} = \int_{r=0}^{\infty} C'_{pp}(r)\, P(r)\, dr \quad , \tag{2.34}$$

where r is the particle radius. The above integrals can be evaluated analytically for the Rayleigh approximation, and numerically when using the general Mie solution. The distribution function P(r) that best describes the size distribution of particles in flame systems is the zeroth order lognormal distribution (ZOLD) function.[9,10,31]

The ZOLD is given by

$$P(r) = \frac{\exp(\frac{-\sigma_o}{2})}{\sqrt{2\pi}\sigma_o r_m} \exp\left[\frac{-(\ln\frac{r}{r_m})^2}{2\sigma_o^2}\right], \tag{2.35}$$

where r_m is the most probable radius or modal value of r, and σ_o is a measure of the width and skewness of the distribution. The relations between the modal value r_m, the mean value $\overline{r}$, and the standard deviation σ and σ_o are given by

$$\ln \overline{r} = \ln r_m + 1.5\sigma_o^2, \tag{2.36}$$

and

$$\sigma = r_m \sqrt{\exp(4\sigma_o^2) - \exp(3\sigma_o^2)}\,. \tag{2.37}$$

The ZOLD function is normalized so that the integral of P(r) over all values of r is unity. Figure 2.2 shows the ZOLD function, which has the advantage over other distribution functions, such as the Gaussian distribution function, of not allowing negative values of the particle radius r. As σ_o increases, the width and skewness of the distribution increase. Soot particles in flames display similar behavior, especially at positions away from the nucleation zone.

Another important parameter usually used in characterizing aerosol clouds is the volume fraction f_v, which is defined as the volume occupied by the particles per unit scattering volume (solid particle volume/mixture volume). For monodispersed particle clouds the volume fraction is simply the product of the particle number density N and the particle volume. In the case of polydispersed clouds, the distribution of particle sizes must be taken into account and the volume fraction may be obtained by integrating over all possible particle sizes, namely:

$$f_v = N \int_{r=0}^{\infty} \frac{4}{3} \pi r^3 \, P(r) \, dr. \qquad (2.38)$$

Similarly, the surface area A_s of a monodispersed particle cloud per unit scattering volume is the product of the particle number density and the particle surface area. For polydispersed systems, the surface area is given by

$$A_s = N \int_{r=0}^{\infty} 4 \pi r^2 \, P(r) \, dr. \qquad (2.39)$$

Substituting the ZOLD function expression (2.35) into the above equations and integrating, the volume fraction and surface area equations can be reduced to

$$f_v = \frac{4}{3}\pi N r_m^3 \exp(4\sigma_o^2), \tag{2.40}$$

and

$$A_s = 4\pi N r_m^2 \exp(4\sigma_o^2). \tag{2.41}$$

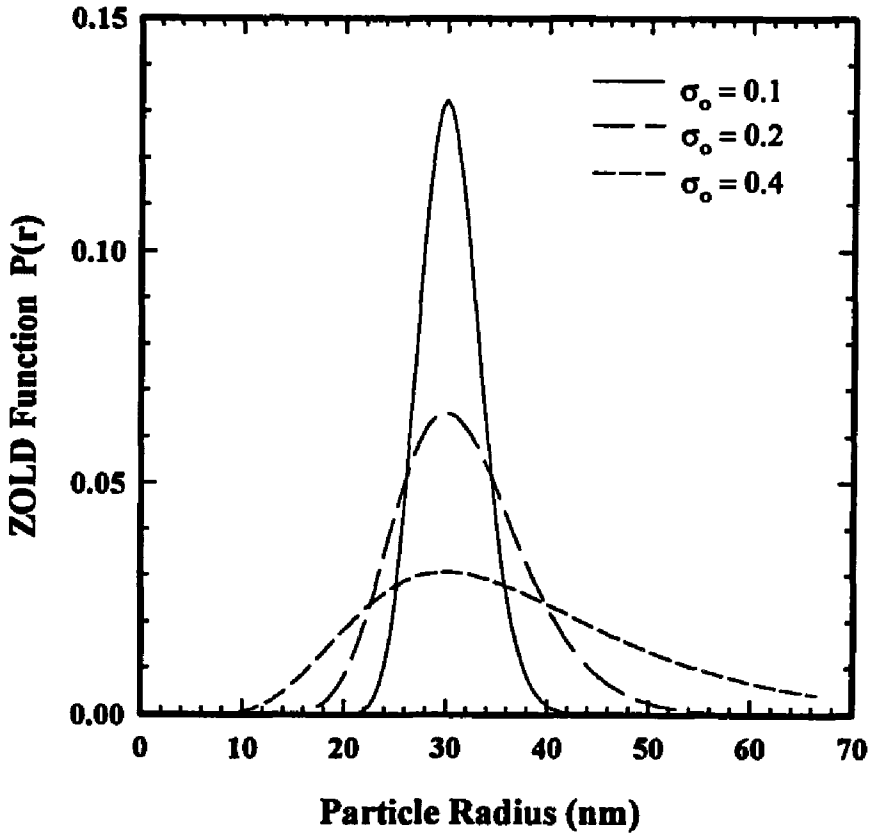

Figure 2.2 The zeroth order lognormal distribution (ZOLD) function for a modal particle radius of 30 nm and different values of σ_o.

2.1.4 Dissymmetry

As shown earlier in section 2.1.2 of this chapter, for particles in the Rayleigh regime the differential scattering cross section C'_{VV} is independent of the scattering angle θ and C'_{HH} is proportional to $\cos^2\theta$, which displays a symmetry about $\theta=90°$. As the size parameter α increases, forward scattering begins to dominate and the symmetry about 90° diminishes. This effect can be seen in Figure 2.3, where the differential scattering cross sections C'_{VV} and C'_{HH} normalized with respect to $C'_{VV}(\theta=0°)$ are plotted for three different size parameters. The particle complex refractive index used in this plot is $\overline{m} = 2 - 1i$. Important information about the particle size can be obtained from the departure of the scattering cross-sections from the symmetry since it increases with increasing size parameter.

The dissymmetry ratio R_{pp} is defined as the ratio of the differential scattering cross section to that of the complimentary angle

$$R_{pp} = \frac{C'_{pp}(\theta)}{C'_{pp}(180° - \theta)}, \qquad (2.42)$$

where the subscripts pp indicate the state of polarization of the incident and scattered beams. Figure 2.4 shows how the dissymmetry ratio R_{VV} increases with increasing size parameter and decreasing scattering angle. The same trend may be observed in Figure 2.5 where the dissymmetry ratio R_{HH} is plotted versus the size parameter for three different scattering angles.

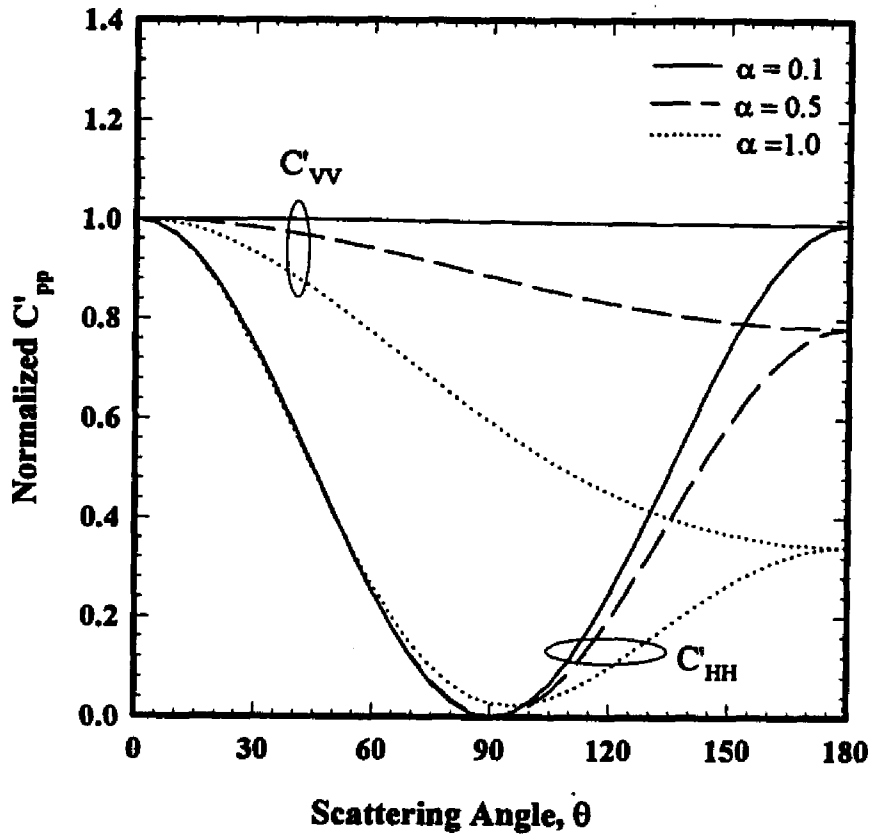

Figure 2.3 Normalized differential scattering cross sections $\{C'_{pp}(\theta) / C'_{VV}(0°)\}$ in the vertical and horizontal polarization orientations as functions of the scattering angle θ, and the size parameter α for a particle with a refractive index of $\overline{m} = 2 - 1i$.

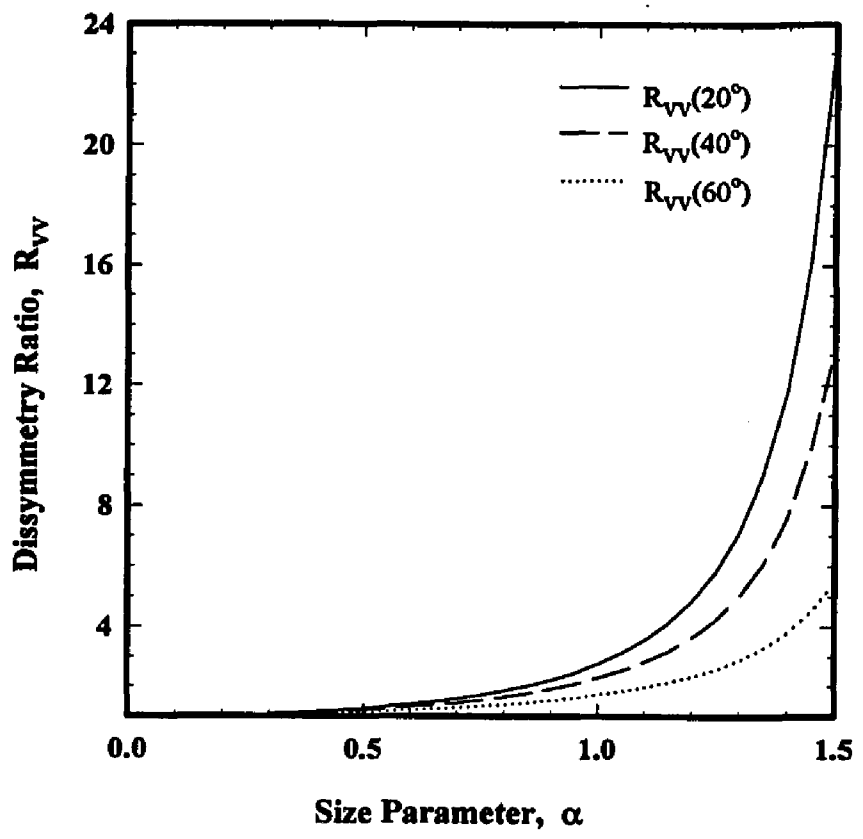

Figure 2.4 Dissymmetry ratio R_{VV} $\{=C'_{VV}(\theta) / C'_{VV}(180° - \theta)\}$ as function of the size parameter α, and the scattering angle θ for a particle with a refractive index of $\overline{m} = 2 - 1i$.

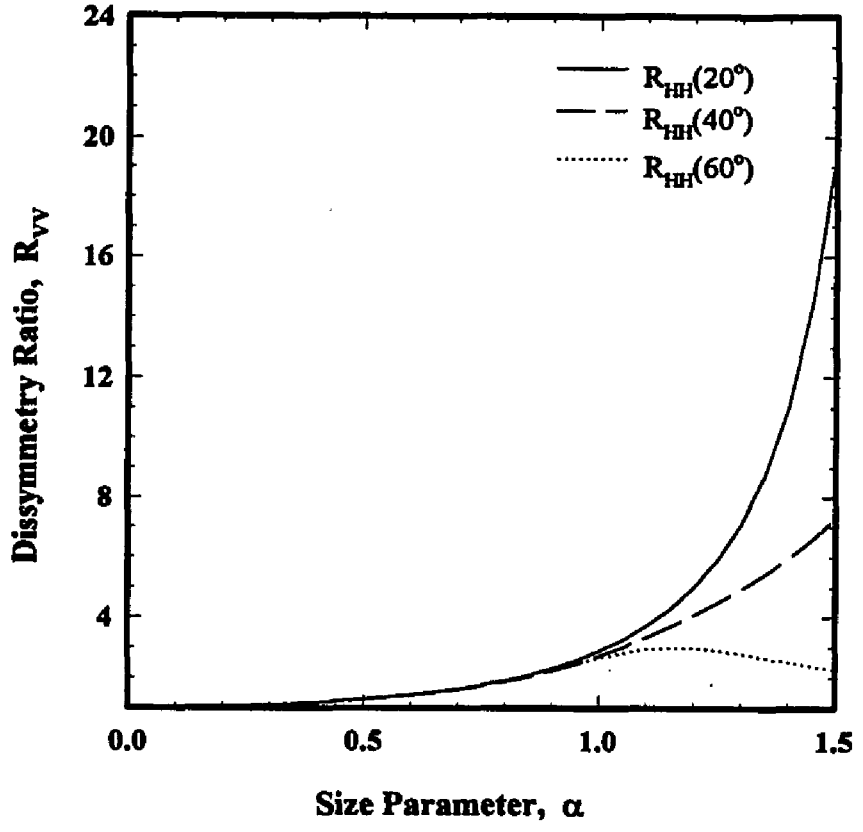

Figure 2.5 Dissymmetry ratio R_{HH} $\{=C'_{HH}(\theta) / C'_{HH}(180° - \theta)\}$ as function of the size parameter α, and the scattering angle θ for a particle with a refractive index of $\overline{m} = 2 - 1i$.

2.2 Scattering by Agglomerates

A number of studies[48-50,54-57,87-90] have dealt with the scattering and extinction characteristics of agglomerates of limiting shapes, such as cylinder-like structures and spherical clusters. Yet there is no technique available that can be used to completely characterize the agglomerates for all ranges of parameters and optical properties. Jones[52-54] developed an exact model for scattering by agglomerates made up of small particles. In Jones' formulation, an assembly of N_p number of Rayleigh size primary particles per agglomerate are considered. The scattered amplitude of the electric field, E_{scat}, at a point (r, θ, ϕ) in the spherical coordinate reference system, is constructed by the internal electric fields of each j^{th} particle (of radius R_j and refractive index m_p) in the agglomerate[52-54]:

$$Escat(r) = \frac{1}{3}(m_p^2 - 1)\frac{\exp(ikr)}{r}\sum_{j=1}^{Np} k^2 R_j^3 \exp(-ikr_j \cos\beta_j)(\Theta_j \theta_1 - \Phi_j \phi_j), \qquad (2.43)$$

where $i = \sqrt{-1}$, $k=2\pi/\lambda$, λ is the wavelength of the incident radiation, θ_1 and ϕ_1 are respectively the unit vectors in the θ and ϕ directions, and

$$\Theta_j = \cos\theta\cos\phi E_x(r_j)+\cos\theta\sin\phi E_y(r_j)-\sin\theta E_z(r_j),$$

$$\Phi_j=\sin\phi E_x(r_j)-\cos\phi E_y(r_j). \qquad (2.44)$$

The center of the j^{th} primary particle is at the point $(x_j,y_j,z_j)\equiv(r_j,\theta_j,\phi_j)$ and

$$\cos\beta_j = \cos\theta_j\cos\theta + \sin\theta_j\sin\theta\cos(\phi_j-\phi). \tag{2.45}$$

The j^{th} primary particle internal electric fields $E_x(r_j)$, $E_y(r_j)$, and $E_z(r_j)$ (equation 2.44), in the rectangular coordinate system, are obtained by simultaneously solving a system of $3xN_p$ linear equations that give the internal electric fields of each particle in the agglomerate,

$$E(r_n) - \frac{1}{3}\left|\frac{m_p^2-1}{m_p^2+1}\right|\sum_{\substack{j=1\\ j\neq n}}^{Np}(kR)^3 T_{nj}E(r_j) = \frac{3}{m_p^2+1}E_{inc}(r_n), \tag{2.46}$$

where the term E_{inc} and E are the incident and internal electric fields. The second term in the left-hand side of the above equation takes into account the contributions to the internal field from the neighboring particles. The matrix T_{nj} is a 3x3 matrix that represents the contribution of the field interaction. The elements of the matrix are first kind spherical Hankel functions and Legendre functions. Details of the matrix T_{nj} can be found in the above given references.[52-54] The Rayleigh size particle approximation allows one to assume that the internal electric fields are constant within each primary particle. The internal fields may be substituted into the integral equation for the electric field at any point in space (equation 2.43) to yield the scattered electric field. A more detailed description of the Jones solution may be found in the above references. Although an exact

model, the Jones agglomerate model is computationally intensive[55,70,74,86] and has not been extensively used. Felske et al[55] used the Jones model to develop approximate analytical expressions to predict the vertical-vertical differential scattering cross section at 90°, the extinction cross section, and the vertical-vertical dissymmetry ratio at 45°, from the scattering characteristics of a single equivalent sphere that has the same scattering characteristics as the agglomerate. The equivalent sphere size parameter is related to the agglomerate primary particle size parameter and the agglomerate maximum length, and expressions for different agglomerate structures are given.

The Jones solution has been corrected for the appropriate representation of the refractive index[57] and the extinction efficiency factor.[85] Ku and Shim[86] also compared it to other agglomerate scattering solutions proposed by Purcel and Pennypacker[87] (P-P), and Iskander et al[88] (I-C-P). The Jones solution was rated as the least accurate of the three, and generally unreliable for resulting in negative extinction and/or scattering efficiency factors for the densely packed agglomerates.

Recently, Lou and Charalampopoulos[90] showed that all three proposed solutions for light scattering by agglomerates, namely; Jones, P-P, and I-C-P, do not satisfy the energy conservation requirement for the extinction, absorprtion and scattering efficiencies. Furthermore, they showed that the internal electric field equation in the Jones formulation is not invariant to coordinate transformations. Lou and Charalampopoulos[90] developed an exact form of the internal field equation for an assembly of Rayleigh size spherical particles irradiated by an electromagnetic wave. The following are the features of the new formulation: (i) The multiple scattering effects are accounted for by the T matrix. The

matrix T is a second order tensor, and therefore, the internal electric field equation is invariant to coordinate transformations; (ii) The electric field self-contribution effects are taken into account; (iii) The general exact solution for the internal electric field can be reduced to the form of the equation originally developed by Jones,[52-54] and to the solutions by Purcel and Pennypacker,[87] and Iskander et al,[88] as well as to the two-sphere analytical solution by Goedecke and O'Brien,[89] depending on how the self-contribution term is approximated; and (iv) The general electric field equation satisfies the energy balance requirement for the extinction, total scattering and absorption. The new formulation perfectly matches the analytical solution[89] for scattering by two Rayleigh size spheres, which confirmed the mathematical development and allowed verification of the new computer program developed for the calculation of the agglomerate scattering, extinction, and absorption characteristics.

The proceeding part of this section summarizes the new formulation[90] for the light scattering by agglomerates consisting of N_p Rayleigh size particles. The scattered amplitude of the electric field, E_{sca}, at a point (r,θ,ϕ) in the spherical coordinate reference system, is constructed by the internal electric fields of each j^{th} primary particle (of radius R_j and refractive index m_p) in the agglomerate:

$$E_{sca}(r) = \frac{m_p^2 - 1}{3}\frac{\exp(ikr)}{kr}\sum_{j=1}^{Np}(kR_j)^3 \exp(-ikr_j\cos\beta_j)(\Theta_j e_\theta - \Phi_j e_\phi), \qquad (2.47)$$

where $k=2\pi/\lambda$, and e_θ and e_ϕ are respectively the unit vectors in the θ and ϕ directions. The terms Θ_j, Φ_j, and $\cos\beta_j$, are given by equations (2.44) and (2.45). The j^{th} primary particle internal electric fields (equation 2.44) in the rectangular coordinate system $E_x(r_j)$, $E_y(r_j)$, and $E_z(r_j)$ are obtained by simultaneously solving a system of $3xN_p$ linear equations that give the internal electric field of each particle in the agglomerate, and are given by

$$E(r_n) = E_{inc}(r_n) + \frac{m_p^2 - 1}{3}\left\{-3 + 2i(kR_A)^2 h_1(kR_n)\right\}E(r_n) +$$

$$+\frac{m_p^2 - 1}{3} i \sum_{\substack{j=1 \\ j\neq n}}^{N_p} (kR_j)^2 j_1(kR_j) T_{nj} E(r_j) \quad . \tag{2.48}$$

The second term on the right side of the above equation represents the electric field self contribution effects in the particle being considered, and the third term accounts for the contributions to the electric field by the neighboring particles in the agglomerate. The matrix T_{nj} represents the contributions to the electric field interaction and is a second order tensor given by[90]

$$T = \begin{bmatrix} a & b & c \\ b & a' & a \\ c & d & e \end{bmatrix}, \tag{2.49}$$

with its elements defined as

$$a = 2h_0(kD) - h_2(kD)\left\{P_2(\cos\chi) - \frac{1}{2}\cos 2\psi P_2^2(\cos\chi)\right\}$$

$$a' = 2h_0(kD) - h_2(kD)\left\{P_2(\cos\chi) + \frac{1}{2}\cos 2\psi P_2^2(\cos\chi)\right\}$$

$$b = \frac{1}{2}h_2(kD)\sin 2\psi P_2^2(\cos\chi)$$

$$c = -h_2(kD)\cos 2\psi P_2^1(\cos\chi)$$

$$d = -h_2(kD)\sin\psi P_2^1(\cos\chi)$$

$$e = 2h_0(kD) + 2h_2(kD)P_2(\cos\chi)$$

$$\cos\chi = \frac{z_j - z_n}{D}$$

$$\tan\psi = \frac{y_j - y_n}{x_j - x_n}$$

$$D^2 = (x_j - x_n)^2 + (y_j - y_n)^2 + (z_j - z_n)^2, \qquad (2.50)$$

where h_0, h_2 are the first kind spherical Hankel functions, and P_2, P_2^1, and P_2^2 are the associated Legendre functions. Equations (2.48)-(2.50) above are given in the general form and no approximations were used in their development. With a third order approximation for the self-contribution term, equation (2.48) may be reduced[90] to

$$E(r_n)\left\{1 - \frac{m_p^2 - 1}{m_p^2 + 2}x^2\left(1 + \frac{2}{3}xi\right)\right\} - \frac{i}{3}\frac{m_p^2 - 1}{m_p^2 + 2}\sum_{\substack{j=1 \\ j\neq n}}^{Np} x_j^3 T_{nj} E(r_j) = \frac{3}{m_p^2 + 2}E_{inc}(r_n). \qquad (2.51)$$

The matrix **T** in the equations (2.51 and 2.48) above is a second order tensor, and therefore, the internal electric field equation is conformable or invariant to coordinate transformation (rotation). The advantage of the conformity of the internal electric field equation is further discussed in the later part of this section, and in the next chapter. Expressions for the extinction and absorption cross sections are also given by Lou and Charalampopoulos.[90] The extinction cross section C_{ext} for agglomerates of uniformly sized spherical particles is given by

$$C_{ext} = 4\pi R^2 j_1(x)\,\mathrm{Im}\left\{(m_p^2 - 1)\sum_{j=1}^{N_p} E_j \cdot E_{inc}^*\right\}, \qquad (2.52)$$

and the absorption cross section C_{abs} by

$$C_{abs} = 4\pi R^2 j_1(x)\,\mathrm{Im}(m_p^2 - 1)\sum_{j=1}^{N_p}\left|E_j\right|^2, \qquad (2.53)$$

where the asterisk denotes the complex conjucate, Im is the imaginary part of a complex number, E_j is the internal electric field of the j^{th} particle in the agglomerate, and j_1 is the spherical Bessel function. The differential scattering intensities, I_{sca}^V and I_{sca}^H, in respectively the vertical and horizontal planes of polarization, are given by[90]

$$I_{sca}^{V} = \frac{1}{r^2}\left|m_p^2 - 1\right|^2 k^2 R^4 j_1^2(x) \sum_{j=1}^{Np} \sum_{n=1}^{Np} \exp\left\{ik(r_j \cos\beta_j - r_n \cos\beta_n)\Phi_n \Phi_j^*\right\}, \qquad (2.54)$$

and

$$I_{sca}^{H} = \frac{1}{r^2}\left|m_p^2 - 1\right|^2 k^2 R^4 j_1^2(x) \sum_{j=1}^{Np} \sum_{n=1}^{Np} \exp\left\{ik(r_j \cos\beta_j - r_n \cos\beta_n)\Theta_n \Theta_j^*\right\}. \qquad (2.55)$$

The assumption for the development of the above relations is that the agglomerate is oriented randomly with respect to the incident electromagnetic wave. In order to simulate realistic light scattering results, the computational scheme developed (for calculating the agglomerate light scattering characteristics) averages the scattering results over a large number of agglomerate orientations. Specifically, a total of 10x10 azimuth stations (or agglomerate orientations with respect to the incident electromagnetic wave) are used[54-54,90] in the averaging of the results. The general and reduced internal electric field equations (2.48) and (2.51) may be written[90] in a matrix form as

$$\mathbf{M}\,\mathbf{E} = \mathbf{B}, \qquad (2.56)$$

where **M** is a $3N_p x 3N_p$ matrix, and **E** and **B** are $3N_p x 1$ matrices representing respectively the unknown electric field and the incoming electromagnetic wave. With a coordinate system fixed to the incident wave coordinate system, **M** varies and **B** remains fixed during the averaging over the 10x10 different agglomerate orientations. For each agglomerate orientation, **M** is established and the $\mathbf{M}^{-1}$ is evaluated. The evaluation and inversion of **M** for 100 orientations becomes computationally cumbersome. Lou and Charalampopoulos[90]

recognized that the matrix **T** is a second order tensor and therefore, **M** in equation (2.56) is invariant to coordinate transformation. If the agglomerate is fixed at one orientation, a structural coordinate system (x',y',z') can be established. The matrix **M** can now remain fixed, and the matrix **B** for the incident wave can be rotated at all 100 azimuth stations, thus requiring the evaluation of **M** and its inverse $\mathbf{M}^{-1}$ only once. By keeping the agglomerate fixed and rotating the incident electromagnetic wave, the efficiency of the computations improves by approximately 99%.

Additional improvements in the efficiency of the agglomerate light scattering computations were achieved by optimizing the computer program. The details of the optimization are presented in the next chapter along with the sensitivity analysis performed for the type of measurements that are being considered in this study. Specifically, the aim of this work is to measure the extinction and differential scattering cross sections, the dissymmetry ratios in both VV and HH planes of polarization, and the depolarization ratio, of soot agglomerates formed in flat, laminar, and fuel rich propane/oxygen flames. The measured quantities will be used with the new agglomerate formulation[90] to infer the stuctural and optical properties of the soot agglomerates. The appropriate equations and unknown parameter to be used in the analysis are given in the next chapter.

CHAPTER 3

COMPUTATIONS AND SENSITIVITY ANALYSIS

3.1 Computer Program Optimization

One of the main disadvantages in computations of the scattering characteristics of a randomly branched chain in the past, was that it required extremely long processing times.[55,70,74,85,90] The original FORTRAN programs that were developed based on the Jones agglomerate model were separated into three programs: the straight chain, the cluster, and the randomly branched chain. All computations were performed in single precision. Also, the scattering characteristics of an agglomerate were computed for only the vertical or the horizontal polarization state of the incident beam. In the cases where both the vertical and horizontal states of polarization were investigated, the computational effort was doubled. The computations were also limited to agglomerates consisting of up to about 30 primary particles, because of central processor memory considerations. Furthermore, an external mathematical function library (IMSL) was required for generating the randomly branched chains. One of the objectives of the current work is to optimize the computer program so that shorter computational times are required for calculations of the scattering characteristics of randomly branched chain agglomerates.

The computer programs were consolidated into one subroutine that handles all three agglomerate structures, namely: straight chains, clusters, and randomly branched chains.[90] The agglomerate scattering characteristics can now be calculated simultaneously

for both the vertical and the horizontal polarization states of the incident electromagnetic radiation, in both single and double precision. The program was modified to handle straight and randomly branched chain agglomerates consisting of up to 100 primary particles[90] or more, depending on the memory capability of the computer. A random number generator subroutine used for generating the randomly branched chains was added to the program, making it portable to machines that do not support the appropriate mathematical function libraries (IMSL). The above changes did not account for any improvements in the computational times required, but made the program more versatile, portable, and easier to use.

As mentioned in section 2.2, the original computer program calculated the scattering characteristics of the agglomerate by averaging over all possible orientations of the agglomerate in a three-dimensional space. The averaging is achieved by rotating the agglomerate at 10x10 orientations with respect to the incident electromagnetic wave. By confirming that the governing equation for the internal field of the agglomerate primary spheres is conformable or invariant to coordinate transformation (rotation), the incident incoming wave can be rotated at all angles instead of the agglomerate. This change in the computational scheme improved the efficiency of the computations by approximately 99%.[90] A diagnostic test performed on the program revealed severe inefficiencies. A large amount (33.1%) of the computational effort was being consumed in the evaluation of trigonometric functions. "Hot spots" in the program, such as inefficient loops and computationally intensive FORTRAN statements were also identified. The program was optimized by restructuring the inefficient loops and storing information used repeatedly in

easy to access temporary memory storage locations. Also, the trigonometric functions are calculated directly from the agglomerate geometry. The optimization of the program resulted in an impressive improvement in the computational efficiency of the computer code. Table 3.1 shows the improvements in the computational times required for calculating all the scattering and absorption characteristics of the three different agglomerate geometries. The following parameters are computed in the program performance tests: the total scattering, absorption and extinction efficiencies; the differential scattering cross sections in the VV, VH, HH and HV polarization states and at all angles (0°-180°); the dissymmetry ratios R_{VV} and R_{HH} at all angles (0°-90°); the depolarization ratios ρ_V and ρ_H at all angles (0°-180°); and the agglomerate maximum length. The agglomerates used in the efficiency tests consist of 20 primary particles of size parameter 0.125 and refractive index m=1.7 - 0.7i. The same computations were performed on three different mainframe computers to obtain the fastest system available by the LSU computing services. Table 3.1 compares the CPU times required by the double precision version of the new optimized program to the those of the single precision original program. On all machines except the UNIX RS6000, the computations performed in double precision are actually more time-consuming than those in single precision. The computational time requirements between the single and double precision versions of the new program are compared in Table 3.2. The agglomerate parameters are the same as those used for the computations presented in the previous table. As it can be seen, the most efficient computations were obtained with the double precision version of the

program on the UNIX RS6000 cluster. For this reason, the rest of the computational efficiency tests presented in this section were performed on the RS6000 machine.

Table 3.1 Comparison of the computational times required by the original and the new programs for calculations of light scattering by an agglomerate. The CPU times for the randomly branched chains are for the simulation of 100 agglomerates.

	CPU TIME (seconds)					
	VAX 7000		IBM 3090		UNIX RS6000	
Agglomerate Structure	Original Program	New Program	Original Program	New Program	Original Program	New Program
Straight Chain	36.1	6.3	33.6	15.6	6.0	1.1
Cluster	27.7	6.3	40.8	15.0	10.6	0.98
Random Chain	2792.8	607.5	3631.2	580.8	900.1	94.6

Table 3.2 Comparison of the computational times required by the single and double precision versions of the new program for light scattering by an agglomerate. The CPU times for the randomly branched chains are for the simulation of 100 agglomerates.

	CPU TIME (seconds)					
	VAX 7000		IBM 3090		UNIX RS6000	
Agglomerate Structure	Single Precision	Double Precision	Single Precision	Double Precision	Single Precision	Double Precision
Straight Chain	3.4	6.3	15.0	15.6	1.5	1.1
Cluster	3.4	6.3	13.8	15.0	1.5	0.98
Random Chain	322.4	607.5	520.8	580.8	126.8	94.6

The efficiency of the computations of all the scattering, absorption, and extinction characteristics of agglomerates consisting of primary particles of 0.125 size parameter and refractive index of m=1.7-0.7i was investigated for different cases of number of primary particles N_p. The new program becomes more efficient as the number of primary particles increases. This effect is shown in Figure 3.1, where the new straight chain agglomerate program is about 1.9 times faster than the old program for the case of 5 primary particles. In the case of a chain of 50 primary particles, the new program is 8.7 times faster than the old. A similar behavior is observed in the case of cluster agglomerated structures. The new program is 5.7 times faster for 5 primary particles, and about 10 times faster for 30 primary particle calculations (Figure 3.2).

When randomly branched chain agglomerates are studied, a large number of agglomerates must be simulated in order to account for the multiple possible structures that can exist. Of course, the more simulated agglomerate structures used in the averaging process, the better (statistically) the results. For the purposes of these computer program efficiency tests, the average results of the simulation of 500 randomly branched chains were considered. Since each iteration for a new agglomerate simulation does not depend on the previous iterations, a parallel processing scheme can be used to make the computer program even more efficient. The Parallel Virtual Machine (PVM) version 3.3.2 software was used to incorporate 4 serial computers to work concurrently as one computational resource. In very simple terms, the PVM software system uses a master program that distributes a sequential program (called the slave program) to be concurrently run on a homogeneous or heterogeneous network of computers. The master program assigns

different tasks to each slave program and handles the communications between the slave and master programs. In the specific case of the randomly branched chain program, the task of simulating 500 agglomerates was divided between four processors running concurrently, with each processor simulating 125 agglomerates. A master program was used to initiate the slave programs at each processor, and to communicate with them for assigning tasks and receiving the results. Details of the PVM master and slave programs, as well as the necessary commands used to run them, are given in the appendix. It was observed that the computational effort was reduced by a factor of four using PVM parallel processing on the four processors available on the UNIX RS6000 system. Figure 3.3 shows the results of the comparison of the computational efficiency of the original, new (sequential), and new (PVM) agglomerate programs. For an agglomerate consisting of 50 primary particles it was found that the new program is 11.8 times faster than the original version. When PVM is used, the computational effort is 47.8 times more efficient. The results also demonstrate that with more processors available, the CPU times required for computations using PVM can be reduced by approximately Nx10 times; where N is the number of processors available.

As mentioned earlier, in the case of a randomly branched chain, a large number of agglomerates is required to give statistically meaningful results. This raises a logical question: How many randomly branched agglomerates are required for a good statistical average? Since these agglomerates are generated by randomly building the structure using a specified number of primary particles, one should be concerned with simulating enough agglomerates, especially when using a large number of primary particles, so that all the

possible ways of building the agglomerate are used. The effect of the number of simulated agglomerates on the calculated average scattering results was investigated for agglomerates of different number of primary particles N_p.

Up to 2000 agglomerates, consisting of different number of primary particles N_p, of 0.125 size parameter and refractive index of m=1.7-0.7i, were generated. The results obtained from the averaging of 2000 randomly branched agglomerates were considered to be the optimum total number of agglomerates needed. These were used to normalize the rest of the results so that a comparison could be made between the average results from agglomerates with different number of primary particles N_p. Figures 3.4 -3.9 show respectively the normalized average results of: the ratio of: the differential scattering cross section at 20° to the extinction cross section; the dissymmetry ratio R_{VV} at 20°; the dissymmetry ratio R_{HH} at 20°; the depolarization ratio ρ_V at 160°; the depolarization ratio ρ_H at 160°; and the agglomerate size parameter x_l , for randomly branched chain agglomerates consisting of 10, 30, 50, 75 and 100 primary particles. It can be observed from these figures that the average results of 600 or more agglomerates simulated, are within a maximum of 2% from the results obtained when 2000 agglomerates are used.

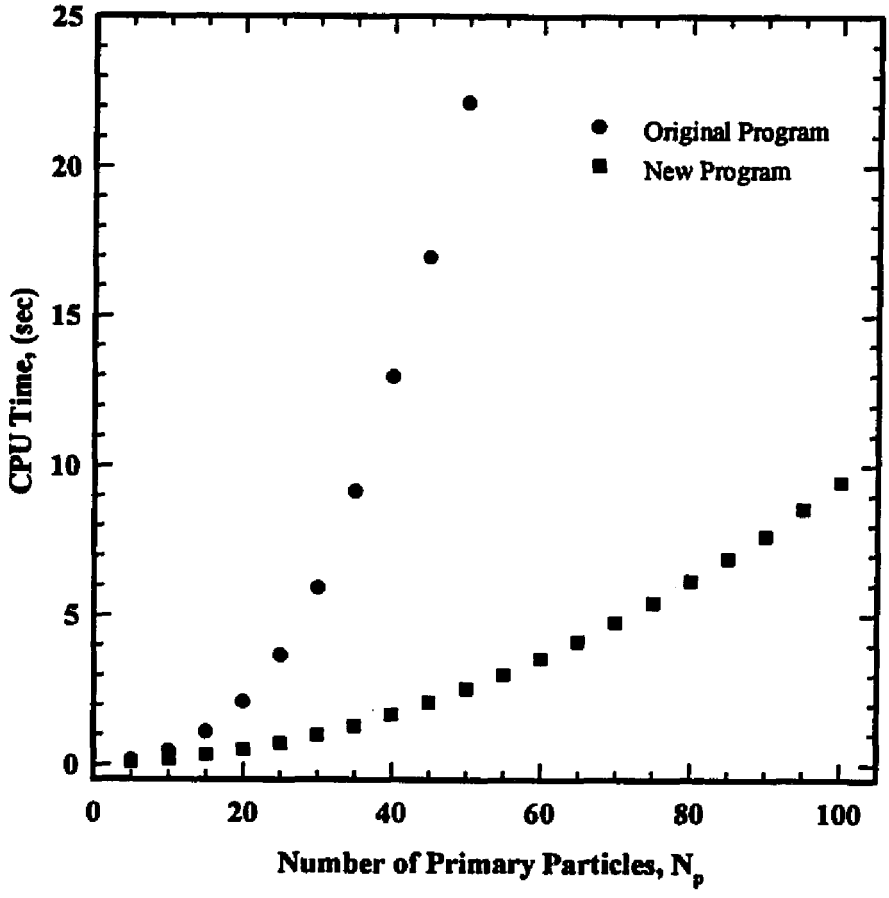

Figure 3.1 Comparison of the computational times required by the original and new programs for calculating all the scattering and absorption characteristics of a straight chain agglomerate consisting of primary particles with 0.125 size parameter and refractive index m=1.7-0.7i.

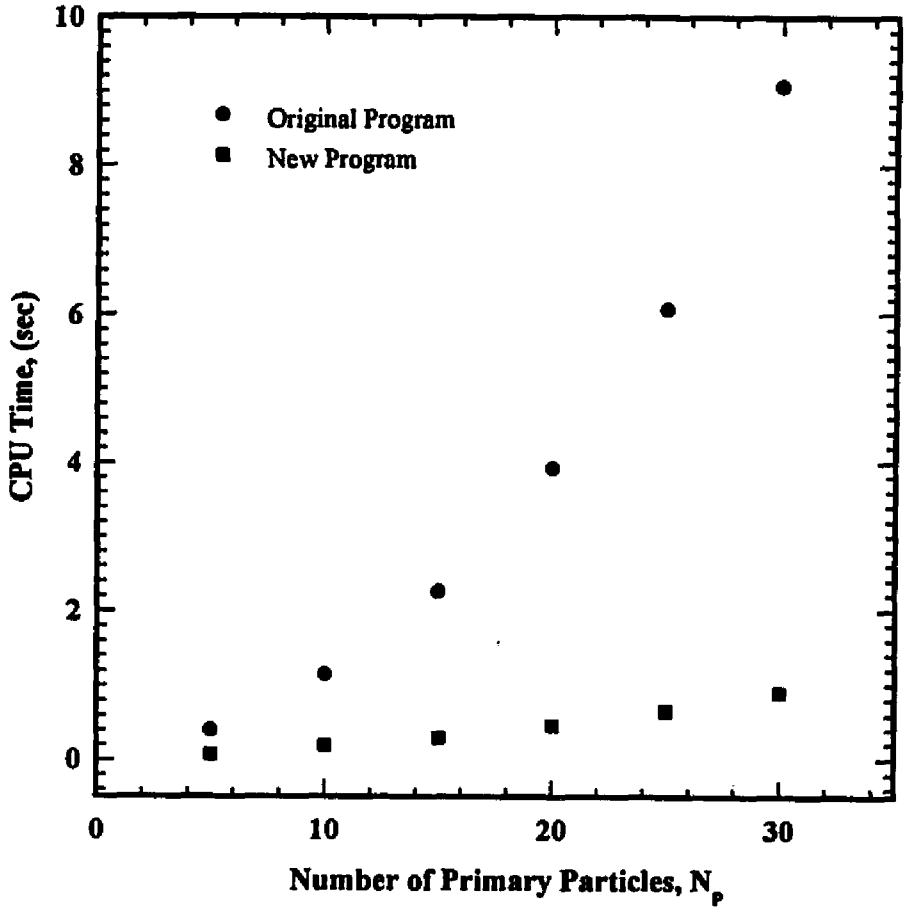

Figure 3.2 Comparison of the computational times required by the original and new programs for calculating all the scattering and absorption characteristics of a cluster consisting of primary particles with 0.125 size parameter and refractive index m=1.7-0.7i.

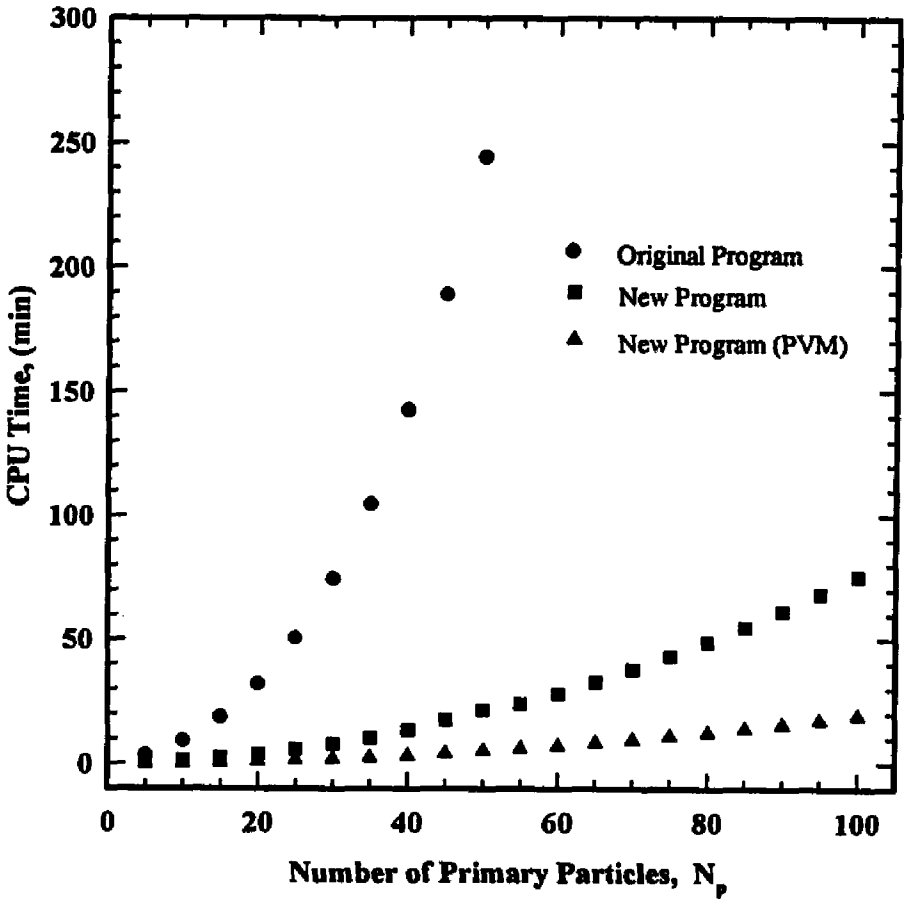

Figure 3.3 Comparison of the computational times required by the original, new program, and new PVM program, for calculating all the scattering and absorption characteristics, averaged over 500 randomly branched chain agglomerates consisting of primary particles with 0.125 size parameter and refractive index m=1.7-0.7i.

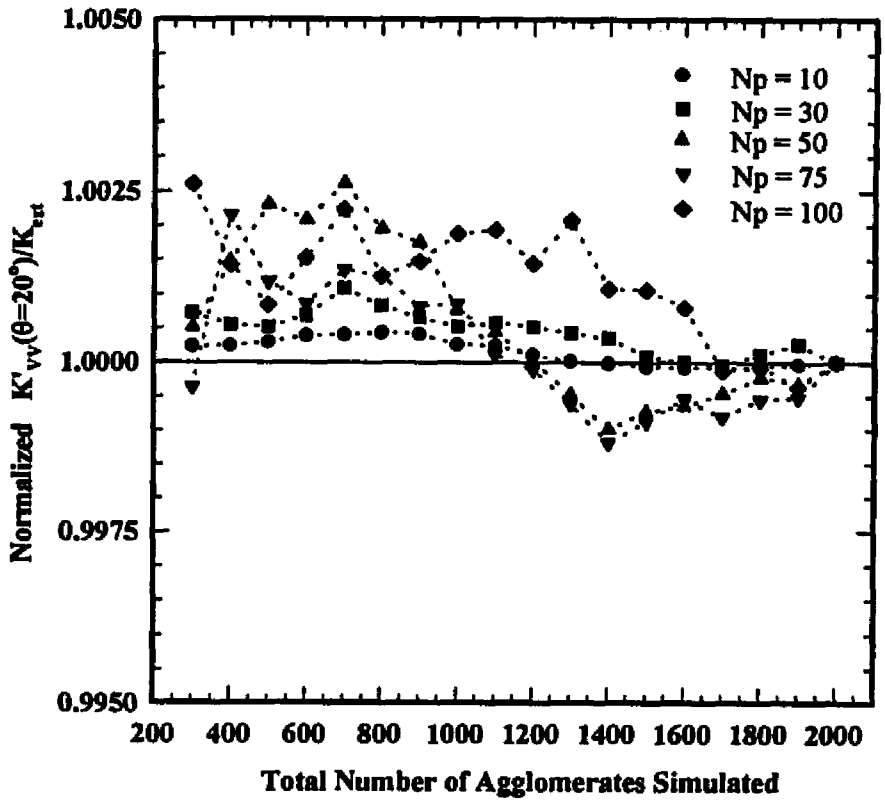

Figure 3.4 Normalized average results of the ratio for the differential scattering cross section at 20° to the extinction cross section for randomly branched chain agglomerates as a function of the number of agglomerates simulated and used in the averaging. The agglomerates consist of 10, 30, 50, 75, and 100 primary particles.

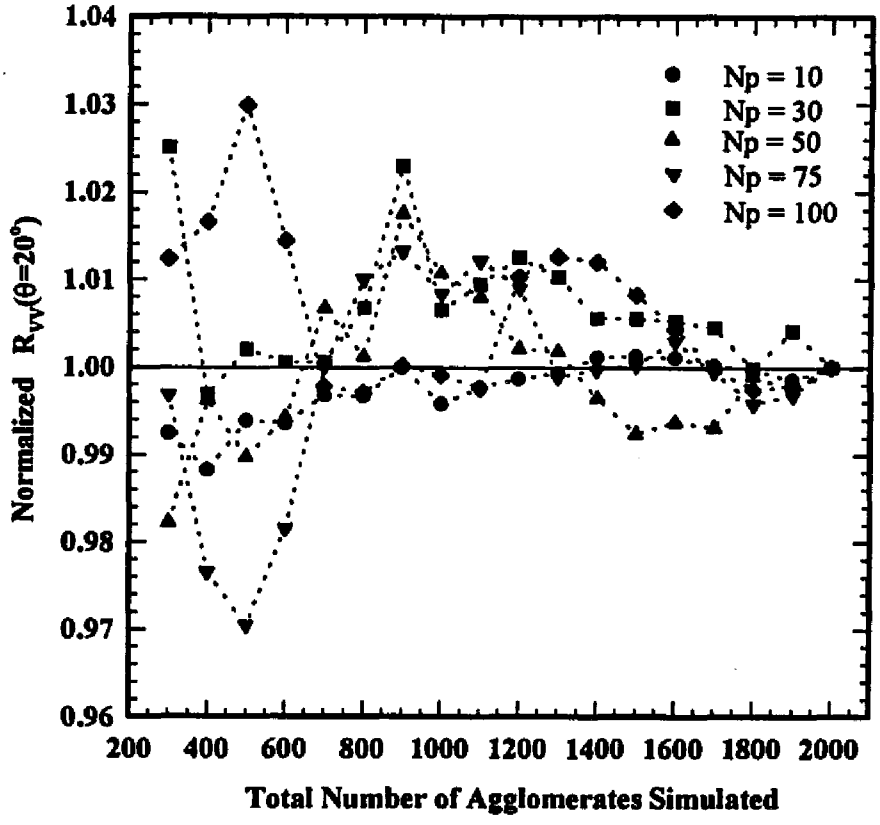

Figure 3.5 Normalized average results of the dissymmetry ratio R_{VV} at 20° for randomly branched chain agglomerates as a function of the number of agglomerates simulated and used in the averaging. The agglomerates consist of 10, 30, 50, 75, and 100 primary particles.

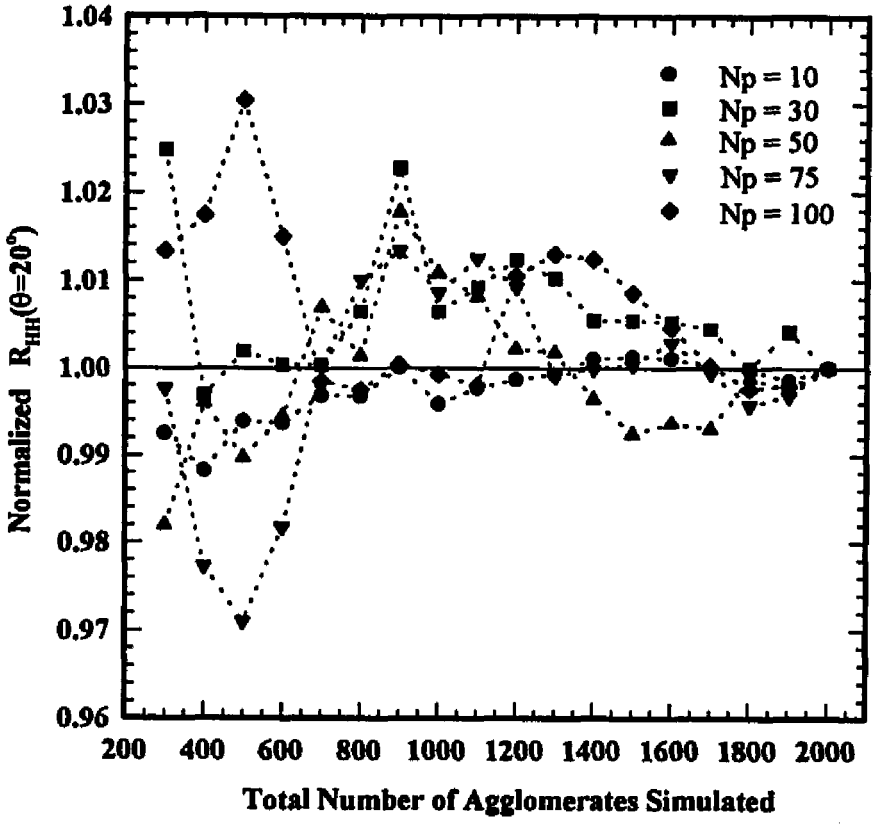

Figure 3.6 Normalized average results of the dissymmetry ratio R_{HH} at 20° for randomly branched chain agglomerates as a function of the number of agglomerates simulated and used in the averaging. The agglomerates consist of 10, 30, 50, 75, and 100 primary particles.

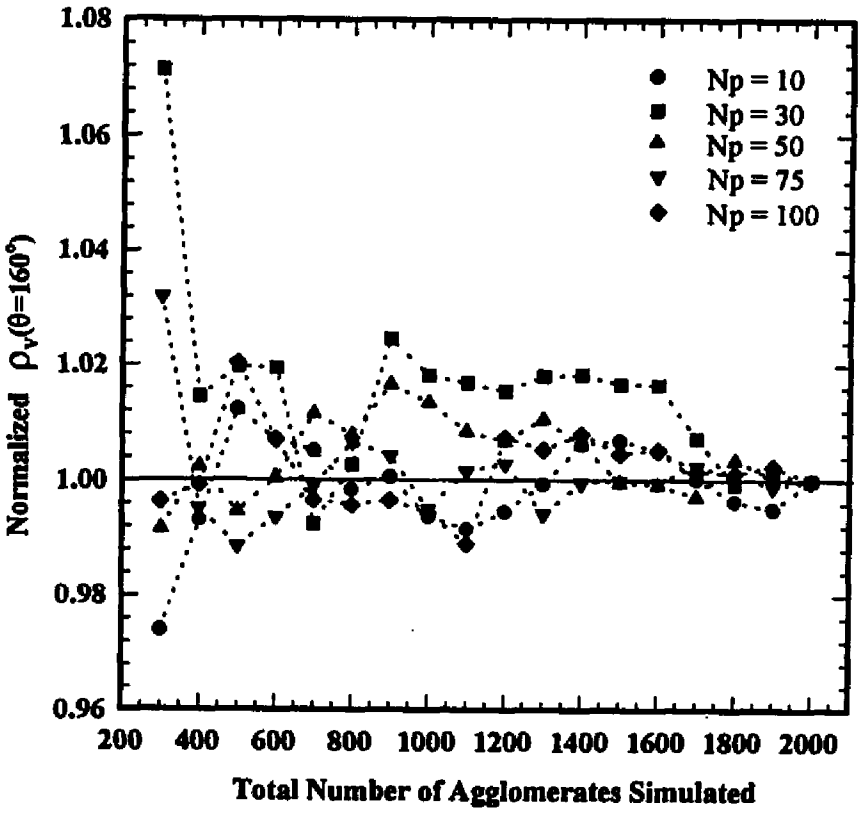

Figure 3.7 Normalized average results of the depolarization ratio ρ_V at 160° for randomly branched chain agglomerates as a function of the number of agglomerates simulated and used in the averaging. The agglomerates consist of 10, 30, 50, 75, and 100 primary particles.

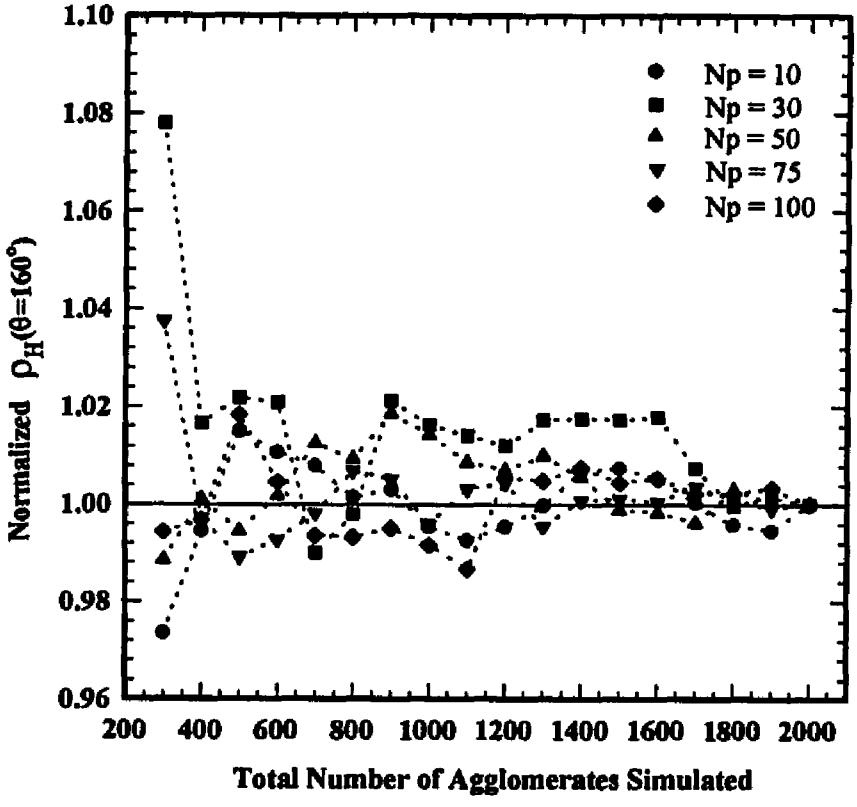

Figure 3.8 Normalized average results of the depolarization ratio ρ_H at 160° for randomly branched chain agglomerates as a function of the number of agglomerates simulated and used in the averaging. The agglomerates consist of 10, 30, 50, 75, and 100 primary particles.

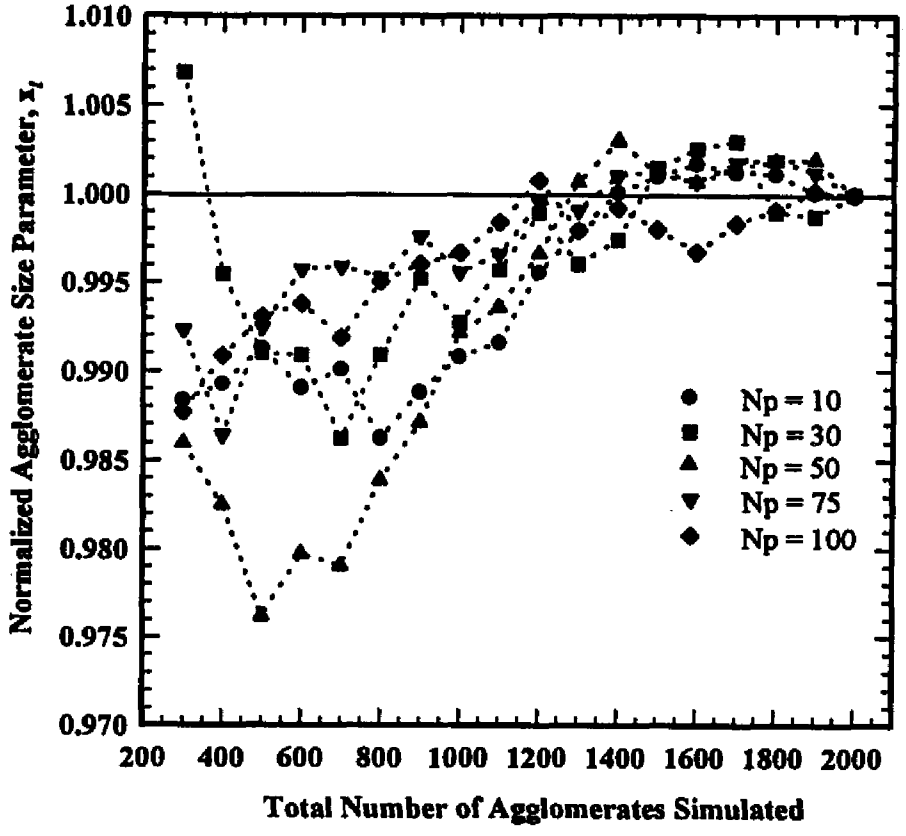

Figure 3.9 Normalized average results of the agglomerate size parameter x_f for randomly branched chain agglomerates as a function of the number of agglomerates simulated and used in the averaging. The agglomerates consist of 10, 30, 50, 75, and 100 primary particles.

3.2 Agglomerate Simulations and Sensitivity Analysis

As mentioned previously, the objective of this work is to develop a new method for determining the properties of agglomerated structures in flame reacting systems. For a simple monodispersed system of agglomerated structures, the unknown parameters are: (i) the particle size d_p of the primary particles; (ii) the number of primary particles per agglomerate N_p; (iii) the real n and imaginary k parts of the refractive index of the primary particle; and (iv) the number density N of monosized agglomerates. The functional form of the expressions relating the above parameters to the measured quantities are summarized in the following section.

a. Differential scattering coefficient, K'_{VV}, for a cloud of agglomerates

$$K'_{VV}(\theta) = NC'_{VV,Aggl}(\theta) = N f_1(\theta, N_p, \alpha_p, n, k), \qquad (3.1)$$

where $C'_{VV,Aggl}$ is the scattering cross section of each agglomerate, which is a function of the scattering angle θ, the number of primary particles N_p, the size parameter α_p ($= \pi d_p/\lambda$), and the refractive index m_p=n-ik. The subscripts VV signify the state of the polarization of the incident and scattered electromagnetic wave of wavelength λ. As mentioned, the vertical and horizontal states of polarization will be represented by V and H respectively.

b. Extinction coefficient of the cloud of agglomerates, K_{ext},

$$K_{ext} = NC_{ext,Aggl} = N f_2(N_p, \alpha_p, n, k), \tag{3.2}$$

where $C_{ext,Aggl}$ is the extinction cross section of a single agglomerate.

c. Dissymmetry ratio in the vertical-vertical orientation, R_{VV},

$$R_{VV}(\theta) = \frac{C'_{VV,Aggl}(\theta)}{C'_{VV,Aggl}(180^\circ - \theta)} = f_3(\theta, N_p, \alpha_p, n, k). \tag{3.3}$$

d. Dissymmetry ratio in the horizontal-horizontal orientation, R_{HH},

$$R_{HH}(\theta) = \frac{C'_{HH,Aggl}(\theta)}{C'_{HH,Aggl}(180^\circ - \theta)} = f_4(\theta, N_p, \alpha_p, n, k). \tag{3.4}$$

e. Depolarization ratio, ρ_V,

$$\rho_V(\theta) = \frac{C'_{VH,Aggl}(\theta)}{C'_{VV,Aggl}(\theta)} = f_5(\theta, N_p, \alpha_p, n, k). \tag{3.5}$$

By combining equations (3.1) and (3.2), the agglomerate number density N can be eliminated. The result is a system of four nonlinear equations with four unknown parameters, namely N_p, d_p, n, and k.

$$\frac{K'_{VV}(\theta)}{K_{ext}} = \frac{C'_{VV,Aggl}(\theta)}{C_{ext,Aggl}} = F_1(\theta, N_p, \alpha_p, n, k), \tag{3.6}$$

$$R_{VV}(\theta) = \frac{C'_{VV,Aggl}(\theta)}{C'_{VV,Aggl}(180^\circ - \theta)} = F_2(\theta, N_p, \alpha_p, n, k), \qquad (3.7)$$

$$R_{HH}(\theta) = \frac{C'_{HH,Aggl}(\theta)}{C'_{HH,Aggl}(180^\circ - \theta)} = F_3(\theta, N_p, \alpha_p, n, k), \qquad (3.8)$$

and

$$\rho_V(\theta) = \frac{C'_{VH,Aggl}(\theta)}{C'_{VV,Aggl}(\theta)} = F_4(\theta, N_p, \alpha_p, n, k). \qquad (3.9)$$

The agglomerate scattering and extinction characteristics given by equations (3.6)-(3.9) were calculated as functions of the scattering angle for randomly branched chain agglomerates consisting of 20 primary particles, of primary particle size parameter 0.125, and refractive index of m=1.7-0.7i. The effects of each of the agglomerate parameters N_p, α_p, n, and k are shown in the following three-dimensional plots where three of the four parameters are kept constant, and the fourth one is varied over the appropriate range of values that apply to the flames investigated. The range of values used in the calculations are: α_p=0.01 - 0.5, N_p=4 - 100, n=1.0 - 1.9, and k=0.3 - 0.9. Figures 3.10 - 3.13 show the effect of the primary particle size parameter, α_p, and the scattering angle, θ, on the agglomerate scattering and extinction characteristics. The agglomerate scattering characteristics $K'_{VV}(\theta)/K_{ext}$, R_{VV}, and R_{HH}, display a larger dependence with larger primary particle size parameters and in the forward scattering angles. The agglomerate depolarization ρ_V displays a large dependence with larger primary particle size parameters

and in the backward scattering angles. The same behavior can be observed when the effect of the number of primary particles N_p, and the scattering angle θ on the agglomerate scattering characteristics are studied (Figures 3.14-3.17). Namely, the agglomerate parameters $K'_{vv}(\theta)/K_{ext}$, R_{VV}, and R_{HH}, display stronger dependence with larger number of primary particles N_p and in the forward scattering angles, while the depolarization ratio ρ_V is stronger in the backward scattering angles and for larger number of primary particles. Figures 3.18-3.21 show the effects of the real part of the primary particle refractive index and the scattering angle on the agglomerate scattering characteristics. The ratio of the differential scattering to extinction cross sections $K'_{vv}(\theta)/K_{ext}$, displays strong dependence on the real part of the refractive index in the forward scattering angles. Both the dissymmetry ratios R_{VV} and R_{HH} are very weak functions of the refractive index. The depolarization ratio ρ_V is again a strong function of the real part of the refractive index, and the scattering angle. In the cases of the effects on the agglomerate scattering characteristics of the imaginary part k of the primary particle refractive index and the scattering angle, only the depolarization ratio ρ_V proved to be a strong function of both the parameters k and θ (see Figures 3.22-3.25). The ratio $K'_{vv}(\theta)/K_{ext}$ is a weaker function of k, while both the dissymmetry ratios are very weak functions of k. Similar behavior to the one shown by Figures 3.10-3.25 was observed when straight chain or cluster agglomerates are considered. The results for straight chain and cluster agglomerates are presented in Appendix A. In summary, the three-dimensional plots of the agglomerate scattering characteristics given by equations (3.6)-(3.9) indicate that: (1) the ratio of the differential scattering to extinction cross section $\{K'_{vv}(\theta)/K_{ext}\}$

measurement is more sensitive with a decreasing scattering angle, an increasing number of primary particles, and an increasing primary particle size parameter. The measurement is less sensitive to the real part of the refractive index, and has a weak dependence on the imaginary part; (2) the measurements of the dissymmetry ratios R_{VV} and R_{HH} are sensitive with an increasing number of primary particles, an increasing primary particle size parameter, and a decreasing scattering angle. There is a very weak dependence on both the real and imaginary parts of the refractive index; and (3) the depolarization ratio ρ_V is more sensitive with an increasing scattering angle, an increasing primary particle size parameter, an increasing number of primary particles, and increasing real and imaginary parts of the refractive index.

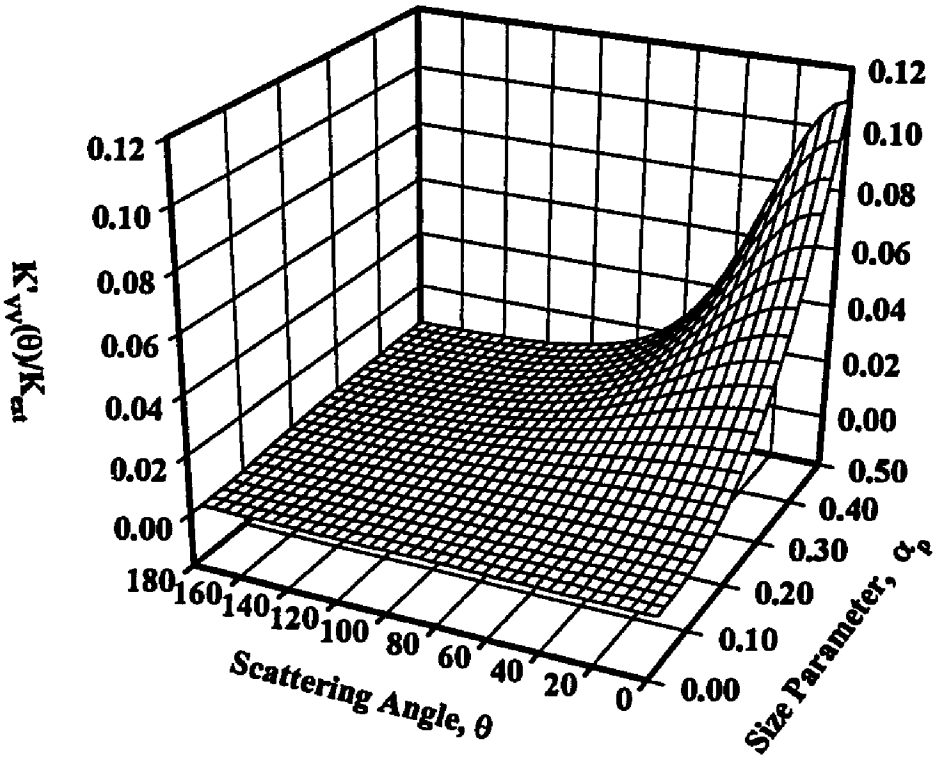

Figure 3.10 The differential scattering cross section to extinction cross section ratio $\{K'_{vv}(\theta)/K_{ext}\}$ as a function of the scattering angle θ, and the primary particle size parameter α_p, for a randomly branched chain agglomerate of N_p=20 and m=1.5-0.5i.

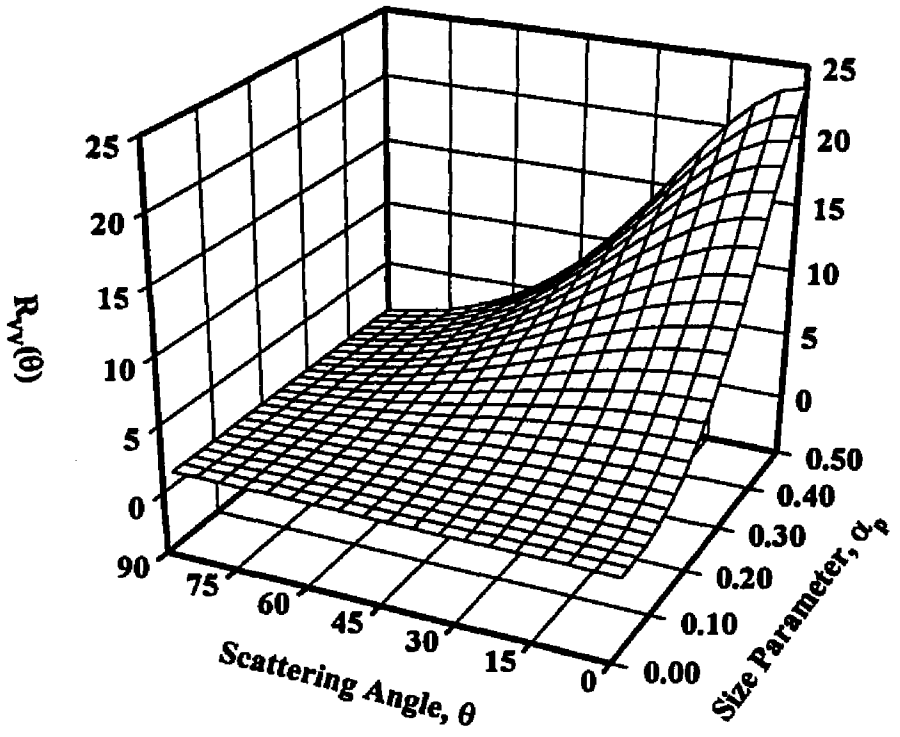

Figure 3.11 The dissymmetry ratio R_{VV} as a function of the scattering angle θ, and the primary particle size parameter α_p, for a randomly branched chain agglomerate of N_p=20 and m=1.5-0.5i.

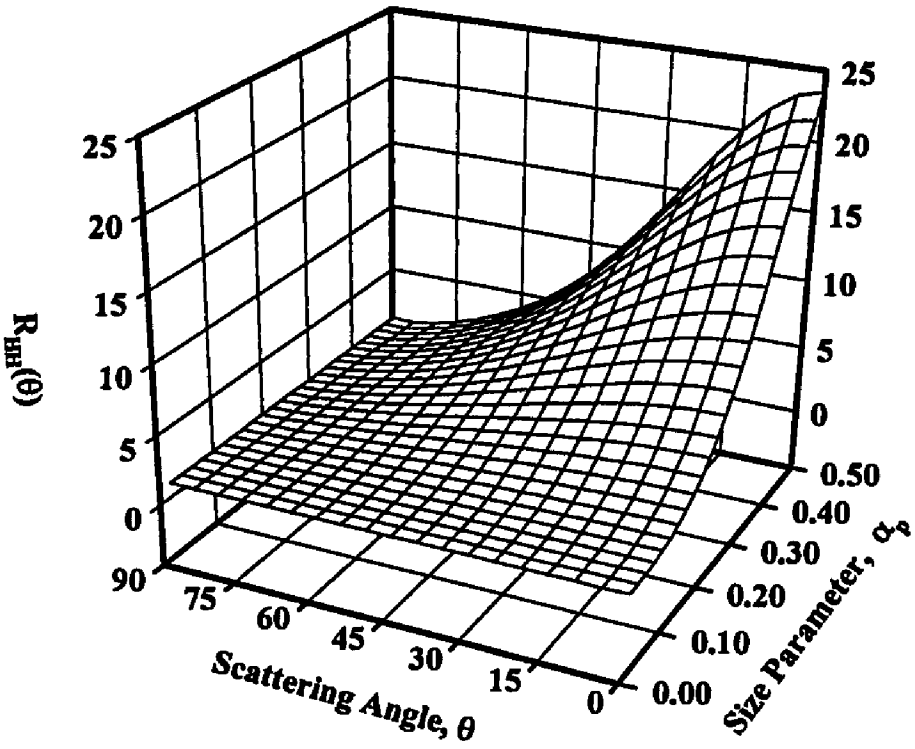

Figure 3.12 The dissymmetry ratio R_{HH} as a function of the scattering angle θ, and the primary particle size parameter α_p, for a randomly branched chain agglomerate of N_p=20 and m=1.5-0.5i.

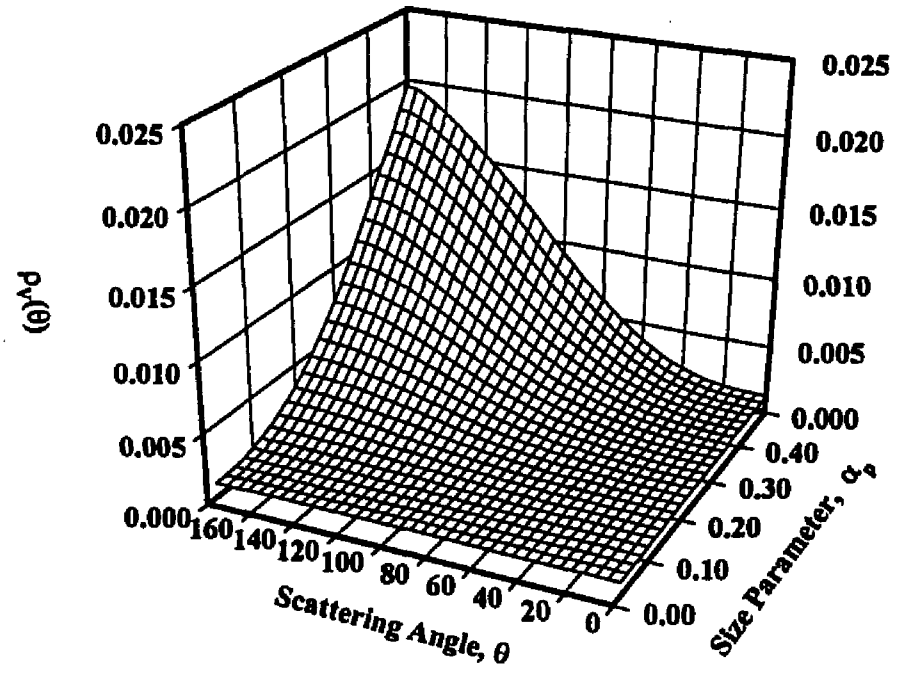

Figure 3.13 The depolarization ratio ρ_v as a function of the scattering angle θ, and the primary particle size parameter α_p, for a randomly branched chain agglomerate of N_p=20 and m=1.5-0.5i.

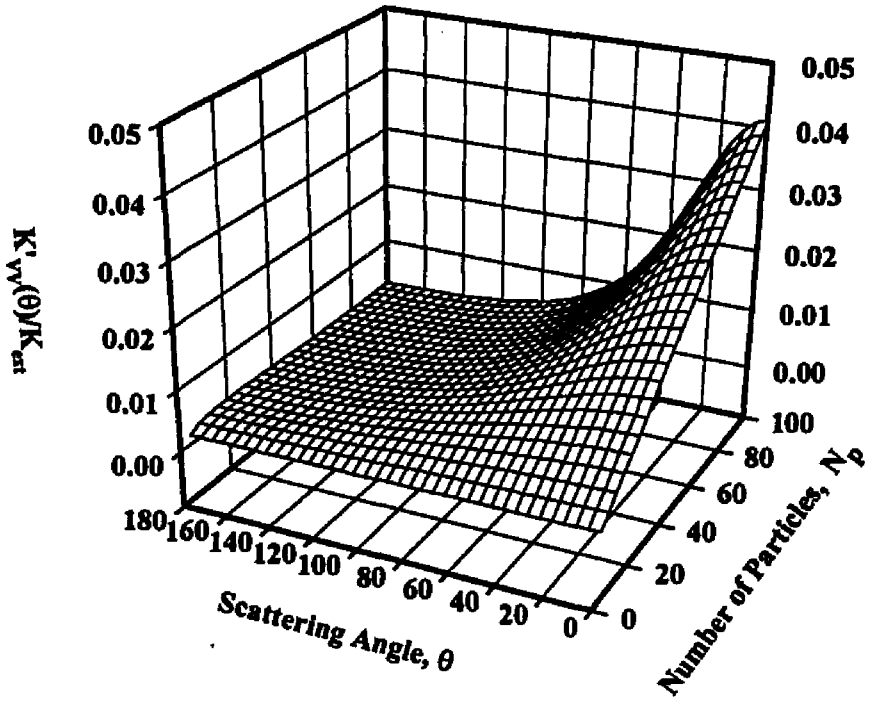

Figure 3.14 The differential scattering cross section to extinction cross section ratio $\{K'_{vv}(\theta)/K_{ext}\}$ as a function of the scattering angle θ, and the number of primary particles N_p, for a randomly branched chain agglomerate of α_p=20 and m=1.5-0.5i.

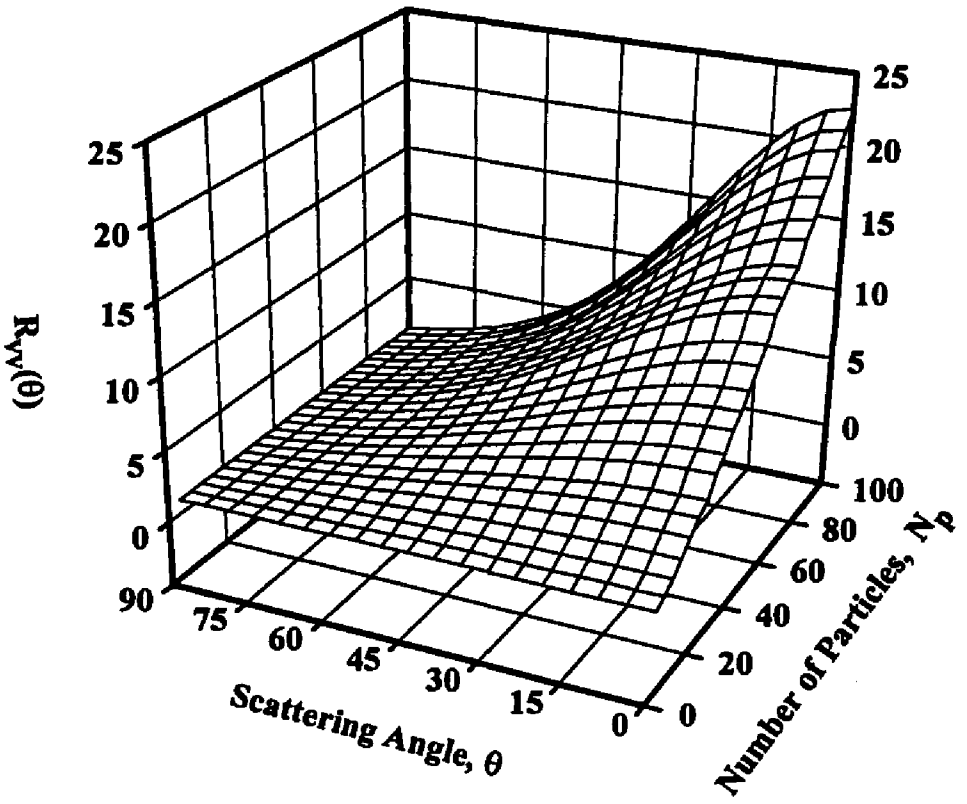

Figure 3.15 The dissymmetry ratio R_{VV} as a function of the scattering angle θ, and the number of primary particles N_p, for a randomly branched chain agglomerate of α_p=0.125 and m=1.5-0.5i.

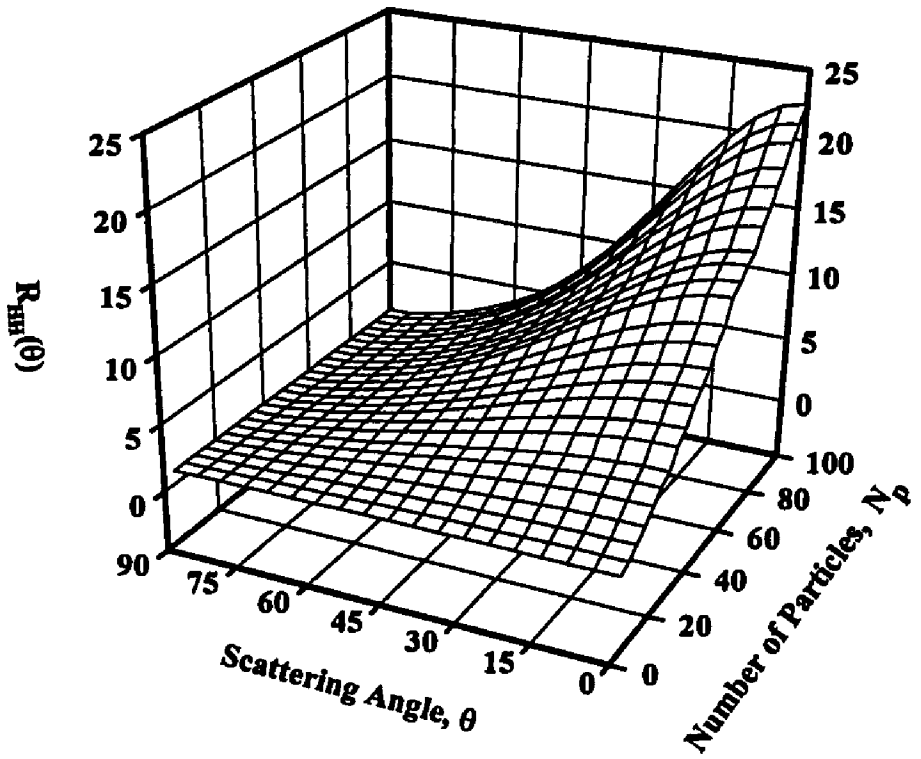

Figure 3.16 The dissymmetry ratio R_{HH} as a function of the scattering angle θ, and the number of primary particles N_p, for a randomly branched chain agglomerate of α_p=0.125 and m=1.5-0.5i.

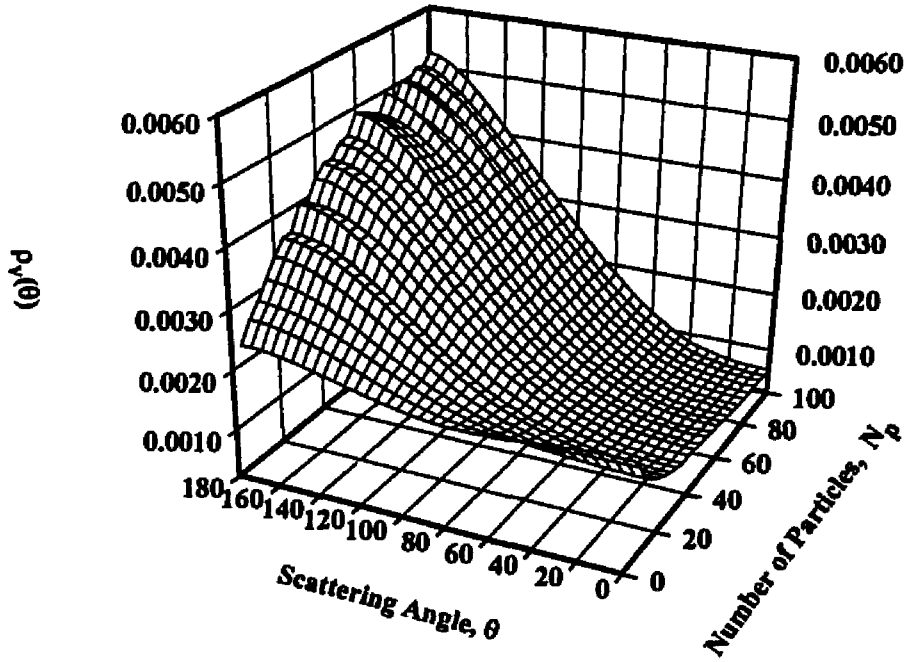

Figure 3.17 The depolarization ratio ρ_V as a function of the scattering angle θ, and the number of primary particles N_p, for a randomly branched chain agglomerate of α_p=0.125 and m=1.5-0.5i.

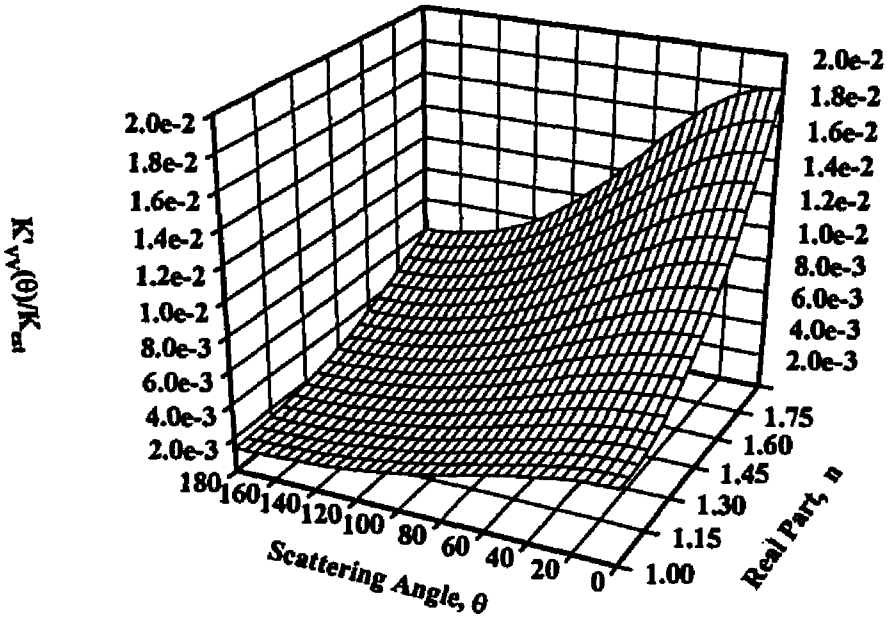

Figure 3.18 The differential scattering cross section to extinction cross section ratio $\{K'_{vv}(\theta)/K_{ext}\}$ as a function of the scattering angle θ, and the real part of the refractive index, for a randomly branched chain agglomerate of N_p=20, α_p=0.125 and imaginary part of the refractive index k=0.5.

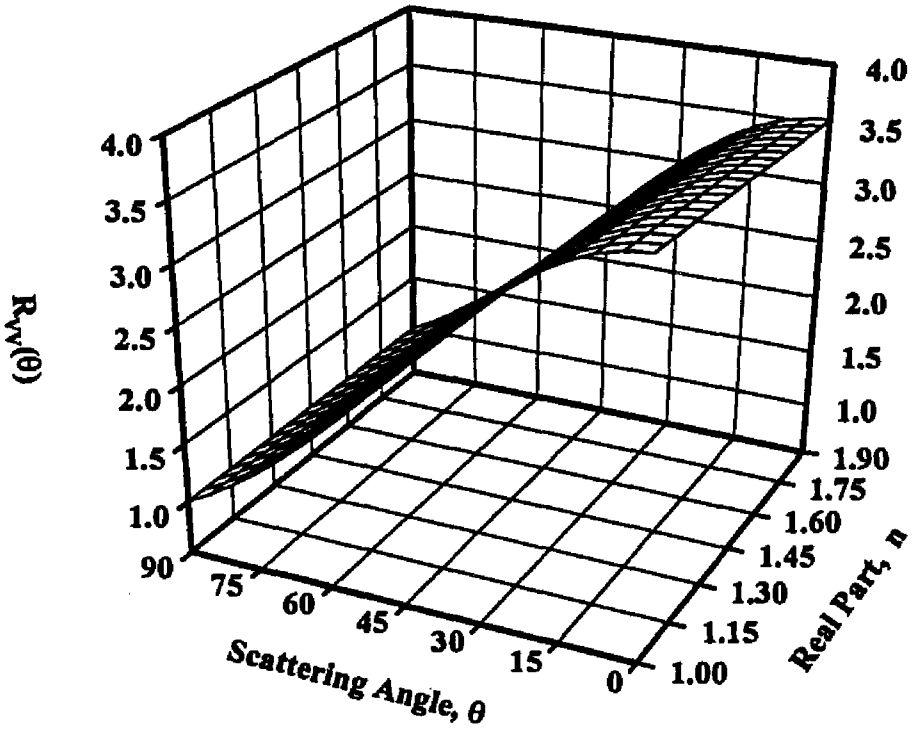

Figure 3.19 The dissymmetry ratio $R_{VV}(\theta)$ as a function of the scattering angle θ, and the real part of the refractive index, for a randomly branched chain agglomerate of N_p=20, α_p=0.125 and imaginary part of the refractive index k=0.5.

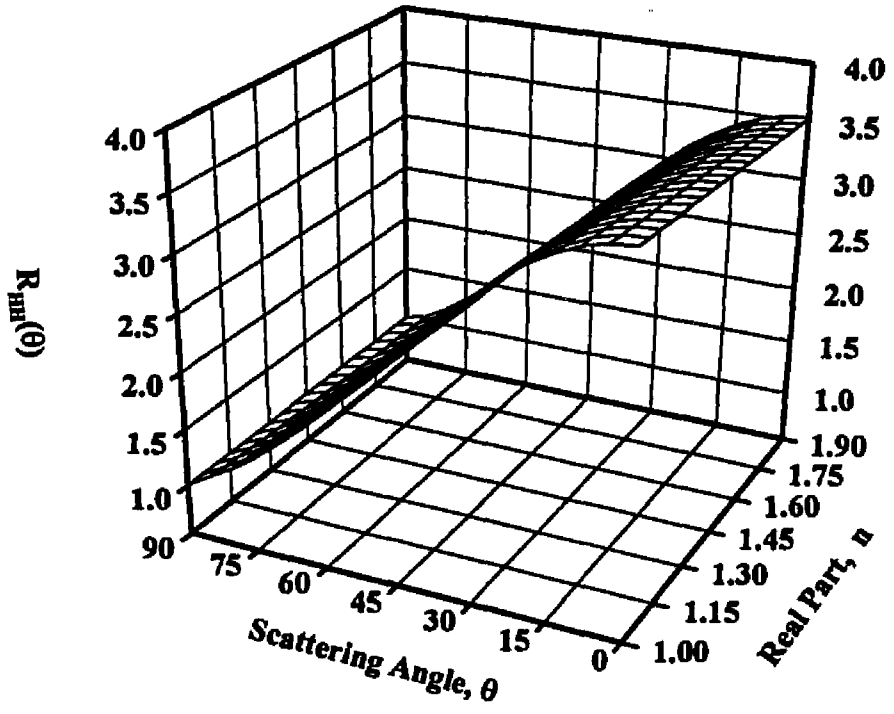

Figure 3.20 The dissymmetry ratio $R_{HH}(\theta)$ as a function of the scattering angle θ, and the real part of the refractive index, for a randomly branched chain agglomerate of N_p=20, α_p=0.125 and imaginary part of the refractive index k=0.5.

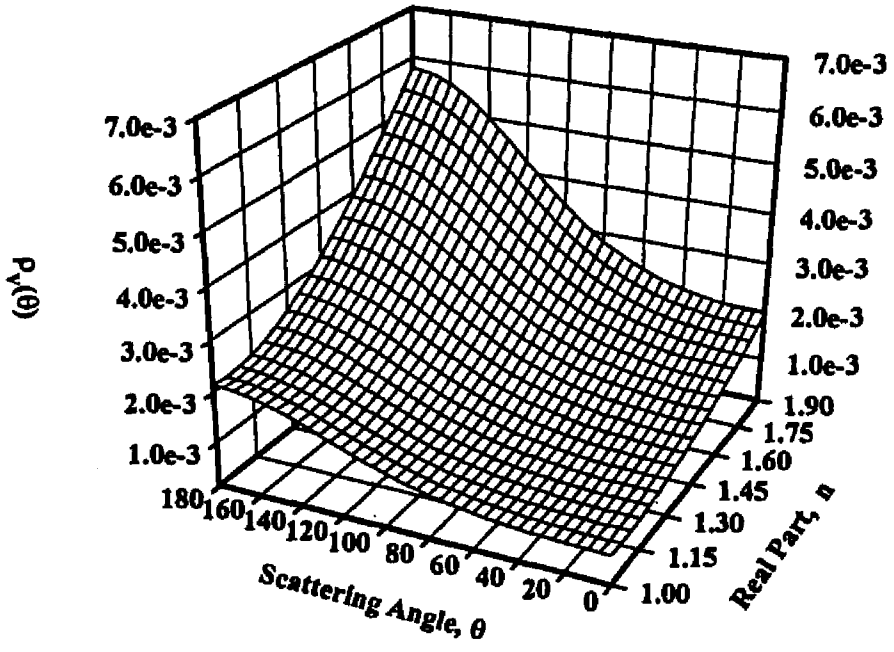

Figure 3.21 The dissymmetry ratio $\rho_v(\theta)$ as a function of the scattering angle θ, and the real part of the refractive index, for a randomly branched chain agglomerate of N_p=20, α_p=0.125 and imaginary part of the refractive index k=0.5.

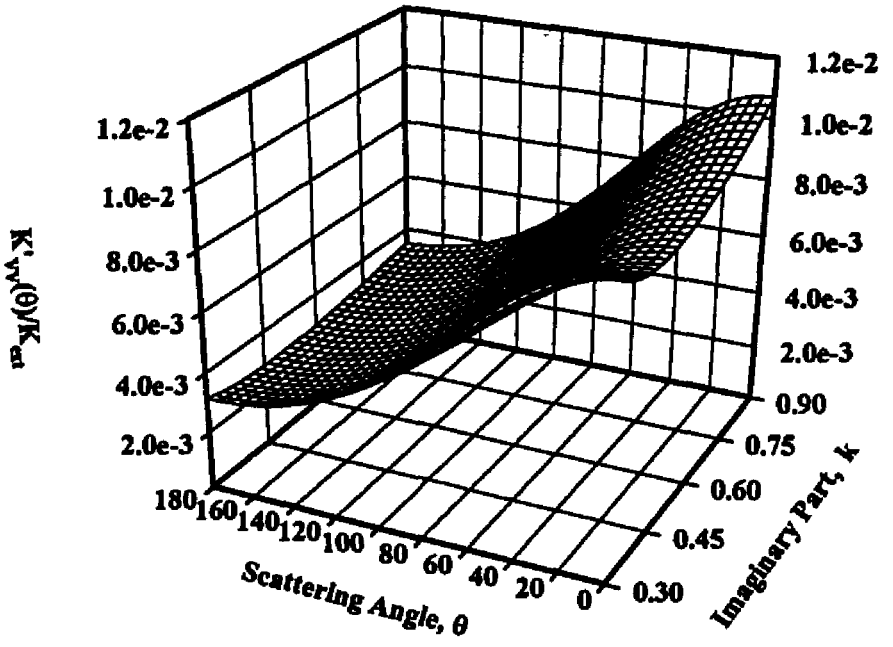

Figure 3.22 The differential scattering cross section to extinction cross section ratio $\{K'_{vv}(\theta)/K_{ext}\}$ as a function of the scattering angle θ, and the imaginary part of the refractive index, for a randomly branched chain agglomerate of N_p=20, α_p=0.125 and real part of the refractive index n=0.5.

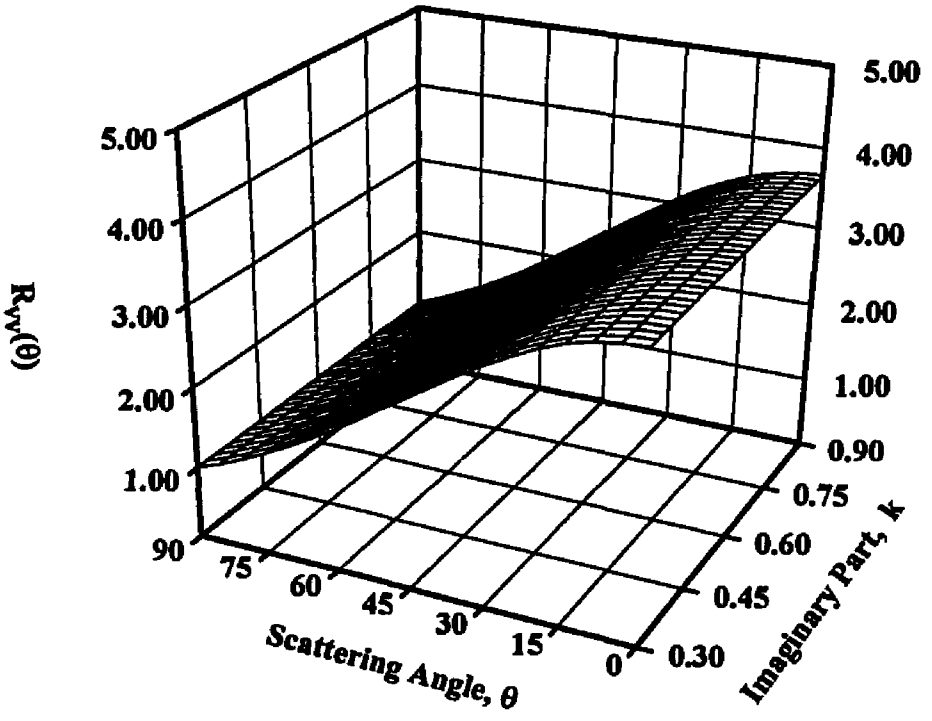

Figure 3.23 The dissymmetry ratio $R_{VV}(\theta)$ as a function of the scattering angle θ, and the imaginary part of the refractive index, for a randomly branched chain agglomerate of N_p=20, α_p=0.125 and real part of the refractive index n=0.5.

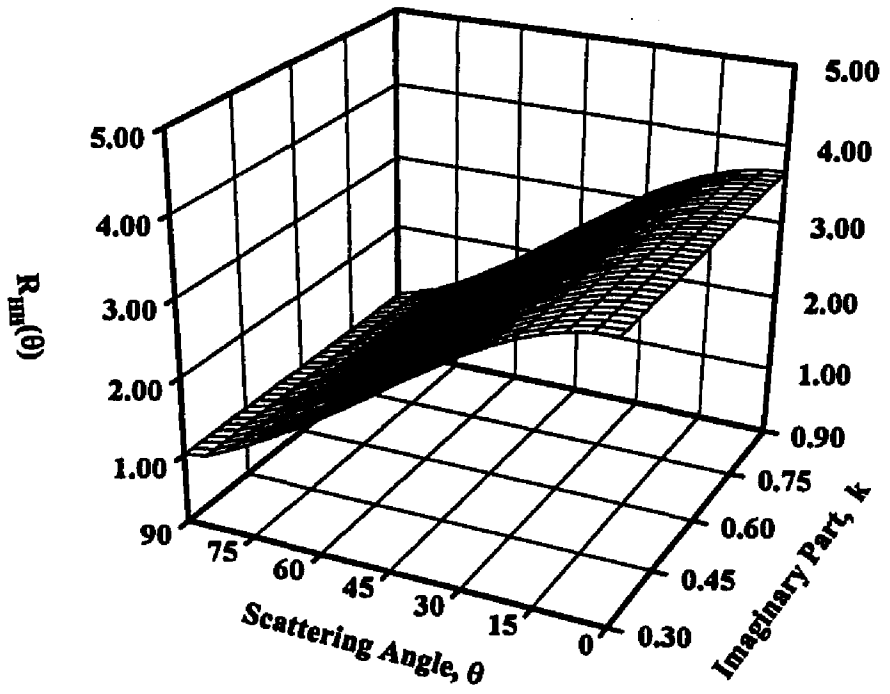

Figure 3.24 The dissymmetry ratio $R_{HH}(\theta)$ as a function of the scattering angle θ, and the imaginary part of the refractive index, for a randomly branched chain agglomerate of N_p=20, α_p=0.125 and real part of the refractive index n=0.5.

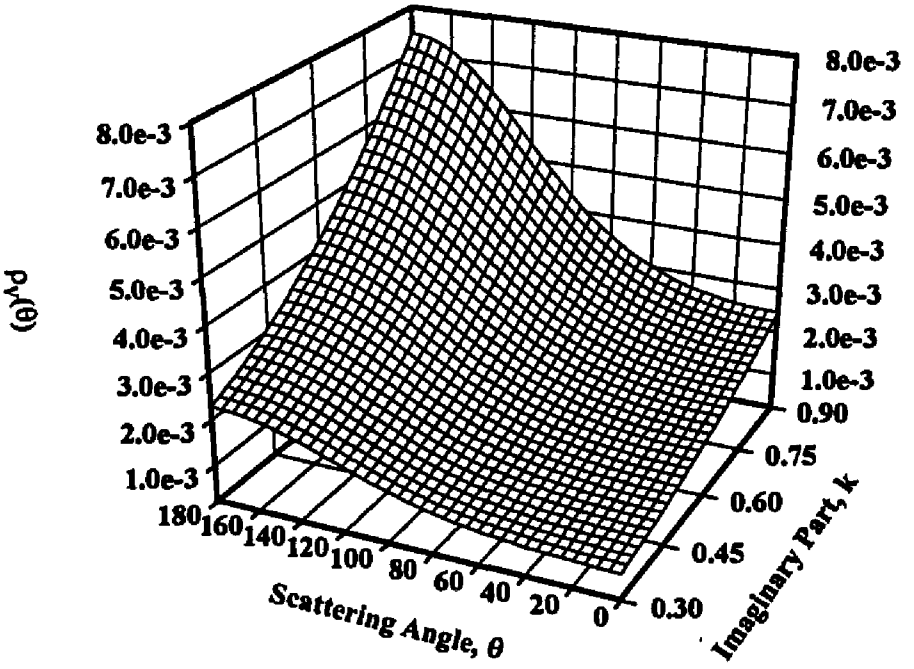

Figure 3.25 The depolarization ratio $\rho_V(\theta)$ as a function of the scattering angle θ, and the imaginary part of the refractive index, for a randomly branched chain agglomerate of N_p=20, α_p=0.125 and real part of the refractive index n=0.5.

The objective of the sensitivity analysis is to determine the optimum scattering angle θ, or the range of angles, for which the measurements will yield the best possible results. Stagg and Charalampopoulos[81] and Stagg[82] introduced a technique by which the sensitivity of inferring from experimental measurements the real and imaginary part of the complex refractive index of a surface (using the reflection and photometric ellipsometry techniques) can be numerically assessed. In this technique the sensitivity is assigned a numerical value, thereby allowing a quantitative comparison of the sensitivity for different angles of incidence, reflection and polarization states of the electromagnetic radiation. A detailed presentation of the technique can be found in the above works.[81-82] A similar optimization for the system of four equations, (3.6)-(3.9), can be performed by extending the above technique for the system with four unknown parameters N_p, d_p, n, k. For convenience the measured terms in equations (3.6)-(3.9) can be represented as:

$$M_1 = \frac{C'_{VV,Aggl}(\theta)}{C_{ext,Aggl}} = F_1(\theta, N_p, \alpha_p, n, k), \tag{3.10}$$

$$M_2 = \frac{C'_{VV,Aggl}(\theta)}{C'_{VV,Aggl}(180^\circ - \theta)} = F_2(\theta, N_p, \alpha_p, n, k), \tag{3.11}$$

$$M_3 = \frac{C'_{HH,Aggl}(\theta)}{C'_{HH,Aggl}(180^\circ - \theta)} = F_3(\theta, N_p, \alpha_p, n, k), \tag{3.12}$$

and

$$M_4 = \frac{C'_{VH,Aggl}(\theta)}{C'_{VV,Aggl}(\theta)} = F_4(\theta, N_p, \alpha_p, n, k). \qquad (3.13)$$

Differentiation of the above equations with respect to the unknown parameters (N_p, $d_p=\alpha_p\lambda/\pi$, n, and k) yields:

$$dM_1 = \frac{\partial F_1}{\partial N_p}dN_p + \frac{\partial F_1}{\partial d_p}dd_p + \frac{\partial F_1}{\partial n}dn + \frac{\partial F_1}{\partial k}dk, \qquad (3.14)$$

$$dM_2 = \frac{\partial F_2}{\partial N_p}dN_p + \frac{\partial F_2}{\partial d_p}dd_p + \frac{\partial F_2}{\partial n}dn + \frac{\partial F_2}{\partial k}dk, \qquad (3.15)$$

$$dM_3 = \frac{\partial F_3}{\partial N_p}dN_p + \frac{\partial F_3}{\partial d_p}dd_p + \frac{\partial F_3}{\partial n}dn + \frac{\partial F_3}{\partial k}dk, \qquad (3.16)$$

and

$$dM_4 = \frac{\partial F_4}{\partial N_p}dN_p + \frac{\partial F_4}{\partial d_p}dd_p + \frac{\partial F_4}{\partial n}dn + \frac{\partial F_4}{\partial k}dk. \qquad (3.17)$$

Equations (3.14)-(3.17) can also be represented in a matrix form as:

$$\begin{bmatrix} dM_1 \\ dM_2 \\ dM_3 \\ dM_4 \end{bmatrix} = \begin{bmatrix} dN_p \\ dd_p \\ dn \\ dk \end{bmatrix} \begin{bmatrix} \frac{\partial F_1}{\partial N_p} & \frac{\partial F_1}{\partial d_p} & \frac{\partial F_1}{\partial n} & \frac{\partial F_1}{\partial k} \\ \frac{\partial F_2}{\partial N_p} & \frac{\partial F_2}{\partial d_p} & \frac{\partial F_2}{\partial n} & \frac{\partial F_2}{\partial k} \\ \frac{\partial F_3}{\partial N_p} & \frac{\partial F_3}{\partial d_p} & \frac{\partial F_3}{\partial n} & \frac{\partial F_3}{\partial k} \\ \frac{\partial F_4}{\partial N_p} & \frac{\partial F_4}{\partial d_p} & \frac{\partial F_4}{\partial n} & \frac{\partial F_4}{\partial k} \end{bmatrix} \tag{3.18}$$

or,

$$\begin{bmatrix} dN_p \\ dd_p \\ dn \\ dk \end{bmatrix} = \frac{\begin{bmatrix} dM_1 \\ dM_2 \\ dM_3 \\ dM_4 \end{bmatrix}}{\begin{bmatrix} \frac{\partial F_1}{\partial N_p} & \frac{\partial F_1}{\partial d_p} & \frac{\partial F_1}{\partial n} & \frac{\partial F_1}{\partial k} \\ \frac{\partial F_2}{\partial N_p} & \frac{\partial F_2}{\partial d_p} & \frac{\partial F_2}{\partial n} & \frac{\partial F_2}{\partial k} \\ \frac{\partial F_3}{\partial N_p} & \frac{\partial F_3}{\partial d_p} & \frac{\partial F_3}{\partial n} & \frac{\partial F_3}{\partial k} \\ \frac{\partial F_4}{\partial N_p} & \frac{\partial F_4}{\partial d_p} & \frac{\partial F_4}{\partial n} & \frac{\partial F_4}{\partial k} \end{bmatrix}} \tag{3.19}$$

The terms dN_p, dd_p, dn and dk, above represent the uncertainty in the calculated parameters N_p, dp, n and k. The uncertainties in the measured experimental parameters are represented by dM_1, dM_2, dM_3 and dM_4. The denominator is the Jacobian[83] of the system of non-linear equations (3.14)-(3.17). The objective is to minimize the uncertainty in the calculated parameters. Since there is an inherent experimental uncertainty associated with the measured quantities, maximizing the denominator in equation (3.18)

will minimize the uncertainty in the inferred parameters, N_p, d_p, n and k. Because of this effect, the denominator may be thought of as the sensitivity of the set of equations. Therefore, it can be seen that maximizing the sensitivity of the experimental conditions is equivalent to maximizing the determinant of the Jacobian matrix [J] of the system of nonlinear equations. Thus, by evaluating the determinant of the Jacobian, det[J], a numerical value can be assigned to the sensitivity of the measurements. The optimum settings can be obtained by comparing the sensitivity values at different conditions. However, since ill-conditioning of the Jacobian matrix can yield inaccurate results under certain conditions,[83-84] caution must be exercised in the interpretation of the optimization analysis results. Ill-conditioning of the system of nonlinear equations can be detected by using the criterion[84]:

$$\frac{\det[J]}{\sqrt{\sum_{i=1}^{n}\sum_{j=1}^{n} J_{ij}^2}} << 1. \qquad (3.20)$$

The denominator in the above equation is called the Euclidean norm of the matrix [J], and is simply the square root of the sum of the squares of the Jacobian matrix coefficients. The effect of ill-conditioning can be attributed to round off error in the numerical calculations, or to very small Jacobian. The accuracy of the calculations can be improved in some cases by using Double Precision in the computations.

The following discussion addresses the sensitivity analysis performed on the system of non-linear equations given by the equation (3.14)-(3.17). The angles θ_1, θ_2, θ_3

and θ_4 are defined as the optimum angles corresponding to the best settings for the measurement of the differential scattering cross section, the dissymmetry ratio in the VV orientation, the dissymmetry ratio in the HH orientation, and the depolarization ratio respectively. The combination of these optimum angular settings for maximum sensitivity has been numerically calculated by using the optimization routine DBCPOL of the IMSL routine library on the LSU VAX computer system. The elements of the Jacobian matrix [J] have been numerically calculated by using the agglomerate theory computer codes for straight chain, and cluster agglomerate structures. The determinant of the Jacobian, det[J], was then calculated and normalized by the Euclidean norm of [J]. This value was taken as the sensitivity, S, of the system of equations. The routine DBCPOL was then used to minimize the function

$$F = \frac{1}{S^2}, \tag{3.21}$$

thereby maximizing the determinant of the Jacobian matrix [J]. The optimum values of the angles θ_1, θ_2, θ_3 and θ_4, at which det[J] is maximum, were calculated for different experimental conditions that are typical[10,28-29,70,82] in the flame being investigated in this work. The refractive index used in the optimization analysis was m=1.48-0.35i. Different number of primary particles (up to 30), and primary particle diameters (10 - 40 nm), were also used for the agglomerate systems of particles, consisting of straight chain, cluster, and random chain structures. The optimum experimental settings were restricted to the range of scattering angles from 15° to 165°, since that is the usable range of angles for the experiments.

The measurement optimization results obtained for the straight chain agglomerates are given in Table 3.3. The optimum angle θ_1 for the differential scattering cross section measurement (equation 3.15) was found to be 15° for all the cases investigated. The optimum setting for the dissymmetry ratio R_{VV} (equation 3.16) is given by θ_2 and it was also found to be 15°. The optimum angle θ_4 for the depolarization ratio ρ_V (equation 3.17) was found to be 165°. The optimum angle θ_3 for the dissymmetry ratio R_{HH} has a wide range of values and no particular trend or pattern can be observed.

Table 3.3 Optimum experimental scattering angle settings for a straight chain agglomerate made of N_p primary particles with d_p primary particle diameter and a refractive index of m=1.48-0.35i.

		Optimum Scattering Angle (deg)			
N_p	d_p (nm)	θ_1	θ_2	θ_3	θ_4
5	10	15	15	86	165
5	20	15	15	85	165
5	30	15	15	85	165
5	40	15	15	84	165
10	10	15	15	85	165
10	20	15	15	84	165
10	30	15	15	79	165
10	40	15	15	45	165
15	10	15	15	85	165
15	20	15	15	80	165
15	30	15	15	36	165
15	40	15	15	15	165
20	10	15	15	85	165
20	20	15	15	45	165
20	30	15	15	36	165
20	40	15	15	15	165

Apparently the combination of small primary particle diameters d_p, and small numbers of primary particles N_p, along with the fact that the dissymmetry ratios R_{VV} and R_{HH} have a very weak dependence on the real and imaginary parts of the refractive index, cause the Jacobian matrix to be ill-conditioned; an effect that was confirmed by checking the criterion given by equation (3.20). Therefore, the cause of the large range of values for the optimum angle θ_3 may be attributed to the ill-conditioning effects.

The effects of the weak dependence of the dissymmetry ratios R_{VV} and R_{HH} on the effectiveness of the method of simultaneously solving the four equations (3.6)-(3.9) for the four unknown parameters N_p, d_p, n and k, were investigated using simulated results. The ratio of the differential scattering at 20° to extinction cross sections $K'_{VV}(20°)/K_{ext}$, the dissymmetry ratios R_{VV} and R_{HH} at 20°, and the depolarization ratio ρ_V at 160°, for a straight chain agglomerate consisting of 20 primary particles of 20 nm diameter, and a refractive index of m=1.60-0.53i were calculated. The scattering results were then considered to be the experimental measurement results, and a minimization technique was used to solve simultaneously for the unknown parameters. Due to the fact that the minimization techniques available commercially can solve only N number of equations for N number of either real or integer unknowns (but not a combination of real and integer), the number of primary particles N_p was taken as known, and the system of four equations (3.6)-(3.9) was simultaneously solved for the unknowns d_p, n and k. The IMSL subroutine NEQNF, which solves a system of N equations for N unknowns with a modified Powell hybrid algorithm and a finite-difference approximation to the Jacobian, was used. Different cases were considered, by introducing experimental error to the

measurement values. Table 3.4 shows the results of the minimization of the system of four equations for three unknowns for the different cases. The first four columns in Table 3.4 give the percent difference error introduced to the simulated experimental measurements, and the last three columns give the percent difference in the inferred unknown parameters d_p, n, and k with N_p considered as known.

Table 3.4 Error in the inferred unknown parameters d_p, n, and k, with N_p being considered as known, for different error values introduced to the simulated experimental measurements for a straight chain agglomerate.

Error (% Diff.) Introduced to Measurements				Error (% Diff.) in the Unknowns		
$\frac{K'_{VV}(20°)}{K_{ext}}$	$R_{VV}(20°)$	$R_{HH}(20°)$	$\rho_V(160°)$	d_p	n	k
0	0	0	0	0.002	0.003	0.0006
+5	+5	+5	+5	5.9	4.1	11.7
-5	-5	-5	-5	6.4	3.5	13.4
+5	0	0	0	0.4	1.1	2.7
0	+5	0	0	0.4	1.1	2.6
0	0	+5	0	4.8	6.5	11.5
0	0	0	+5	0.2	0.09	5.4
+5	-5	0	0	0.04	0.1	0.3
0	+5	-5	0	5.4	6.4	16.1
0	0	+5	-5	4.8	6.1	6.3
+5	-5	+5	-5	4.6	6.4	6.8
-5	+5	-5	+5	5.4	5.8	7.6

As it can be seen in the table above, as much as 6.4% difference in the diameter d_p is possible by introducing 5% difference error in the measurement values. The percent difference in this example corresponds to only 1.3 nm difference in the inferred diameter. In the case of the real part n of the refractive index, 6.4% difference corresponds to a value of 0.01 difference. A percent difference by as much as 16.1 in the imaginary part k

though, corresponds to the difference between the values of 0.53 and 0.44. Such an error in inferring the unknown parameters indicates that the inversion technique is not sensitive enough, at least for the imaginary part k of the refractive index. It should also be emphasized that the number of primary particles N_p was considered known in the inversion scheme. By treating N_p as an unknown, the errors in all the inferred parameters become larger. The only minimization technique available at this time that can be used to minimize the system of four equations (3.6)-(3.9) for the four unknowns (one integer and three real numbers) is a direct search in the four-dimensional space. The Hooke algorithm[91] was modified to handle the integer number N_p and used in inverting the simulated experimental data. The direct search technique has the advantage of not requiring derivatives in minimizing a multivariable function. However, if more than one minimum exists (which is the case here) the technique cannot distinguish the global minimum from the local minima. The results from this type of analysis must therefore be treated very carefully. Because of the unreliability of the technique, the results of the direct search approach are not shown here.

The same analysis as the one performed for the results shown in Table 3.4 was performed for a cluster agglomerate. Table 3.5 shows the errors in inferring the three unknown parameters d_p, n and k, by using simulated experimental measurement values, and by treating the number of primary particles N_p in the cluster as a known. As shown in the results of Table 3.5, the errors become larger in the case of the cluster agglomerate analysis. This behavior is because of the compactness of the cluster's construction, which causes the dissymmetry and depolarization ratios to obtain smaller and less agglomerate

anisotropy dependent values than the values obtained in the case of a straight chain agglomerate analysis. The stronger the dependence is on the agglomerate anisotropy, the better the inversion technique will work.

Table 3.5 Error in the inferred unknown parameters d_p, n, and k, with N_p being considered as known, for different error values introduced to the simulated experimental measurements for a custer agglomerate.

Error (% Diff.) Introduced to Measurements				Error (% Diff.) in the Unknowns		
$\frac{K'_{VV}(20°)}{K_{ext}}$	$R_{VV}(20°)$	$R_{HH}(20°)$	$\rho_V(160°)$	d_p	n	k
0	0	0	0	0.01	0.01	0.01
+5	+5	+5	+5	14.1	13.9	19.5
-5	-5	-5	-5	16.9	11.1	29.4
+5	0	0	0	0.025	1.5	3.6
0	+5	0	0	0.02	1.4	3.4
0	0	+5	0	14.4	19.6	21.4
0	0	0	+5	0.08	0.1	4.8
+5	-5	0	0	0.02	0.2	0.38
0	+5	-5	0	17.0	14.1	34.0
0	0	+5	-5	14.4	18.3	17.0
+5	-5	+5	-5	14.4	19.1	17.7
-5	+5	-5	+5	17.1	14.6	26.8

In summary, the proposed technique of solving simultaneously four equations (3.6)-(3.9) for the four unknown agglomerate parameters N_p, d_p, n and k, is not sensitive enough to allow the evaluation of the particle refractive index. Both the dissymmetry ratios R_{VV} and R_{HH} display a very weak dependence on the real and imaginary part of the particle refractive index. This causes the system of the four nonlinear equations used in the inversion scheme to be ill-conditioned. Ill-conditioning effects can result in erroneous values for the unknown parameters. The analysis shown by Tables 3.4 and 3.5 indicates

that as much as a 5% difference error in the experimental measurements of the extinction cross section, the differential scattering cross section, the dissymmetry ratios, and the depolarization ratio, can result in large errors in inferring the unknown parameters. For these reasons, it was decided that the refractive index used in the analysis in this study must be considered a known parameter, and only the agglomerate structural characteristics will be investigated by using the light scattering measurements.

CHAPTER 4

EXPERIMENTAL FACILITY / FLAME CHARACTERIZATION

4.1 Flat Flame Burner

The laminar premixed propane/oxygen flat flame to be used in this work is supported on a water-cooled burner. A flat flame is a one-dimensional flame in which the flame parameters vary only in the axial direction with respect to a cylindrical coordinate system. This is achieved by having the fuel/oxygen mixture passing through a stationary, planar, reaction zone. A flat flame burner can be either a solid plug burner, or a multiple cell burner. In this study, a solid plug burner is used, and it is constructed of a porous sintered bronze plug. The fuel/oxygen mixture flows through the 6 cm water-cooled porous plug (Figure 4.1). The burner plug is surrounded by a porous sintered bronze annulus, through which inert gas flows to isolate the flame from the surroundings. The flame is stabilized by a honeycomb ceramic material (4 cells/cm_2), positioned 3 cm above the burner surface. The flame stabilizer allows the unrestricted escape of the post flame gases and soot particulates, prohibits recirculation effects from affecting the quality of the measurements, and keeps the shape of the flame to a nearly cylindrical shape over longer periods of time. The fuel/oxygen mixture is delivered at 10 psig and the flow rates are controlled and monitored by fine adjustment needle valves, and digital mass flow-meters, with an accuracy of 1% of the full scale (5.0 *l*/min). A hot wire anemometer was used to evaluate the uniformity of the burner exit cold gas velocity profile. A nickel fiber-wire

probe (DISA, model 55R03) with 75 μm diameter and 1.25 mm length operating at 200° C was used to measure the radial profiles at different angular cross sections and heights above the burner surface. The measured radial velocity profiles are presented in Figure 4.2 for a Nitrogen cold gas flow rate of 3 cm/sec based on volumetric flow. The uniformity of the velocity profiles can be established without absolute calibration of the hot wire anemometer readings. Figure 4.2 shows typical radial velocity profiles at a height of 5 mm above the burner surface at two angular cross sections 90° apart from each other. The maximum fluctuations in the hot wire anemometer voltage readings from the mean voltage reading were generally less than 0.15%. The same figure also shows the edge effects of a jet stream flow into a quiescent medium. Similar profiles were measured at other heights (in the range of 1-10 mm) above the burner surface. The burner is positioned in the center of a modified goniometer and can be moved vertically with respect to the stationary laser beam and detection optics.

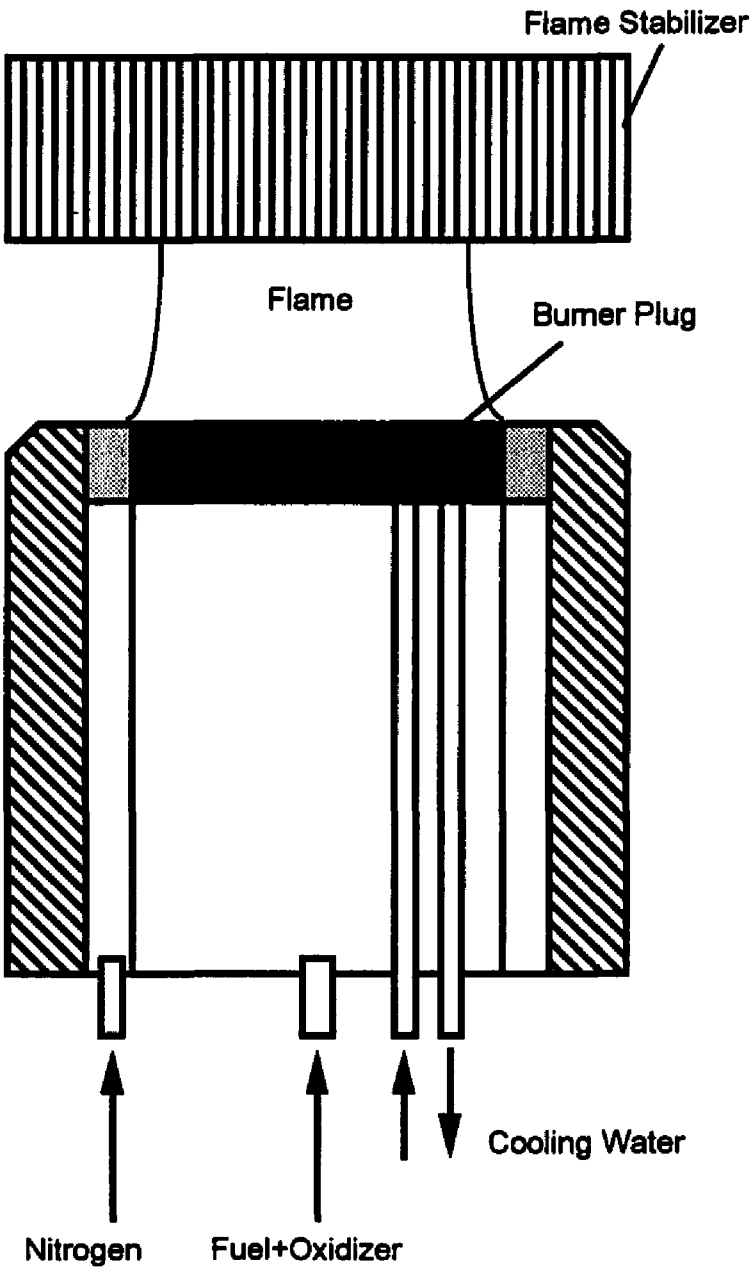

Figure 4.1 Water-cooled porous plug burner.

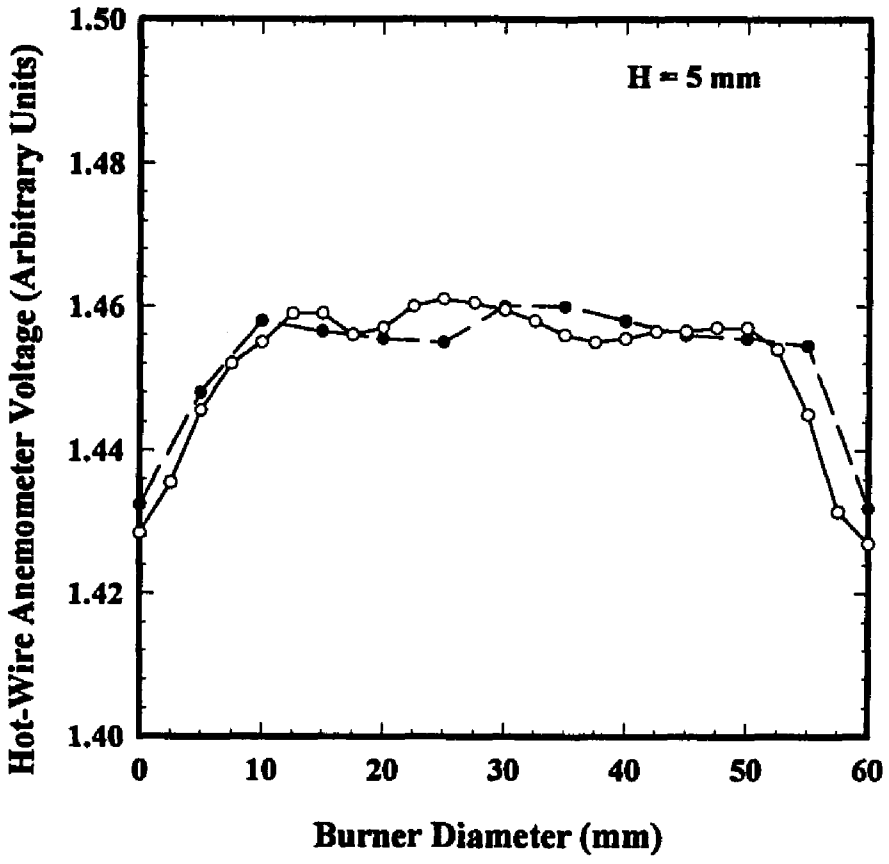

Figure 4.2. Measured radial velocity profiles of the flat flame burner at a height H=5 mm above the burner surface for cold Nitrogen gas velocity of 3 cm/sec.

4.2 Light Scattering Facility

The light scattering facility consists of the goniometer, the light sources, the focusing optics, the detection optics, and the signal processing electronics. A schematic of the facility is shown in Figure 4.3. The goniometer has two arms positioned 180° with respect to each other to allow dissymmetry measurements to be performed. The range of angles of 0°-180° can be scanned with an accuracy of 0.01°. However, because of interference from the focusing and detection optics, only the range of 15°-165° is usable.

The laser probe beam derived from a 10 Watts Argon-Ion laser (Spectra Physics, Model 2085A-20) is focused by the focusing optics at the center of the burner with a beam spot of 0.2 mm. The polarization of the laser beam can be rotated with a half-wave plate made of mica (Karl Lambrecht). A calcite crystal polarizer (Karl Lambrecht, Model MGLQD8) with extinction ratio of 1.0×10^{-6} improves the polarization of the laser beam. A continuous light source (Oriel, Model 7340) can also be used for absorption measurements as a function of the wavelength. The beam from the continuous light source is focused at the center of the burner by a lens. A pulsed Nd-YAG laser beam (Spectra Physics, Model Quanta Ray DCR-3) of 1064 nm wavelength and 1 J/pulse energy delivery is focused at the center of the burner at a distance of 2.5 mm below the Argon-Ion laser beam. The pulsed laser beam is used for soot particle velocity measurements. The details of these measurements will be discussed in Section 4.5 of this chapter.

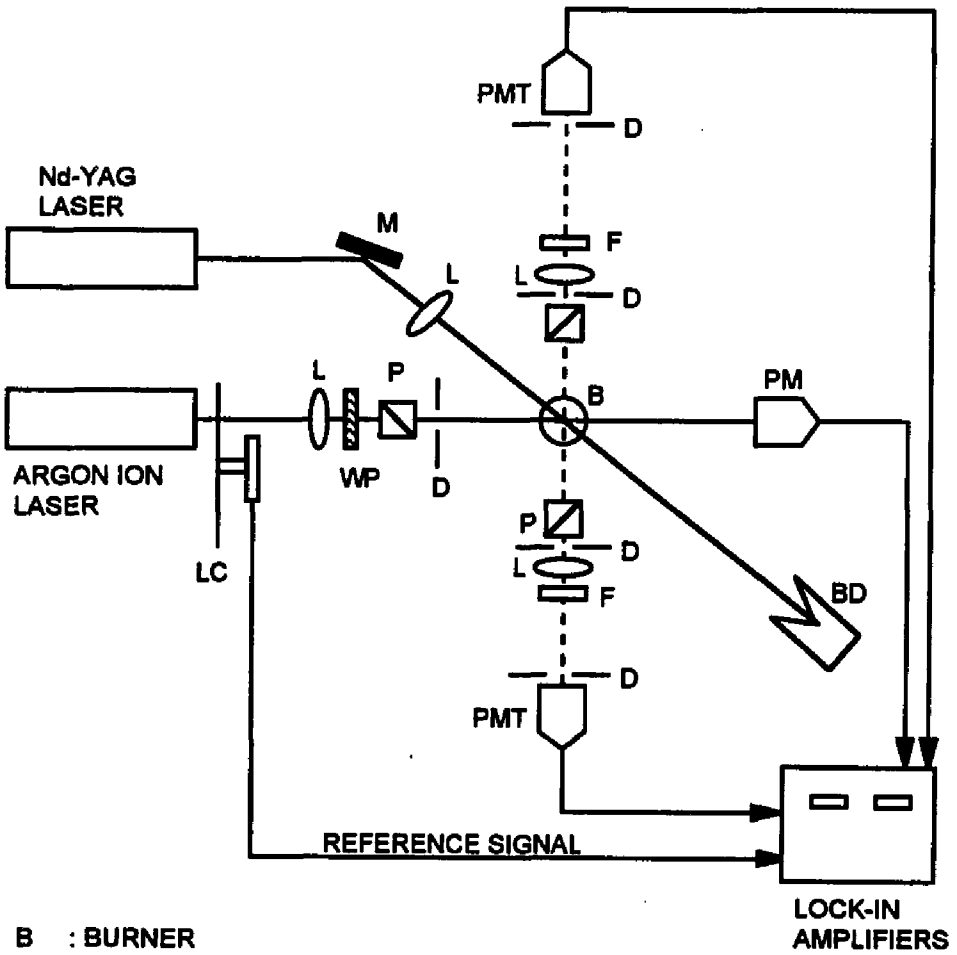

B : BURNER
BD : BEAM DUMP
D : DIAPHRAGM
F : FILTER
L : LENS
LC : LIGHT CHOPPER
M : MIRROR
PM : POWER METER
PMT : PHOTOMULTIPLIER TUBE
WP : HALF WAVE PLATE

Figure 4.3 Experimental setup for light scattering, extinction, dissymmetry ratio, depolarization ratio, and flame velocity measurements.

The scattered light is collected by the detection optics that form an image (with magnification of one) of the scattering volume on the center of an iris diaphragm positioned in front of the photomultiplier tube detectors. The polarization of the observed scattered light is set by calcite crystal polarizers (Karl Lambrecht, Model MGLSW8). In order to reduce the flame emission background signal that is being detected simultaneously with the scattered signal, a narrow band laser line interference filter (Oriel, Model 52650, FWHM 10nm, λ=488 nm) is used. The iris diaphragm in front of the detection optics defines the detection solid angle, while the diaphragm in front of the detector blocks stray light from reaching the detector. The transmission ratio of the laser beam intensity through the flame is measured by a power meter (Spectra Physics, Model 404, 0.02mW - 5 W).

A reference signature is applied to all continuous wave light beams with a mechanical light chopper (EG&G PARC, Model 196). The signals are pre-amplified and fed into the lock-in amplifiers (EG&G PARC, Models 5207 and 5209) which filter out any signals that do not carry the signature set by the light chopper. This way, any contributions to the detected signal from dark current from the photomultiplier tubes and flame emission that passes through the narrow band laser line interference filter are reduced to a nondetectable level.

4.3 Premixed Flame Parameters

The experimental measurements were performed with a fuel rich premixed propane-oxygen flat flame of fuel equivalence ratio of ϕ=2.1. The fuel equivalence ratio gives the relative amounts of fuel and oxygen and is defined as

$$\varphi = \frac{\left(\frac{\text{mass of fuel}}{\text{mass of oxygen}}\right)_{\text{actual}}}{\left(\frac{\text{mass of fuel}}{\text{mass of oxygen}}\right)_{\text{stoich.}}} \qquad (4.1)$$

The gas flow rates for the flame investigated are summarized in Table 4.1. The flame was isolated from the surroundings by a nitrogen shroud flow. The total cold gas velocity for the fuel/oxygen mixture was 3 cm/sec. All the gases used were of ultrahigh grade (>99.99 %) and were supplied from cylinders regulated by two-stage pressure regulators. The gas flow rates were monitored by digital mass flow meters with an accuracy of 1 % of the full scale flow rate (5 *l*/min).

Table 4.1. Flow rates of the premixed gases for the flame investigated.

Gas	Flow Rate (*l*/min)
Propane	1.35
Oxygen	3.32
Total	4.67

4.4 Optical Path Length and Temperature Measurements

The optical path length L at each location in the flame is necessary in determining the extinction coefficient K_{ext} (see equation 2.30). The burner was appropriately positioned so that the focused Argon-Ion laser beam passed through the center of the flame at the desired height at which the optical path length was to be measured. The flames were then photographed while the laser beam intensity was set at maximum. The scattering of the laser beam by the soot particulates provided a clear trace of the beam through the flame on the photographs. The optical path lengths at different heights were then determined from scaled measurements of the beam trace on the photographs. The results of the path length measurements are summarized in Table 4.2.

Table 4.2. Optical path lengths for each height above the burner surface.

Height (mm)	Optical Path Length (mm)
4	53.5
6	51.0
8	49.0
10	46.5
12	45.5
14	45.0
16	42.5
18	44.0
20	44.5
22	47.0

As seen from the measurements of the flame diameter at various positions above the burner surface (Table 4.2), the flame does not display a perfect cylindrical shape. Its diameter decreases near the middle and increases near the burner surface and the stabilizer.

This may be attributed to the fact that the flame is anchored onto the flame stabilizer, causing an expansion of the top of the flame.

The axial temperature profile of the flame was measured with a Platinum vs Platinum-10 % Rhodium thermocouple with ceramic high temperature shielding and a bead diameter of 0.5 mm. The thermocouple was mounted on a horizontal translation mechanism that allowed the accurate positioning of the thermocouple at the exact center of the flame. The thermocouple was inserted rapidly into the flame and kept there until a peak voltage reading was recorded. Soot deposition on the thermocouple bead caused the thermocouple output voltage reading to begin decreasing because of the enhanced radiation losses. The peak value of the voltage reading was taken as the correct value for the temperature measurement. The thermocouple bead was cleaned with a compressed air jet, to remove the soot deposits, before it was inserted back into the flame. The measured temperatures were corrected for radiation losses by using the following equation,

$$T_{flame} = \frac{\varepsilon\sigma}{h}(T_t^4 - T_\infty^4) + T_t, \qquad (4.2)$$

where the term T_{flame} is the corrected flame temperature, T_t is the measured temperature, T_∞ is the ambient temperature, ε is the emissivity of the thermocouple bead, σ is the Stephan-Boltzmann constant, and h is the convection heat transfer coefficient between the thermocouple bead and the flame gases. The emissivity of the thermocouple bead[75] used was 0.2. The convection coefficient was calculated by using the measured flame temperatures, the composition of the flame, and the measured flame velocities for each

height. The corrected flame temperature versus height are presented in Table 4.3. The effects of soot formation and growth on the flame temperatures are easily seen in the plot of the flame temperatures (Figure 4.4).

Table 4.3. Corrected axial flame temperatures for the flame investigated.

Height (mm)	Flame Temperature (K)
1	1579
2	1491
3	1436
4	1399
5	1378
6	1372
7	1346
8	1332
9	1324
10	1311
11	1300
12	1297
13	1289
14	1279
15	1268
16	1260
17	1249
18	1247
19	1243
20	1233
21	1226
22	1219

Lower temperatures at the higher heights in the flame indicate enhanced radiation losses that may be attributed to: (a) higher soot emissivities that result in higher heat transfer rates; and (b) radiation losses to the flame stabilizer surface.

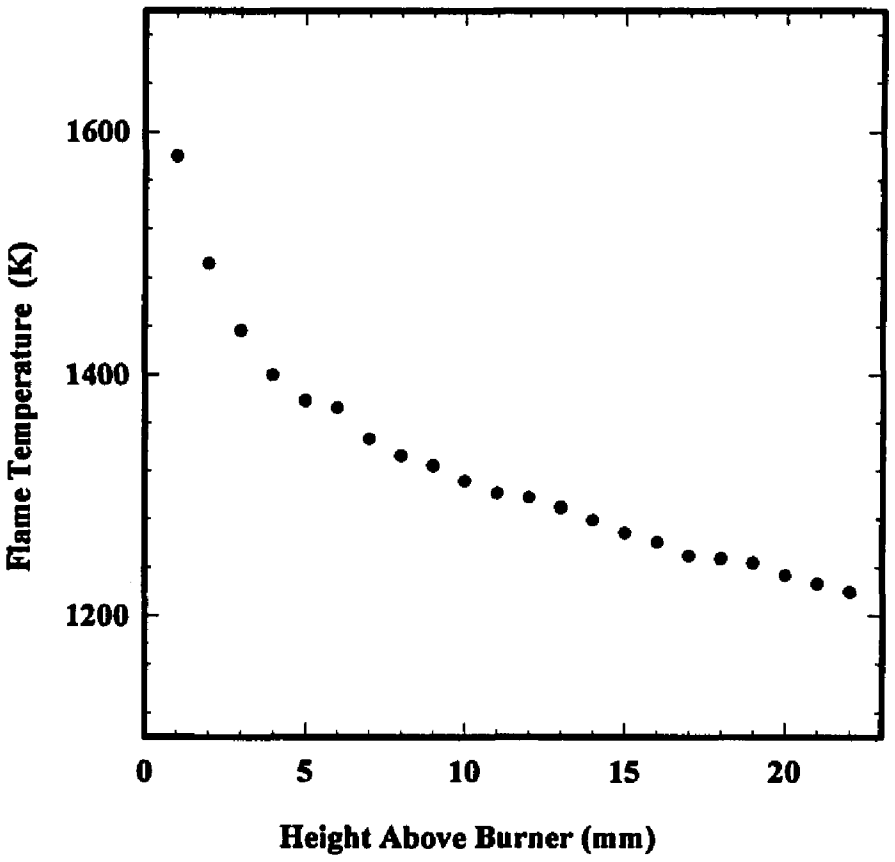

Figure 4.4 Corrected axial flame temperature profile measurements for the ϕ=2.1 Propane/Oxygen flat flame.

4.5 Flame Velocity Measurements

In evaluating the soot properties such as growth rates and the time dependency of the soot particle parameters, the characteristic flame residence times of the soot particles are required. In order to evaluate the soot residence times, the flame velocities must be known. The flame velocities can be calculated from the initial mass flux, the gas composition, the flame cross sectional area, and the temperature at any point in the flame. Computer codes are available that solve numerically the mass, momentum, and energy conservation equations for the flame velocities. The disadvantages of such computer codes are that they are computationally intensive and they have limitations regarding the treatment of soot formation. Experimentally determined velocities are an alternative to numerical calculations. Dasch[76] developed a technique to measure flame velocities by using a high power pulsed laser beam to vaporize soot particles. By focusing a high power pulsed laser beam on the center of the flame, a volume of vaporized soot particles is created. The reduced in diameter particles in the vaporized volume or "void" (it does not mean absence of particles) follow the flame gas accelerations because of their small size. The void persists for several milliseconds because soot diffusion and growth rates are sufficiently slower. When such a void, traveling at the same velocities as the flame gases, passes by the scattering volume of a scattering/extinction continuous wave (cw) beam probe, there is a significant change in the level of both the scattering and transmission signals. The reason for this effect is the dependence of the scattered intensity on the sixth power of the particle diameter, and the dependence of the absorbed intensity on the third power of the particle diameter (see equations 2.26 and 2.27). A typical setup

for such an experiment is shown in Figure 4.2. The high power pulsed laser beam is focused at a known distance exactly below the cw laser probe beam. By measuring the time taken for the void to travel the two beam separation distance, the velocity of the flame can be determined. This technique was successfully implemented by Lawton[77] and Hahn[29] to measure axial flame velocities in premixed flat flames.

The axial velocity profile of the flame investigated was measured by using the technique described above. A pulsed Nd-YAG laser beam with wavelength of 1064 nm (Spectra Physics DCR3, pulse duration 7 ns, 1 J/pulse) was used to generate a void by vaporizing the soot particles in a beam spot of 1 mm. A cw Argon-Ion laser beam (Spectra Physics 164,1 W, 488 nm) was used to monitor the scattering signal at 90° for perturbations as the void passed through the scattering volume. The two beams were arranged to form a 45° angle between them (see Figure 4.3) and were axially separated by a known distance (Figure 4.5). The separation distance was determined by burning a beam spot on a photographic film. The scattered signal was detected by a photomultiplier tube, amplified and fed into a boxcar averager/gated integrator (Stanford Research Systems SR250). The boxcar averager was triggered by the pulsed laser with a trigger delay of 240 μsec after the actual firing of the high power light pulse. The total time taken from the moment the pulse was fired until the void was detected by the cw laser probe was measured. The local flame velocity was then determined by dividing the beam separation distance by the transit time of the "void". The measured velocity was an average velocity over the separation distance and was assumed to be halfway between the two beams. A typical time scan of the scattering signal is shown in Figure 4.6. While there is a visible

fluctuation in the detected signal, the minimum point that corresponds to the passing of the "void" through the scattering volume is readily identifiable. The scattering signal was first smoothed (Figure 4.7) and then its derivative was taken (Figure 4.8). The exact total transit time of the void was determined from the zero crossing of the derivative on the time axis. The measured axial flame velocity profiles for the flames investigated are presented in Figure 4.9. The flame velocity results indicate a rapid acceleration of the flame gases from the burner exit velocity of 3 cm/sec to velocities greater than 35 cm/sec, followed by a gradual deceleration to velocities below 30 cm/sec. The decrease in flame velocity is caused by the decrease in the flame temperature beyond the reaction zone in the flame.

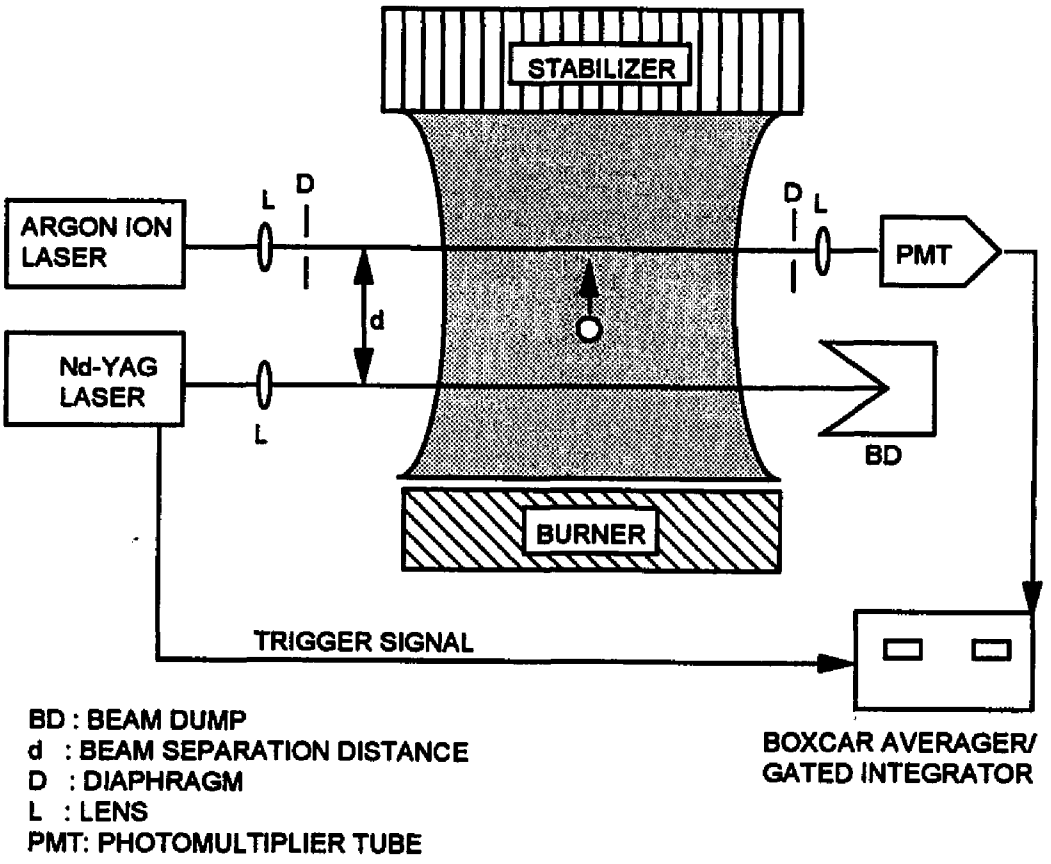

Figure 4.5 Experimental set-up for flat flame axial velocity measurements.

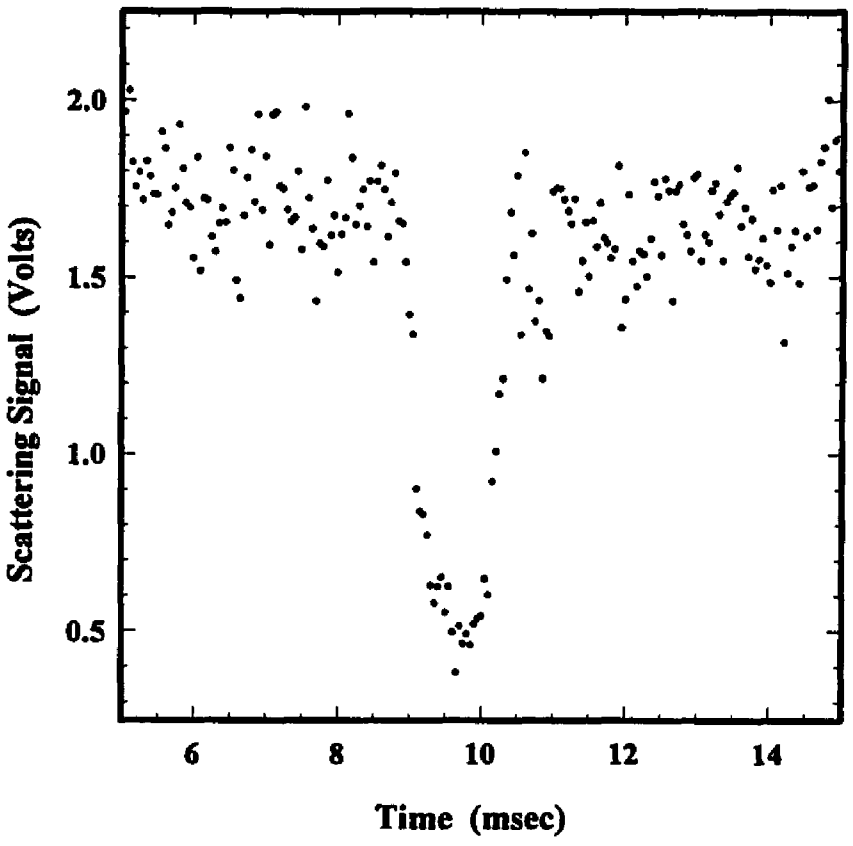

Figure 4.6 Time scan of the scattering signal for the ϕ=2.1 Propane/Oxygen flame at 16 mm above the burner surface.

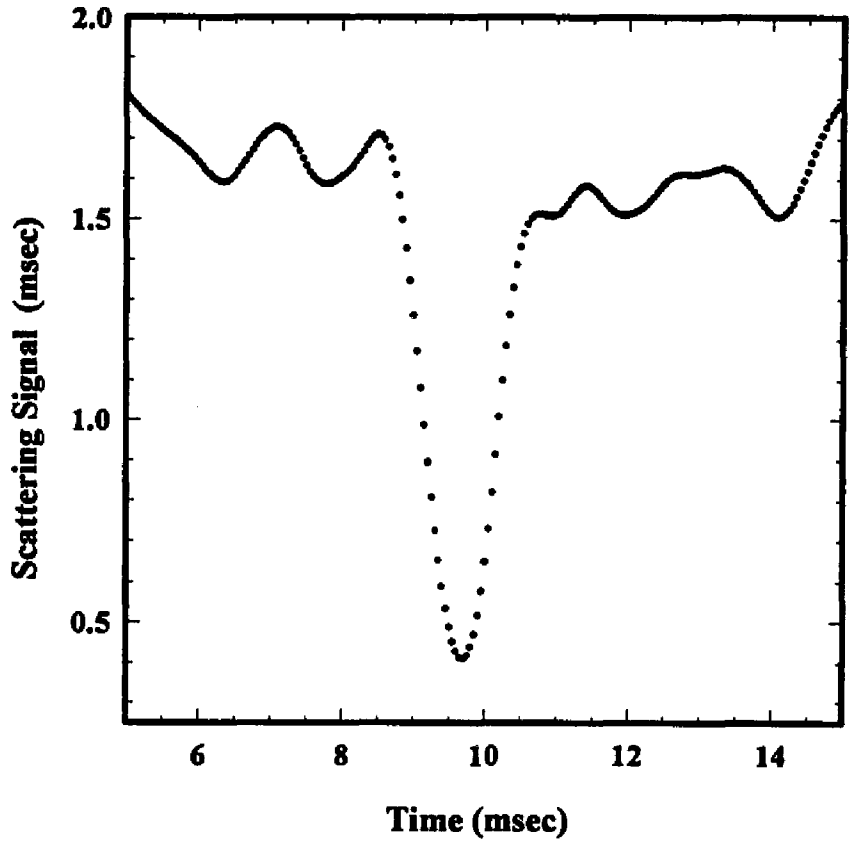

Figure 4.7 Smoothed time scan of the scattering signal for the ϕ=2.1 Propane/Oxygen flame at 16 mm above the burner surface.

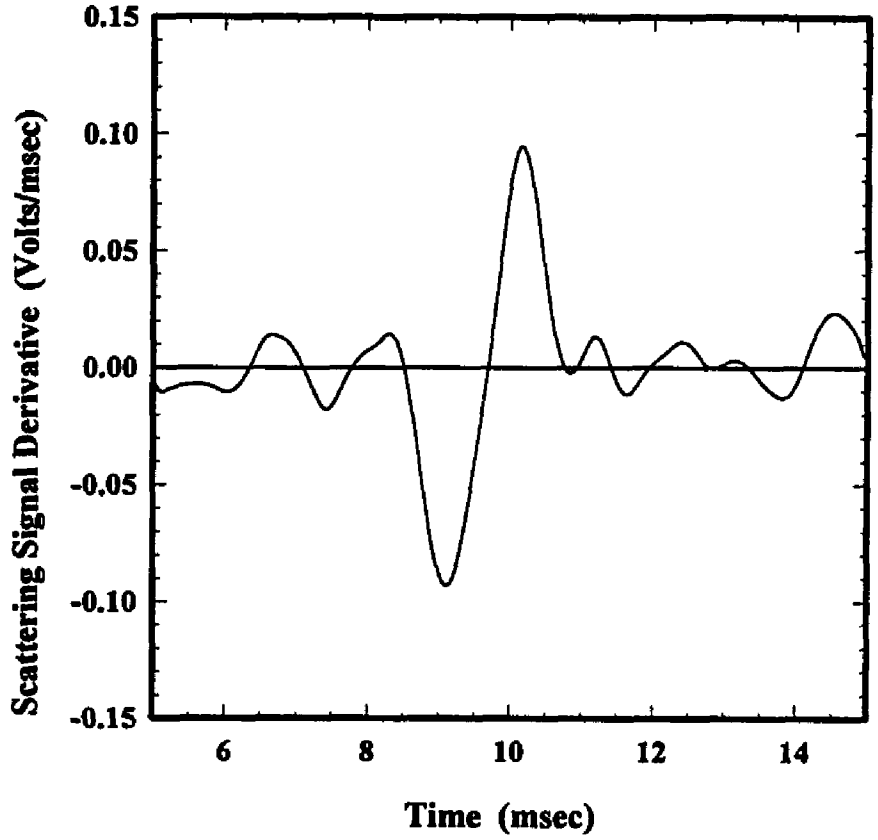

Figure 4.8 Derivative of the time scan of the scattering signal for the ϕ=2.1 Propane/Oxygen flame at 16 mm above the burner surface.

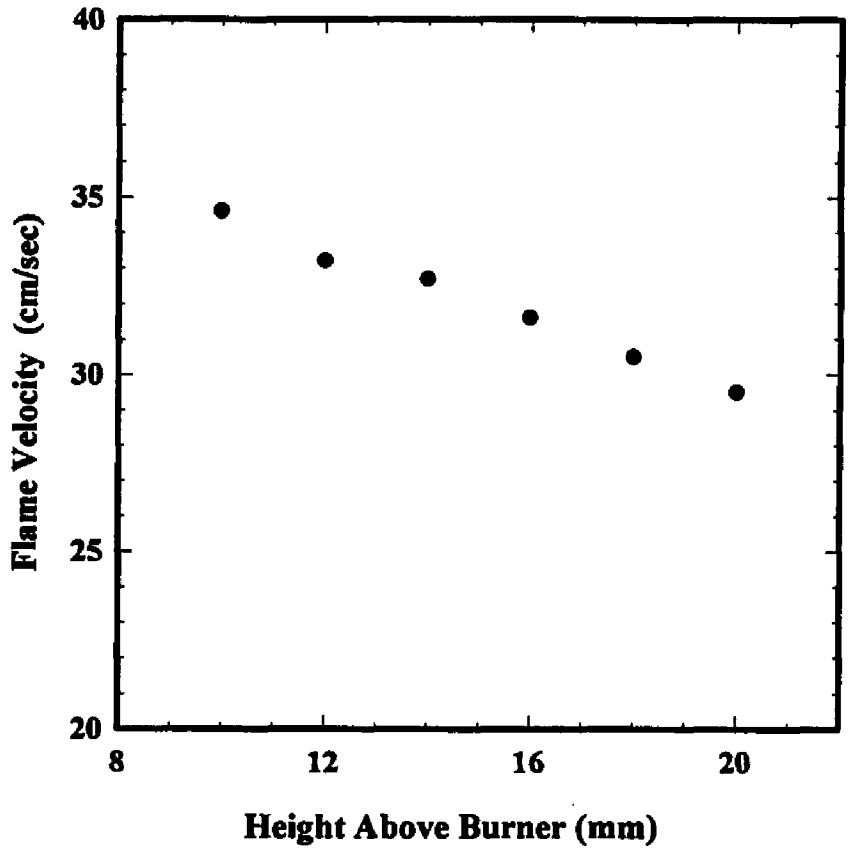

Figure 4.9 Measured axial flame velocity profile for the ϕ=2.1 Propane/Oxygen flame at different heights above the burner surface.

4.6 Calibration of the Scattering Signal

The output of the detectors in a light scattering experiment must be converted from voltage to differential scattering cross sections. Two photomultiplier tubes, positioned 180° apart, are used in these experiments to measure (at a specific scattering angle θ) the differential scattering cross section $K'_{VV}(\theta)$, the dissymmetry ratios $R_{VV}(\theta)$ and $R_{HH}(\theta)$, and the depolarization ratio $\rho_V(\theta)$. In all cases the signal needs to be calibrated to a known standard. The following techniques can be used to calibrate the scattering signal from soot:

a. An attenuated portion of the incident beam may be directed on the photomultiplier tube cathode and the absolute response of the detection system can then be measured. In order to avoid damaging the photomultiplier tube with the intense laser beam, a very large attenuation (typically $x10^{11}$) of the beam is required. The success of such calibration will strongly depend on how accurately the attenuation of the laser beam is measured.

b. The light scattering signal from a monodispersed suspension of spherical scatterers of known size can be used to calibrate the detector response. Polystyrene latex spheres of diameters down to 20 nm and very narrow size distributions are comercially available and can be used in a liquid suspension for calibration purposes. However, such a calibration technique requires a special optical quality cylindrical sample holder, so that angular calibration measurements can be performed.

c. The Rayleigh scattering of light from gas atoms or molecules at 1-atm pressure is measurable and can be used in calibrating the detection system. This technique is easily implemented in the burner system used in this study. Ultrahigh purity methane and

nitrogen are used as the calibration gases. Since the differential scattering cross sections of the calibrating gases are known, the absolute response of the detection system can be determined.

The differential scattering cross section of the soot particulates can be determined using the relation:[10]

$$K'_{VV,SOOT}(\theta) = K'_{VV,GAS}(\theta)\frac{S_{VV,SOOT}}{S_{VV,GAS}}\frac{\tau_{GAS}}{\tau_{SOOT}}, \qquad (4.3)$$

where $S_{VV,SOOT}$ is the measured scattering signal from the flame, and $S_{VV,GAS}$ is the measured molecular scattering signal from methane gas at room temperature and pressure. Methane and nitrogen are used as the calibration gases. The ratio τ_{GAS}/τ_{SOOT} is introduced to account for the difference in the attenuation of the incident and scattered laser beam through the calibrating gas and the flame.[10,29] The above calibration procedure is performed before each experiment, and the scattering signals from the calibrating gases flowing through the scattering volume are measured. The differential scattering cross section for the methane and nitrogen gases at room pressure and temperature are known. Rudder and Bach[92] give experimental and theoretical values for the differential scattering cross sections and depolarization ratios of different gases. The differential scattering cross sections of anisotropic molecules (such as diatomic molecules) in the VV, HH, VH and HV polarization orientations are given by:[92]

$$K'_{VV}(\theta) = K'_{o}, \qquad (4.4)$$

$$K'_{VH}(\theta) = K'_{HV}(\theta) = \rho_V K'_o, \tag{4.5}$$

and

$$K'_{HH}(\theta) = \left\{(1-\rho_V)\cos^2\theta + \rho_V\right\}\ K'_o, \tag{4.6}$$

where

$$K'_o \equiv \frac{4\pi^2(m-1)^2}{N^2\lambda^4}\ \frac{3}{3-4\rho_V}, \tag{4.7}$$

and m is the refractive index, λ the incident beam wavelength, N is the number density of the gas molecules and ρ_V is the depolarization ratio. Figures 4.10 and 4.11 show respectively the differential scattering cross sections for methane and nitrogen, at 1-atm pressure and room temperature, calculated by using the relations given by the equations above, and the experimental values reported by Rudder and Bach.[92] As seen from the figures, the differential scattering cross sections in the VH or HV polarization orientation obtain very small values and cannot be measured with the current experimental setup. The same is true for the HH component at angles near and about 90°. Molecular scattering with cross sections in the order of 10^{-8} ($cm^{-1}sr^{-1}$) or larger is measurable with the current experimental setup. Not being able to measure the HV molecular calibration signal creates problems in evaluating the depolarization ratio of soot. To overcome this difficulty, the HV signal from soot was calibrated using the VV signal from the molecular scattering from methane. This practice is probably inaccurate, but in the absence of a better way of calibrating the HV signal, it was assumed to be sufficient.

The molecular scattering from the calibration gases can also be used in checking the alignment of the detection optics. The ratio of the methane to nitrogen differential scattering cross sections (in the VV orientation) at the wavelength of 488 nm is equal to 2.3. By measuring the scattering signals from both calibration gases, the level of contamination of the scattering signal from stray light effects can be assesed. Stray light impinging on the detectors will decrease the measured methane to nitrogen signal ratio to values lower than 2.3. The methane to nitrogen signal ratio was measured before each light scattering experiment, and it typically ranged from 2.1 to 2.25.

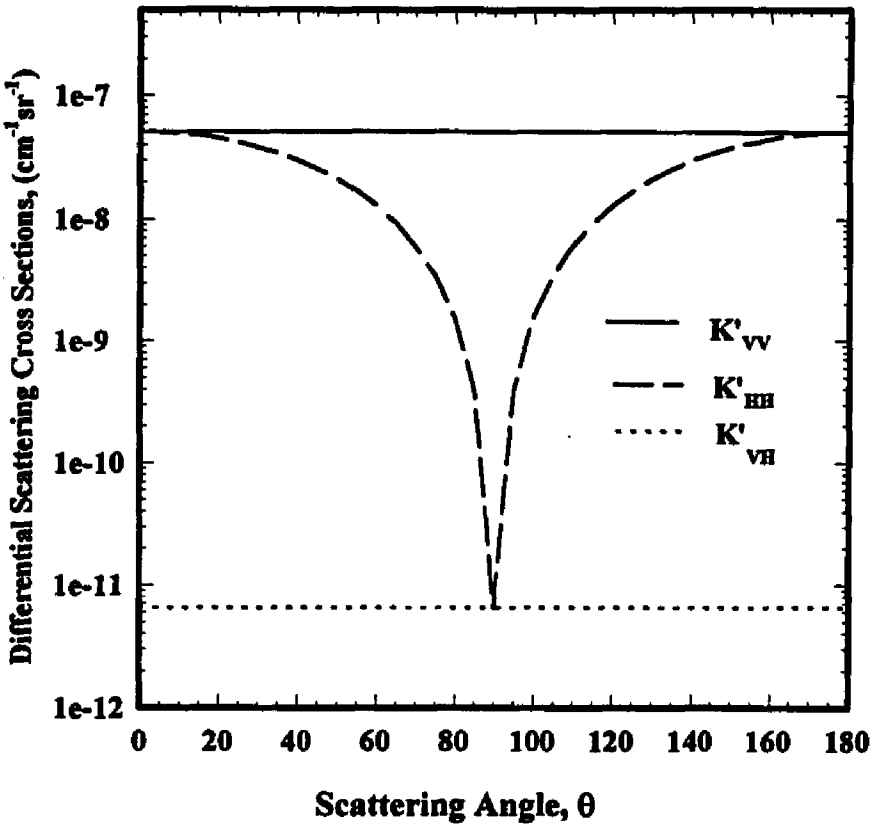

Figure 4.10 The differential scattering cross sections as functions of the scattering angle for methane gas at 1-atm pressure and room temperature.

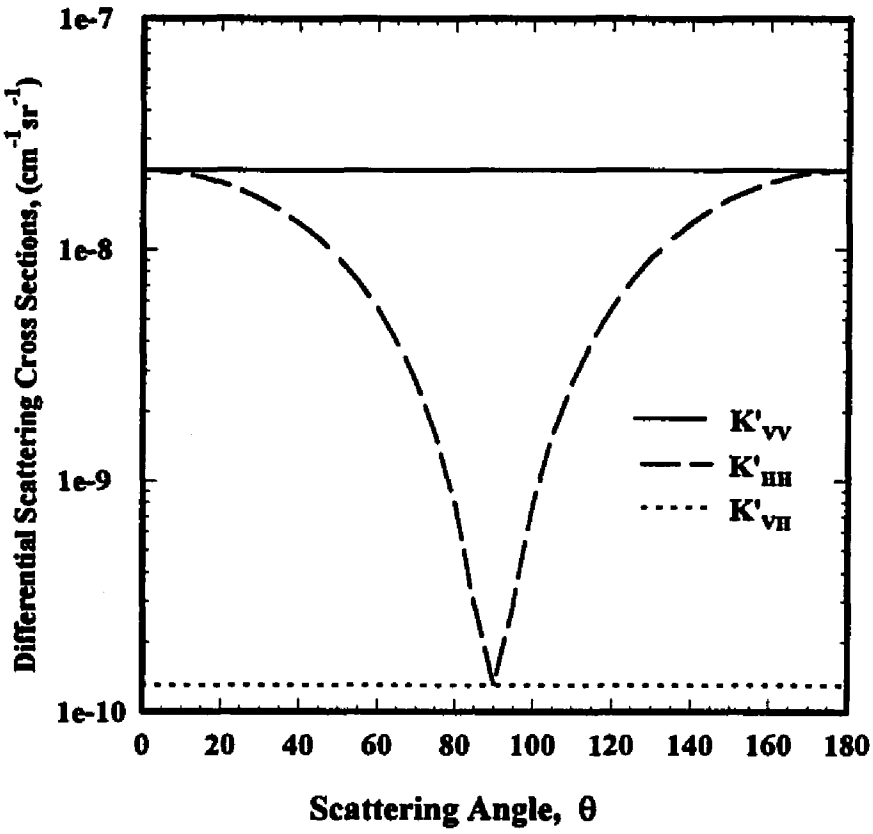

Figure 4.11 The differential scattering cross sections as functions of the scattering angle for nitrogen gas at 1-atm pressure and room temperature.

4.7 Testing of the Light Scattering Facility

In measuring the dissymmetry ratios R_{VV} and R_{HH}, caution must be applied so that the two detectors are aligned 180° apart and they detect the same scattering volume in the flame (see Figure 4.3). Unfortunately, visual inspection of the detector alignment is not sufficient since minute misalignment can introduce error in the measurements. The classical light scattering theory presented in Chapter 2 shows that the dissymmetry ratios R_{VV} and R_{HH} (equation 2.42) at 90° are unity, and that they are independent of the particulate morphology (i.e. single sphere, chain, cluster, or randomly branched chain agglomerate). This property was used to test the light scattering facility. The dissymmetry ratio at 90° was determined from the simultaneous measurement by the two detectors of the differential scattering cross sections. The dissymmetry ratio R_{VV} results obtained by the above described procedure at different heights above the burner surface are given by Table 4.4. The ratios were calculated from the averages of ten different measurements of the $K_{VV}(90°)$ values by the two detectors. The R_{VV} ratio for each experimental run was within 3% from unity.

4.8 Particle Sampling

The sampling of the soot particles at different heights above the burner surface was performed by using two different *ex-situ* techniques: thermophoretic sampling, and sampling with a probe.

Table 4.4. Dissymmetry ratio $R_{VV}(90°)$ at different heights above the burner surface for the flame investigated.

Height (mm)	Detector #1 $K'_{VV}(90°)$ ($cm^{-1}sr^{-1}$)	Standard Error	Detector #2 $K'_{VV}(90°)$ ($cm^{-1}sr^{-1}$)	Standard Error	R_{VV}
4	$3.55x10^{-7}$	± 5.3%	$3.63x10^{-7}$	± 4.9%	0.98
6	$6.27x10^{-6}$	± 4.5%	$6.20x10^{-6}$	± 4.7%	1.01
8	$2.41x10^{-5}$	± 4.6%	$2.41x10^{-5}$	± 5.2%	1.00
10	$5.37x10^{-5}$	± 3.5%	$5.39x10^{-5}$	± 4.2%	0.99
12	$8.97x10^{-5}$	± 3.9%	$9.15x10^{-5}$	± 4.8%	0.98
14	$1.33x10^{-4}$	± 3.8%	$1.37x10^{-4}$	± 4.4%	0.97
16	$1.74x10^{-4}$	± 3.7%	$1.81x10^{-4}$	± 4.6%	0.96
18	$2.21x10^{-4}$	± 3.2%	$2.28x10^{-4}$	± 3.8%	0.97
20	$2.26x10^{-4}$	± 3.2%	$2.74x10^{-4}$	± 4.0%	0.97
22	$3.19x10^{-4}$	± 3.7%	$3.28x10^{-4}$	± 4.0%	0.97

Soot deposition directly onto an electron microscopy grid can be achieved by rapidly introducing the grid into a hot soot-laden flow field. Thermophoretic deposition is driven by the temperature gradient between the gas stream and the cold surface. Dobbins and Megaridis[93] discussed a variety of probe configurations based on thermophoretic sampling. This technique is well suited for electron microscopy analysis of the particle morphology, as it eliminates the additional steps usually required in preparing soot samples extracted with a probe. Particle sampling with an extractive probe must be performed carefully to avoid problems such as, continuing agglomeration within the probe, biasing to larger or smaller particles due to sub or super-isokinetic sampling, and water condensation within and/or on the outer surface the probe.[94] In addition, further preparation of the extracted

soot for electron microscopy analysis requires dilution of the samples in a surfactant medium, agitation , and then deposition onto the microscopy grids. These procedures could only add uncertainties to the soot agglomerate characterization. Thermophoretic sampling, on the other hand, has the advantage of being unbiased to particle size and structure.[69,93,95]

A pneumatic double acting piston, controlled with a fast acting solenoid valve actuated by a computer trigger, was used to rapidly insert and retract the microscopy grids into the center of the flame. The grids were supported with adhesive tape on a thin stainless steel plate (4cm x 5 mm x 0.2 mm). The copper microscopy grids (200 mesh, 3mm in diameter) were coated with a fomvar-carbon substrate, onto which the soot was thermophoretically deposited. The grids were inserted vertically into the flame (ie the grid was parallel to the flow), in a path that followed the radial direction of the flame. The triggers used to actuate the pneumatic piston varied from 75 to 150 msec, depending on the height above the burner. Larger sampling times were required at lower heights, as a result of the lower particle number densities.

Soot particle samples were also taken with an extracting probe for comparison with the thermophoretic sampling results. The sampling probe used was a gas 6 inch gas chromatography stainless steel tube of 1/16 inch outside diameter and 0.050 inch inside diameter. The probe was inserted from the top of the flame stabilizer and down the z axis of the flame to the appropriate height above the burner. The probe was connected, by a system of three-way valves and tubing, to the sample filter holder line, to a bypass line, and to a nitrogen purging line. Both the filter line ans the bypass line were connected to a

vacuum pump with a gas flow-meter in between to monitor the sample gas flow rates. Nitrogen was continuously purged through the probe, and into the flame, to avoid blocking of the probe inlet during the time period required from flame ignition until a sample was taken. By simultaneously discontinuing the purging and establishing a vacuum, the sample gas stream was diverted to the bypass line. The sample gas flow rates were then set to achieve isokinetic sampling at this stage of the sampling process. The flame velocity measurements shown by Figure 4.9 were used to calculate the appropriate sample gas flow rates at each height above the burner surface investigated. Once the flow rates were set the sample gas flow was diverted to the filter holder line. Glass fiber filters (3 cm in diameter and 1 μm porocity) were used to collect the extracted soot particles. Samples were collected for about 5 minutes, yielding about 1 mg of soot. The samples were vacuum dried and stored in glass containers purged with nitrogen.

CHAPTER 5

EXPERIMENTAL RESULTS AND DISCUSSION

5.1 Extinction Cross Section Measurements

The extinction coefficients for the flame investigated were determined by measuring the transmission of the laser beam through the known optical path length of the flame. The extinction coefficient is related to the transmission ratio, τ, and the optical path length (see equation 2.30) by the following relation:

$$K_{ext} = -\frac{1}{L} \ln(\tau) \qquad (5.1)$$

The transmission ratio is defined as the ratio of the intensity, I, of the laser beam transmitted through the flame to incident beam intensity I_o. The measured transmission ratios at different height above the burner surface are given in Table 5.1. The transmission ratio decreases with increasing height above the burner surface due to larger particle diameters and soot volume fractions. The inferred extinction coefficients at different heights above the burner surface are shown in Table 5.2. All the experimental results presented in this Chapter are the average results of a minimum of 10 independent measurements for each parameter being measured.

Table 5.1. The measured transmission ratio τ, and standard error at different heights above the burner surface, for the ϕ=2.1 Propane/Oxygen flame.

Height (mm)	τ
6	0.95 ±0.11%
8	0.93 ±0.11%
10	0.92 ±0.11%
12	0.91 ±0.11%
14	0.90 ±0.11%
16	0.89 ±0.11%
18	0.88 ±0.11%
20	0.87 ±0.23%
22	0.85 ±0.23%

Table 5.2. The extinction coefficient K_{ext}, and standard error at different heights above the burner surface, for the ϕ=2.1 Propane/Oxygen flame.

Height (mm)	K_{ext} (cm^{-1})
6	0.0142 ±0.98%
8	0.0192 ±1.03%
10	0.0227 ±1.08%
12	0.0281 ±1.10%
14	0.0309 ±1.12%
16	0.0549 ±1.18%
18	0.0363 ±1.14%
20	0.0419 ±1.15%
22	0.0556 ±1.09%

5.2 Differential Scattering Cross Section Measurements

The differential scattering cross section K'_{vv} at the scattering angles of 20° and 45^0 was measured at different heights above the burner surface. Since the dissymmetry ratio R_{vv} was also measured at 20° and 45°, the signal from the front detector was used to obtain the differential scattering cross sections at the same angles. The average results of K'_{vv} and the standard error are presented in Table 5.3. Figures 5.1 and 5.2 also show the plots (with linear and logarithmic axis scaling) of K'_{vv} as a function of the height above the burner surface. The increase of the K'_{vv} values with increasing height indicates the presence of larger agglomerates, and/or larger primary particles, at higher heights in the flame. Also, as predicted by the sensitivity analysis, the values of K'_{vv} at the scattering angle of 20° are larger than those at the scattering angle of 45°.

Table 5.3. The measured differential scattering cross sections K'_{vv}, and standard error, at the scattering angles of 20° and 45°, and at different heights above the burner surface, for the ϕ=2.1 Propane/Oxygen flame.

Height (mm)	$K'_{vv}(20°)$ ($cm^{-1}sr^{-1}$)	$K'_{vv}(45°)$ ($cm^{-1}sr^{-1}$)
6	8.21×10^{-6} ±3.42%	8.11×10^{-6} ±3.77%
8	3.35×10^{-5} ±4.18%	3.22×10^{-5} ±4.04%
10	8.24×10^{-5} ±3.65%	7.67×10^{-5} ±3.75%
12	1.51×10^{-4} ±3.89%	1.37×10^{-4} ±4.01%
14	2.42×10^{-4} ±3.84%	2.13×10^{-4} ±3.85%
16	3.41×10^{-4} ±3.34%	2.97×10^{-4} ±3.94%
18	4.68×10^{-4} ±3.56%	3.89×10^{-4} ±3.37%
20	6.17×10^{-4} ±3.86%	5.05×10^{-4} ±3.45%
22	8.62×10^{-4} ±3.39%	6.65×10^{-4} ±3.74%

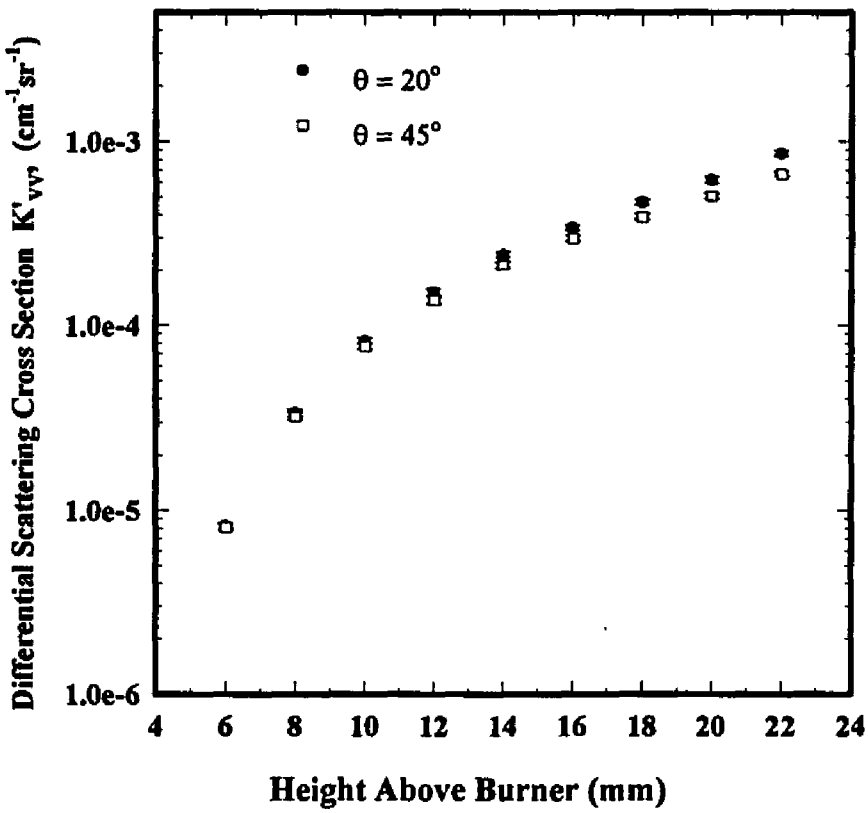

Figure 5.1 Semi-logarithmic plot of the measured differential scattering cross sections at the scattering angles of 20° and 45°, as function of the height above the burner.

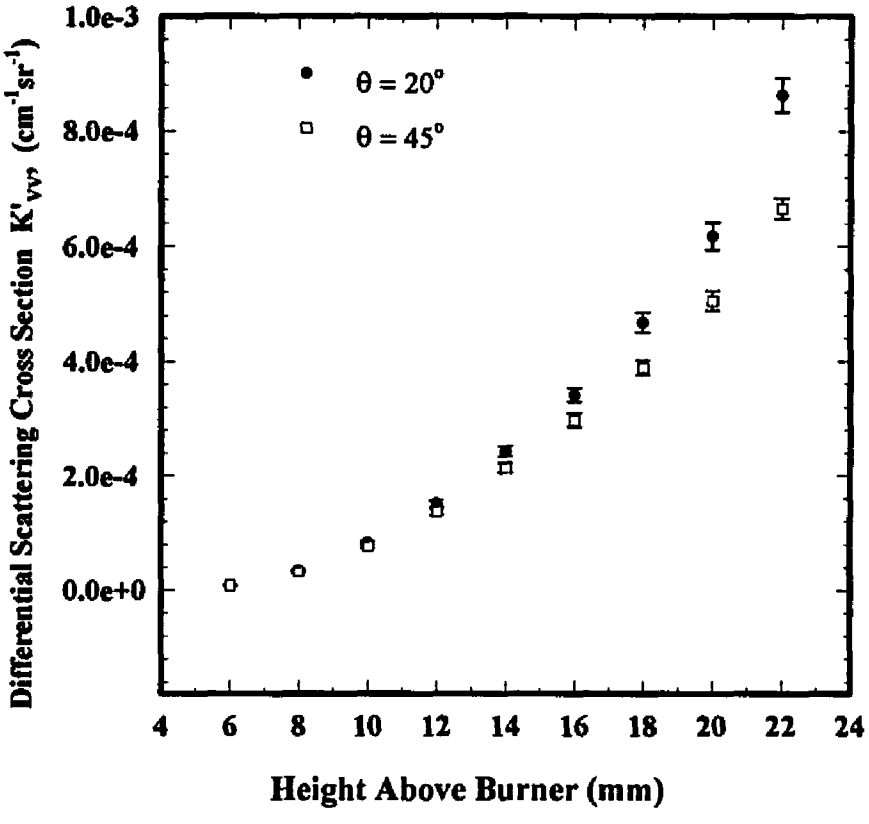

Figure 5.2 Linear plot of the measured differential scattering cross sections at the scattering angles of 20° and 45°, as function of the height above the burner.

5.3 Measurements of the Dissymmetry Ratios R_{VV} and R_{HH}

The dissymmetry ratios R_{VV} and R_{HH} were measured by using the two detector (180° apart) setup described in section 4.2 of the previous chapter. The half-wave plate and the polarizers were rotated to give the horizontal-horizontal orientation for the incident and the scattered beams, which is required in the R_{HH} ratio measurement. Tables 5.4 and 5.5 give respectively the measured dissymmetry ratios R_{VV} and R_{HH}, and the corresponding standard errors, at the scattering angles of 20° and 45°, and as functions of the height above the burner surface. Figures 5.3 and 5.4 show the plots of the dissymmetry ratio results. As seen from the figures both the dissymmetry ratios R_{VV} and R_{HH} increase with increasing height above the burner surface, indicating increasing anisotropy with inreasing height. Again, the results follow the trends predicted by the sensitivity analysis. In other words, the dissymmetry ratios at the scattering angle of 20° obtain larger values than those at the scattering angle of 45° for a fixed position in the flame. However, the sensitivity analysis predicts that the R_{HH} ratios for either a chain, a cluster, or a randomly branched chain, obtain values approximately equal to or slightly smaller than the values of the R_{VV} ratio. A comparison of the values of the R_{VV} and R_{HH} measurements at the scattering angle of 20°, shows that the R_{HH} ratios at all heights are slightly larger than the R_{VV} values. The repeatability of the measurements at 20°, however, is excellent. The possibility of contaminated signals reaching the detectors was eliminated, because the ratios obtained from the calibration signals of methane and nitrogen were between 2.1 and 2.25 for all the experimantal runs. High ratios of the methane to nitrogen calibration signal indicate lower levels of stray light effects. No

explanation can be offered for this effect at this time. A good agreement with the trends predicted is displayed by the results at the scattering angle of 45°.

Table 5.4. The measured dissymmetry ratio R_{VV}, and standard error, at the scattering angles of 20° and 45°, and at different heights above the burner surface, for the ϕ=2.1 Propane/Oxygen flame.

Height (mm)	$R_{VV}(20°)$	$R_{VV}(45°)$
6	1.26 ± 0.38%	1.16 ± 0.57%
8	1.37 ± 0.31%	1.24 ± 0.62%
10	1.54 ± 0.57%	1.34 ± 0.48%
12	1.71 ± 0.41%	1.45 ± 0.64%
14	1.92 ± 0.49%	1.57 ± 0.73%
16	2.14 ± 0.55%	1.69 ± 0.92%
18	2.42 ± 0.60%	1.82 ± 0.99%
20	2.73 ± 0.94%	1.98 ± 0.99%
22	3.10 ± 0.97%	2.16 ± 0.93%

Table 5.5. The measured dissymmetry ratio R_{HH}, and standard error, at the scattering angles of 20° and 45°, and at different heights above the burner surface, for the ϕ=2.1 Propane/Oxygen flame.

Height (mm)	$R_{HH}(20°)$	$R_{HH}(45°)$
6	1.35 ± 0.76%	1.16 ± 0.49%
8	1.54 ± 1.88%	1.25 ± 0.60%
10	1.71 ± 0.71%	1.34 ± 0.65%
12	1.89 ± 0.44%	1.44 ± 0.45%
14	2.13 ± 0.43%	1.56 ± 0.69%
16	2.36 ± 0.53%	1.67 ± 0.86%
18	2.67 ± 0.50%	1.81 ± 0.83%
20	3.01 ± 0.98%	1.93 ± 1.03%
22	3.33 ± 1.04%	2.09 ± 1.14%

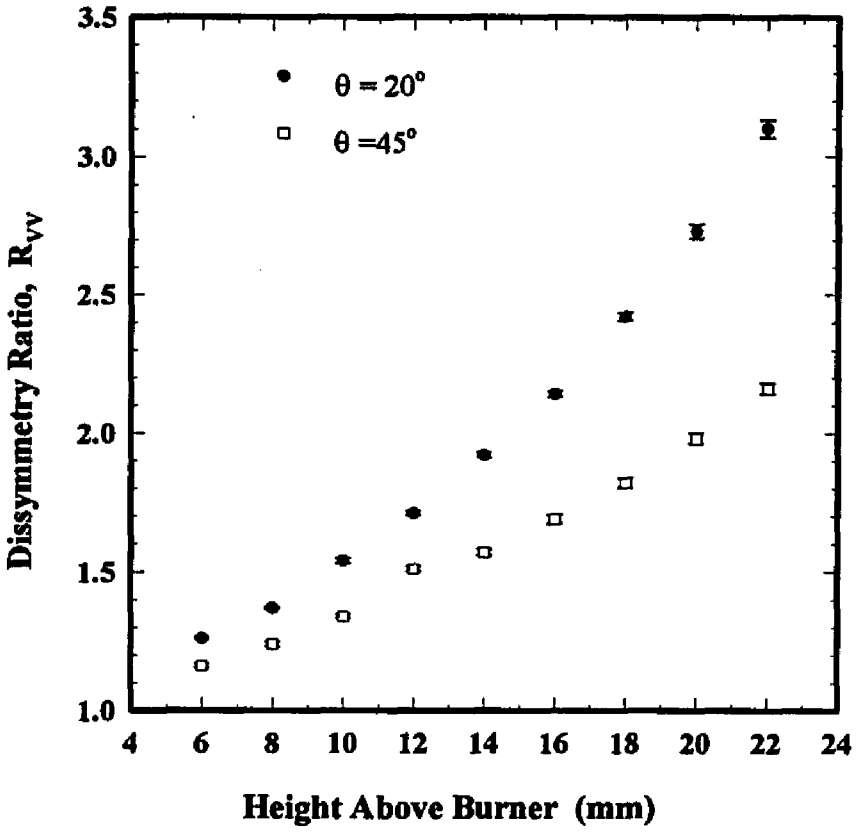

Figure 5.3 The measured dissymmetry ratio R_{VV} at the scattering angles of 20° and 45°, as function of the height above the burner.

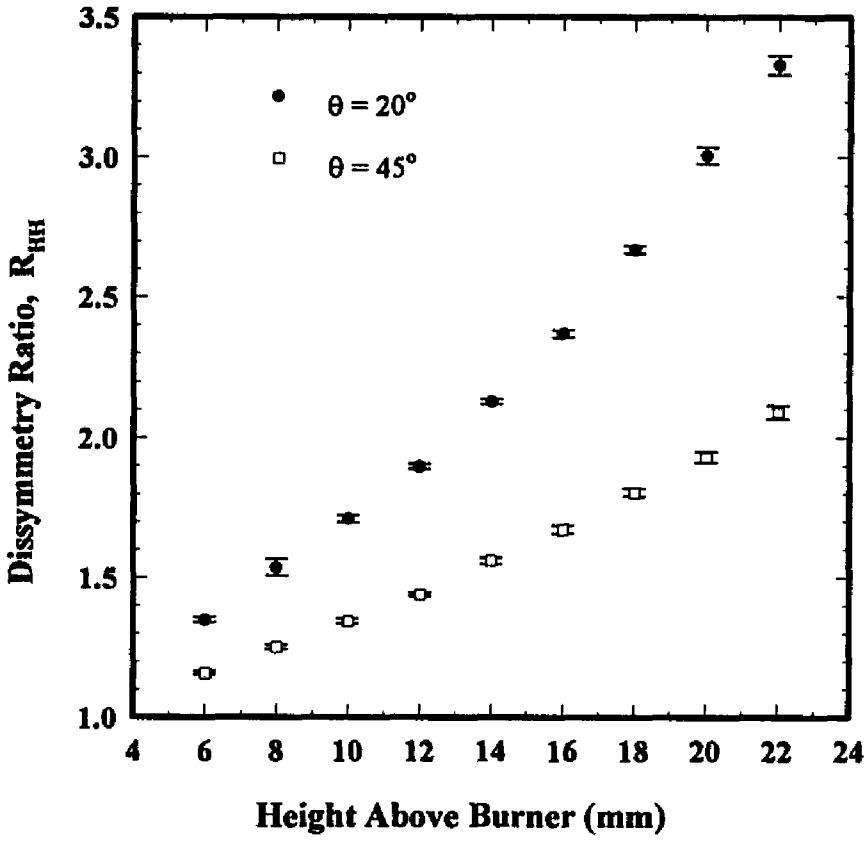

Figure 5.4 The measured dissymmetry ratio R_{HH} at the scattering angles of 20° and 45°, as function of the height above the burner.

5.4 Depolarization Ratio Measurements

The depolarization ratio ρ_V was measured at the scattering angles of 160° and 135°. As explained with the sensitivity analysis results, the ratio ρ_V obtains larger values at the backward scattering angles. The VH component of the scattered light is not as strong a function of the scattering angle as the VV component. The differential scattering cross section K'_{VV} decreases with increasing scattering angle. Since the ratio of the VH and VV differential scattering cross sections is used to measure ρ_V, a measurement in the backward scattering angle will result in larger values. Since the VH component of the molecular scattering signal from methane was not measurable, the VV molecular scattering signal from methane was used to calibrate both the VV and VH measured signals. Table 5.6 shows the results of the depolarization ρ_V measurement. The same results are also shown by Figure 5.5. The results do not follow the trends predicted by the sensitivity analysis, where larger values of ρ_V are expected for the scattering angle of 160°. Instead, the measured depolarization ratio at the scattering angle of 135° had larger values than that at 160°. The only explanation that can be given for the deviations of the measured quantities from the predicted trends, is that the flame may not be perfectly cylindrical. In such a case the signals may be attenuated by a different amount at each angle before they reach the detector, and therefore causing the effect observed here. In addition, using two signals that differ by three orders of magnitude to determine the ratio can also introduce uncertainties. The repeatability of the measurements, however, was excellent in this case.

Table 5.6. The measured depolarization ratio ρ_V, and standard error, at the scattering angles of 160° and 135°, and at different heights above the burner surface, for the ϕ=2.1 Propane/Oxygen flame.

Height (mm)	$\rho_V(160°)$	$\rho_V(135°)$
6	0.0131 ± 1.84%	0.0163 ± 1.21%
8	0.0123 ± 1.16%	0.0144 ± 1.37%
10	0.0114 ± 1.14%	0.0137 ± 0.88%
12	0.0113 ± 1.10%	0.0136 ± 1.12%
14	0.0112 ± 1.45%	0.0133 ± 0.66%
16	0.0113 ± 1.33%	0.0133 ± 0.82%
18	0.0115 ± 1.50%	0.0134 ± 0.90%
20	0.0119 ± 2.06%	0.0137 ± 1.55%
22	0.0122 ± 1.75%	0.0137 ± 1.01%

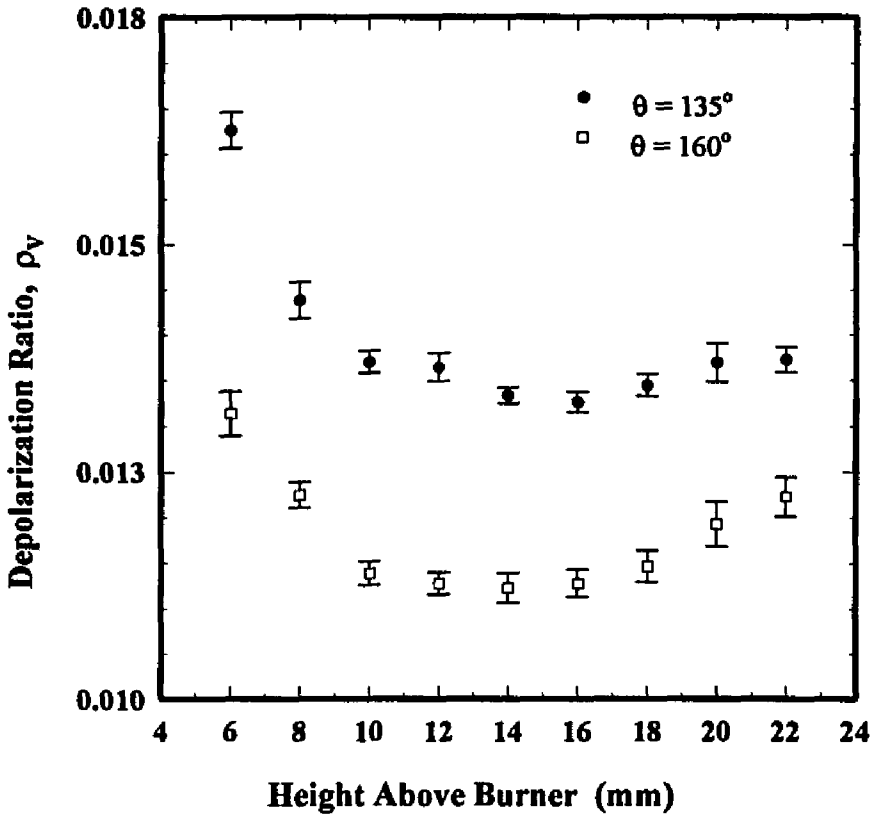

Figure 5.5 The measured depolarization ratio ρ_V at the scattering angles of 160° and 135°, as function of the height above the burner.

5.5 Agglomerate Model Analysis

The experimental measurements presented in the previous sections of this chapter were divided into two sets, which were used for inferring the agglomerate parameters by using the agglomerate model developed by Lou and Charalampopoulos.[90] Tables 5.7 and 5.8 show respectively the two sets of measurements as used in the computations.

Table 5.7. First set of the measured quantities as used in the agglomerate analysis.

Height (mm)	$K'_{vv}(20°)/K_{ext}$ (sr)	$R_{VV}(20°)$	$R_{HH}(20°)$	$\rho_V(160°)$
6	5.770×10^{-4}	1.26	1.35	0.0131
8	1.741×10^{-3}	1.37	1.54	0.0122
10	3.637×10^{-3}	1.54	1.71	0.0114
12	5.375×10^{-3}	1.71	1.90	0.0113
14	7.820×10^{-3}	1.92	2.13	0.0112
16	9.609×10^{-3}	2.14	2.37	0.0113
18	1.267×10^{-2}	2.42	2.67	0.0115
20	1.474×10^{-2}	2.73	3.00	0.0119
22	1.550×10^{-2}	3.10	3.33	0.0122

Table 5.8. Second set of the measured quantities as used in the agglomerate analysis.

Height (mm)	$K'_{vv}(45°)/K_{ext}$ (sr)	$R_{VV}(45°)$	$R_{HH}(45°)$	$\rho_V(135°)$
6	5.699×10^{-4}	1.16	1.16	0.0168
8	1.673×10^{-3}	1.24	1.25	0.0144
10	3.385×10^{-3}	1.34	1.34	0.0137
12	4.876×10^{-3}	1.45	1.44	0.0136
14	6.883×10^{-3}	1.57	1.56	0.0133
16	8.369×10^{-3}	1.69	1.67	0.0133
18	1.053×10^{-2}	1.82	1.81	0.0134
20	1.206×10^{-2}	1.98	1.93	0.0137
22	1.196×10^{-2}	2.16	2.09	0.0137

The ratio of the differential scattering and extinction cross sections $K'_{VV}(\theta)/K_{ext}$ (equation 3.6), and the dissymmetry ratio $R_{VV}(\theta)$ (equation 3.7), were used in the agglomerate analysis. The two equations were simultaneously solved for the two unknown parameters; N_p and d_p. The parameters N_p and d_p were found by minimizing the function S,

$$S = \left\{(X_{exp} - X_{sim})\ C\right\}^2 + \left\{(Y_{exp} - Y_{sim})\right\}^2, \tag{5.1}$$

where,

$$X = \frac{K'_{VV}(\theta)}{K_{ext}}, \tag{5.2}$$

$$Y = R_{VV}(\theta), \tag{5.3}$$

and

$$C = \frac{\left(R_{VV}\right)_{exp}}{\left(\frac{K'_{VV}(\theta)}{K_{ext}}\right)_{exp}}. \tag{5.4}$$

The subscripts **exp** and **sim** denote respectively the measured and simulated quantities. The factor C in equation (5.1) was used for easier convergence. Since the $K'_{VV}(\theta)/K_{ext}$ has values of two to four orders of magnitude smaller than the values of $R_{VV}(\theta)$, the first term on the right hand side of equation (5.1) will not greatly influence the function S. By scaling the term by a factor C, it is brought to the same level as that of the R_{VV} term. The

simulated values of the $K'_{vv}(\theta)/K_{ext}$ and $R_{vv}(\theta)$, were calculated by using a known refractive index. Four different values of the refractive index (from previous works[10,70,82]) were used in the analysis of the results. Once the N_p and d_p parameters were determined, the agglomerate number density N (number of agglomerates/cm^3) was calculated using either one of the equations (3.1) and (3.2). The percent difference between the experimental and simulated results was also calculated in an attempt to assess the validity assumption used in the agglomerate analysis. Only the results of the straight chain, cluster and randomly branched chain agglomerate analysis, using the refractive index of m=1.48-0.35i, will be presented in this chapter. The rest of the results are presented in the Appendix B.

Table 5.9 shows the inferred parameters for a straight chain agglomerate analysis of the results at the scattering angle of 20°, and using the refractive index of m=1.48-0.35i. The last four columns in the table display the percent difference between the experimental and simulated values. Table 5.10 shows the results of the straight chain analysis of the experimental measurements at the scattering angle of 45°, using the refractive m=1.48-0.35i. The results from the cluster analysis using the same refractive index are shown in Table 5.11 and 5.12. Finally, Tables 5.13 and 5.14 summarize the results of the randomly branched agglomerate analysis.

Table 5.9. Straight Chain agglomerate analysis of the experimental measurements summarized in Table 5.6.

Straight Chain, θ=20°, m=1.48-0.35i							
	Inferred Parameters			% Diff. Between Measurement and Simulation			
H (mm)	N_p	d_p (nm)	N	K'_{vv}/K_{ext}	R_{VV}	R_{HH}	ρ_V
6	7	17.7	$9.7x10^9$	0.7	0.3	7.7	105
8	5	28.8	$4.2x10^9$	0.3	1.8	14.7	103
10	5	36.0	$2.5x10^9$	0.4	0.6	10.9	62.8
12	5	42.3	$1.8x10^9$	0.6	2.7	8.7	39.5
14	5	48.2	$1.3x10^9$	0.9	2.6	8.9	23.1
16	6	48.5	$1.2x10^9$	0.3	7.9	3.2	2.7
18	7	50.0	$9.9x10^8$	9.5	9.9	1.0	6.5
20	8	50.0	$1.0x10^9$	13.8	8.0	3.8	8.4
22	9	50.0	$1.2x10^9$	8.9	4.9	5.6	10.9

Table 5.10. Straight Chain agglomerate analysis of the experimental measurements summarized in Table 5.7.

Straight Chain, θ=45°, m=1.48-0.35i							
	Inferred Parameters			% Diff. Between Measurement and Simulation			
H (mm)	N_p	d_p (nm)	N	K'_{vv}/K_{ext}	R_{VV}	R_{HH}	ρ_V
6	6	18.7	$9.7x10^9$	0.6	0.6	1.8	186
8	5	28.8	$4.2x10^9$	0.3	0.9	1.6	153
10	4	39.5	$2.3x10^9$	0.2	0.3	4.9	158
12	5	42.1	$1.9x10^9$	0.5	1.0	2.2	86.3
14	5	47.7	$1.4x10^9$	1.7	5.1	1.4	62.2
16	6	44.9	$3.4x10^8$	0.05	2.2	17.2	24.9
18	33	49.7	$2.1x10^8$	0.2	0.02	8.6	30.2
20	42	50.0	$1.9x10^8$	8.7	1.0	2.6	30.1
22	45	50.0	$2.3x10^8$	7.3	4.5	8.1	29.4

Table 5.11. Cluster agglomerate analysis of the experimental measurements summarized in Table 5.6.

Cluster, θ=20°, m=1.48-0.35i							
	Inferred Parameters			% Diff. Between Measurement and Simulation			
H (mm)	N_p	d_p (nm)	N	K'_{VV}/K_{ext}	R_{VV}	R_{HH}	ρ_V
6	20	12.5	9.9×10^{9}	1.1	18.1	26.5	9976
8	20	18.1	4.3×10^{9}	5.5	19.7	34.5	8033
10	20	22.8	2.4×10^{9}	2.3	24.4	38.0	6233
12	20	26.9	1.8×10^{9}	3.4	27.1	40.9	5550
14	20	30.8	1.3×10^{9}	4.4	29.8	43.7	4566
16	20	33.3	1.1×10^{9}	5.6	35.2	49.3	4246
18	20	37.1	8.2×10^{8}	7.7	36.1	49.5	3493
20	20	39.4	7.7×10^{8}	8.8	41.9	55.7	3205
22	20	40.4	9.5×10^{8}	10.4	55.4	66.1	3110

Table 5.12. Cluster agglomerate analysis of the experimental measurements summarized in Table 5.7.

Cluster, θ=45°, m=1.48-0.35i							
	Inferred Parameters			% Diff. Between Measurement and Simulation			
H (mm)	N_p	d_p (nm)	N	K'_{VV}/K_{ext}	R_{VV}	R_{HH}	ρ_V
6	23	11.9	1.0×10^{10}	0.9	10.4	10.1	8478
8	23	17.1	4.5×10^{9}	0.2	11.9	12.3	6757
10	23	21.9	2.4×10^{9}	1.5	13.2	12.3	5608
12	23	24.9	2.0×10^{9}	1.7	21.4	14.4	4937
14	23	28.3	1.5×10^{9}	3.0	18.2	15.7	4333
16	23	30.4	1.3×10^{9}	3.1	21.6	18.1	4056
18	23	33.2	1.0×10^{9}	3.9	22.5	19.2	3622
20	23	35.1	9.8×10^{8}	5.1	26.9	20.7	3412
22	23	35.2	1.3×10^{9}	6.6	38.0	30.3	3325

Table 5.13. Randomly branched chain agglomerate analysis of the experimental measurements summarized in Table 5.6.

Randomly Branched Chain, θ=20°, m=1.48-0.35i							
	Inferred Parameters			% Diff. Between Measurement and Simulation			
H (mm)	N_p	d_p (nm)	N	K'_{vv}/K_{ext}	R_{VV}	R_{HH}	ρ_V
6	20	12.5	$9.9x10^9$	0.4	1.6	8.8	1412
8	11	22.0	$4.4x10^9$	1.3	0.7	11.6	817
10	9	29.5	$2.5x10^9$	0.7	1.5	9.5	559
12	7	38.0	$1.8x10^9$	1.7	1.1	12.3	449
14	7	43.0	$1.4x10^9$	0.4	2.0	8.7	352
16	7	46.0	$1.3x10^9$	1.9	0.7	10.1	305
18	7	50.0	$1.0x10^9$	6.4	1.7	8.5	249
20	8	50.0	$1.0x10^9$	9.5	4.0	5.9	220
22	9	49.5	$1.2x10^8$	6.3	4.7	2.6	202

Table 5.14. Randomly branched chain agglomerate analysis of the experimental measurements summarized in Table 5.7.

Randomly Branched Chain, θ=45°, m=1.48-0.35i							
	Inferred Parameters			% Diff. Between Measurement and Simulation			
H (mm)	N_p	d_p (nm)	N	K'_{vv}/K_{ext}	R_{VV}	R_{HH}	ρ_V
6	23	12.0	$9.7x10^9$	0.2	5.7	13.4	1548
8	18	19.0	$4.2x10^9$	0.7	0.4	12.3	1049
10	14	26.0	$2.4x10^9$	0.7	0.07	11.5	732
12	11	33.5	$1.7x10^9$	1.2	1.0	10.5	510
14	10	39.5	$1.2x10^9$	0.05	0.5	11.0	390
16	10	43.0	$1.1x10^9$	1.6	0.5	10.9	329
18	9	49.5	$7.9x10^8$	1.5	0.2	11.5	250
20	10	50.0	$7.9x10^8$	3.2	1.4	12.7	238
22	13	48.0	$9.1x10^8$	1.0	0.3	8.1	249

The results summarized in the tables above do not indicate any of the trends that were expected. Specifically an increase of the number of primary particles in the agglomerate N_p, along with an increase in the primary particle d_p, was expected with increasing height (or flame residence time of the soot particles) above the burner surface. In fact, the results obtained show almost all the cases a primary particle diameter increase only and no or very small change in the number of primary particles in the agglomerate. The straight chain analysis results had the least deviation between the simulated and experimental values for the depolarization ratio ρ_V. Even so, the percent errors between the experimental and simulated depolarization ratio values were much larger than those observed for the dissymmetry ratio R_{HH}. The cluster analysis results demonstrate that the assumption of a closely packed (approximately spherical) agglomerate structure is the least accurate of all. The agglomerate number densities calculated decrease with increasing height above the burner surface. A decrease in the number density means increasing agglomeration and particle sizes. However, the results indicate that only the primary particle diameter is influencing the agglomerate number densities.

The next section of this chapter presents the results of the electron microscopy analysis performed on the soot extracted from the flame. A comparison beween the results of this section and the *ex-situ* analysis should be a good indicator of how well the optical technique predicts the agglomerate structural properties.

5.6 Transmission Electron Microscopy Results

The soot samples extracted from the flame using thermophoretic sampling were viewed under the transmission electron microscope. The micrographs shown in this section were taken at locations near the center of the grid, to ensure that the samples were representative of the position in the flame that was being sampled. The Argon-Ion laser beam was used to position and align the thermophoretic probe in the center of the flame. Figures 5.6 -5.14 show the micrographs of the soot samples taken at different positions in the flame. Figure 5.6 shows the soot extracted from the height of 6 mm above the burner surface. The agglomeration effects, although they exist at this height, are not as prominent. Single particles and agglomerates consisting of a few primary particles are observed at this height. The soot sample extracted at 8 mm above the burner surface is shown in Figure 5.7. As seen in this micrograph the agglomeration of the individual soot particles begins to become more prominent at this height, and larger elongated agglomerates are found. However, single particles and small agglomerates can still be found. The trend of increasing agglomeration with height can be seen in the rest of the figures (Figures 5.8 -5.14), where randomly branched structures with increasing complexity are present. Smaller agglomerates and even single particles can be found at all heights above the burner surface. It is quite obvious from these micrographs that the assumption used in the agglomerate model analysis of the optical measurements of all the agglomerates (at a certain position in the flame) consisting of the same number of primary particles is a weak one. If one accepts that thermophoretic sampling can capture an unbiased instantaneous picture of the agglomeration at each position on the flame without

greatly disturbing the process, then it is obvious from the microscopy results, that the agglomerate model used for the analysis of the optical measurements should be changed to include a distribution of the number of primary particles in the agglomerate. The assumption of all the primary particles in the soot agglomerates being monosized seems to be a good assumption.

Soot samples were also sent for detailed microscopy analysis, that includes sizing and agglomeration characterization, to the Operation and Technology Center of the Columbian Chemicals Company. An automated image analysis of the soot samples was performed and the results are summarized in Table 5.15.

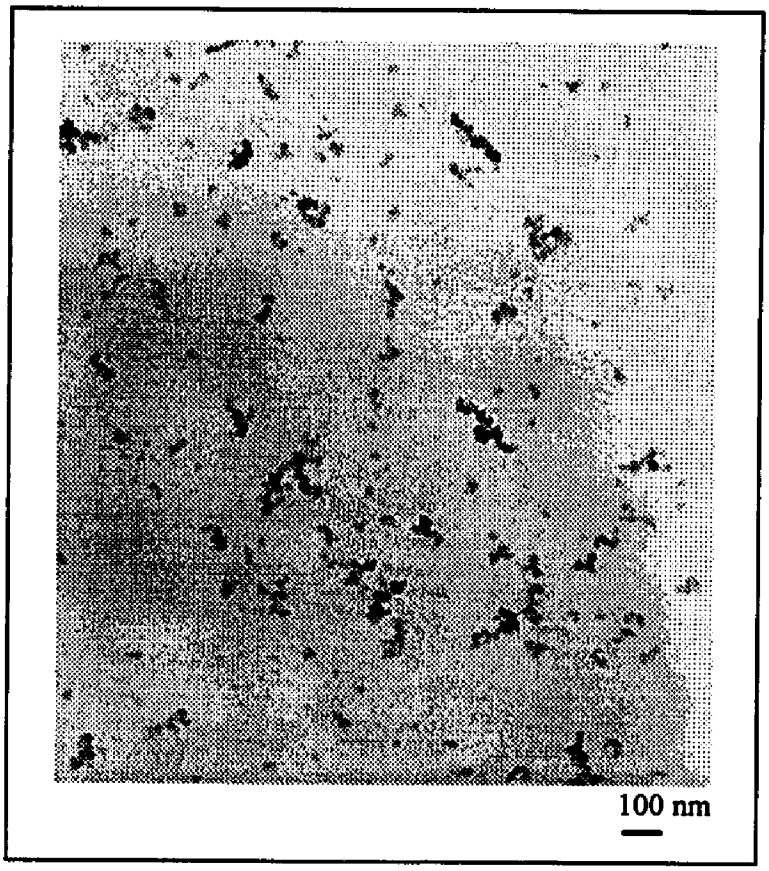

Figure 5.6 Transmission Electron Microscopy micrograph of a soot sample extracted at 6 mm above the burner surface by thermophoretic sampling. (Propane/Oxygen Flame ϕ=2.1, 80 KV, x 50K)

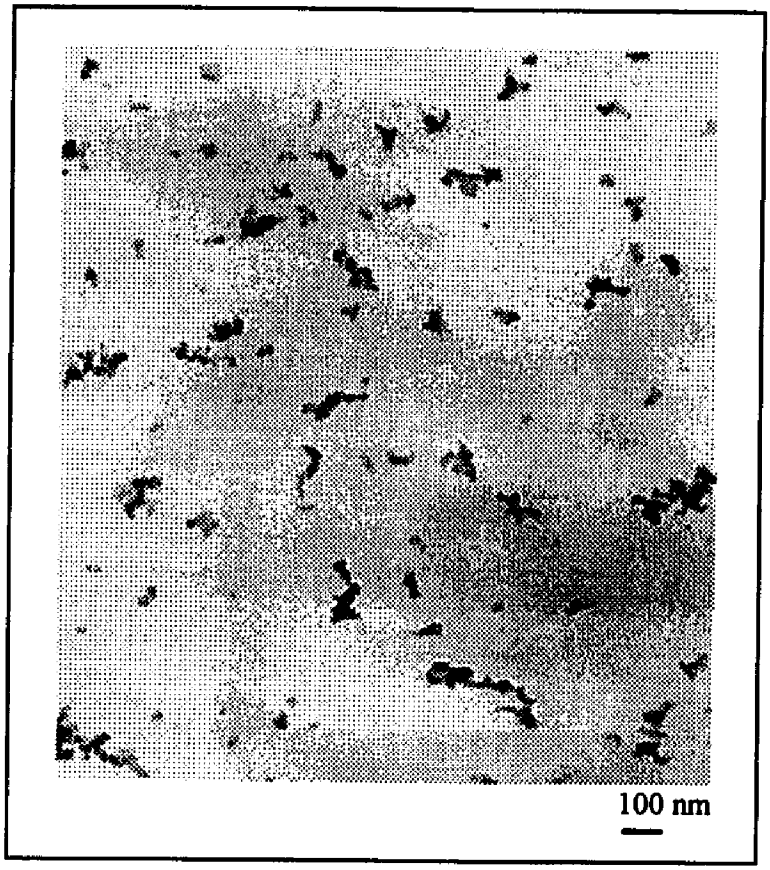

Figure 5.7 Transmission Electron Microscopy micrograph of a soot sample extracted at 8 mm above the burner surface by thermophoretic sampling. (Propane/Oxygen Flame ϕ=2.1, 80 KV, x 50K)

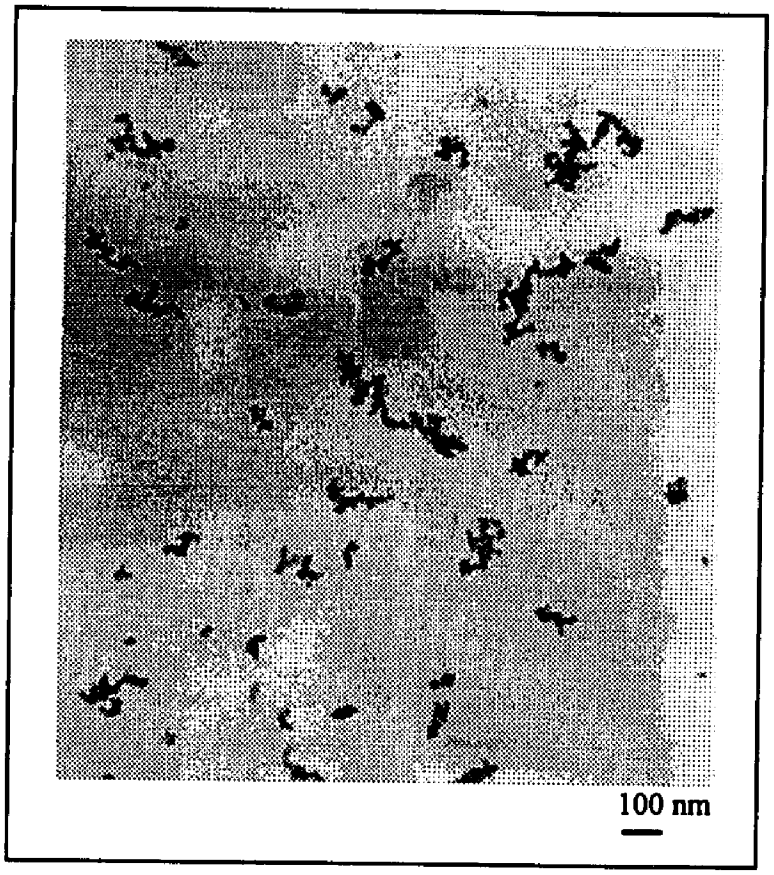

Figure 5.8 Transmission Electron Microscopy micrograph of a soot sample extracted at 10 mm above the burner surface by thermophoretic sampling. (Propane/Oxygen Flame ϕ=2.1, 80 KV, x 50K)

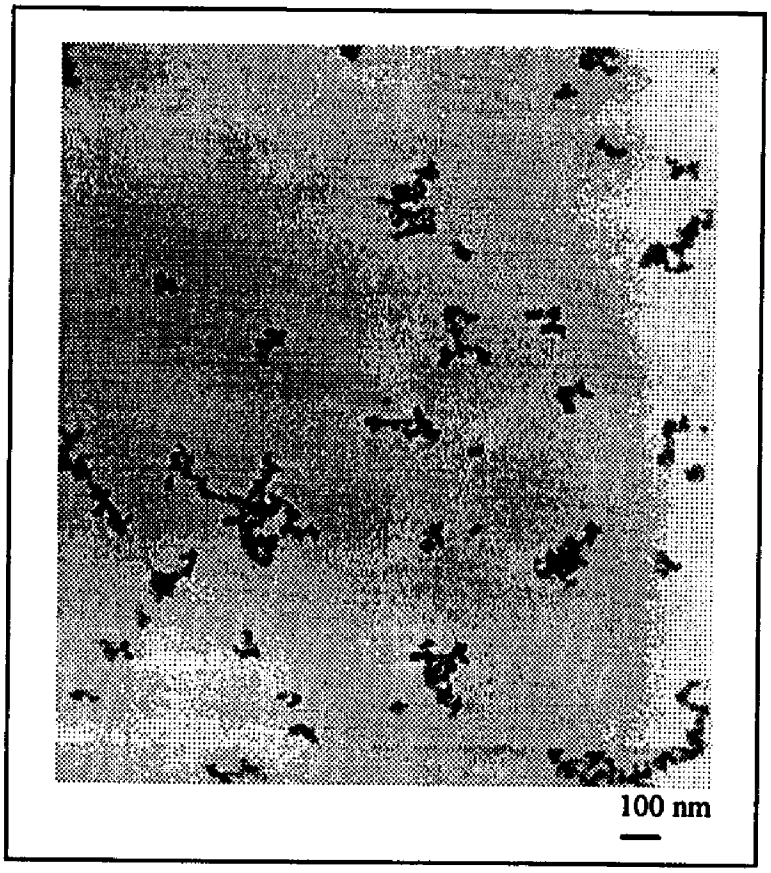

Figure 5.9 Transmission Electron Microscopy micrograph of a soot sample extracted at 12 mm above the burner surface by thermophoretic sampling. (Propane/Oxygen Flame ϕ=2.1, 80 KV, x 50K)

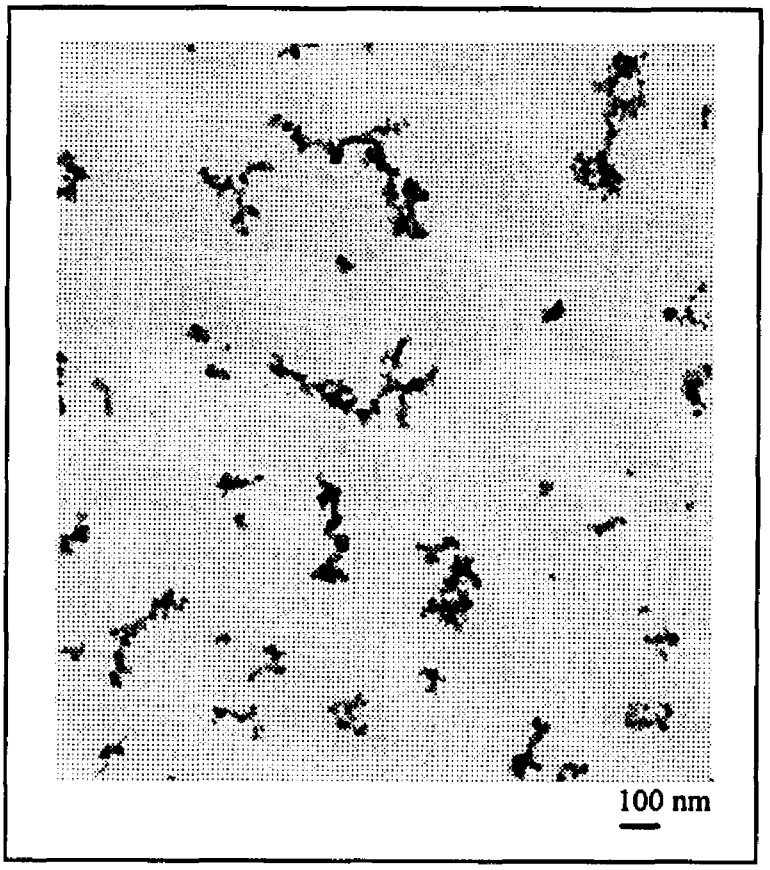

Figure 5.10 Transmission Electron Microscopy micrograph of a soot sample extracted at 14 mm above the burner surface by thermophoretic sampling. (Propane/Oxygen Flame ϕ=2.1, 80 KV, x 50K)

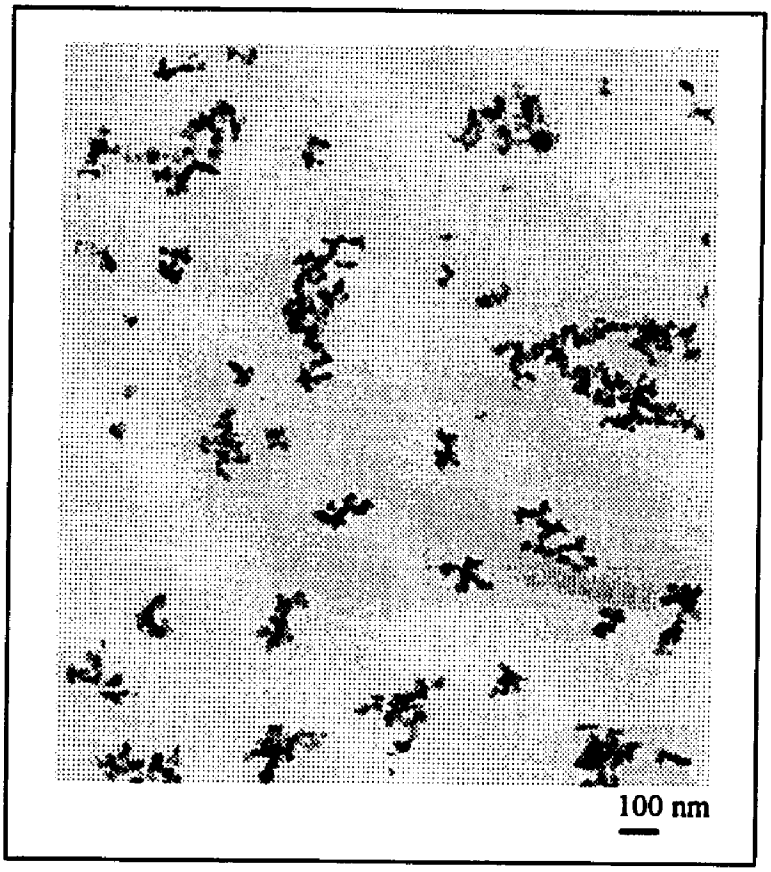

Figure 5.11 Transmission Electron Microscopy micrograph of a soot sample extracted at 16 mm above the burner surface by thermophoretic sampling. (Propane/Oxygen Flame ϕ=2.1, 80 KV, x 50K)

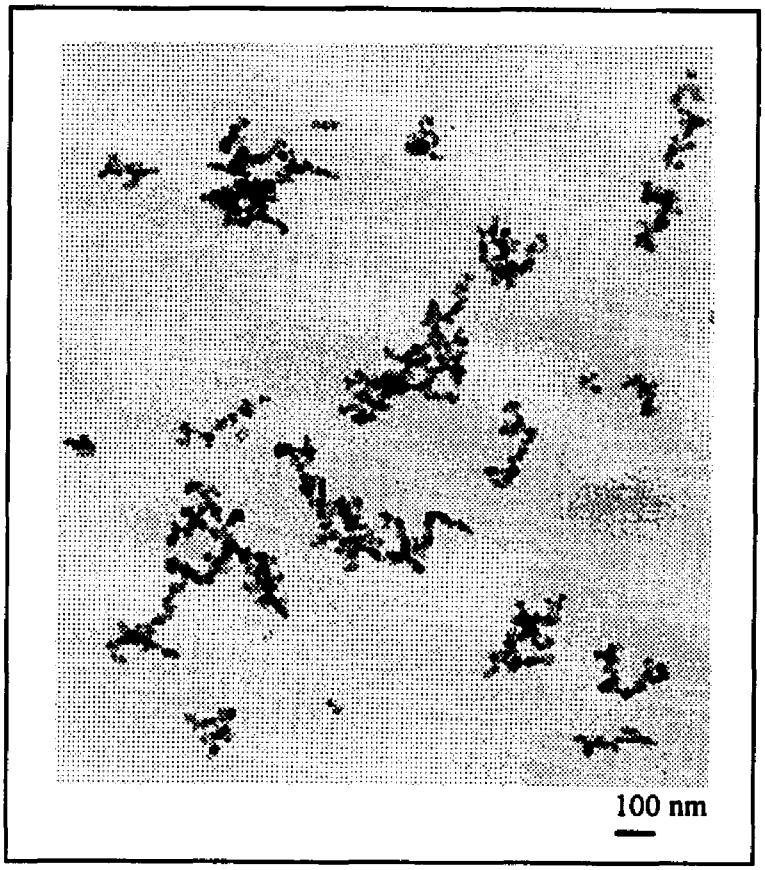

Figure 5.12 Transmission Electron Microscopy micrograph of a soot sample extracted at 18 mm above the burner surface by thermophoretic sampling. (Propane/Oxygen Flame ϕ=2.1, 80 KV, x 50K)

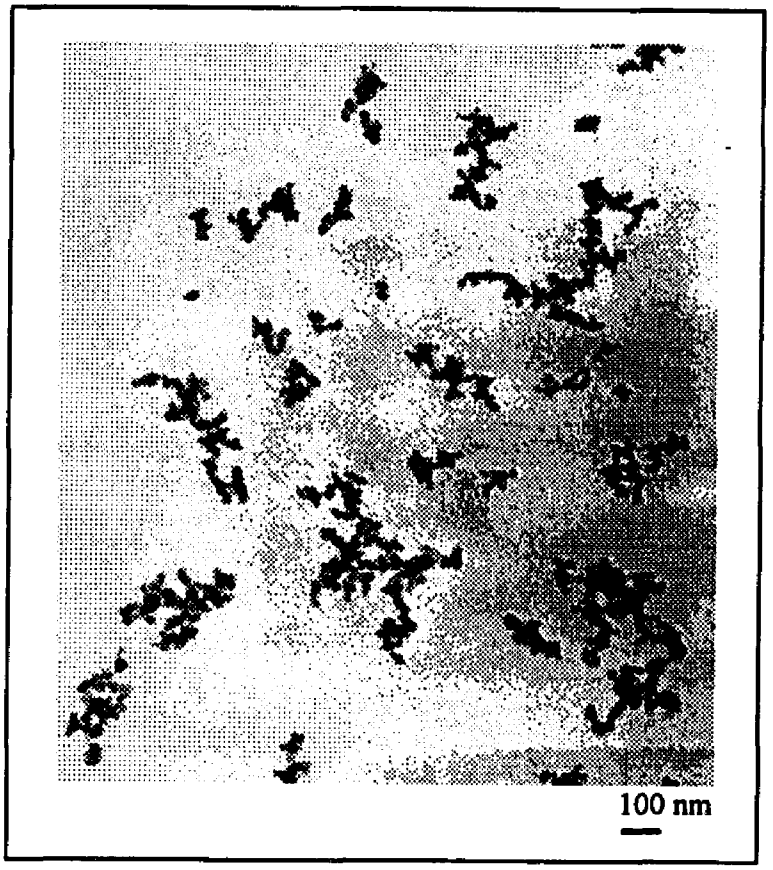

Figure 5.13 Transmission Electron Microscopy micrograph of a soot sample extracted at 20 mm above the burner surface by thermophoretic sampling. (Propane/Oxygen Flame ϕ=2.1, 80 KV, x 50K)

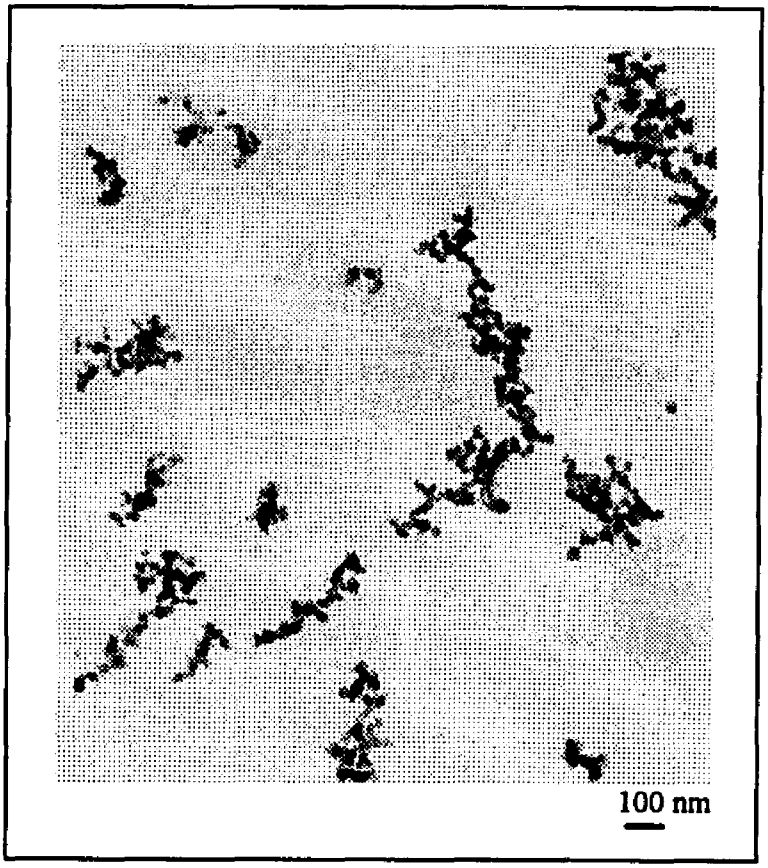

Figure 5.14 Transmission Electron Microscopy micrograph of a soot sample extracted at 22 mm above the burner surface by thermophoretic sampling. (Propane/Oxygen Flame ϕ=2.1, 80 KV, x 50K)

Table 5.15. Electron microscopy analysis results of the soot samples extracted with a sampling probe from the flame investigated.

Transmission Electron Microscopy Results			
Height (mm)	**N_p**	**dp (nm)**	**Stand. Dev. (nm)**
10	54.6	13.6	4.7
12	48.4	12.8	4.8
14	48.7	12.9	4.3
16	64.5	14.9	4.3
18	50.0	13.4	3.6
20	56.8	14.6	3.8
22	53.6	14.4	3.6

The soot samples extracted by using thermophoretic sampling were not suitable for the automated image analysis, because the carbon film support of the microscopy grids was damaged by the adverse flame conditions. Because of this damage, the contrast of the micrographs obtained with the TEM was not suitable for the image analysis. It was suggested that microscopy grids made of tungsten and coated with a carbon film should be used instead. Also, further experimentation with the thermophoretic sampling times is needed, in order to obtain large enough concentrations of soot on the microscopy grids, and at the same time avoid damage of the grid support film by the high flame temperatures.

The soot samples collected with the sampling probe were dispersed in a cloroform solution and agitated in an ultrasonic bath. The suspension of soot was then diluted further and agitated. Once the optimum dilution was obtain a drop of the suspension was deposited on microscopy grids and allowed to dry in air. Two thousand agglomerates at each height were analyzed. Table 5.15 shows the results of the automated image analysis.

The average primary particle diameter remains relatively constant with increasing height. The range of primary particle diameters d_p was from 12.8 - 14.9 nm. Also, the number of primary particles per agglomerate N_p remained relatively constant with increasing height. The values of N_p ranged from 48.4 - 64.5 particles per agglomerate. A self preserved distribution of both the d_p and N_p seems to be the trend observed in these samples. However, the soot samples were extracted with a sampling probe that was not water-cooled. There is no indication at this time about the possibility of the agglomeration process continuing inside the probe. A quantitative analysis of the agglomerate structural properties of soot samples extracted with the thermophoretic sampling probe will remove any ambiguities about the results presented in table 5.15.

In summary, both the qualitative and quantitative analysis of soot samples extracted with sampling probes, indicate that the primary particles in the soot agglomerates are fairly monosized within each agglomerate, and possess diameters d_p in the range 12-15 nm. Also, the agglomerates consist of a large number of primary particles N_p. The micrographs of the soot samples obtained with the thermophoretic sampling probe show very clearly that there exists a mixture of agglomerates of different N_p and maximum aggregate size at all heights above the burner surface.

CHAPTER 6

CONCLUSIONS AND RECOMMENDATIONS

6.1 Summary and Conclusions

The goal of this study was to develop an *in-situ* optical technique, to characterize the structural and optical properties of the soot agglomerates formed during the incomplete combustion of carbonaceous fuels. Specifically the unknown soot agglomerate parameters: (a) agglomerate number density N; (b) number of primary particles per agglomerate N_p; (d) primary particle diameter d_p; (e) real part of the refractive index n; and (f) imaginary part of the refractive index k; were to be inferred from the measurements of: (1) the extinction cross section K_{ext}; (2) the differential scattering cross section $K'_{VV}(\theta)$; (3) the dissymmetry ratio $R_{VV}(\theta)$; (4) the dissymmetry ratio $R_{HH}(\theta)$; and (5) the depolarization ratio $\rho_V(\theta)$. Several studies in the literature demonstrate that knowledge of the agglomerate structural and optical properties is important in calculations of the radiative heat transfer from soot laden clouds. The usual assumption made when such calculations are undertaken is that of the equivalent sphere.

A sensitivity analysis of the technique revealed that both the dissymmetry ratios, R_{VV} and R_{HH}, are very weak functions of the real and imaginary parts, n and k, of the refractive index. Also the ratio of the differential scattering to extinction cross sections is a weak function of k. This causes three equations, in the system of five equations to be solved simultaneously for the five unknown agglomerate parameters, to be insensitive to

the particle refractive index. The ranges of the real and imaginary parts of the refractive index investigated were n: 1.0 - 1.9, and k: 0.3 - 0.9. The insensitivity of the dissymmetry ratios to the refractive index results in an ill-conditioned problem, and therefore, any inferences of the unknown parameters from such a system of equations cannot be trustworthy. For this reason, it was decided that the refractive index should be treated as a known in the agglomerate model analysis.

The *in-situ* optical measurements used in this study were performed, at different scattering angles and at different positions above the burner surface, in a laminar premixed propane/oxygen flat flame, of fuel equivalence ratio of 2.1. Soot samples were also extracted with a sampling probe and a thermophoretic sampling probe, for comparison purposes.

The agglomerate model developed by Lou and Charalampopoulos[90] was used to simultaneously solve the three equations of: (1) the extinction cross section; (2) the differential scattering cross section; and (3) the dissymmetry ratio R_{VV}, and to infer the agglomerate parameters N, N_p, and d_p. The dissymmetry ratio R_{HH} and the depolarization ratio ρ_V were used as independent checks of the validity of the inferred quantities. Two sets of measurements taken at different scattering angles, and four different refractive indices were used in the agglomerate model analysis. The analysis was performed for the structures of straight chain, cluster, and randomly branched chain agglomerates. The agglomerates were assumed to consist of the same number of primary particles, and of monosized primary particles. In the case of the randomly branched chains, 800 agglomerates were simulated, and the light scattering results were averaged to account for

the large number of possibilities in which a randomly branched chain agglomerate can be constructed. The results of the straight chain, cluster and randomly branched agglomerate analysis at different scattering angles and a refractive index of m=1.48-0.35i are summarized in Tables 6.1 and 6.2. The results obtained using the other three refractive indices are summarized in Appendix B. Table 6.3 summarizes the results of the *ex-situ* analysis.

Table 6.1. Summary of the results obtained at the scattering angle of 20°, using the straight chain, cluster, and randomly branched chain agglomerate analysis, and a refractive index of m=1.48-0.35i.

θ = 20°, m = 1.48 - 0.35i						
	Straight Chain		Cluster		Randomly Branched	
Height (mm)	N_p	dp (nm)	N_p	dp (nm)	N_p	dp (nm)
6	7	17.7	20	12.5	20	12.5
8	5	28.8	20	18.1	11	22.0
10	5	36.0	20	22.8	9	29.5
12	5	42.3	20	26.8	7	38.0
14	5	48.2	20	30.8	7	43.0
16	6	48.5	20	33.3	7	46.0
18	7	50.0	20	37.1	7	50.0
20	8	50.0	20	39.4	8	50.0
22	9	50.0	20	40.4	9	49.5

Table 6.2. Summary of the results obtained at the scattering angle of 45°, using the straight chain, cluster, and randomly branched chain agglomerate analysis, and a refractive index of m=1.48-0.35i.

θ = 45°, m = 1.48 - 0.35i						
	Straight Chain		Cluster		Randomly Branched	
Height (mm)	N_p	dp (nm)	N_p	dp (nm)	N_p	dp (nm)
6	6	18.7	23	11.9	23	12.0
8	5	28.8	23	17.1	18	19.0
10	4	39.5	23	21.9	14	26.0
12	5	42.1	23	24.9	11	33.5
14	5	47.7	23	28.3	10	39.5
16	6	44.9	23	30.4	10	43.0
18	33	49.7	23	33.2	9	49.5
20	42	50.0	23	35.1	10	50.0
22	45	50.0	23	35.2	13	48.0

Table 6.3. Summary of the results obtained from the electron microscopy analysis of soot samples extracted using a thermophoretic sampling probe.

Transmission Electron Microscopy Results			
Height (mm)	N_p	dp (nm)	Stand. Dev. (nm)
10	54.6	13.6	4.7
12	48.4	12.8	4.8
14	48.7	12.9	4.3
16	64.5	14.9	4.3
18	50.0	13.4	3.6
20	56.8	14.6	3.8
22	53.6	14.4	3.6

A comparison between the simulated and the measured quantities indicates that the depolarization ratio ρ_V had the largest error. The least deviation between all the measured and simulated quantities was obtained when a straight chain was used in the analysis, and the largest was obtained with the cluster assumption.

A qualitative comparison of the results of the agglomerate model analysis to the micrographs of the soot samples obtained with thermophoretic sampling indicates that the agglomerate model fails to predict the degree of agglomeration of soot, especially at the higher heights above the burner surface. The reason for the poor performance in the analysis of the *in-situ* measurements is attributed to the fact that the agglomerate model assumes that all the agglomerates at a given position in the flame will have exactly the same structure (straight chain, or cluster) and the same number of primary particles. The microscopy results indicate that this is not the case. Not only do the soot agglomerates extracted at a given position in the flame have different number of primary particles, they also have different shapes (from cluster-like to randomly branched chain). It is obvious that the effects of a distribution of number of primary particles N_p, must be taken into account. Such an approach to the analysis of the *in-situ* results will prove extremely computationally demanding. The assumption of monosized primary particles seems to be a good assumption and should be kept. The effects of using a mixture of different types of agglomerate structures should also be investigated.

In summary, the following trends and results were obtained during the investigation of the soot agglomeration in the flame investigated:

a. The *in-situ* measurements indicate an increasing anisotropy of the soot agglomerates with increasing height above the burner.

b. The *ex-situ* analysis of the soot samples extracted from the flame confirm the above effect. The agglomeration increases with increasing height above the burner surface.

c. The *ex-situ* analysis also indicates that different types of soot agglomerates, consisting of different number of primary particles, can be found at all heights.

d. The data reduction of the *in-situ* measurement results, using the agglomerate model, and with the refractive index taken as known, fails to predict the increase in the agglomeration of soot with height.

e. No unique solution for the system of equations was found. In fact, as many as 20 combinations of N_p and d_p values can be found to fit all three of the measurements of the: extinction and differential scattering cross sections, and the dissymetry ratio, with a deviation of less 5 percent difference.

Even though the original goals of this study were not met in a satisfactory manner, useful experience was gained in approaching the soot agglomeration problem. In the past, several investigators used only: the extinction cross section; the differential scattering cross section; and the dissymmetry ratio measurements, to infer the agglomerate parameters. Results were reported for straight chain, or cluster, or randomly branched chain agglomerates but no attempt was usually made to investigate the validity of the agglomerate structure assumptions. The results of this study show that further research is needed in developing an agglomerate characterization technique that truly describes the soot agglomeration effects.

6.2 Recommendations for Future Work

In addition to the present study, the recommendations for future work in this field can be divided into two major categories: (a) theoretical work; and (b) experimental work

Theoretical Work:

1. Develop a computer algorithm that will solve system of N non-linear equations with a mixture of N number of real and integer unknowns. The algorithm should not require the derivatives of the functions, since it will increase the computational time required, and it should not be susceptible to local minima.

2. Develop an agglomerate model routine that includes a distribution of the number of primary particles per agglomerate, as well as a mixture of different structures. The effects of such a combination should be studied thoroughly.

3. Develop a randomly branched chain agglomerate construction routine that takes into account the fractality of the soot agglomerates. There have been a large number of studies of the soot agglomerate fractal dimension in the recent years. Instead of randomly generating an agglomerate chain, a routine can be developed to randomly generate an agglomerate structure of N_p particles that will display certain fractal characteristics.

4. Develop a true parallel processing (FORTRAN 90) version of the computer program for calculating the light scattering characteristics of an agglomerate, so that shorter computational times are required. The parallel computational scheme developed for this study is extremely faster than that of the previous versions of the agglomerate program, but still computationally intensive.

Experimental Work:

1. Recent advances in the lock-in amplifier technology allow the detection, without the problems of signal drift, of signals down to the order of nV. This new technology should be implemented in measuring the small signals obtained in the depolarization measurement.

2. Further work needs to be done in developing a calibration technique of the depolarized signal from the light scattering in the VH orientation.

3. Neutral density filters should be introduced in front of the photomultiplier tubes, so that all the measurements of the VV, HH, VH and HV signals are brought to the same level as the calibration signals. This will allow the use of higher detector voltages and, therefore, better sensitivity in the signal detection. Any nonlinearity effects that may influence the results will definitely be eliminated.

4. A better controlled system of agglomerated particles should be introduced for a more detailed study of the effectiveness and limitations of the *in-situ* technique. Such a system may be a combustion system or a particle suspension system.

REFERENCES

1. Homann, K.H., "Carbon Formation in Premixed Flames." Combust. Flame 11:265-287(1967).

2. Homann, K.H. and Wagner, H.G., "Some New Aspects of the Mechanism of Carbon Formation in Premixed Flames." Eleventh Symposium (Int.) on Combustion, The Combustion Institute, 371-379(1967).

3. Bittner, J.D. and Howard, J.B., "Pre-Particle Chemistry in Soot Formation." Particulate Carbon, 109-137, Edited by D.C. Siegla and G.W. Smith, Plenum Press, New York, (1981).

4. Howard, J.B., "On the Mechanism of Carbon Formation in Flames." Twelfth Symposium (Int.) on Combustion, The Combustion Institute, 877-886 (1969).

5. Calcote, H.F., "Mechanisms of Soot Nucleation in Flames - A Critical Review." Combust. Flame 42:215-242 (1981).

6. Olson, D.B. and Calcote, H.F., "Ionic Mechanisms of Soot Nucleation in Premixed Flames." Particulate Carbon, 177-201, Plenum Press, New York, (1981).

7. Harris, S.J. and Weiner, A.M. , "Soot Particle Growth in Premixed Toluene/Ethylene Flames." Combust. Sci. and Tech. 38:75-87(1984).

8. Prado, G. and Lahaye, J., "Physical Aspects of Nucleation and Growth of Soot Particles." Particulate Carbon, 143-164, Plenum Press, New York, (1981).

9. King, G.B., Sorensen, C.M., Lester, T.W. and Merklin, J.F., "Photon Correlation Spectroscopy Used as a Particle Size Diagnostic in Sooting Flames." Appl. Optics 21:976-978 (1982).

10. Charalampopoulos T.T. and Chang H., "In-situ Optical Properties of Soot Particles in the Wavelength Range from 340 nm to 600 nm." Combust. Sci. and Tech. 50:401-421 (1988).

11. Fristrom, R.M. and Westenberg, A.A, Flame Structure, McGraw-Hill, New York, (1965).

12. Erickson, W.D., Williams, D.C. and Hottel, H.C., "Light Scattering Measurements on Soot in a Benzene-Air Flame." Combust. Flame 8:127-132(1964).

13. Kunugi, M., and Jinno, H., "Determination of Size and Concentration of Soot Particles in Diffusion Flames by a Light Scattering Technique." Eleventh Symposium (Int.) on Combustion, The Combustion Institute, 257-266(1966).

14. Dalzell, W.H., Williams, W.H. and Hottel, H.C., "A Light Scattering Method for Soot Concentration Measurements." Combust. Flame 14:161-169(1970)

15. D'Alessio, A., Di Lorenzo, A., Sarofim, A.F., Beretta, F., Masi, S. and Venitozzi, C., "Soot Formation in Methane-Oxygen Flames." Fifteenth Symposium (Int.) on Combustion, The Combustion Institute, 1427(1975).

16. D'Alessio, A., Di Lorenzo, A., Beretta, F., Masi, S., "Study of the Soot Nucleation Zone of Rich Methane-Oxygen Flames." Sixteenth Symposium (Int.) on Combustion, The Combustion Institute, 695-701(1977).

17. Bonczyk, P.A., "Measurement of Particulate Size by In-Situ Laser-Optical Methods; A Critical Evaluation Applied to Fuel-Pyrolyzed Carbon." Combust. Flame 35:191-206(1979).

18. Jacoda, I.J., Prado, G. and Lahaye, J., "An Experimental Investication Into Soot Formation and Distribution in Polymer Diffusion Flames." Combust. Flame 37:261-274 (1980).

19. Prado, G., Jacoda, J., Neoh, K. and Lahaye, J., "A Study of Soot Formation in Premixed Propane/Oxygen Flames by In-Situ Optical Techniques and Sampling

Probes." Eighteenth Symposium (Int.) on Combustion, The Combustion Institute, 1127-1136(1981).

20. Lee, S.C., Yu, Q.Z., and Tein, C.L., "Radiation Properties of Soot From Diffusion Flames." J. Quant. Spectrosc. Radiat. Transfer 27(4):387-396(1982).

21. Kent, J.H., and Wagner, H.Gr., "Soot Measurements in Laminar Ethylene Diffusion Flames." Combust. Flame 47:53-65(1982).

22. Santoro, R.J., Semerjian, H.G., and Dobbins, R.A., "Soot Particle Measurements in Diffusion Flames." Combust. Flame 51:203-218(1983).

23. Nishida, O., and Mukhara, S., "Optical Measurements of Soot Particles in a Laminar Diffusion Flame." Combust. Sci. and Tech. 35:157-173(1983).

24. Charalampopoulos, T.T., "Optical Properties of Soot Particles in Flames by Classical And Dynamic Light Scattering." *Ph.D. Dissertation, SUNNY/Buffalo, Mechanical Engineering Dept.* (1985).

25. Charalampopoulos, T.T., "An Automated Light Scattering System and a Method for the In-Situ Measurement of the Index of Refraction of Soot Particles." Review of Scientific Instruments 58(9):1638-1646(1987).

26. Gomez, A., Littman, M.G., and Glassman I., "Comparative Study of Soot Formation on the Centerline of Axisymmetric Laminar Diffusion Flames: Fuel And Temperature Effects." Combust. Flame 70:225-241(1987).

27. Ritrievi, K.E., Longwell, J.P., and Sarofim, A.F., " The Effects of Ferrocene on Soot Particle inception and Growth in Premixed Ethylene Flames." Combust Flame 70:17-31 (1987).

28. Chang, H., and Charalampopoulos T.T., "Determination of the Wavelength Dependence of Refractive Indices of Flame Soot." Proc. R. Soc. Lond. A. 430:577-591(1990).

29. Hahn, D.W., "Soot Suppressing Mechanisms of Iron in Premixed Hydrocarbon Flames." *Ph.D. Dissertation, LSU, Mechanical Engineering Dept.* (1992).

30. Hahn D.W., and Charalampopoulos T.T., "The Role of Iron Additives in Sooting Premixed Flames." *Twenty-Fourth Symposium (Int.) on Combustion*, The Combustion Institute, July 5-10 (1992).

31. Van De Hulst, .C., Light Scattering by Small Particles., John Wiley, New York (1957).

32. Kerker, M., The Scattering of Light and Other Electromagnetic Radiation., Academic Press, New York (1969).

33. Bohren, C.F., and Huffman, D.R., Absorption and Scattering of Light by Small Particles., John Wiley, New York (1983).

34. Berne, B.J., and Pecora, R., Dynamic Light Scattering., John Wiley, New York (1976).

35. Chu, B., Laser Light Scattering., Academic Press, New York (1974).

36. Dahneke, B.E., Measurement of Suspended Particles by Quasi-elastic Light Scattering., John Wiley, New York (1983).

37. Penner, S.S., and Chang, P.H., Power Spectra Observed in Laser Scattering from Moving Polydisperse Particles in Flames-I. Theory." Acta Astronautica 3:69-91(1976).

38. Penner S.S., Bernard, J.M., and Jerskey, T., "Laser Scattering from Moving Polydisperse Particles in Flames-II. Preliminary Experiments." Acta Astronautica 3:69-91(1976).

39. Driscoll, J.F., Mann, D.M., and McGregor, W.K., "Submicron Particle Size Measurements in an Acetylene-Oxygen Flame." Combust. Sci. and Tech. 20:41-47(1979).

40. Chang, P.H., and Penner, S.S., "Particle-Size Measurements in Flames Using Light Scattering; Comparison with Diffusion Broadening Spectroscopy." J. Quant. Spectrosc. Rad. Transfer 25:105-109(1981).

41. Flower, W.L., "Optical Measurements of Soot Formation In Premixed Flames." Combust. Sci. and Tech. 33:17-33(1983).

42. Taylor, T.W., Scrivner, S.M., Sorensen, C.M., and Merklin, J.F., "Determination of the Relative Number Distribution of Particle Sizes Using Photon Correlation Spectroscopy." Appl. Optics 24(22):3713-3717 (1985).

43. Weil, M.E., Lhussier, N., and Gousbet, G., "Mean Diameters and Number Densities in Premixed CH_4-O_2 Flames by DIffusion Broadening Spectroscopy." Appl. Optics 25(10):1676-1683 (1986).

44. Scrivner, S.M., Taylor, T.W., Sorensen, C.M., and Merklin, J.F., "Soot Particle Size Distribution Measurement in a Premixed Flame Using Photon Correlation Spectroscopy." Appl. Optics 25(2):291-297(1986).

45. Bernard, J.M., "Particle Sizing in Combustion Systems Using Light Scattered Laser Light." J. Quant. Spectrosc. Rad. Transfer 40(3):321-330(1988).

46. Venizelos, D., "Particle Size Distribution Measurements in Flames Using Dynamic Light Scattering Techniques." M.Sc. Thesis, LSU, Mechanical Engineering Dept. (1989).

47. Venizelos, D., and Charalampopoulos, T.T., "On the Use of Dynamic Light Scattering to Study Multimodal Size Distributions in Flame Systems." Central States Section, Spring Technical Meeting, p. 183, The Combustion Institute (1989).

48. Jones, A.R., "Scattering and Emission of Radiation by Clouds of Elongated Particles." *J. Phys. D.:Appl. Phys.*, 5:L1-L*A*(1972).

49. Lee, S.C., and Tien, C.L., "Effect of Soot Shape on Soot Radiation." *J. Quant. Spectrosc. Rad. Transfer* 29:259-265 (1983).

50. Mackowski, D.W., Alternkirch, R.A., and Menqüc, M.P., "Extinction and Absorption Coefficients of Cylindrically-Shaped Soot Particles." *Combust. Sci. and Tech.* 53:399-410(1987).

51. Charalampopoulos, T.T., and Hahn, D.W., "Extinction Efficiencies of Elongated Soot Particles." *J. Quant. Spectrosc. Rad. Transfer* 42(3):219-224(1989).

52. Jones, A.R., "Electromagnetic Wave Scattering By Assemblies of Particles in the Rayleigh Approximation." *Proc. R. Soc. Lond. A.* 366:11-127(1979).

53. Jones, A.R., "Scattering Efficiency Factors for Agglomerates of Small Spheres." *J. Phys. D: Appl. Phys.* 12:1661-1672(1979).

54. Jones, A.R., "Correction to 'Electromagnetic Wave Scattering by Assemblies of Particles in the Rayleigh Approximation'." *Proc. R. Soc. Lond. A.* 375:453-454(1981).

55. Felske, J.D., Hsu, P., Ku, J.C., "The Effect of Soot Particle Optical Inhomogeneity and Agglomeration on the Analysis of Light Scattering Measurements in Flames." *J. Quant. Spectrosc. Radiat. Transfer* 36(6):447-465(1986).

56. Drolen, B.L., and Tien, C.L., "Absorption and Scattering of Agglomerated Soot Particulate." *J. Quant. Spectrosc. Radiat. Transfer* 37(5):433-488(1987).

57. Kumar, S., and Tien, C.L., "Effective Diameter of Agglomerates for Radiative Extinction and Scattering." *Combust. Sci. and Techn.* 66:199-216(1989).

58. Mandelbrot, B.B., *Les Objets Fractals, Forme, Hasard et Dimension*, Flammarion. Paris, 1975.

59. Mandelbrot, B.B.,"Fractal Geometry: What Is It, and What Does It Do." *Proc. R. Soc. Lond.* A 423:3-16(1986).

60. Forrest, S.R., and Witten Jr, T.A., "Long-Range Correlations in Smoke-Particle Aggregates." *J. Phys. A: Math. Gen.* 12(5):L109-L117(1979).

61. Berry, M.V., and Percival, I.C., "Optics of Fractal Clusters Such as Smoke." Optica Acta 33(5):577-591(1986).

62. Martin, J.E., Schaefer, D.W., Hurd A.J., "Fractal Geometry of Vapor-Phase Aggregates." *Physical Review* A 33(5):3540-3543(1986).

63. Hurd, A.J., and Flower, W.L., "In-Situ Growth and Structure of Fractal Silica Aggregates in a Flame." *Journal of Colloid and Interface Science* 122(1):178-192(1988).

64. Meakin, P., "The Effects of Rotational Diffusion on The Fractal Dimensionality of Structures Formed by Cluster-Cluster Aggragation." *J. Chem. Phys.* 81(10):4637-4639(1984).

65. Samson, R.J., Mulholland, G.W., Centry, J.W., "Structural Analysis of Soot Agglomerates." *Langmuir* 3:272-281(1987).

66. Zhang, H.X., Sorensen, C.M., Ramer, E.R, Oliver, B.J., Merklin, J.F., "In-Situ Optical Structure Factor Measurements of an Aggregating Soot Aerosol." *Langmuir* 4:867-871(1988).

67. Mountain, R.D., Mulholland, G.W., "Light Scattering from Simulated Smoke Agglomerates." *Langmuir* 4:1321-1326(1988).

68. Dobbins, R.A., and Megaridis, C.M., "Absorption and Scattering of Light by Polydisperse Aggregates." *Appl. Optics* 30(33):4747-4754(1991).

69. Megaridis, C.M., and Dobbins, R.A., "Morphological Description of Flame Generated Materials." *Combust. Sci. and Tech.* 71:95-109(1990).

70. Charalampopoulos, T.T., and Chang, H., "Agglomerate Parameters and Fractal Dimension of Soot Using Light Scattering-Effects on Surface Growth." *Combust. Flame* 87:89-99(1991).

71. Bonczyk, P.A., and Hall, R.J., "Fractal Properties of Soot Agglomerates." *Langmuir* 7:1274-1280(1991).

72. Bonczyk, P.A., and Hall, R.J., "Measurement of the Fractal Dimension of Soot Using UV Laser Radiation." *Langmuir* 8:1666-1670(1992).

73. Jullien, R., and Botet, R., *Aggregation and Fractal Aggregates*, World Scientific, Singapore (1987).

74. Charalampopoulos, T.T., "Morphology and Dynamics of Agglomerated Particulates in Combustion Systems Using Light Scattering Techniques." *Prog. Energy Combust. Sci.* 18:13-45(1992).

75. Seshadri, K., and Rosner, D.E., "Optical Methods and Results of Dew Point and Deposition Rate Measurements in Salt/Ash - Containing Combustion Gases." AIChE *Journal*, 30:187- (1984).

76. Dasch, C.J., "New Soot Diagnostics in Flames Based on Laser Vaporization of Soot." *Twentieth Symposium (Int.) on Combustion*, The Combustion Institute, 1231-1237 (1984).

77. Lawton, S.A., "Comparison of Soot Growth in Plate- and Chimney-Stabilized, Sooting Premixed Flames." *Combust. Sci. and Tech.* 57:163-169(1988).

78. Jones, A.R., "Scattering of Electromagnetic Radiation in Particulate Laden Fluids. *J. Prog. Eng. Comb. Sci.* 5:73-96(1979).

79. Jenkins, F.A. and White, H.E., *Fundamentals of Optics*. McGraw-Hill, New York (1976).

80. Koppel, D., "Analysis of Macromolecular Polydispersity in Intensity Correlation Spectroscopy: The Method of Cumulants." *J. Chem. Physics* 57:4814-4820(1972).

81. Stagg, B.J. and Charalampopoulos, T.T., "Sensitivity of the Reflection Technique: Optimum Angles of Incidence to Determine the Optical Properties of Materials." *Applied Optics* 31(22):4420-4427(1992).

82. Stagg, B.J., "Development of a Technique to Determine the Temperature Dependence of the Refractive Index of Carbonaceous Particulates." *Ph.D. Dissertation, LSU, Mechanical Engineering Dept.* (1992).

83. Carnahan, B., Luther, H.A., and Wilkes, J.O., *Applied Numerical Methods.* John Wiley and Sons, New York (1969)

84. Hornbeck, R.W., *Numerical Methods.* Prentice-Hall/Quantum Publishers, New York (1975).

85. Ku, J.C., "Correction for the Extinction Efficiency Factors Given in the Jones Solution for the Electromagnetic Scattering by Agglomerates of Small Spheres." *J. Phys. D: Appl. Phys.* 24:71-74(1991).

86. Ku, J.C., and Shim, K-H., "A Comparison of Solutions for Light Scattering and Absorption by Agglomerated or Arbirtrarily-Shaped Particles." *J. Quant. Spectrosc. Radiat. Transfer* 47(3):201-220(1992).

87. Purcell, E.M., and Pennypacker, C.R., "Scattering and Absorption of Light by Nonspherical Dielectric Grains" *Astrophys. J.* 186:705-714(1973).

88. Iskander, M.F., Chen, H.Y., and Penner, J.E., "Optical Scattering and Absorption by Branched Chains of Aerosols." *Applied Optics* 28(150:3083-3091(1989).

89. Goedecke, G.H., and O'Brien, S.G., "Scattering by Irregular Inhomogeneous Particles via the Digitized Green's Function Algorithm." *Applied Optics* 27(12):2431-2438(1988).

90. Lou, W., and Charalampopoulos, T.T, "On the Electromagnetic Scattering and Absorption of Agglomerated Small Spherical Particles." *J. Phys. D: Appl. Phys.* 27:1-13(1994).

91. Hooke, R., and Jeeves, T.A., "Direct Search Solution of Numerical and Statistical Problems." *J. Assoc. Comp. Math.* 8:212-229(1961).

92. Rudder, R.R., and Bach, D.R., "Rayleigh Scattering of Ruby-Laser Light by Neutral Gases." *J. Opt. Soc. America* 58(9):1260-1266(1968).

93. Dobbins, R.A., and Megaridis, C.M., "Morphology of Flame-Generated Soot as Determined by Thermophoretic Sampling." *Langmuir* 3:254-259(1987).

94. Samuelsen, G.S, Hack, R.L., Himes, R.M. and Azzary, M., "Effects of Fuel Specification and Additives on Soot Formation." Report # ESL TR-83-17, GA # AD-A13720815.

95. Rosner, D.E., Mackowski, D.W. and Garcia-Ybarra, P., "Size- and Structure-Insensitivity of the Thermophoretic Transport of Aggregated Soot particles in Gases." *Combust. Sci. and Tech.* 80:87-101(1991).

APPENDIX A

STRAIGHT CHAIN AND CLUSTER AGGLOMERATE RESULTS

The light scattering characteristics of straight chain agglomerates are given in this appendix. Figures A1-A16 show the results for a straight chain agglomerate. The results of the cluster agglomerate are shown in Figures A17-A32.

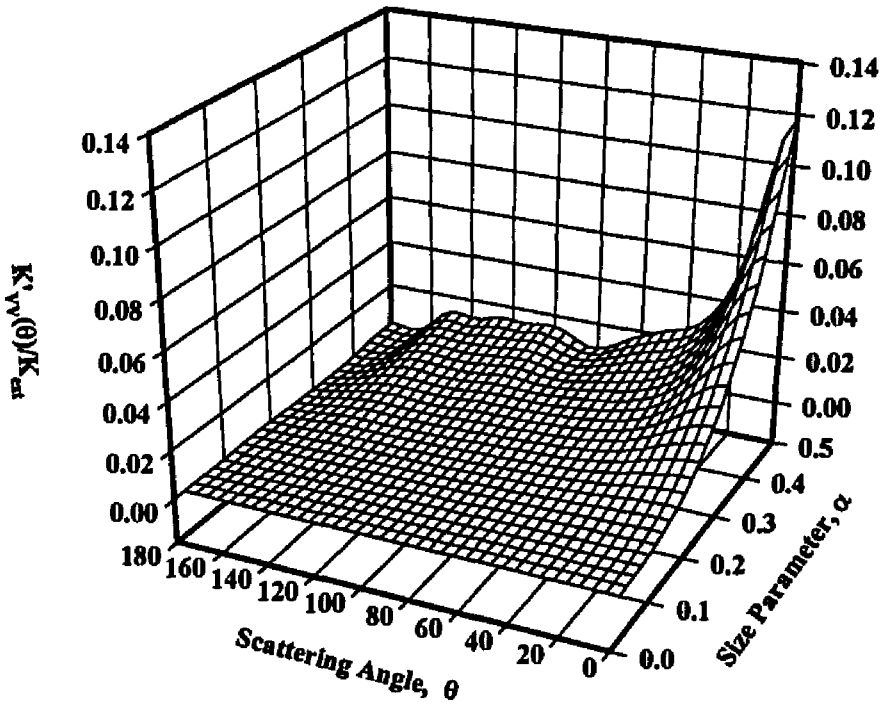

Figure A.1 The differential scattering cross section to extinction cross section ratio $\{K'_{vv}(\theta)/K_{ext}\}$ as a function of the scattering angle θ and the primary particle size parameter α_p, for a straight chain agglomerate of N_p=20 and m=1.5-0.5i.

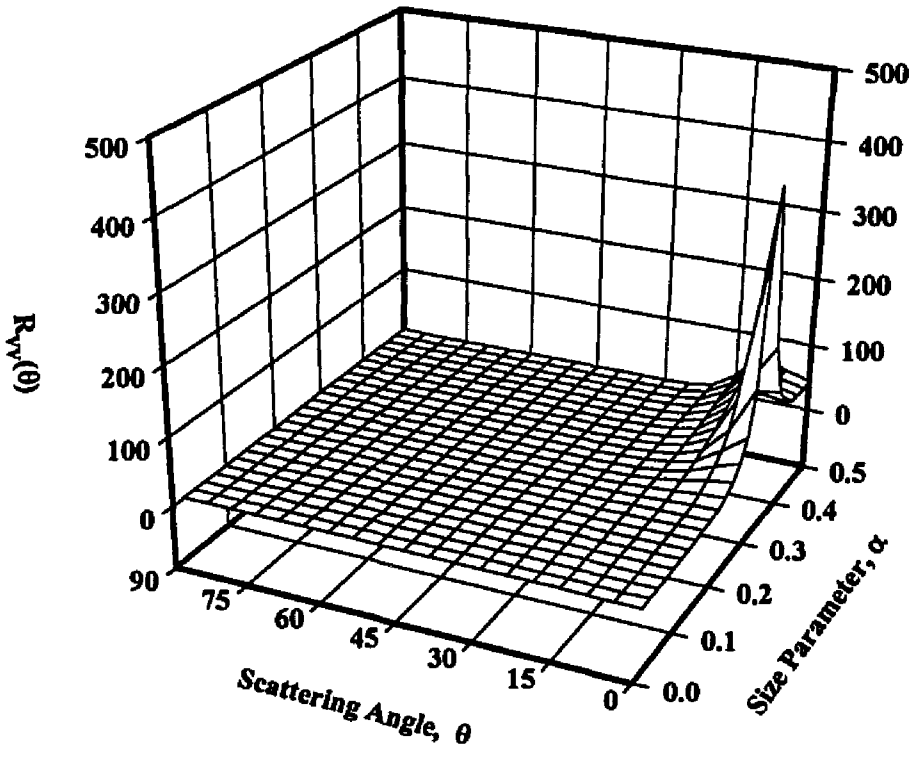

Figure A.2 The dissymmetry ratio $R_{VV}(\theta)$, as a function of the scattering angle θ and the primary particle size parameter α_p, for a straight chain agglomerate of N_p=20 and m=1.5-0.5i.

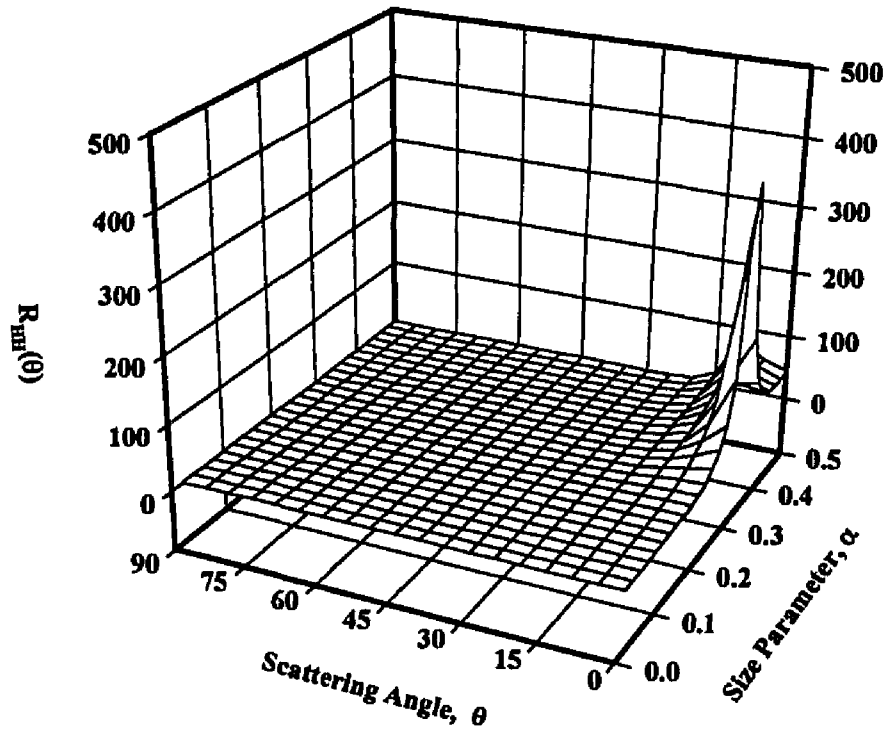

Figure A.3 The dissymmetry ratio $R_{HH}(\theta)$, as a function of the scattering angle θ and the primary particle size parameter α_p, for a straight chain agglomerate of N_p=20 and m=1.5-0.5i.

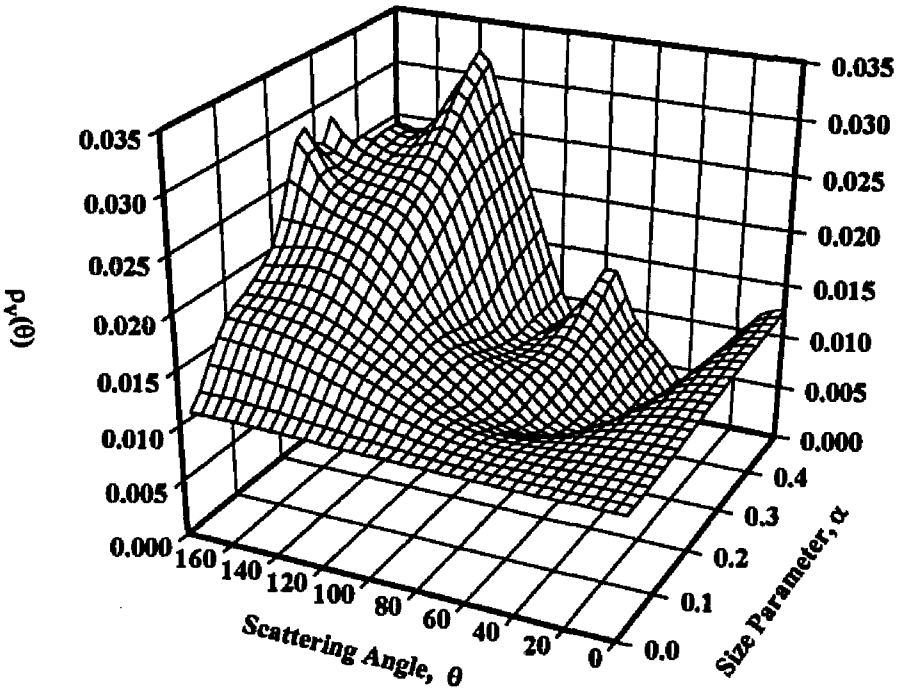

Figure A.4 The depolarization ratio $\rho_V(\theta)$, as a function of the scattering angle θ and the primary particle size parameter α_p, for a straight chain agglomerate of N_p=20 and m=1.5-0.5i.

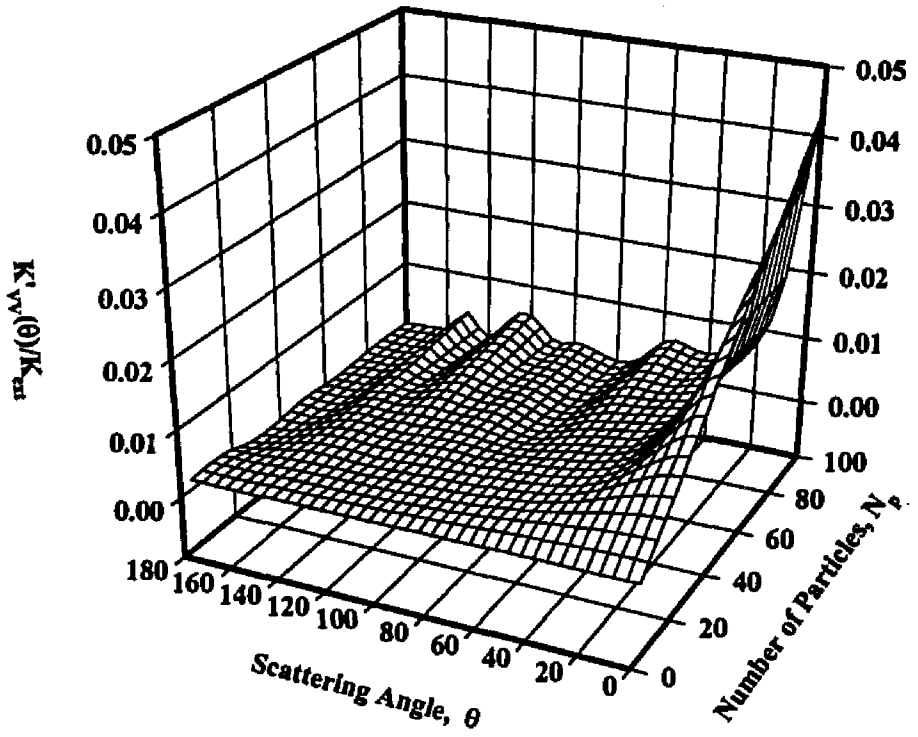

Figure A.5 The differential scattering cross section to extinction cross section ratio $\{K'_{vv}(\theta)/K_{ext}\}$ as a function of the scattering angle θ and the number of primary particles N_p, for a straight chain agglomerate of α_p=0.125 and m=1.5-0.5i.

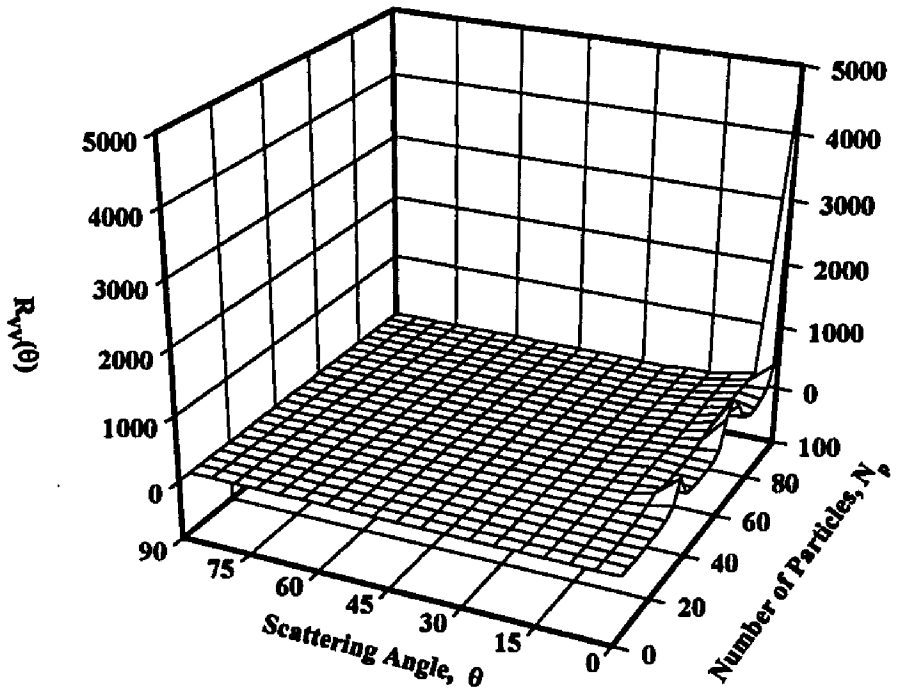

Figure A.6 The dissymmetry ratio $R_{VV}(\theta)$ as a function of the scattering angle θ and the number of primary particles N_p, for a straight chain agglomerate of α_p=0.125 and m=1.5-0.5i.

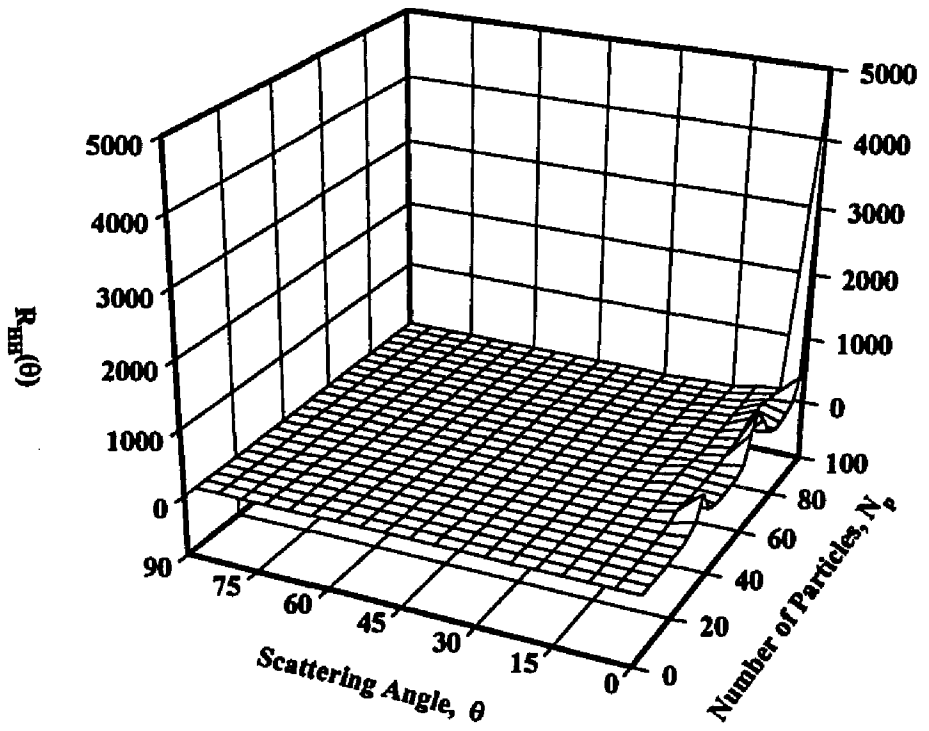

Figure A.7 The dissymmetry ratio $R_{HH}(\theta)$ as a function of the scattering angle θ and the number of primary particles N_p, for a straight chain agglomerate of α_p=0.125 and m=1.5-0.5i.

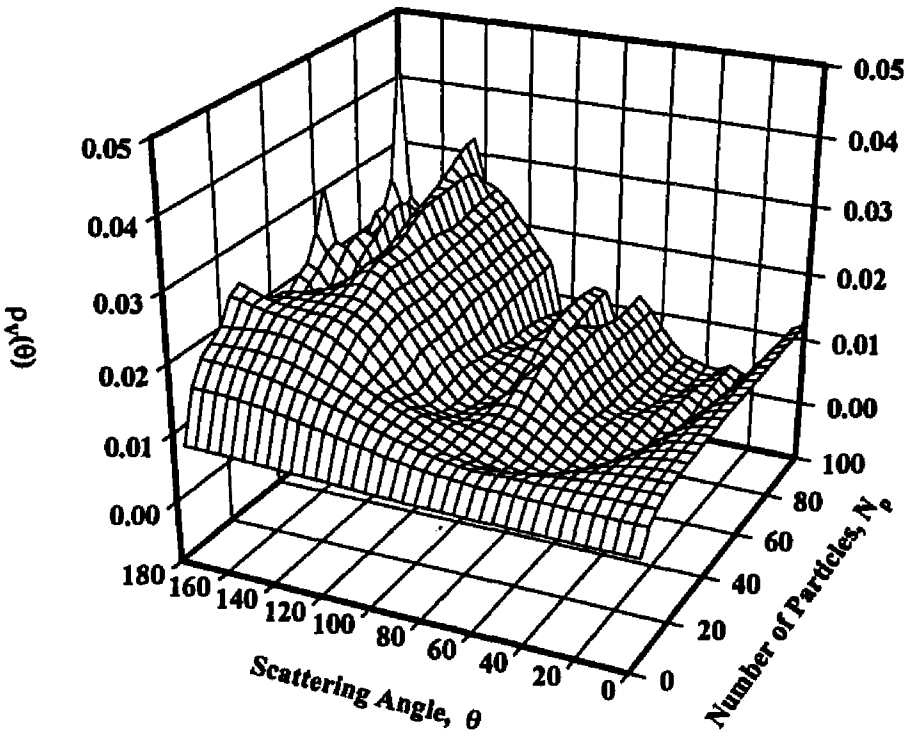

Figure A.8 The depolarization ratio $\rho_V(\theta)$ as a function of the scattering angle θ and the number of primary particles N_p, for a straight chain agglomerate of α_p=0.125 and m=1.5-0.5i.

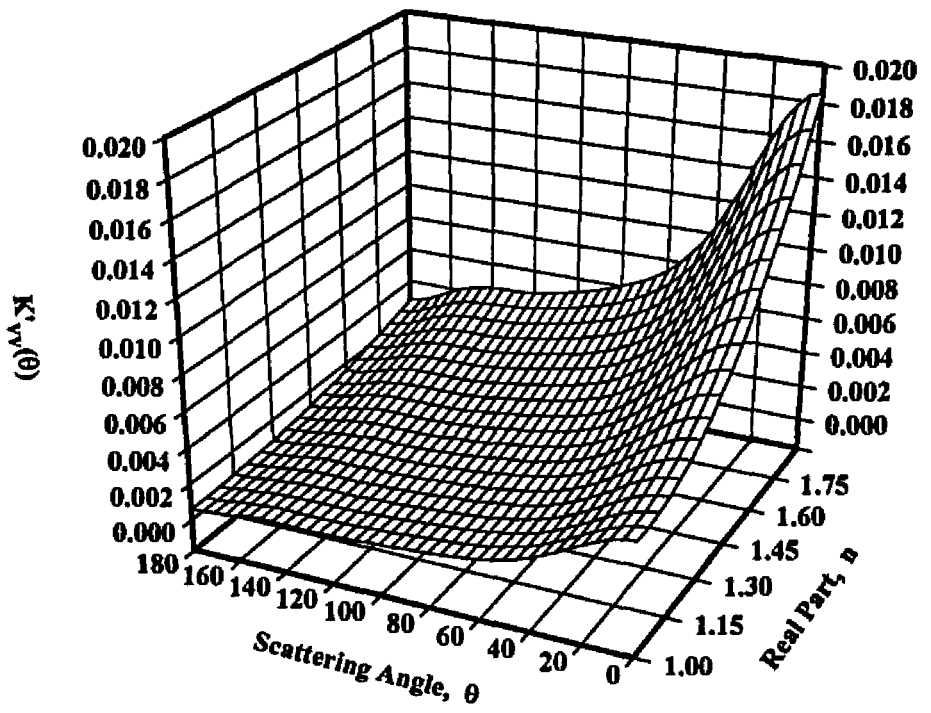

Figure A.9 The differential scattering cross section to extinction cross section ratio $\{K'_{vv}(\theta)/K_{ext}\}$ as a function of the scattering angle θ and the real part of the refractive index n, for a straight chain agglomerate of α_p=0.125, N_p=20 and k=0.5.

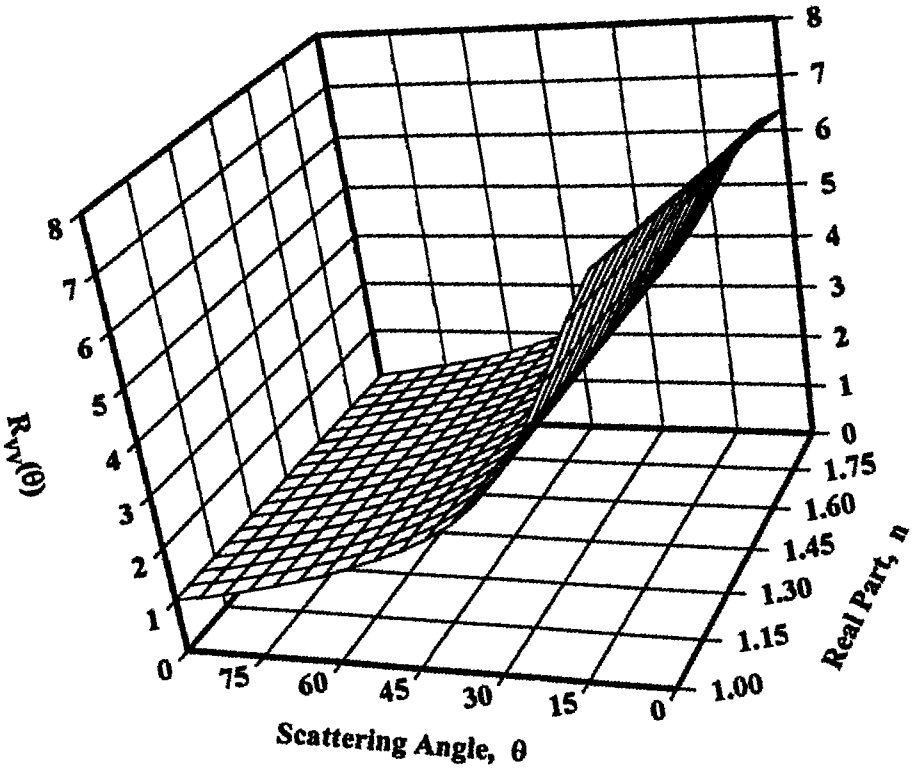

Figure A.10 The dissymmetry ratio $R_{VV}(\theta)$ as a function of the scattering angle θ and the real part of the refractive index n, for a straight chain agglomerate of α_p=0.125, N_p=20 and k=0.5.

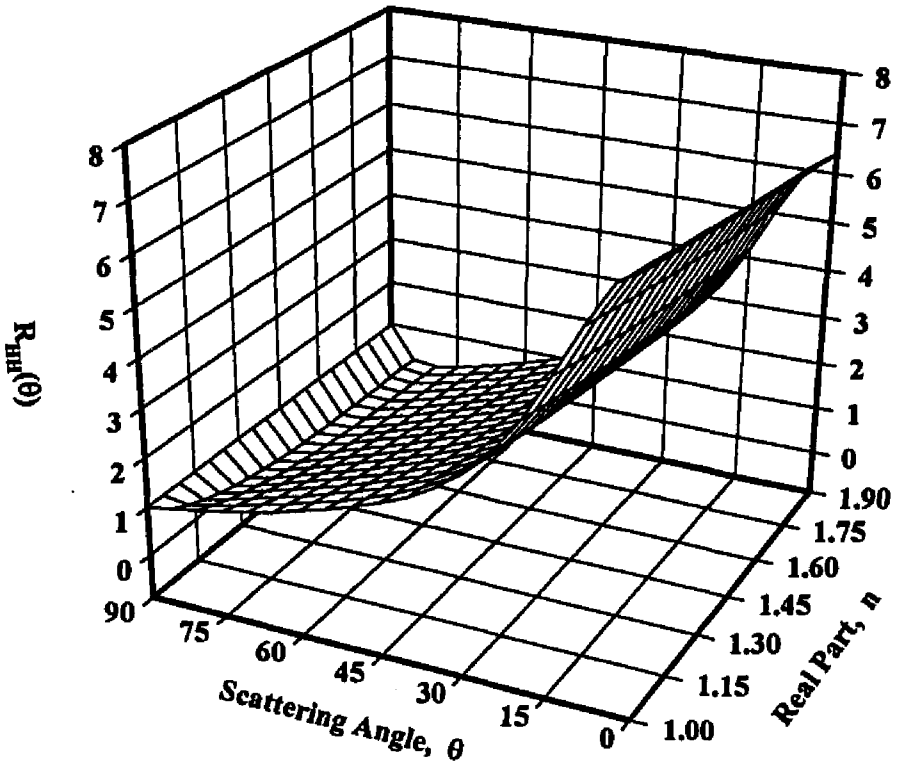

Figure A.11 The dissymmetry ratio $R_{HH}(\theta)$ as a function of the scattering angle θ and the real part of the refractive index n, for a straight chain agglomerate of α_p=0.125, N_p=20 and k=0.5.

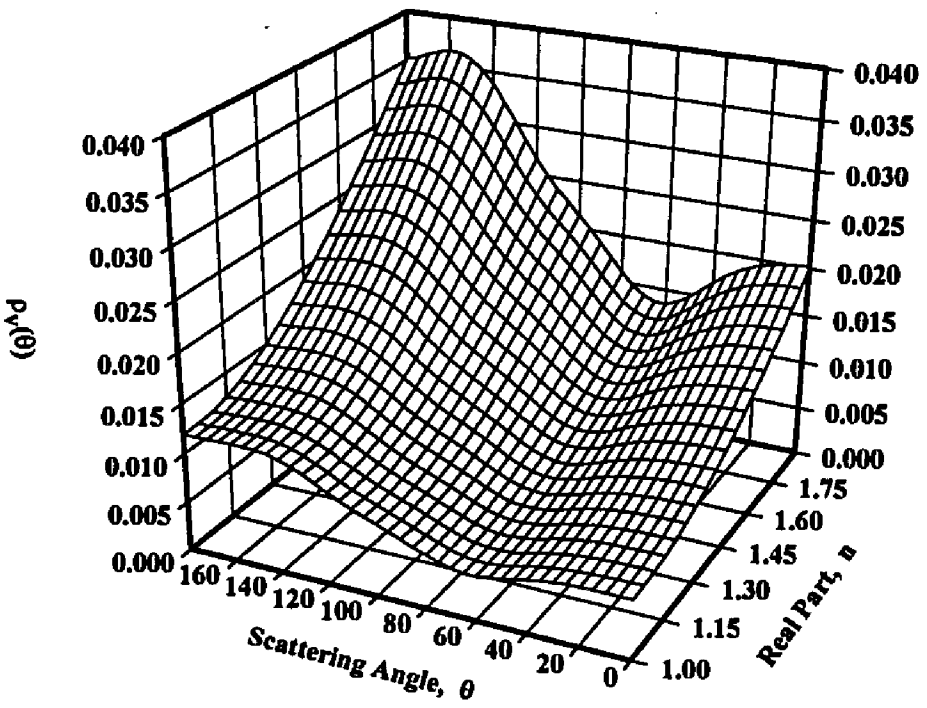

Figure A.12 The depolarization ratio $\rho_V(\theta)$ as a function of the scattering angle θ and the real part of the refractive index n, for a straight chain agglomerate of α_p=0.125, N_p=20 and k=0.5.

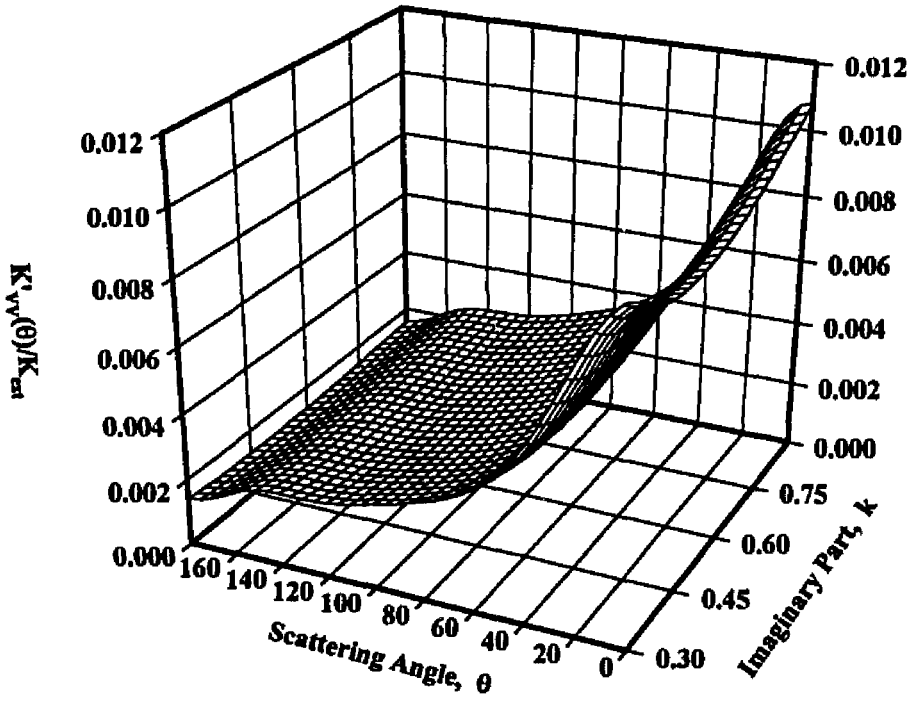

Figure A.13 The differential scattering cross section to extinction cross section ratio $\{K'_{vv}(\theta)/K_{ext}\}$ as a function of the scattering angle θ and the imaginary part of the refractive index k, for a straight chain agglomerate of α_p=0.125, N_p=20 and n=1.5.

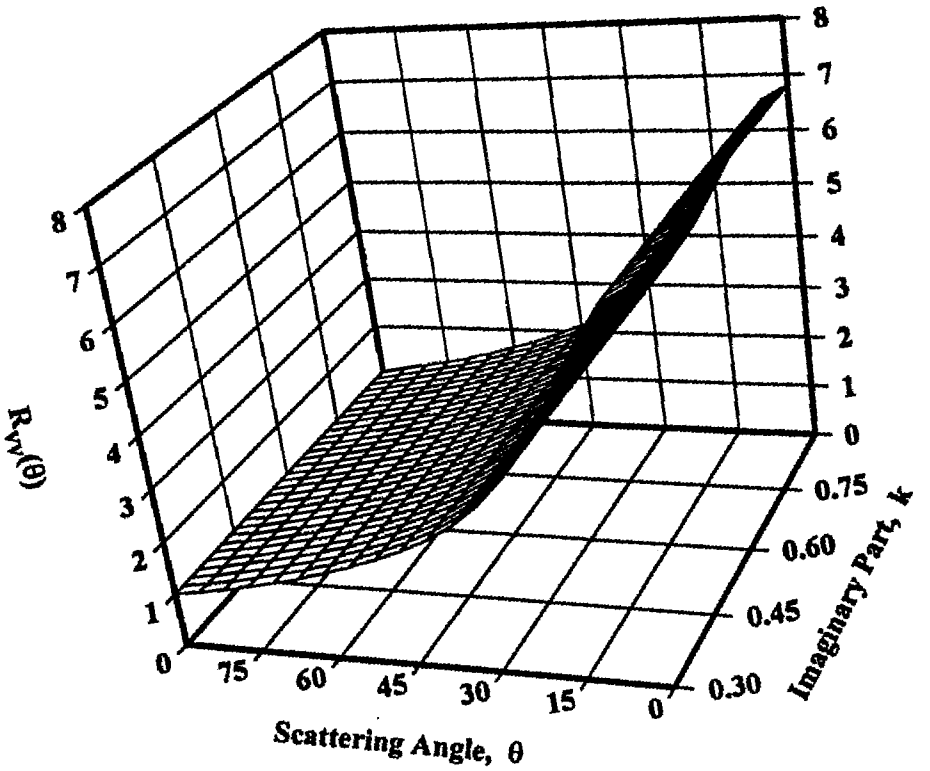

Figure A.14 The dissymmetry ratio $R_{vv}(\theta)$ as a function of the scattering angle θ and the imaginary part of the refractive index k, for a straight chain agglomerate of α_p=0.125, N_p=20 and n=1.5.

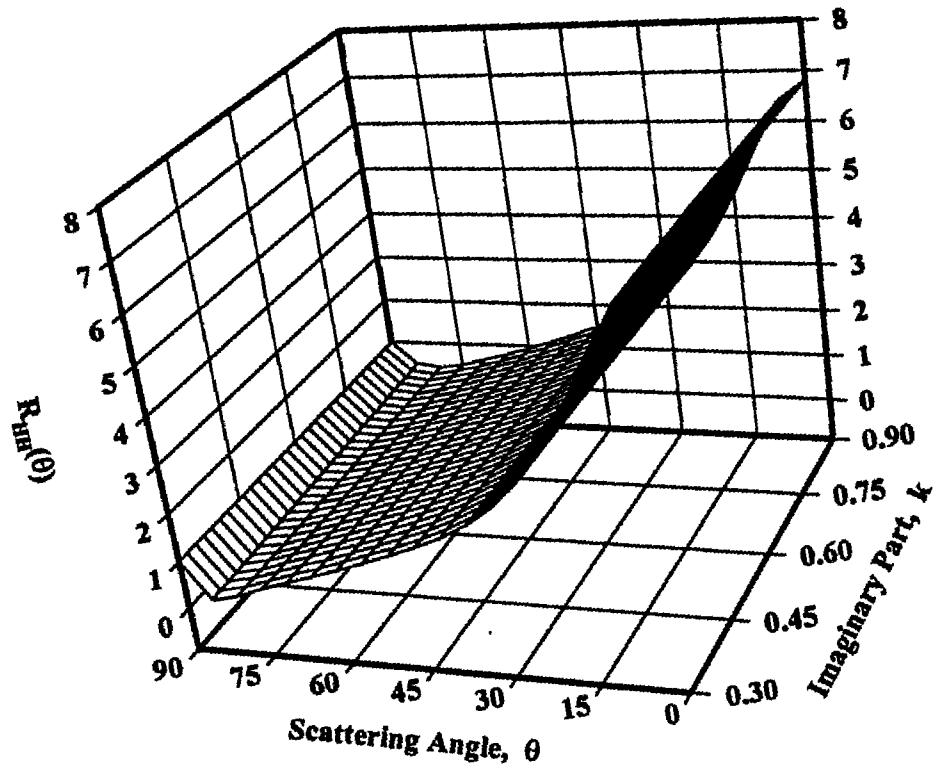

Figure A.15 The dissymmetry ratio $R_{HH}(\theta)$ as a function of the scattering angle θ and the imaginary part of the refractive index k, for a straight chain agglomerate of α_p=0.125, N_p=20 and n=1.5.

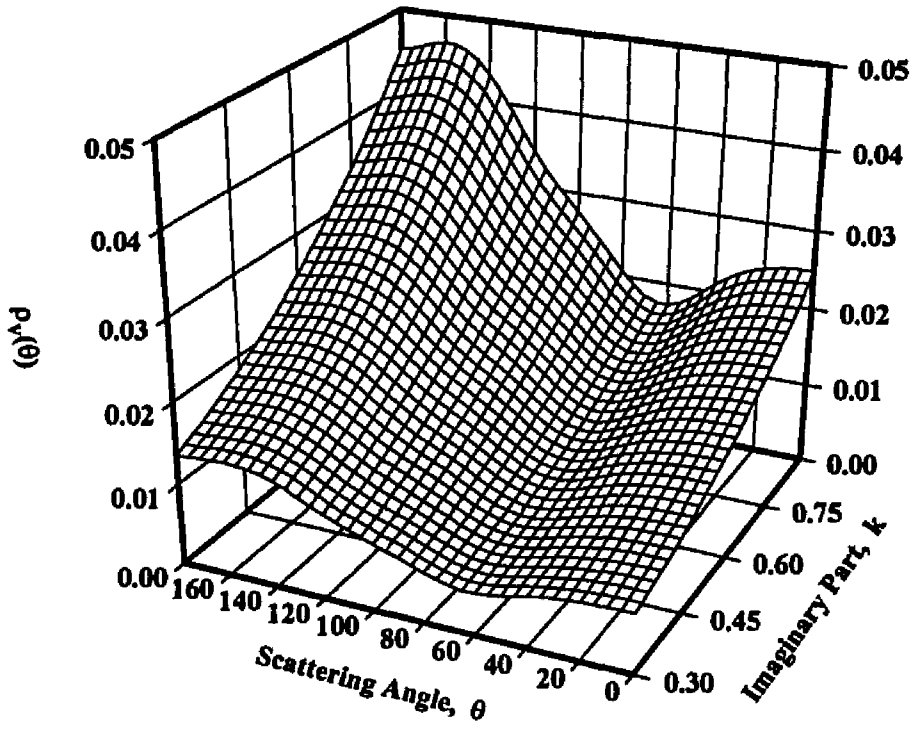

Figure A.16 The depolarization ratio $\rho_V(\theta)$ as a function of the scattering angle θ and the imaginary part of the refractive index k, for a straight chain agglomerate of α_p=0.125, N_p=20 and n=1.5.

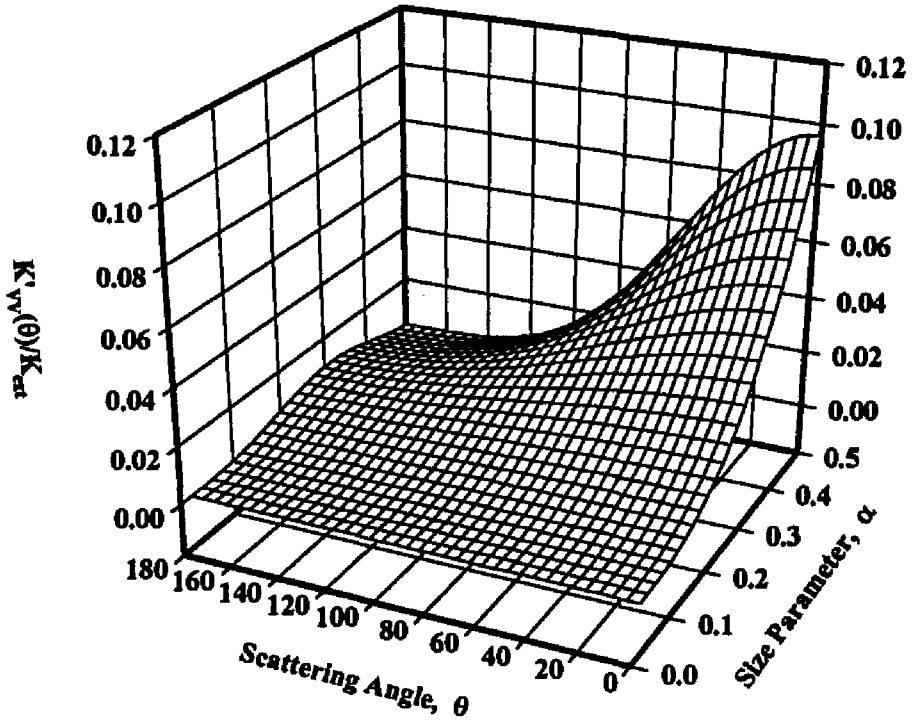

Figure A.17 The differential scattering cross section to extinction cross section ratio $\{K'_{vv}(\theta)/K_{ext}\}$ as a function of the scattering angle θ and the primary particle size parameter α_p, for a cluster agglomerate of N_p=20 and m=1.5-0.5i.

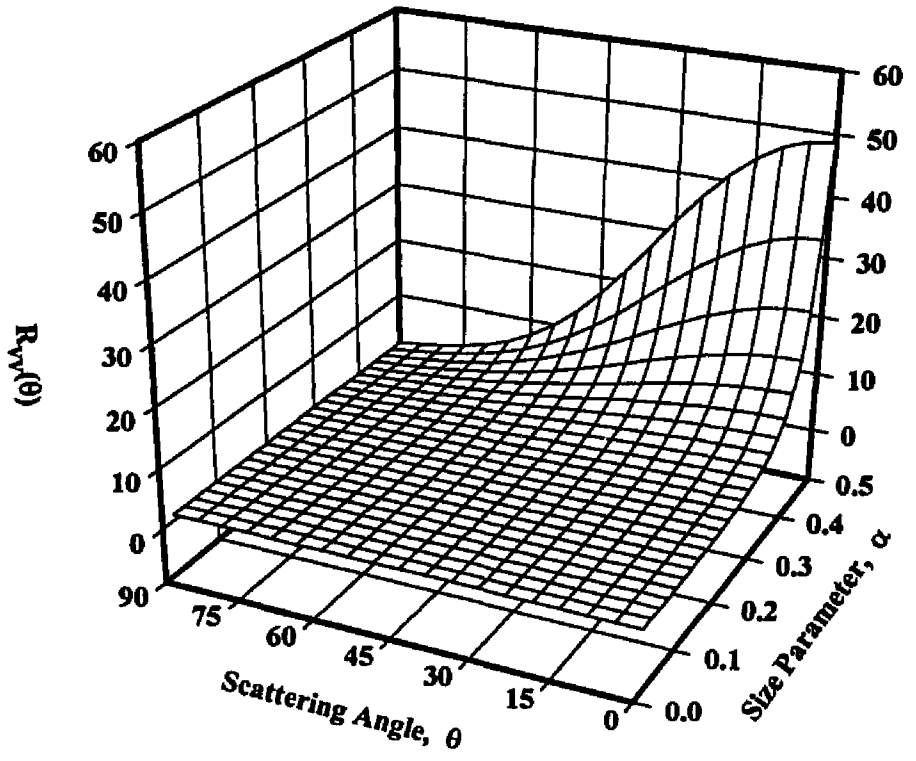

Figure A.18 The dissymmetry ratio $R_{VV}(\theta)$, as a function of the scattering angle θ and the primary particle size parameter α_p, for a cluster agglomerate of N_p=20 and m=1.5-0.5i.

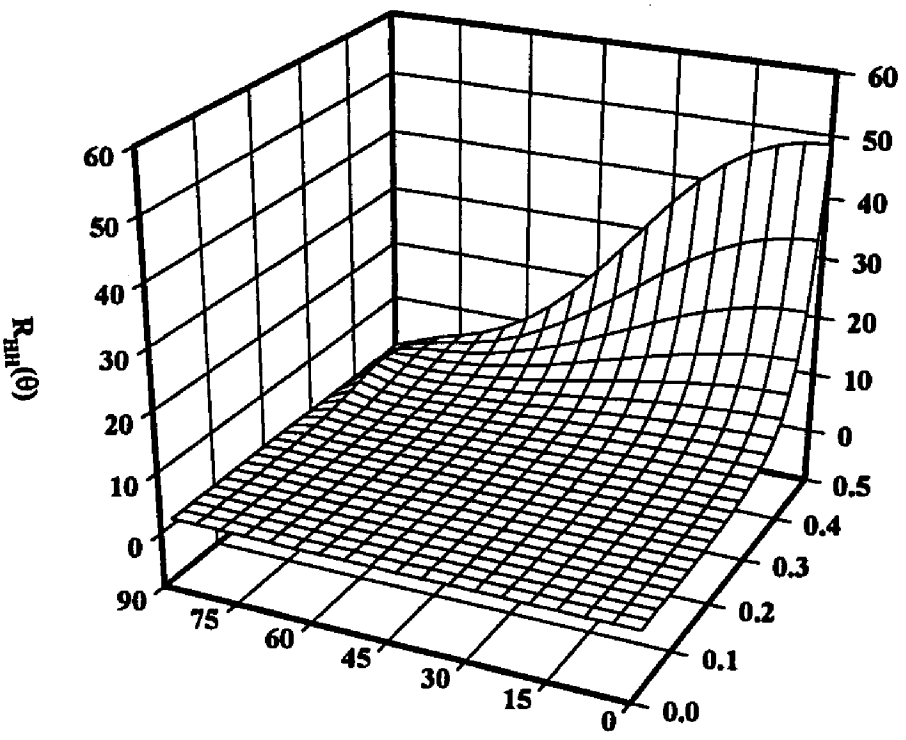

Figure A.19 The dissymmetry ratio $R_{HH}(\theta)$, as a function of the scattering angle θ and the primary particle size parameter α_p, for a cluster agglomerate of N_p=20 and m=1.5-0.5i.

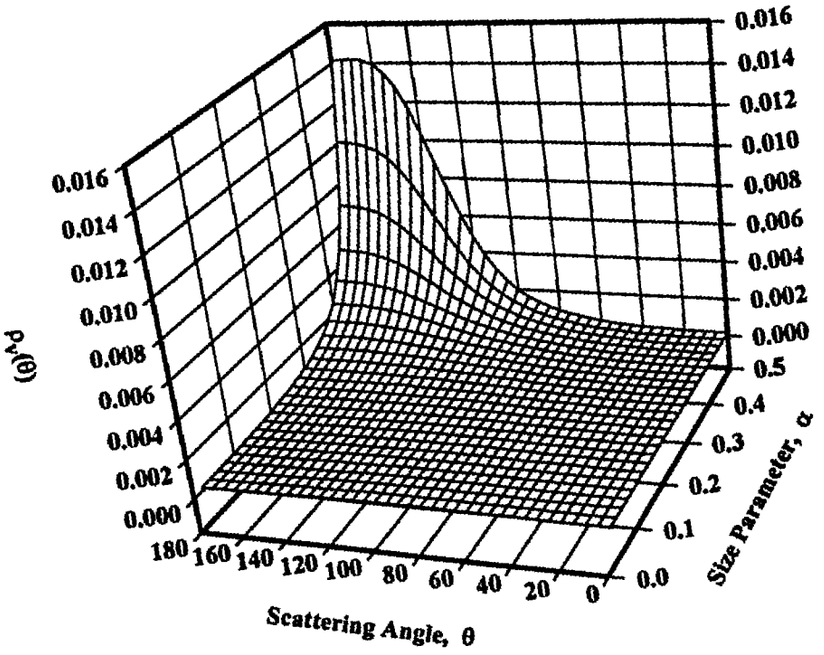

Figure A.20 The depolarization ratio $\rho_V(\theta)$, as a function of the scattering angle θ and the primary particle size parameter α_p, for a cluster agglomerate of N_p=20 and m=1.5-0.5i.

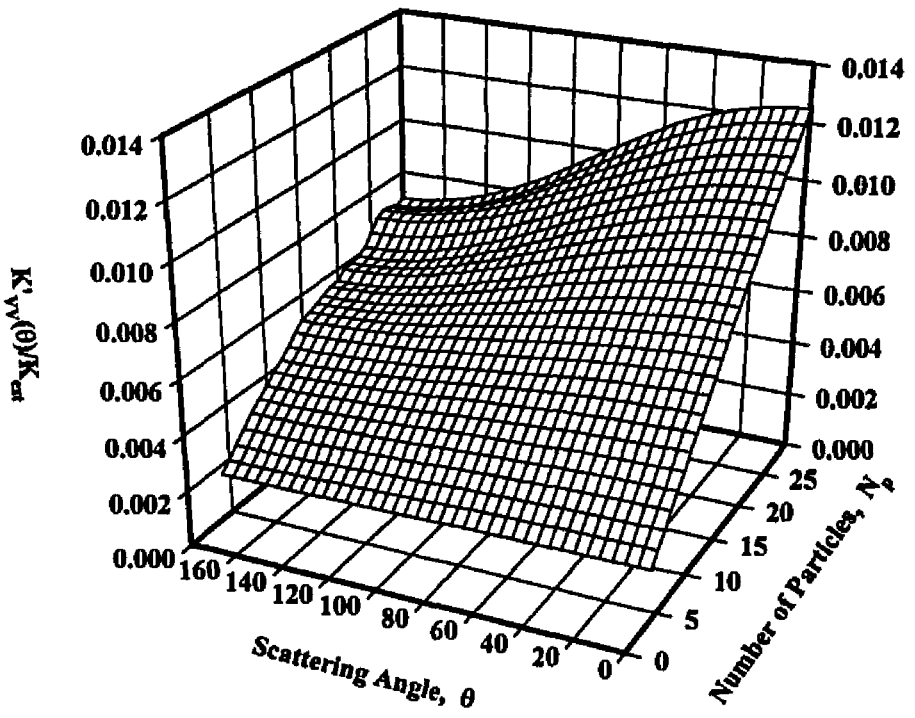

Figure A.21 The differential scattering cross section to extinction cross section ratio $\{K'_{vv}(\theta)/K_{ext}\}$ as a function of the scattering angle θ and the number of primary particles N_p, for a cluster agglomerate of α_p=0.125 and m=1.5-0.5i.

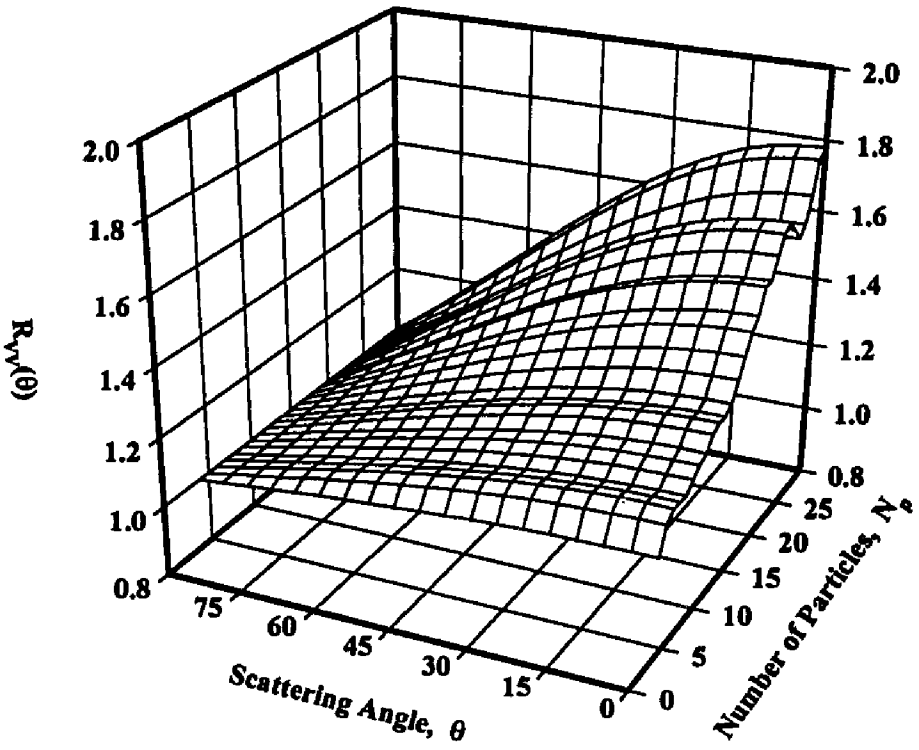

Figure A.22 The dissymmetry ratio $R_{VV}(\theta)$ as a function of the scattering angle θ and the number of primary particles N_p, for a cluster agglomerate of α_p=0.125 and m=1.5-0.5i.

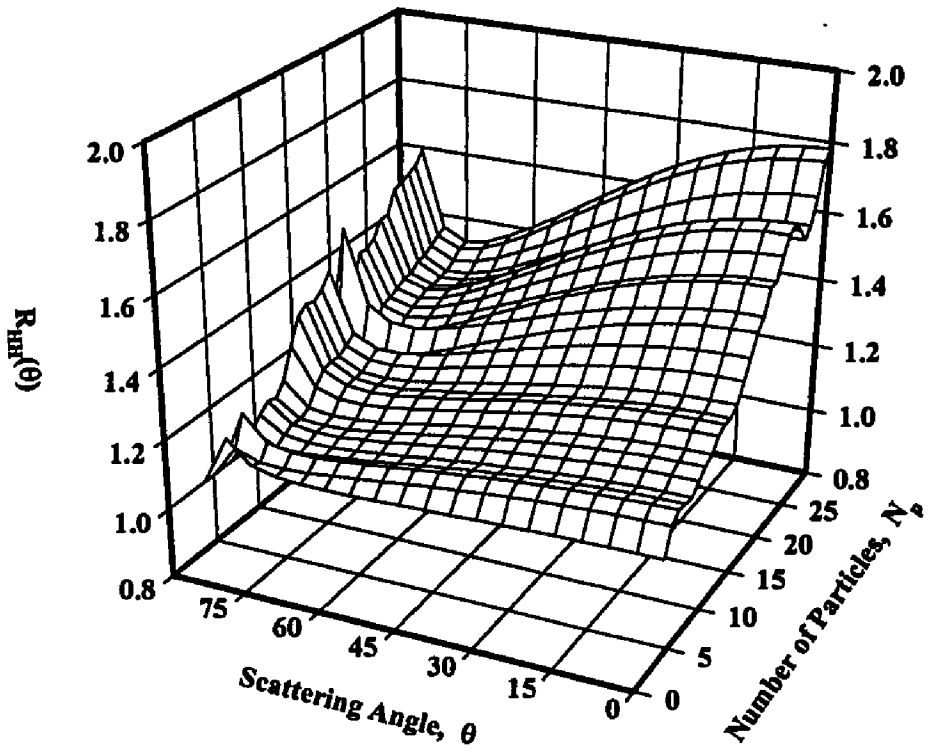

Figure A.23 The dissymmetry ratio $R_{HH}(\theta)$ as a function of the scattering angle θ and the number of primary particles N_p, for a cluster agglomerate of α_p=0.125 and m=1.5-0.5i.

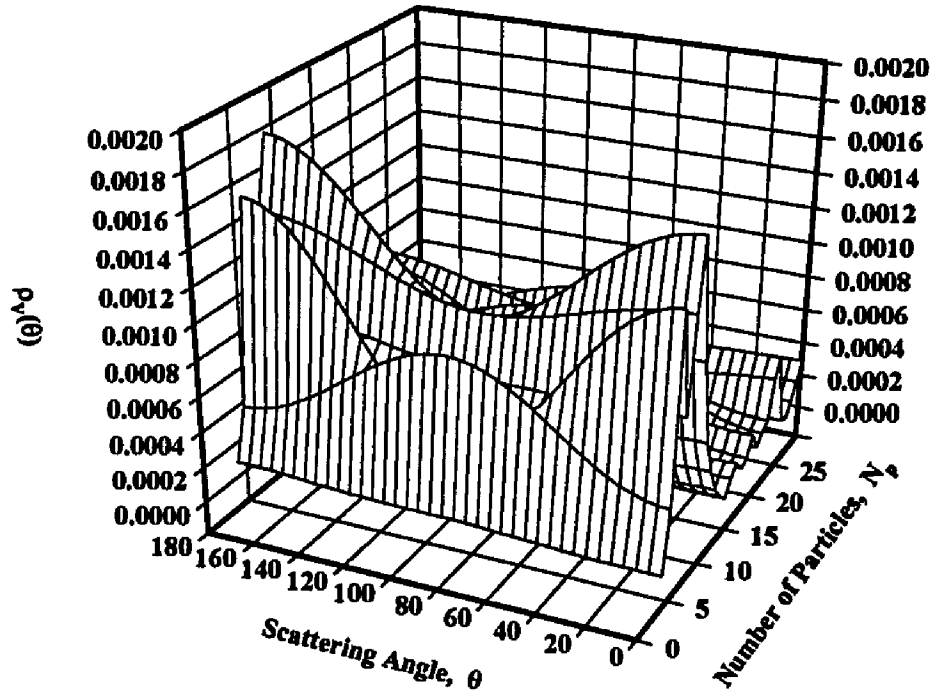

Figure A.24 The depolarization ratio $\rho_V(\theta)$ as a function of the scattering angle θ and the number of primary particles N_p, for a cluster agglomerate of α_p=0.125 and m=1.5-0.5i.

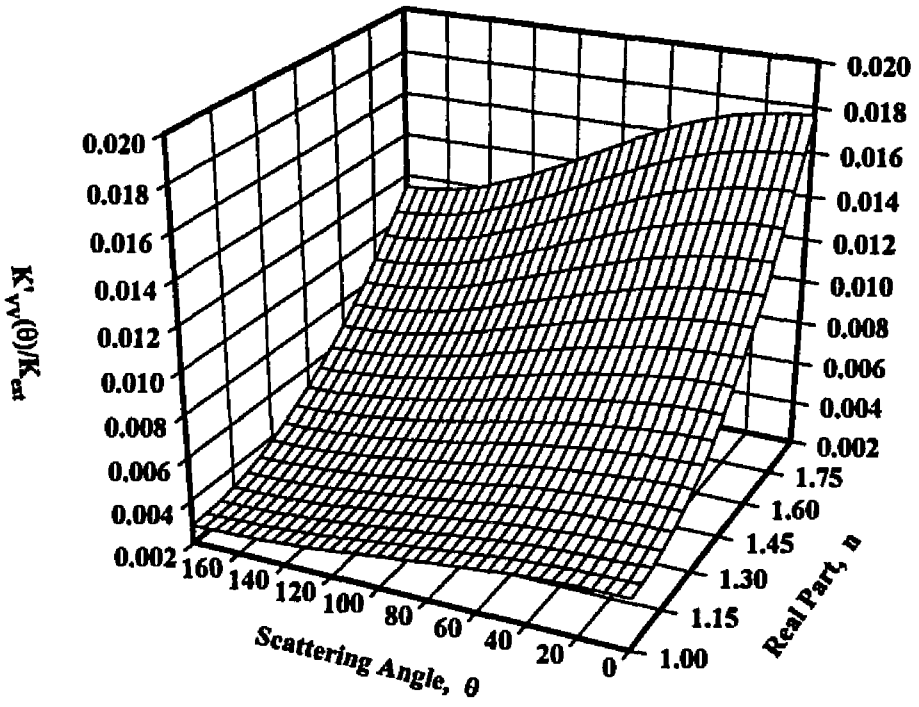

Figure A.25 The differential scattering cross section to extinction cross section ratio $\{K'_{vv}(\theta)/K_{ext}\}$ as a function of the scattering angle θ and the real part of the refractive index n, for a cluster agglomerate of α_p=0.125, N_p=20 and k=0.5.

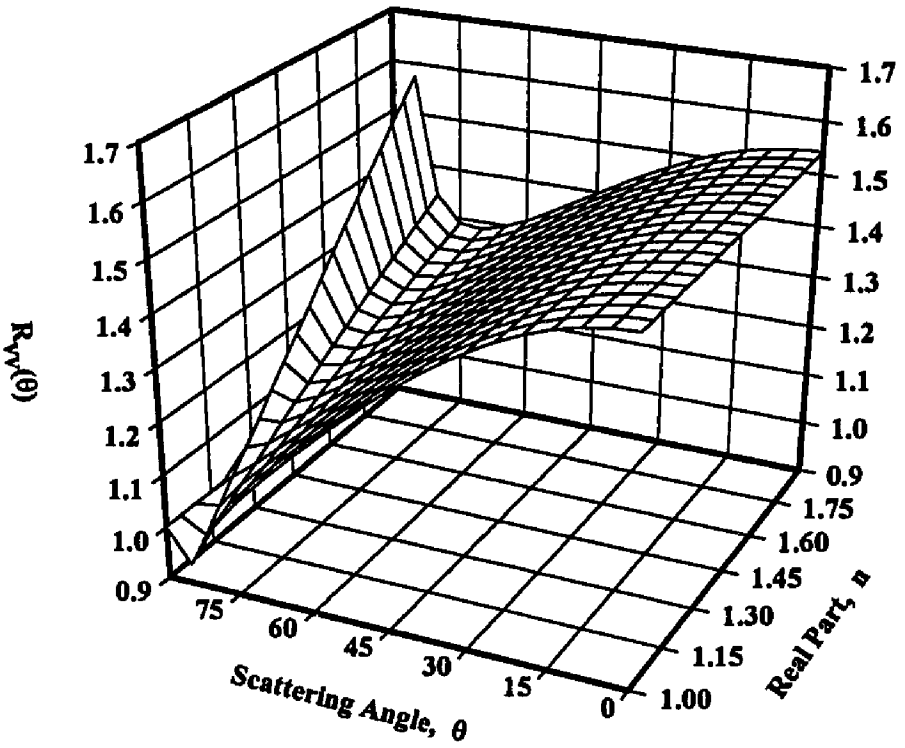

Figure A.26 The dissymmetry ratio $R_{VV}(\theta)$ as a function of the scattering angle θ and the real part of the refractive index n, for a cluster agglomerate of α_p=0.125, N_p=20 and k=0.5.

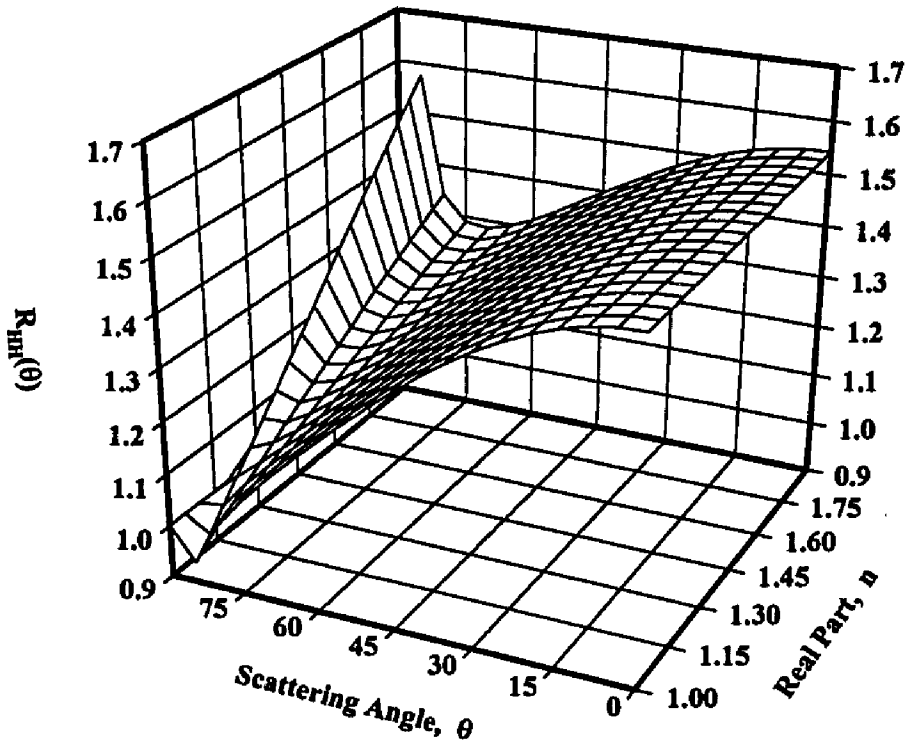

Figure A.27 The dissymmetry ratio $R_{HH}(\theta)$ as a function of the scattering angle θ and the real part of the refractive index n, for a cluster agglomerate of α_p=0.125, N_p=20 and k=0.5.

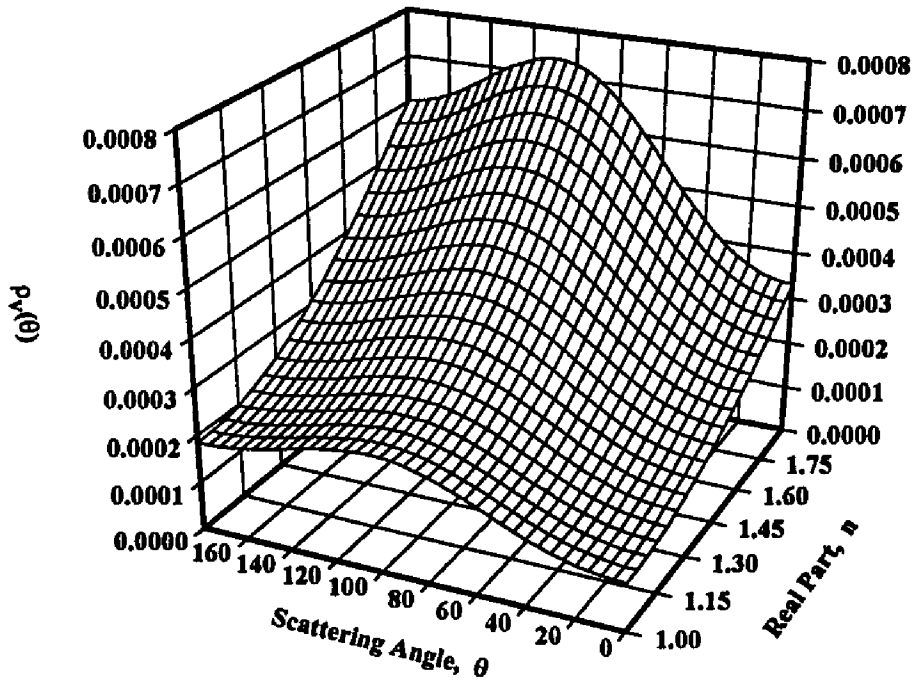

Figure A.28 The depolarization ratio $\rho_V(\theta)$ as a function of the scattering angle θ and the real part of the refractive index n, for a cluster agglomerate of α_p=0.125, N_p=20 and k=0.5.

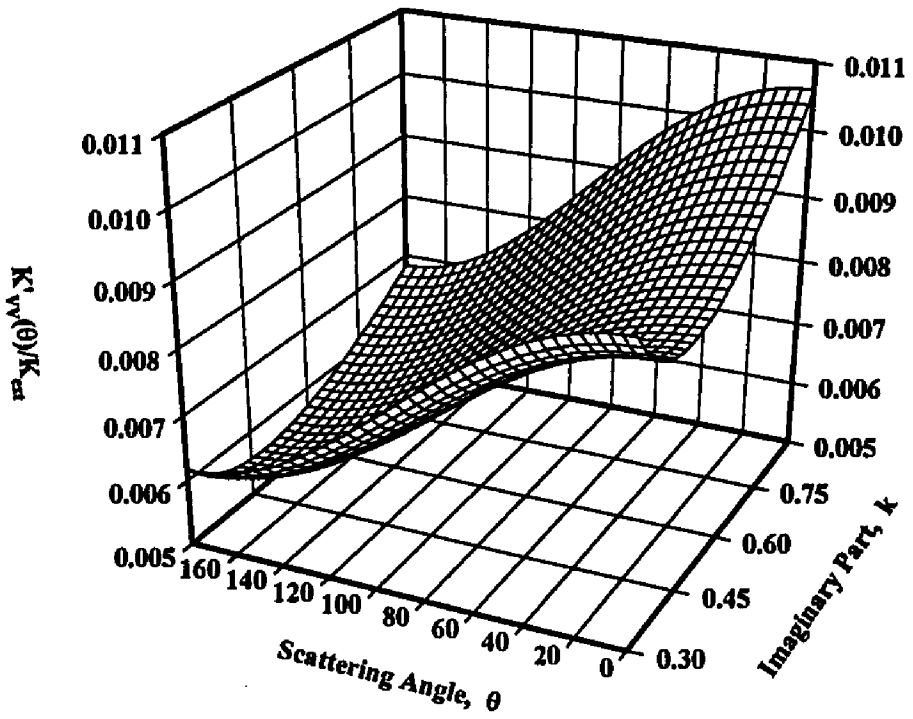

Figure A.29 The differential scattering cross section to extinction cross section ratio $\{K'_{vv}(\theta)/K_{ext}\}$ as a function of the scattering angle θ and the imaginary part of the refractive index k, for a cluster agglomerate of α_p=0.125, N_p=20 and n=1.5.

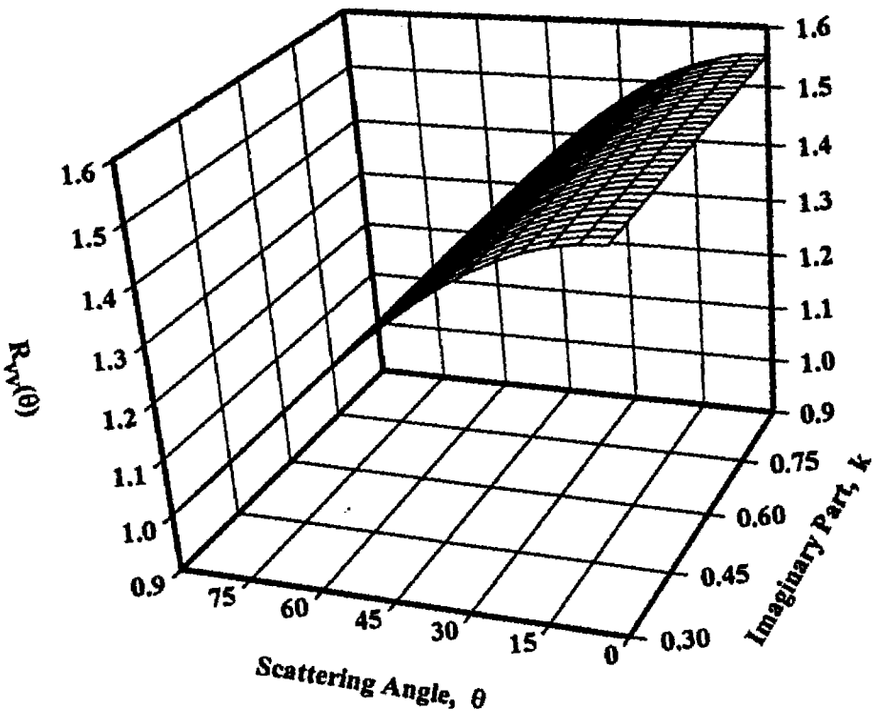

Figure A.30 The dissymmetry ratio $R_{VV}(\theta)$ as a function of the scattering angle θ and the imaginary part of the refractive index k, for a cluster agglomerate of α_p=0.125, N_p=20 and n=1.5.

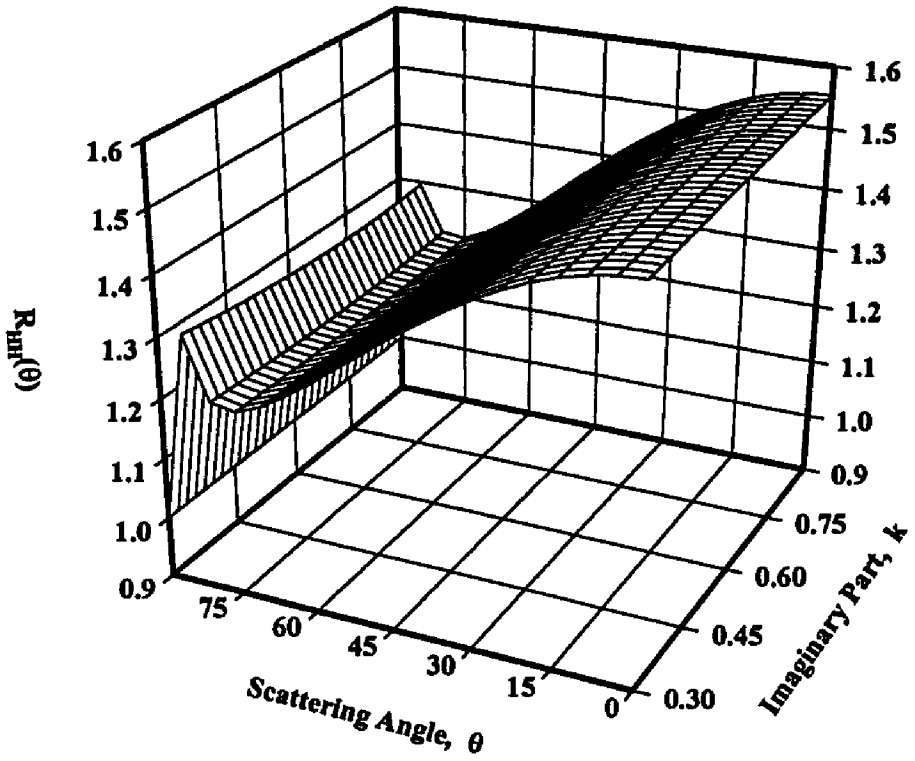

Figure A.31 The dissymmetry ratio $R_{HH}(\theta)$ as a function of the scattering angle θ and the imaginary part of the refractive index k, for a cluster agglomerate of α_p=0.125, N_p=20 and n=1.5.

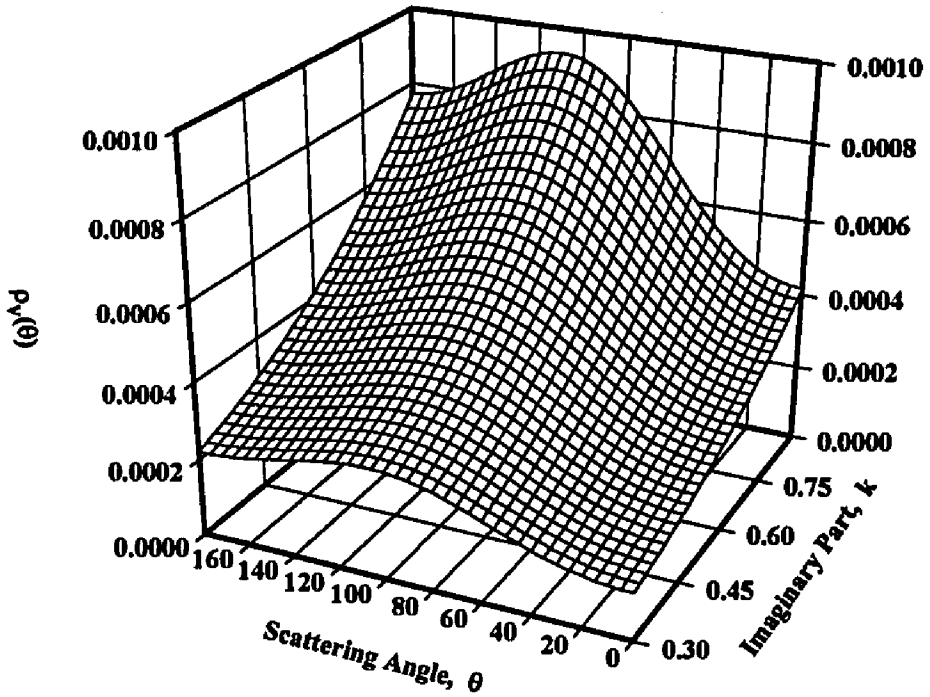

Figure A.32 The depolarization ratio $\rho_V(\theta)$ as a function of the scattering angle θ and the imaginary part of the refractive index k, for a cluster agglomerate of α_p=0.125, N_p=20 and n=1.5.

APPENDIX B

AGGLOMERATE ANALYSIS RESULTS

The results of the agglomerate model analysis are summarized in this appendix. Tables B1 and B2 show the two sets of experimentally measured quantities used in the analysis. Different refractive indices were used. Tables B3 - B22 show the results of the analysis of the experimental measurements. The first three columns in the tables of the results show the inferred agglomerate parameters N_p, d_p, and N. The last four columns in the same tables show the deviation of the simulated from the measured agglomerate scattering and extinction quantities.

Table B1. First set of the measured quantities as used in the agglomerate analysis.

Height (mm)	$K'_{vv}(20^\circ)/K_{ext}$ (sr)	$R_{VV}(20^\circ)$	$R_{HH}(20^\circ)$	$\rho_V(160^\circ)$
6	5.770×10^{-4}	1.26	1.35	0.0131
8	1.741×10^{-3}	1.37	1.54	0.0122
10	3.637×10^{-3}	1.54	1.71	0.0114
12	5.375×10^{-3}	1.71	1.90	0.0113
14	7.820×10^{-3}	1.92	2.13	0.0112
16	9.609×10^{-3}	2.14	2.37	0.0113
18	1.267×10^{-2}	2.42	2.67	0.0115
20	1.474×10^{-2}	2.73	3.00	0.0119
22	1.550×10^{-2}	3.10	3.33	0.0122

Table B2. Second set of the measured quantities as used in the agglomerate analysis.

Height (mm)	$K'_{vv}(45^\circ)/K_{ext}$ (sr)	$R_{VV}(45^\circ)$	$R_{HH}(45^\circ)$	$\rho_V(135^\circ)$
6	5.699×10^{-4}	1.16	1.16	0.0168
8	1.673×10^{-3}	1.24	1.25	0.0144
10	3.385×10^{-3}	1.34	1.34	0.0137
12	4.876×10^{-3}	1.45	1.44	0.0136
14	6.883×10^{-3}	1.57	1.56	0.0133
16	8.369×10^{-3}	1.69	1.67	0.0133
18	1.053×10^{-2}	1.82	1.81	0.0134
20	1.206×10^{-2}	1.98	1.93	0.0137
22	1.196×10^{-2}	2.16	2.09	0.0137

Table B3. Straight Chain agglomerate analysis of the experimental measurements summarized in Table B1.

Straight Chain, θ=20°, m=1.60-0.53i							
	Inferred Parameters			% Diff. Between Measurement and Simulation			
H (mm)	N_p	d_p (nm)	N	K'_{vv}/K_{ext}	R_{VV}	R_{HH}	ρ_V
6	8	15.8	$8.6x10^9$	0.5	0.05	7.50	9.2
8	6	25.2	$3.7x10^9$	0.6	0.4	12.4	3.4
10	6	31.5	$2.2x10^9$	1.4	3.2	8.2	16.2
12	5	39.6	$1.6x10^9$	0.8	3.7	16.1	15.7
14	5	45.2	$1.2x10^9$	1.0	4.4	16.8	25.8
16	6	45.6	$1.1x10^9$	0.7	1.5	10.6	38.6
18	6	50.0	$8.2x10^8$	2.8	2.9	15.3	41.9
20	8	48.5	$7.7x10^8$	1.7	4.5	8.2	47.1
22	9	48.0	$9.4x10^8$	0.1	0.3	11.1	47.6

Table B4. Straight Chain agglomerate analysis of the experimental measurements summarized in Table B1.

Straight Chain, θ=20°, m=1.69-0.61i							
	Inferred Parameters			% Diff. Between Measurement and Simulation			
H (mm)	N_p	d_p (nm)	N	K'_{vv}/K_{ext}	R_{VV}	R_{HH}	ρ_V
6	9	14.4	$9.3x10^9$	1.1	0.7	6.9	26.2
8	6	24.0	$4.0x10^9$	0.5	2.8	16.1	36.7
10	6	30.0	$2.4x10^9$	0.2	1.0	13.0	39.9
12	6	35.3	$1.7x10^9$	0.08	0.8	11.4	47.9
14	6	40.3	$1.3x10^9$	0.06	0.3	12.0	54.2
16	6	43.5	$1.1x10^9$	0.9	3.9	16.8	66.4
18	7	45.6	$8.5x10^8$	0.1	0.5	12.2	64.0
20	8	46.3	$8.1x10^8$	0.3	0.3	13.9	65.7
22	10	44.0	$1.0x10^9$	0.2	0.2	12.3	66.7

Table B5. Straight Chain agglomerate analysis of the experimental measurements summarized in Table B1.

Straight Chain, θ=20°, m=1.73-0.64i							
	Inferred Parameters			% Diff. Between Measurement and Simulation			
H (mm)	N_p	d_p (nm)	N	K'_{vv}/K_{ext}	R_{VV}	R_{HH}	ρ_V
6	9	14.1	9.7×10^9	0.9	0.4	8.1	24.3
8	7	22.3	4.3×10^9	0.01	1.4	1.2	30.7
10	6	29.4	2.5×10^9	0.2	2.7	14.9	37.0
12	6	34.6	1.8×10^9	0.4	1.3	13.7	44.6
14	6	39.5	1.3×10^9	0.5	1.9	14.6	50.7
16	7	40.3	1.2×10^9	0.6	1.9	10.7	57.0
18	7	44.7	8.8×10^8	0.4	1.8	14.8	59.2
20	8	45.4	8.4×10^8	0.9	2.5	16.4	60.7
22	10	43.2	1.0×10^9	0.9	2.0	14.8	61.8

Table B6. Straight Chain agglomerate analysis of the experimental measurements summarized in Table B1.

Straight Chain, θ=20°, m=1.48-0.35i							
	Inferred Parameters			% Diff. Between Measurement and Simulation			
H (mm)	N_p	d_p (nm)	N	K'_{vv}/K_{ext}	R_{VV}	R_{HH}	ρ_V
6	7	17.7	9.7×10^9	0.7	0.3	7.7	105
8	5	28.8	4.2×10^9	0.3	1.8	14.7	103
10	5	36.0	2.5×10^9	0.4	0.6	10.9	62.8
12	5	42.3	1.8×10^9	0.6	2.7	8.7	39.5
14	5	48.2	1.3×10^9	0.9	2.6	8.9	23.1
16	6	48.5	1.2×10^9	0.3	7.9	3.2	2.7
18	7	50.0	9.9×10^8	9.5	9.9	1.0	6.5
20	8	50.0	1.0×10^9	13.8	8.0	3.8	8.4
22	9	50.0	1.2×10^9	8.9	4.9	5.6	10.9

Table B7. Straight Chain agglomerate analysis of the experimental measurements summarized in Table B2.

Straight Chain, θ=45°, m=1.60-0.53i							
	Inferred Parameters			% Diff. Between Measurement and Simulation			
H (mm)	N_p	d_p (nm)	N	K'_{vv}/K_{ext}	R_{VV}	R_{HH}	ρ_V
6	7	16.6	8.5×10^9	1.7	0.06	1.7	52.3
8	5	26.8	3.7×10^9	0.6	2.3	5.0	46.9
10	5	34.3	2.0×10^9	0.1	0.5	2.6	23.4
12	6	37.0	1.7×10^9	1.1	3.4	2.6	3.5
14	5	44.5	1.2×10^9	0.2	0.2	4.7	1.5
16	31	40.2	3.0×10^8	0.0004	0.02	27.4	55.2
18	21	44.8	3.2×10^8	0.1	0.2	33.2	52.1
20	16	48.2	3.9×10^8	0.4	0.9	35.9	48.1
22	13	47.9	6.5×10^8	0.07	0.5	34.3	42.7

Table B8. Straight Chain agglomerate analysis of the experimental measurements summarized in Table B2.

Straight Chain, θ=45°, m=1.69-0.61i							
	Inferred Parameters			% Diff. Between Measurement and Simulation			
H (mm)	N_p	d_p (nm)	N	K'_{vv}/K_{ext}	R_{VV}	R_{HH}	ρ_V
6	8	15.1	9.1×10^9	0.09	0.9	1.3	2.7
8	6	23.9	4.1×10^9	0.6	0.03	3.6	5.0
10	5	32.5	2.2×10^9	0.4	2.6	5.8	24.6
12	6	35.1	1.8×10^9	0.1	0.6	1.6	29.4
14	6	39.8	1.3×10^9	1.1	3.3	3.3	37.9
16	30	36.8	3.7×10^8	0.05	0.2	35.7	69.2
18	22	41.3	3.6×10^8	0.3	0.5	41.6	69.4
20	7	48.2	8.1×10^8	0.04	0.5	12.3	92.1
22	13	44.2	7.6×10^8	0.07	0.1	36.9	91.6

Table B9. Straight Chain agglomerate analysis of the experimental measurements summarized in Table B2.

Straight Chain, θ=45°, m=1.73-0.64i							
	Inferred Parameters			% Diff. Between Measurement and Simulation			
H (mm)	N_p	d_p (nm)	N	K'_{vv}/K_{ext}	R_{VV}	R_{HH}	ρ_V
6	8	14.8	9.4×10^9	0.7	0.2	2.1	2.5
8	6	23.4	4.3×10^9	0.3	1.0	4.7	4.6
10	6	30.0	2.3×10^9	0.4	2.2	2.3	19.9
12	6	34.4	1.9×10^9	0.7	2.1	3.3	27.3
14	6	39.0	1.4×10^9	0.2	1.7	5.2	35.1
16	30	35.5	4.1×10^8	0.06	0.4	39.0	64.8
18	23	39.8	3.8×10^8	0.3	0.5	46.1	64.2
20	18	42.7	4.6×10^8	0.3	0.3	50.4	61.7
22	13	42.8	8.2×10^8	0.1	0.07	38.1	56.1

Table B10. Straight Chain agglomerate analysis of the experimental measurements summarized in Table B2.

Straight Chain, θ=45°, m=1.48-0.35i							
	Inferred Parameters			% Diff. Between Measurement and Simulation			
H (mm)	N_p	d_p (nm)	N	K'_{vv}/K_{ext}	R_{VV}	R_{HH}	ρ_V
6	6	18.7	9.7×10^9	0.6	0.6	1.8	186
8	5	28.8	4.2×10^9	0.3	0.9	1.6	153
10	4	39.5	2.3×10^9	0.2	0.3	4.9	158
12	5	42.1	1.9×10^9	0.5	1.0	2.2	86.3
14	5	47.7	1.4×10^9	1.7	5.1	1.4	62.2
16	6	44.9	3.4×10^8	0.05	2.2	17.2	24.9
18	33	49.7	2.1×10^8	0.2	0.02	8.6	30.2
20	42	50.0	1.9×10^8	8.7	1.0	2.6	30.1
22	45	50.0	2.3×10^8	7.3	4.5	8.1	29.4

Table B11. Cluster agglomerate analysis of the experimental measurements summarized in Table B1.

Cluster, θ=20°, m=1.60-0.53i							
	Inferred Parameters			% Diff. Between Measurement and Simulation			
H (mm)	N_p	d_p (nm)	N	K'_{vv}/K_{ext}	R_{VV}	R_{HH}	ρ_V
6	20	11.6	9.1×10^9	0.1	19.0	27.5	5595
8	20	16.9	3.8×10^9	1.4	21.6	36.6	4592
10	20	21.2	2.2×10^9	1.9	27.7	41.6	3700
12	20	25.0	1.6×10^9	2.8	31.8	46.2	3223
14	20	28.7	1.1×10^9	4.5	36.1	50.6	2771
16	20	31.0	1.0×10^9	5.5	43.0	57.9	2527
18	20	34.5	7.4×10^8	7.2	46.3	60.7	2200
20	20	36.7	6.9×10^8	8.7	53.8	68.7	2025
22	20	37.5	8.5×10^8	9.4	69.9	81.6	2003

Table B12. Cluster agglomerate analysis of the experimental measurements summarized in Table B1.

Cluster, θ=20°, m=1.69-0.61i							
	Inferred Parameters			% Diff. Between Measurement and Simulation			
H (mm)	N_p	d_p (nm)	N	K'_{vv}/K_{ext}	R_{VV}	R_{HH}	ρ_V
6	20	11.0	1.0×10^9	0.2	19.6	28.1	4406
8	20	16.0	4.3×10^9	1.0	22.9	38.1	3587
10	20	20.1	2.4×10^9	1.9	29.9	44.1	2972
12	20	23.7	1.8×10^9	2.8	35.1	49.8	2583
14	20	27.2	1.2×10^9	4.4	40.7	55.6	2274
16	20	29.4	1.1×10^9	5.5	48.6	64.1	2067
18	20	32.7	8.0×10^8	6.9	53.7	68.9	1842
20	20	34.7	7.5×10^8	7.8	63.3	79.1	1724
22	20	35.5	9.2×10^8	8.8	80.8	93.2	1688

Table B13. Cluster agglomerate analysis of the experimental measurements summarized in Table B1.

Cluster, θ=20°, m=1.73-0.64i							
	Inferred Parameters			% Diff. Between Measurement and Simulation			
H (mm)	N_p	d_p (nm)	N	K'_{vv}/K_{ext}	R_{VV}	R_{HH}	ρ_v
6	20	10.8	$1.0x10^{10}$	1.3	19.8	28.3	3993
8	20	15.7	$4.5x10^{9}$	1.9	23.4	38.6	3288
10	20	19.7	$2.6x10^{9}$	2.5	30.7	44.9	2750
12	20	23.2	$1.9x10^{9}$	2.9	36.3	51.1	2411
14	20	26.6	$1.3x10^{9}$	4.3	42.5	57.6	2096
16	20	28.7	$1.2x10^{9}$	4.9	51.1	66.8	1954
18	20	32.0	$8.4x10^{8}$	7.0	56.6	72.0	1725
20	20	34.0	$7.8x10^{8}$	8.1	66.6	82.7	1624
22	20	34.7	$9.7x10^{8}$	8.5	85.1	97.8	1594

Table B14. Cluster agglomerate analysis of the experimental measurements summarized in Table B1.

Cluster, θ=20°, m=1.48-0.35i							
	Inferred Parameters			% Diff. Between Measurement and Simulation			
H (mm)	N_p	d_p (nm)	N	K'_{vv}/K_{ext}	R_{VV}	R_{HH}	ρ_v
6	20	12.5	$9.9x10^{9}$	1.1	18.1	26.5	9976
8	20	18.1	$4.3x10^{9}$	5.5	19.7	34.5	8033
10	20	22.8	$2.4x10^{9}$	2.3	24.4	38.0	6233
12	20	26.9	$1.8x10^{9}$	3.4	27.1	40.9	5550
14	20	30.8	$1.3x10^{9}$	4.4	29.8	43.7	4566
16	20	33.3	$1.1x10^{9}$	5.6	35.2	49.3	4246
18	20	37.1	$8.2x10^{8}$	7.7	36.1	49.5	3493
20	20	39.4	$7.7x10^{8}$	8.8	41.9	55.7	3205
22	20	40.4	$9.5x10^{8}$	10.4	55.4	66.1	3110

Table B15. Cluster agglomerate analysis of the experimental measurements summarized in Table B2.

Cluster, θ=45°, m=1.60-0.53i							
	Inferred Parameters			% Diff. Between Measurement and Simulation			
H (mm)	N_p	d_p (nm)	N	K'_{vv}/K_{ext}	R_{VV}	R_{HH}	ρ_V
6	24	10.9	9.2×10^9	0.3	11.1	10.8	5158
8	23	15.9	4.0×10^9	0.05	13.4	13.7	3791
10	23	20.3	2.2×10^9	0.6	15.8	14.7	3241
12	23	23.2	1.8×10^9	2.2	24.7	17.4	2922
14	23	26.3	1.3×10^9	2.8	22.6	19.9	2560
16	23	28.3	1.2×10^9	3.5	26.8	22.9	2363
18	23	30.9	9.1×10^8	4.2	28.9	25.2	2171
20	23	32.7	8.7×10^8	5.6	34.2	27.3	2074
22	23	32.6	1.2×10^9	5.7	46.8	38.2	2074

Table B16. Cluster agglomerate analysis of the experimental measurements summarized in Table B2.

Cluster, θ=45°, m=1.69-0.61i							
	Inferred Parameters			% Diff. Between Measurement and Simulation			
H (mm)	N_p	d_p (nm)	N	K'_{vv}/K_{ext}	R_{VV}	R_{HH}	ρ_V
6	23	10.5	9.9×10^9	0.9	11.5	11.2	3960
8	23	15.1	4.4×10^9	0.6	14.3	14.6	2963
10	23	19.3	2.4×10^9	1.5	17.3	16.1	2534
12	23	22.0	1.9×10^9	2.4	26.9	19.6	2328
14	23	24.9	1.4×10^9	2.7	25.7	22.8	2080
16	23	26.8	1.3×10^9	3.4	30.4	26.4	1946
18	23	29.3	9.9×10^8	4.5	33.3	29.4	1761
20	23	30.9	9.6×10^8	5.1	39.8	32.6	1702
22	23	30.9	1.3×10^9	5.9	52.6	43.6	1702

Table B17. Cluster agglomerate analysis of the experimental measurements summarized in Table B2.

Cluster, θ=45°, m=1.73-0.64i							
	Inferred Parameters			% Diff. Between Measurement and Simulation			
H (mm)	N_p	d_p (nm)	N	K'_{vv}/K_{ext}	R_{VV}	R_{HH}	ρ_V
6	24	10.1	$1.1x10^{10}$	0.9	10.4	10.1	8478
8	23	14.8	$4.6x10^{9}$	0.2	11.9	12.3	6757
10	23	28.9	$2.5x10^{9}$	1.5	13.2	12.3	5608
12	23	21.5	$2.1x10^{9}$	1.7	21.4	14.4	4937
14	23	24.3	$1.5x10^{9}$	3.0	18.2	15.7	4333
16	23	26.2	$1.4x10^{9}$	3.1	21.6	18.1	4056
18	23	28.6	$1.1x10^{9}$	3.9	22.5	19.2	3622
20	23	30.2	$1.0x10^{9}$	5.1	26.9	20.7	3412
22	23	30.2	$1.4x10^{9}$	6.6	38.0	30.3	3325

Table B18. Cluster agglomerate analysis of the experimental measurements summarized in Table B2.

Cluster, θ=45°, m=1.48-0.35i							
	Inferred Parameters			% Diff. Between Measurement and Simulation			
H (mm)	N_p	d_p (nm)	N	K'_{vv}/K_{ext}	R_{VV}	R_{HH}	ρ_V
6	23	11.9	$1.0x10^{10}$	0.9	10.4	10.1	8478
8	23	17.1	$4.5x10^{9}$	0.2	11.9	12.3	6757
10	23	21.9	$2.4x10^{9}$	1.5	13.2	12.3	5608
12	23	24.9	$2.0x10^{9}$	1.7	21.4	14.4	4937
14	23	28.3	$1.5x10^{9}$	3.0	18.2	15.7	4333
16	23	30.4	$1.3x10^{9}$	3.1	21.6	18.1	4056
18	23	33.2	$1.0x10^{9}$	3.9	22.5	19.2	3622
20	23	35.1	$9.8x10^{8}$	5.1	26.9	20.7	3412
22	23	35.2	$1.3x10^{9}$	6.6	38.0	30.3	3325

Table B19. Randomly Branched Chain agglomerate analysis of the experimental measurements summarized in Table B1.

Randomly Branched Chain, θ=20°, m=1.60-0.53i							
	Inferred Parameters			% Diff. Between Measurement and Simulation			
H (mm)	N_p	d_p (nm)	N	K'_{vv}/K_{ext}	R_{VV}	R_{HH}	ρ_V
6	32	10.0	$8.8x10^9$	1.5	0.2	7.0	998
8	14	19.0	$3.9x10^9$	0.05	0.3	12.7	524
10	12	25.0	$2.0x10^9$	0.4	1.6	9.3	354
12	9	32.5	$1.7x10^9$	1.2	0.6	10.5	240
14	8	38.5	$1.2x10^9$	0.9	1.4	12.6	181
16	8	41.5	$1.1x10^9$	1.5	2.1	13.3	151
18	8	45.5	$8.3x10^8$	0.5	0.2	10.7	116
20	8	48.5	$7.7x10^8$	1.9	1.1	11.7	97.2
22	10	45.5	$1.0x10^9$	0.2	0.3	7.3	99.7

Table B20. Randomly Branched Chain agglomerate analysis of the experimental measurements summarized in Table B1.

Randomly Branched Chain, θ=20°, m=1.69-0.61i							
	Inferred Parameters			% Diff. Between Measurement and Simulation			
H (mm)	N_p	d_p (nm)	N	K'_{vv}/K_{ext}	R_{VV}	R_{HH}	ρ_V
6	32	9.5	$9.6x10^9$	1.9	1.8	9.2	775
8	18	16.5	$4.3x10^9$	1.4	0.7	11.7	449
10	14	22.5	$2.5x10^9$	0.8	0.3	10.8	301
12	11	28.5	$1.9x10^9$	2.3	0.1	11.3	201
14	10	34.0	$1.3x10^9$	1.6	1.1	9.9	140
16	10	36.5	$1.2x10^9$	1.0	1.7	11.1	117
18	10	40.0	$9.1x10^8$	1.1	1.6	8.7	89.0
20	10	42.5	$8.6x10^8$	0.5	0.02	10.5	74.4
22	13	39.5	$1.1x10^9$	0.7	0.1	8.9	94.1

Table B21. Randomly Branched Chain agglomerate analysis of the experimental measurements summarized in Table B1.

Randomly Branched Chain, θ=20°, m=1.73-0.64i							
	Inferred Parameters			% Diff. Between Measurement and Simulation			
H (mm)	N_p	d_p (nm)	N	K'_{vv}/K_{ext}	R_{VV}	R_{HH}	ρ_V
6	35	9.0	$1.0x10^{10}$	1.1	1.8	9.1	727
8	17	16.5	$4.5x10^{9}$	0.6	1.3	14.0	409
10	15	21.5	$2.6x10^{9}$	1.1	0.8	10.1	279
12	13	26.5	$1.9x10^{9}$	1.0	0.8	10.3	209
14	11	32.0	$1.4x10^{9}$	0.4	1.7	9.2	135
16	11	34.5	$1.3x10^{9}$	0.2	1.1	9.7	111
18	10	39.5	$9.3x10^{8}$	1.4	0.6	11.1	77.5
20	12	39.0	$9.1x10^{8}$	0.6	1.3	9.1	79.2
22	14	38	$1.1x10^{9}$	1.3	0.9	6.7	84.7

Table B22. Randomly Branched Chain agglomerate analysis of the experimental measurements summarized in Table B1.

Randomly Branched Chain, θ=20°, m=1.48-0.35i							
	Inferred Parameters			% Diff. Between Measurement and Simulation			
H (mm)	N_p	d_p (nm)	N	K'_{vv}/K_{ext}	R_{VV}	R_{HH}	ρ_V
6	20	12.5	$9.9x10^{9}$	0.4	1.6	8.8	1412
8	11	22.0	$4.4x10^{9}$	1.3	0.7	11.6	817
10	9	29.5	$2.5x10^{9}$	0.7	1.5	9.5	559
12	7	38.0	$1.8x10^{9}$	1.7	1.1	12.3	449
14	7	43.0	$1.4x10^{9}$	0.4	2.0	8.7	352
16	7	46.0	$1.3x10^{9}$	1.9	0.7	10.1	305
18	7	50.0	$1.0x10^{9}$	6.4	1.7	8.5	249
20	8	50.0	$1.0x10^{9}$	9.5	4.0	5.9	220
22	9	49.5	$1.2x10^{8}$	6.3	4.7	2.6	202

Table B23. Randomly Branched Chain agglomerate analysis of the experimental measurements summarized in Table B2.

Randomly Branched Chain, θ=45°, m=1.48-0.35i							
	Inferred Parameters			% Diff. Between Measurement and Simulation			
H (mm)	N_p	d_p (nm)	N	K'_{vv}/K_{ext}	R_{VV}	R_{HH}	ρ_V
6	23	12.0	9.7×10^9	0.2	5.7	13.4	1548
8	18	19.0	4.2×10^9	0.7	0.4	12.3	1049
10	14	26.0	2.4×10^9	0.7	0.07	11.5	732
12	11	33.5	1.7×10^9	1.2	1.0	10.5	510
14	10	39.5	1.2×10^9	0.05	0.5	11.0	390
16	10	43.0	1.1×10^9	1.6	0.5	10.9	329
18	9	49.5	7.9×10^8	1.5	0.2	11.5	250
20	10	50.0	7.9×10^8	3.2	1.4	12.7	238
22	13	48.0	9.1×10^8	1.0	0.3	8.1	249

APPENDIX C

COMPUTER PROGRAMS

The computer program described in this appendix is run on the UNIX RS6000 cluster using the Parallel Virtual Machine (PVM) version 3.3.2 software. The PVM software was originally started in 1989 at the Oak Ridge National Laboratory (ORNL) and is currently an ongoing project involving researchers at ORNL, Emory University, University of Tennessee, Carnegie Mellon University and Pittsburgh Supercomputer Center. The PVM software is distributed freely through the internet. The PVM software incorporates serial computers (homogeneous or heterogeneous) to work concurrently as one computational resource. A heterogeneous group of processors consists of different computer machines built with different architectures. PVM can use all types of processors, from mainframes to a desktop personal computers linked to the internet system. PVM also handles all the incompatibility problems that may arise when heterogeneous processors are linked together, and it supplies the supporting FORTRAN or C language commands to assign tasks to each processor and handle the communications and data transfer between processors. The commands may be called from the user programs as subroutines using the CALL statements. Detailed descriptions of these commands may be found in the software manuals available on line on the UNIX.

An important component of the PVM system is the PVM daemon or "pvmd". The daemon is a server process that resides at each processor on the network, and handles

communications and process control through the network. Each daemon maintains connections with the rest of the daemons residing at the processors in the network. The daemons must be initiated before a program is run and stopped when the program has finished running. Once the daemons are initiated at each processor, then the master PVM program is run. The master program sends a copy (or spawn) of the slave program to each processor and assigns tasks. The master and slave programs are user defined programs and can be written in FORTRAN or C language. The master and slave programs should be located in a specific directory, and a soft link with the PVM libraries must be established. The directory in which the master and slave programs reside is: **$HOME/pvm3/bin/RS6K** , where $HOME is the home directory assigned to the user and RS6K matches the architecture of the UNIX processors. The master program used in this work is a FORTRAN program, named **grid_master.f**, and it spawns the slaves at four processors. The slave program is the agglomerate subroutine and is named **grid_slave.f**. The master program requests the slave to calculate the average light scattering characteristics of an agglomerate given the refractive index, number of primary particles in the agglomerate and the primary particle size. Each slave simulates 200 agglomerates, calculates the average of the light scattering results, and sends the results back to the master program for storing in data files. A command file named **makefile,** residing in the same directory as the master and slave programs and containing the appropriate compilation and link commands is used to compile and link the master and slave programs with the appropriate FORTRAN and PVM libraries. A command file named **hostsfile** residing in the home directory is used to tell PVM which processors are to be used for the

parallel processing assignment. The job is submitted with the command file **grid_pvm.com**, that initiates the daemons, runs the master file (which in turn spawns the slave programs), and stops the daemons after the job is finished.

In summary, the following steps are necessary to run a PVM process on the UNIX RS6000 cluster:

1. Create the master and slave programs in the **$HOME/pvm3/bin/RS6K** directory.
2. Create the **makefile** command file in the the **$HOME/pvm3/bin/RS6K** directory, to compile and link the master and slave programs. The command **make -f makefile** is used to run the **makefile**.
3. Create the **hostsfile** comand file in the home directory, containing the processors' internet addresses that will be used by the PVM process.
4. Create the command file **grid_pvm.com**, that contains the commands to initiate the daemons at the processors indicated by the **hostsfile**, run the master program, and stop the daemons after the job is finished. Submit the job using the command **qsub -G pvm 4 grid_pvm.com**.

The proceeding part of Appendix A shows the **grid_pvm.com** command file, the **hostsfile** command file, the **makefile** command file, the **grid_master.f** master program and the **grid_slave.f** slave program. The details of the UNIX, PVM, and FORTRAN commands used in these files are available on line on the LSU UNIX system.

GRID_PVM.COM Command File

This file contains the commands necessary to initiate the PVM daemons at the processors specified by the **hostsfile**, start the master program, and stop the daemons after the job is finished. The command **qsub -G pvm 4 grid_pvm.com** is used to submit the PVM process on four concurrently running processors. This file must reside in the home directory.

```
#!/bin/csh
pvmd3 hostsfile
sleep 5
pvm3/bin/RS6K/grid_master
echo "halt" | pvm
sleep 5
```

HOSTSFILE Command File

This file contains the UNIX processor internet addresses. The parameter **-t** requests the system to use the token ring communications network that links each processor, which allows much faster communications between each processor. The file must reside in the home directory.

```
unix3.sncc.lsu.edu-t
unix4.sncc.lsu.edu-t
unix5.sncc.lsu.edu-t
unix6.sncc.lsu.edu-t
```

MAKEFILE Command File

This file must reside in the **$HOME/pvm3/bin/RS6K** directory, and contains the commands necessary to compile and link the master and slave programs with the appropriate PVM and FORTRAN libraries. The command **make -f makefile** is used to run the process.

```
##################################################
#                PVM TEMPLATE CODES
#                PVM VERSION: 3.x
##################################################

F77             = xlf
MASTER          = grid_master
MASTERSRC       = grid_master.f
WORKER          = grid_slave
WORKERSRC       = grid_slave.f
INCLUDE         = -I/usr/local/src/pvm3.3.2/include
LIBS            = -L/usr/local/lib -lfpvm3 -lpvm3

        ${MASTER} ${WORKER}

${MASTER}: ${MASTERSRC}
        ${F77} -O3 -qarch=pwr2 ${MASTERSRC} ${INCLUDE} ${LIBS} -o
${MASTER}

${WORKER}: ${WORKERSRC}
        ${F77} -O3 -qarch=pwr2 ${WORKERSRC} ${INCLUDE} ${LIBS} -o
${WORKER}
```

GRID_MASTER.F Master Program

The master program must reside in the **$HOME/pvm3/bin/RS6K** directory. It spawns the slave programs to each of the 4 processors specified by the **hostsfile** command file, and requests the calculation of the average agglomerate scattering results from each slave, given the particle refractive index, number of primary particles in the agglomerate and the primary particle size parameter. The program is set to stop if for whatever reason there is no response from any of the slaves. Synchronization of the slave processes with the master process is important so that the correct tasks are assigned and the correct results are returned for storage in the data files. A grid of N_pXd_p (48X47) points and a constant refractive index is generated by this program. Double precision is used throughout all the agglomerate light scattering calculations.

```
C*****************************************************************
C                        RANDOM BRANCHED CHAIN
C
C            MASTER PROGRAM TO DRIVE THE SLAVE PROGRAMS
C                 IN PARALLEL ON THE UNIX CLUSTER
C
C  KEEPS DP AND RFINDX CONSTANT
C  CALCULATES CHANGE OF SCATTERING CHARACTERISTICS VERSUS
TOTAL
C  NO OF  SIMULATED AGGLOMERATES FOR EACH NP
C
C PROGRAM: GRID_MASTER.F
C***************************************************************** *
C
      PROGRAM MASTER
C
C=====>include fortran pvm header file
      INCLUDE 'fpvm3.h'
C
```

```
      IMPLICIT REAL*8 (A-H,O-Z)
      INTEGER*4 NPROC
      PARAMETER (NPROC=4)
      INTEGER*4 I,J,K,NP,NITER,TOT
      INTEGER*4 TIDS(NPROC),INFO,NUMT,MYTID
      REAL*8 SEXTA(NPROC),XLA(NPROC)
      REAL*8 SVVA20(NPROC),SVVA30(NPROC),SVVA45(NPROC)
      REAL*8 RVVA20(NPROC),RVVA30(NPROC),RVVA45(NPROC)
      REAL*8 RHHA20(NPROC),RHHA30(NPROC),RHHA45(NPROC)
      REAL*8 ROVA160(NPROC),ROVA150(NPROC),ROVA135(NPROC)
      REAL*8 ROHA160(NPROC),ROHA150(NPROC),ROHA135(NPROC)
      CHARACTER*80 Z1,Z2,Z3,Z4,Z5,Z6
      CHARACTER*80 NODENAME
      CHARACTER*7 NOTYET,YESNOW
      C
C*************************************************************
      Z1='/home3/me/meveni/data/random/grid2/scarnd3.dat'
      Z2='/home3/me/meveni/data/random/grid2/rvvrnd3.dat'
      Z3='/home3/me/meveni/data/random/grid2/rhhrnd3.dat'
      Z4='/home3/me/meveni/data/random/grid2/rovrnd3.dat'
      Z5='/home3/me/meveni/data/random/grid2/rohrnd3.dat'
      Z6='/home3/me/meveni/data/random/grid2/extrnd3.dat'
      OPEN(UNIT=11,FILE=Z1,STATUS='UNKNOWN')
      OPEN(UNIT=12,FILE=Z2,STATUS='UNKNOWN')
      OPEN(UNIT=13,FILE=Z3,STATUS='UNKNOWN')
      OPEN(UNIT=14,FILE=Z4,STATUS='UNKNOWN')
      OPEN(UNIT=15,FILE=Z5,STATUS='UNKNOWN')
      OPEN(UNIT=16,FILE=Z6,STATUS='UNKNOWN')
C*************************************************************
C=====>give PVM the name of the slave program
      NODENAME='grid_slave'
C*************************************************************
C
      WL=0.488D0
      PI=DACOS(-1.0D0)
      RIN=1.69D0
      RIK=0.61D0
C
C====>enroll this program in PVM
      CALL PVMFMYTID(MYTID)
      WRITE(6,*) 'MASTER ID#: ',MYTID
      WRITE(6,*)
C=====>start spawning the slave programs
      DO 2 K=1,NPROC
      CALL PVMFSPAWN(NODENAME,PVMDEFAULT," ",1,TIDS(K),NUMT)
```

```
      IF (NUMT .LT. 0) THEN
       WRITE(6,*) 'ERROR IN SPAWNING SLAVE #',K
       STOP
      ENDIF
      WRITE(6,*) 'SLAVE #',K,' ID#',TIDS(K),'  SPAWNED AND WORKING'
 2    CONTINUE
C*****************************************************************
C
C*****************************************************************
C
C
      NITER=200
      NP=4
      DO 999 I=1,48
C     DO 999 I=1,47
      DIAP=0.005D0
      DO 888 J=1,91
      ALPHA=PI*DIAP/WL
C
C=====>send a "don't quit yet" message to slaves
      MESSG=30
      DO 5 K=1,NPROC
      CALL PVMFINITSEND(PVMRAW,INFO)
      CALL PVMFPACK(STRING,NOTYET,7,1,INFO)
      CALL PVMFSEND(TIDS(K),MESSG,INFO)
      IF (INFO .LT. 0) THEN
      WRITE(6,*) 'ERROR SENDING NOT-YET MESSAGE TO SLAVE # ',K
      STOP
      ENDIF
 5    CONTINUE
C
C===============================================================
C                       data sending
C=====>set message number for "data send"
      MESSG=10
      DO 10 K=1,NPROC
C=====>clear send buffer and send message encoding
      CALL PVMFINITSEND(PVMRAW,INFO)
      IF (INFO .LT. 0) THEN
      WRITE(6,*) 'ERROR IN CLEARING THE SEND BUFFER'
      STOP
      ENDIF
C=====>pack the data and encode before sending to buffer
      CALL PVMFPACK(REAL8,RIN,1,1,INFO)
      CALL PVMFPACK(REAL8,RIK,1,1,INFO)
```

```
      CALL PVMFPACK(INTEGER4,NP,1,1,INFO)
      CALL PVMFPACK(REAL8,ALPHA,1,1,INFO)
      CALL PVMFPACK(INTEGER4,NITER,1,1,INFO)
C=====>send the packed data to slave with the specified tid
      CALL PVMFSEND(TIDS(K),MESSG,INFO)
      IF (INFO .LT. 0) THEN
       WRITE(6,*) 'ERROR IN SENDING THE DATA TO PROCESSOR # ',K
       STOP
      ENDIF
 10   CONTINUE
C
C=============================================================
C
C=============================================================
C                       data receiving
C
      DO 40 K=1,NPROC
C=====>set "receive data" message number
      MESSG=20
C=====>receive data from each slave
      CALL PVMFRECV(TIDS(K),MESSG,INFO)
      IF (INFO .LT. 0) THEN
      WRITE(6,*) 'ERROR IN RECEIVING FROM PROCESSOR # ',K
      STOP
      ENDIF
C=====>unpack the data and store in the appropriate arrays
      CALL PVMFUNPACK(REAL8,XL,1,1,INFO)
      CALL PVMFUNPACK(REAL8,SEXT,1,1,INFO)
      CALL PVMFUNPACK(REAL8,SVV20,1,1,INFO)
      CALL PVMFUNPACK(REAL8,SVV30,1,1,INFO)
      CALL PVMFUNPACK(REAL8,SVV45,1,1,INFO)
      CALL PVMFUNPACK(REAL8,RVV20,1,1,INFO)
      CALL PVMFUNPACK(REAL8,RVV30,1,1,INFO)
      CALL PVMFUNPACK(REAL8,RVV45,1,1,INFO)
      CALL PVMFUNPACK(REAL8,RHH20,1,1,INFO)
      CALL PVMFUNPACK(REAL8,RHH30,1,1,INFO)
      CALL PVMFUNPACK(REAL8,RHH45,1,1,INFO)
      CALL PVMFUNPACK(REAL8,ROV160,1,1,INFO)
      CALL PVMFUNPACK(REAL8,ROV150,1,1,INFO)
      CALL PVMFUNPACK(REAL8,ROV135,1,1,INFO)
      CALL PVMFUNPACK(REAL8,ROH160,1,1,INFO)
      CALL PVMFUNPACK(REAL8,ROH150,1,1,INFO)
      CALL PVMFUNPACK(REAL8,ROH135,1,1,INFO)
C
      SEXTA(K)=SEXT
```

```
      XLA(K)=XL
      SVVA20(K)=SVV20
      SVVA30(K)=SVV30
      SVVA45(K)=SVV45
      RVVA20(K)=RVV20
      RVVA30(K)=RVV30
      RVVA45(K)=RVV45
      RHHA20(K)=RHH20
      RHHA30(K)=RHH30
      RHHA45(K)=RHH45
      ROVA160(K)=ROV160
      ROVA150(K)=ROV150
      ROVA135(K)=ROV135
      ROHA160(K)=ROH160
      ROHA150(K)=ROH150
      ROHA135(K)=ROH135
C
 40   CONTINUE
C=====================================================================
C
      SEXTSM=0.0D0
      XLSM=0.0D0
      SVV20SM=0.0D0
      SVV30SM=0.0D0
      SVV45SM=0.0D0
      RVV20SM=0.0D0
      RVV30SM=0.0D0
      RVV45SM=0.0D0
      RHH20SM=0.0D0
      RHH30SM=0.0D0
      RHH45SM=0.0D0
      ROV160SM=0.0D0
      ROV150SM=0.0D0
      ROV135SM=0.0D0
      ROH160SM=0.0D0
      ROH150SM=0.0D0
      ROH135SM=0.0D0
C
      DO 60 K=1,NPROC
      SEXTSM=SEXTSM+SEXTA(K)
      XLSM=XLSM+XLA(K)
      SVV20SM=SVV20SM+SVVA20(K)
      SVV30SM=SVV30SM+SVVA30(K)
      SVV45SM=SVV45SM+SVVA45(K)
      RVV20SM=RVV20SM+RVVA20(K)
```

```
      RVV30SM=RVV30SM+RVVA30(K)
      RVV45SM=RVV45SM+RVVA45(K)
      RHH20SM=RHH20SM+RHHA20(K)
      RHH30SM=RHH30SM+RHHA30(K)
      RHH45SM=RHH45SM+RHHA45(K)
      ROV160SM=ROV160SM+ROVA160(K)
      ROV150SM=ROV150SM+ROVA150(K)
      ROV135SM=ROV135SM+ROVA135(K)
      ROH160SM=ROH160SM+ROHA160(K)
      ROH150SM=ROH150SM+ROHA150(K)
      ROH135SM=ROH135SM+ROHA135(K)
 60   CONTINUE
      DIV1=DFLOAT(NPROC)
      SEXT=SEXTSM/DIV1
      XL=XLSM/DIV1
      SVV20=SVV20SM/DIV1
      SVV30=SVV30SM/DIV1
      SVV45=SVV45SM/DIV1
      SCA20=SVV20/SEXT
      SCA30=SVV30/SEXT
      SCA45=SVV45/SEXT
      RVV20=RVV20SM/DIV1
      RVV30=RVV30SM/DIV1
      RVV45=RVV45SM/DIV1
      RHH20=RHH20SM/DIV1
      RHH30=RHH30SM/DIV1
      RHH45=RHH45SM/DIV1
      ROV160=ROV160SM/DIV1
      ROV150=ROV150SM/DIV1
      ROV135=ROV135SM/DIV1
      ROH160=ROH160SM/DIV1
      ROH150=ROH150SM/DIV1
      ROH135=ROH135SM/DIV1
C
      WRITE(11,99) NP,DIAP,SCA20,SCA30,SCA45
      WRITE(12,99) NP,DIAP,RVV20,RVV30,RVV45
      WRITE(13,99) NP,DIAP,RHH20,RHH30,RHH45
      WRITE(14,99) NP,DIAP,ROV160,ROV150,ROV135
      WRITE(15,99) NP,DIAP,ROH160,ROH150,ROH135
      WRITE(16,98) NP,DIAP,SEXT,XL
C
C
      DIAP=DIAP+0.0005D0
 888  CONTINUE
      NP=NP+1
```

```
 999    CONTINUE
C
 99     FORMAT(2X,I3,2X,F6.4,2X,E14.6,2X,E14.6,2X,E14.6)
 98     FORMAT(2X,I3,2X,F6.4,2X,E14.6,2X,E14.6)
C
C=====>notify each slave to exit
        MESSG=30
        DO 1010 K=1,NPROC
        CALL PVMFINITSEND(PVMRAW,INFO)
        CALL PVMFPACK(STRING,YESNOW,7,1,INFO)
        CALL PVMFSEND(TIDS(K),MESSG,INFO)
        IF (INFO .LT. 0) THEN
         WRITE(6,*) 'CANNOT SEND THE QUIT MESSAGE TO SLAVE # ',K
        ENDIF
        WRITE(6,*) 'NOTIFIED SLAVE #',K, 'TO QUIT NOW'
 1010   CONTINUE
C
        CALL PVMFEXIT(INFO)
        STOP
        END
C*********************************************************************
```

GRID_SLAVE.F Slave Program

The slave program must reside at the **$HOME/pvm3/bin/RS6K** directory. The master program sends an identical copy of the slave program to each processor. The slave receives the task assignment from the master program and simulates the specified number of agglomerates and averages the agglomerate light scattering results. Since identical copies of the slave program are spawned to each of the four processors used in the PVM, caution should be exercised so that the agglomerates generated at each processor are not identical. In other words, not only the agglomerates generated at each processor should have a different structure during each iteration, but they should also differ from those generated concurrently by the other processors. The random number generator responsible for randomly building the agglomerate structure is seeded with an integer number that changes with each new iteration. Also the integer slave process identification number is added to the seed ensuring that the agglomerates generated at each iteration and by each processor are unique and there is no duplication.

```
C**********************************************************************
C                    RANDOMLY BRANCHED CHAIN
C
C      SLAVE PROGRAM
C  CALCULATES SCATTERING CHARACTERISTICS AS FUNCTION OF ANGLE
C  FOR A GIVEN NP,ALPHA,RIN AND RIK
C  Does not require IMSL library
C
C RPOGRAM: GRID_SLAVE.F
C**********************************************************************
C
```

```
      PROGRAM SLAVE
C
      INCLUDE 'fpvm3.h'
C
      IMPLICIT REAL*8 (A-H,O-Z)
      INTEGER*4 I,J,K
      INTEGER*4 NP,MYTID,MASTERID,INFO,MESSG
      INTEGER*4 NTOT,SEED,NSCA,NITER
      PARAMETER (NTOT=500)
      PARAMETER (NSCA=37)
      REAL*8 SEXT(NTOT),XLMAX(NTOT)
      REAL*8 SVV20(NTOT),SVV30(NTOT),SVV45(NTOT)
      REAL*8 RVV20(NTOT),RVV30(NTOT),RVV45(NTOT)
      REAL*8 RHH20(NTOT),RHH30(NTOT),RHH45(NTOT)
      REAL*8 ROV160(NTOT),ROV150(NTOT),ROV135(NTOT)
      REAL*8 ROH160(NTOT),ROH150(NTOT),ROH135(NTOT)
      CHARACTER*7 ANSW
C
      REAL*8 SCAHH(181),SCAVV(181),SCAHV(181),SCAVH(181)
C
C******* COMMON BLOCK FOR JONESCL ****************************
      CHARACTER EFF*1,POL*1,CHAIN*1
      COMPLEX*16 RFINDX
      COMMON/C2/EFF
      COMMON/P2/POL
      COMMON/P3/CHAIN
      COMMON/J2S/SCAHH,SCAVV,SCAHV,SCAVH
      COMMON/RAN/XL
C
C*****************************************************************
C=====>find this slave's id
      CALL PVMFMYTID(MYTID)
C=====>find the master,s id
      CALL PVMFPARENT(MASTERID)
C*****************************************************************
C
      WL=.488D0
      PI = DACOS(-1.0D0)
      REFMED = 1.0D0
      EFF='F'
      POL='H'
      CHAIN='R'
C
C=================================================================
C=====>check for message to stop or continue
```

```
 1      MESSG=30
        CALL PVMFRECV(MASTERID,MESSG,INFO)
        IF (INFO .LT. 0) THEN
         PRINT *,'ERROR IN RECEIVE MESSG QUIT/NOT FROM MASTER'
         STOP
        ENDIF
C=====>unpack the message
        CALL PVMFUNPACK(STRING,ANSW,7,1,INFO)
        IF (ANSW .EQ. 'YES NOW') THEN
        GOTO 1111
        ENDIF
C
C=====>receive tha data from the master
        MESSG=10
        CALL PVMFRECV(MASTERID,MESSG,INFO)
        IF (INFO .LT. 0) THEN
         PRINT *,'ERROR IN RECEIVE MESSG 30 FROM MASTER'
         STOP
        ENDIF
        CALL PVMFUNPACK(REAL8,RIN,1,1,INFO)
        CALL PVMFUNPACK(REAL8,RIK,1,1,INFO)
        CALL PVMFUNPACK(INTEGER4,NP,1,1,INFO)
        CALL PVMFUNPACK(REAL8,ALPHA,1,1,INFO)
        CALL PVMFUNPACK(INTEGER4,NITER,1,1,INFO)
C
C=======================================================================
C
        RFINDX = CMPLX(RIN,RIK)/REFMED
        DIAP = ALPHA*WL/PI
C
        PND=1.0D0
C
C**********************************************************************
C
        DO 100 K=1,NITER
        SEED=MYTID+K
C
        CALL JONESCL(NP,ALPHA,RFINDX,NSCA,QSCA,QEXT,QABS,SEED)
C
        SEXT(K)=PND*PI*(DIAP*DIAP/4.0D0)*QEXT*DFLOAT(NP)*1.0D-8
        XLMAX(K) = XL*ALPHA
        SVV20(K)=PND*SCAVV(5)*(WL*1.0D-4)*(WL*1.0D-4)/(4.0D0*PI*PI)
        SVV30(K)=PND*SCAVV(7)*(WL*1.0D-4)*(WL*1.0D-4)/(4.0D0*PI*PI)
        SVV45(K)=PND*SCAVV(10)*(WL*1.0D-4)*(WL*1.0D-4)/(4.0D0*PI*PI)
        RVV20(K)=SCAVV(5)/SCAVV(33)
```

```
      RVV30(K)=SCAVV(7)/SCAVV(31)
      RVV45(K)=SCAVV(10)/SCAVV(28)
      RHH20(K)=SCAHH(5)/SCAHH(33)
      RHH30(K)=SCAHH(7)/SCAHH(31)
      RHH45(K)=SCAHH(10)/SCAHH(28)
      ROV160(K)=SCAHV(33)/SCAVV(33)
      ROV150(K)=SCAHV(31)/SCAVV(31)
      ROV135(K)=SCAHV(28)/SCAVV(28)
      ROH160(K)=SCAVH(33)/SCAHH(33)
      ROH150(K)=SCAVH(31)/SCAHH(31)
      ROH135(K)=SCAVH(28)/SCAHH(28)
 100  CONTINUE
C
      DIV1=DFLOAT(NITER)
C
      SEXTSM=0.0D0
      XLMAXSM=0.0D0
      SVV20SM=0.0D0
      SVV30SM=0.0D0
      SVV45SM=0.0D0
      RVV20SM=0.0D0
      RVV30SM=0.0D0
      RVV45SM=0.0D0
      RHH20SM=0.0D0
      RHH30SM=0.0D0
      RHH45SM=0.0D0
      ROV160SM=0.0D0
      ROV150SM=0.0D0
      ROV135SM=0.0D0
      ROH160SM=0.0D0
      ROH150SM=0.0D0
      ROH135SM=0.0D0
C
      DO 110 J=1,NITER
      SEXTSM=SEXTSM+SEXT(J)
      XLMAXSM=XLMAXSM+XLMAX(J)
      SVV20SM=SVV20SM+SVV20(J)
      SVV30SM=SVV30SM+SVV30(J)
      SVV45SM=SVV45SM+SVV45(J)
      RVV20SM=RVV20SM+RVV20(J)
      RVV30SM=RVV30SM+RVV30(J)
      RVV45SM=RVV45SM+RVV45(J)
      RHH20SM=RHH20SM+RHH20(J)
      RHH30SM=RHH30SM+RHH30(J)
      RHH45SM=RHH45SM+RHH45(J)
```

```
      ROV160SM=ROV160SM+ROV160(J)
      ROV150SM=ROV150SM+ROV150(J)
      ROV135SM=ROV135SM+ROV135(J)
      ROH160SM=ROH160SM+ROH160(J)
      ROH150SM=ROH150SM+ROH150(J)
      ROH135SM=ROH135SM+ROH135(J)
110   CONTINUE
      AEXT=SEXTSM/DIV1
      AXLMAX=XLMAXSM/DIV1
      ASVV20=SVV20SM/DIV1
      ASVV30=SVV30SM/DIV1
      ASVV45=SVV45SM/DIV1
      ARVV20=RVV20SM/DIV1
      ARVV30=RVV30SM/DIV1
      ARVV45=RVV45SM/DIV1
      ARHH20=RHH20SM/DIV1
      ARHH30=RHH30SM/DIV1
      ARHH45=RHH45SM/DIV1
      AROV160=ROV160SM/DIV1
      AROV150=ROV150SM/DIV1
      AROV135=ROV135SM/DIV1
      AROH160=ROH160SM/DIV1
      AROH150=ROH150SM/DIV1
      AROH135=ROH135SM/DIV1
C
C=============================================================
C=====>send results to master and go back to start and wait for
C=====>instructions to either continue or quit
      MESSG=20
      CALL PVMFINITSEND(PVMRAW,INFO)
      CALL PVMFPACK(REAL8,AXLMAX,1,1,INFO)
      CALL PVMFPACK(REAL8,AEXT,1,1,INFO)
      CALL PVMFPACK(REAL8,ASVV20,1,1,INFO)
      CALL PVMFPACK(REAL8,ASVV30,1,1,INFO)
      CALL PVMFPACK(REAL8,ASVV45,1,1,INFO)
      CALL PVMFPACK(REAL8,ARVV20,1,1,INFO)
      CALL PVMFPACK(REAL8,ARVV30,1,1,INFO)
      CALL PVMFPACK(REAL8,ARVV45,1,1,INFO)
      CALL PVMFPACK(REAL8,ARHH20,1,1,INFO)
      CALL PVMFPACK(REAL8,ARHH30,1,1,INFO)
      CALL PVMFPACK(REAL8,ARHH45,1,1,INFO)
      CALL PVMFPACK(REAL8,AROV160,1,1,INFO)
      CALL PVMFPACK(REAL8,AROV150,1,1,INFO)
      CALL PVMFPACK(REAL8,AROV135,1,1,INFO)
      CALL PVMFPACK(REAL8,AROH160,1,1,INFO)
```

```
      CALL PVMFPACK(REAL8,AROH150,1,1,INFO)
      CALL PVMFPACK(REAL8,AROH135,1,1,INFO)
      CALL PVMFSEND(MASTERID,MESSG,INFO)
      IF (INFO .LT. 0) THEN
      PRINT *, 'ERROR SENDING TO MASTER'
      STOP
      ENDIF
      GOTO 1
C
C=============================================================
C
 1111 CONTINUE
      CALL PVMFEXIT(INFO)
      STOP
      END
C
C
C
C**********************************************************************
C*                                                                    *
C*                          JONES SUBROUTINE                          *
C*                          DOUBLE PRECISION                          *
C*                          CORRECTED/OPTIMIZED                       *
C*     DOES NOT REQUIRE THE IMSL RANDOM NUMBER GENERATOR              *
C*                                                                    *
C*                    AUGUST 94 / D. VENIZELOS & W. LOU               *
C*                                                                    *
C**********************************************************************
C* INPUT:                                                             *
C* NP:  NUMBER OF PARTICLES                                           *
C* ALPHA:PRIMARY PARTICLE SIZE PARAMETER                              *
C* REFINDX: COMPLEX REFRACTIVE INDEX  M=N-IK                  *
C* NSCA = # OF SCATTERING ANGLES (MAX OF 181)                 *
C* POL: POLARIZATION OF INCIDENT WAVE                                 *
C*     'U'= UNPOLARIZED                                               *
C*     'V'= VERTICAL                                                  *
C*     'H'= HORIZONTAL                                                *
C* EFF: INTERNAL FIELDS COUPLING                                      *
C*     'F'= FULL COUPLING                                     *
C*     'W'= WEAK COUPLING                                             *
C*     'N'= NO COUPLING                                               *
C* CHAIN: TYPE OF CHAINS                                              *
C*     'R'= RANDOM STRUCTURED CHAIN                                   *
C*     'C'= CLUSTER WITH 30 PARTICLES OR LESS                         *
C*     'S'= STRAIGHT CHAIN                                            *
C* ISEED: INTEGER NUMBER FOR SEEDING THE RANDOM NUMBER        *
C* GENERATOR SUBROUTINE                                               *
```

```
C* OUTPUT:                                                          *
C*  SCAVV(I): VERTICAL SCATTERING, VERTICAL INCIDENT BEAM    *
C*  SCAHV(I): HORIZONTAL SCATTERING, VERTICAL INCIDENT BEAM  *
C*  SCAHH(I): HORIZONTAL SCATT., HORIZONTAL INCIDENT BEAM    *
C*  SCAVH(I): VERTICAL SCATT., HORIZONTAL INCIDENT BEAM      *
C*  QSCA   : SCATTERING EFFICIENCY                           *
C*  QEXT   : EXTINCTION EFFICIENCY WITH VERTICAL INCIDENT BEAM*
C*  QSCAH : SCATT. EFFICIENCY WITH HORIZONTAL INCIDENT BEAM  *
C*  QEXTH : EXTINCTION EFF. WITH HORIZONTAL INCIDENT BEAM    *
C*  QABS   : ABSORPTION EFFICIENCY                           *
C*  XL     : AGGOMERATE MAXIMUM LENGTH                       *
C*  NOTE: ALL SUBROUTINES ARE INCLUDED IN JONESCL.           *
C*  MULTIPLY XL BY ALPHA TO GET AGGLOMERATE MAXIMUM LENGTH.*
C*************************************************************
C
C*************************************************************
C*                    OPTIMIZED CODE LATEST VERSION          *
C*                    CORRECTED / AUGUST 94 / Venizelos & Lou*
C*                                                           *
C****** 3SUB: A COLLECTION OF ALL SUBROUTINES ******************
C-------------------------------------------------------------
C---SUB: JONESCL ----------------------------------------------
C------ SCATTERING ANALYSIS FOR PARTICLES IN RAYLEIGH LIMIT-----
C------ REFERENCES: COORD, SOSYS1, SOSYS3.----------------------
C-------------------------------------------------------------
C
      SUBROUTINE JONESCL (NP,ALPHA,RFINDX,NSCA,QSCA,QEXT,QABS,ISEED)
C
C=============================================================
      INTEGER*4 MNP,NP,NS,NSCA,IP,IC,K,J,JJ,ISEED
      parameter (mnp=100)
      REAL*8 PI,PI2,TEMPEPSL,ALPHA,ALPHA4,ALPHA6,TEMPCEPL,TEMPCEPS
      REAL*8 QEXT,QSCA,QABS,QEXTH,QSCAH,QEI,QSI,QAI,QEIH,QSIH,PSI
      REAL*8 ESUMA,CHI,CHISIN,TEMP1,TEMP2,DXJ,DYJ,DZJ,DJ,DJ2,C
      REAL*8 RJ,RJ2,PSIJCOS,PSIJSIN,PSIJSIN2,PSIJCOS2,CHIJCOS
      REAL*8 CHIJSIN,ANGLECOS,ANGLESIN,ANGLE,COSB,WIPPI2,TWIC
      REAL*8 BJ0,BJ2,P20,P21,P22,RJA(MNP),DJA(MNP,MNP)
      REAL*8 X(mnp),Y(mnp),Z(mnp)
      REAL*8 x0(mnp),y0(mnp),z0(mnp)
      REAL*8 SCAHH(181), SCAVV(181), SCAHV(181), SCAVH(181)
      REAL*8 ZX(10),W(10)
      COMPLEX*16 RFINDX,EPSLON,E(3,mnp),ESUM,FSUM,THETA,PHI
      COMPLEX*16 CM, EH(3,mnp), ESUMH,FSUMH,THETAH,PHIH
      COMPLEX*16 E1J,E2J,E3J,EH1J,EH2J,EH3J
      COMPLEX*16 E1JJ,E2JJ,E3JJ,EH1JJ,EH2JJ,EH3JJ
      COMPLEX*16 EP1,EP2,EP3,EP4,EP5,EP6
      COMPLEX*16 EPH1,EPH2,EPH3,EPH4,EPH5,EPH6
      COMPLEX*16 CTEMP1,CTEMP2,CTEMP3,CHTEMP1,CHTEMP2,CHTEMP3
```

```
      CHARACTER POL*1,CHAIN*1
C
      COMMON/P2/POL
      COMMON/P3/CHAIN
      COMMON/JL/E, EH
      COMMON/L2/X,Y,Z
      common/L1/x0,y0,z0
      COMMON/J2S/SCAHH,SCAVV,SCAHV,SCAVH
C=======================================================================
C
C*****ABSCISSAS +-ZX AND WEIGHT FACTORS W FOR GAUSSIAN INTEGRATION
C*****WITH n=10
      DATA ZX/-.97390653,-.86506337,-.67940957,-.43339539,
     $ -.14887434,.14887434,.43339539,.67940957,.86506337,
     & .97390653/,
     & W/.06667134,.14945135,.2190864,.2692667,.29552422,
     &  .29552422,.2692667,.2190864,.14945135,.06667134/
C
      PI=DACOS(-1.0D0)
      PI2=PI*0.5
      EPSLON=RFINDX*RFINDX
      TEMPEPSL=DIMAG(EPSLON-1.0)
      ALPHA4=ALPHA*ALPHA*ALPHA*ALPHA
      ALPHA6=ALPHA4*ALPHA*ALPHA
      TEMPCEPL=CDABS(EPSLON-1.0)
      TEMPCEPS=TEMPCEPL*TEMPCEPL
      NS=NSCA
C
      IF (CHAIN .EQ. 'R') THEN
       CALL RANDOM(NP,ISEED)
      ELSE IF (CHAIN .EQ. 'S') THEN
       CALL STRAIT(NP)
      ELSE IF (CHAIN .EQ. 'C') THEN
       CALL CLUSTR(NP)
      ELSE
       PRINT *, 'NO SUCH CHOICE OF CHAIN'
       STOP
      ENDIF
C
      CALL COORD(NP,ALPHA,0.0D1,0.0D1)
      CALL SOSYS1(NP,ALPHA,EPSLON)
C
      QEXT=0.
      QSCA=0.
      QABS=0.
```

```
      QEXTH=0.
      QSCAH=0.
C
      DO 5 J=1,NP
      RJA(J)=DSQRT(X(J)*X(J)+Y(J)*Y(J)+Z(J)*Z(J))
        DO 5 JJ=1,NP
        DXJ=X(J)-X(JJ)
        DYJ=Y(J)-Y(JJ)
        DZJ=Z(J)-Z(JJ)
        DJA(J,JJ)=DSQRT(DXJ*DXJ+DYJ*DYJ+DZJ*DZJ)
 5    CONTINUE
C
      DO 10 K=1,NS
      SCAHH(K)=0.
      SCAHV(K)=0.
      SCAVV(K)=0.
 10   SCAVH(K)=0.
C
      DO 150 IP=1,10
        QEI=0.
        QSI=0.
        QAI=0.
        QEIH=0.
        QSIH=0.
        PSI=(ZX(IP)+1.)*PI
        WIPPI2=W(IP)*PI2
C
        DO 140 IC=1,10
            ESUMA=0.0
            ESUM=(0.,0.)
            FSUM=(0.,0.)
            ESUMH=(0.,0.)
            FSUMH=(0.,0.)
            CHI=(ZX(IC)+1.)*PI2
            CHISIN=DSIN(CHI)
            CALL COORD(NP,ALPHA,CHI,PSI)
            CALL SOSYS3(NP,EPSLON)
            DO 80 J=1,NP
            TEMP1=DCOS(Z(J))
            TEMP2=-DSIN(Z(J))
            CM=DCMPLX(TEMP1,TEMP2)
C
            E1J=E(1,J)
            E2J=E(2,J)
            E3J=E(3,J)
```

```
            EH1J=EH(1,J)
            EH2J=EH(2,J)
            EH3J=EH(3,J)
            CTEMP1=DCONJG(E1J)
            CTEMP2=DCONJG(E2J)
            CTEMP3=DCONJG(E3J)
            CHTEMP1=DCONJG(EH1J)
            CHTEMP2=DCONJG(EH2J)
            CHTEMP3=DCONJG(EH3J)
C
            ESUM=ESUM+ E1J*CM
            ESUMH=ESUMH+EH2J*CM
            ESUMA=ESUMA+E1J*CTEMP1+E2J*CTEMP2+E3J*CTEMP3
C
            DO 80 JJ=1,NP
C
            E1JJ=E(1,JJ)
            E2JJ=E(2,JJ)
            E3JJ=E(3,JJ)
            EH1JJ=EH(1,JJ)
            EH2JJ=EH(2,JJ)
            EH3JJ=EH(3,JJ)
C
            EP1=CTEMP1*E1JJ
            EP2=CTEMP2*E2JJ
            EP3=CTEMP3*E3JJ
            EPH1=CHTEMP1*EH1JJ
            EPH2=CHTEMP2*EH2JJ
            EPH3=CHTEMP3*EH3JJ
            IF(JJ .NE. J) GOTO 60
            FSUM=FSUM+4.*(EP1+EP2+EP3)
            FSUMH=FSUMH+4.*(EPH1+EPH2+EPH3)
            GOTO 80
60      DXJ=X(J)-X(JJ)
        DYJ=Y(J)-Y(JJ)
        DZJ=Z(J)-Z(JJ)
        DJ=DJA(J,JJ)
        DJ2=DSQRT(DXJ*DXJ+DYJ*DYJ)
        IF(DJ2.LE.0.1E-30)THEN
        PSIJCOS=1.0
        PSIJSIN=0.0
        PSIJSIN2=0.0
        PSIJCOS2=1.0
        ELSE
        PSIJCOS=DXJ/DJ2
```

```
      PSIJSIN=DYJ/DJ2
      PSIJSIN2=2.0*PSIJCOS*PSIJSIN
      PSIJCOS2=PSIJCOS*PSIJCOS-PSIJSIN*PSIJSIN
      END IF
      CHIJCOS=DZJ/DJ
      CHIJSIN=DJ2/DJ
      BJ0=DSIN(DJ)/DJ
      BJ2=((3./DJ/DJ-1.)*DSIN(DJ)-3./DJ*DCOS(DJ))/DJ
      P20=0.5*(3.*(CHIJCOS*CHIJCOS)-1.)
      P21=-3.0*CHIJCOS*CHIJSIN
      P22=3.0*CHIJSIN*CHIJSIN
C
      EP4=CTEMP1*E2JJ+E1JJ*CTEMP2
      EP5=CTEMP2*E3JJ+E2JJ*CTEMP3
      EP6=CTEMP1*E3JJ+E1JJ*CTEMP3
C
      FSUM=FSUM+4.*BJ0*(EP1+EP2+EP3)-BJ2*(2.*P20*
     & (EP1+EP2-2.*EP3)-P22*(PSIJCOS2*(EP1-EP2)+
     & PSIJSIN2*EP4)+2.*P21*(PSIJCOS*EP6+PSIJSIN*EP5))
C
      EPH4=CHTEMP1*EH2JJ+EH1JJ*CHTEMP2
      EPH5=CHTEMP2*EH3JJ+EH2JJ*CHTEMP3
      EPH6=CHTEMP1*EH3JJ+EH1JJ*CHTEMP3
C
      FSUMH=FSUMH+4.*BJ0*(EPH1+EPH2+EPH3)-BJ2*(2.*P20*
     & (EPH1+EPH2-2.*EPH3)-P22*(PSIJCOS2*(EPH1-EPH2)+
     & PSIJSIN2*EPH4)+2.*P21*(PSIJCOS*EPH6+PSIJSIN*EPH5))
C
 80   CONTINUE
      QSI=QSI+W(IC)*CHISIN*DREAL(FSUM)
      QSIH=QSIH+W(IC)*CHISIN*DREAL(FSUMH)
      IF(TEMPEPSL .EQ. 0.) THEN
        QEI=QSI
        QEIH=QSIH
      ELSE
        QEI=QEI+W(IC)*CHISIN*DIMAG((EPSLON-1.)*ESUM)
        QAI=QAI+W(IC)*CHISIN*TEMPEPSL*ESUMA
        QEIH=QEIH+W(IC)*CHISIN*DIMAG((EPSLON-1.)*ESUMH)
      ENDIF
 100  DO 135 K=1,NS
      ANGLE=PI/DFLOAT(NS-1)*DFLOAT(K-1)
      ANGLECOS=DCOS(ANGLE)
      ANGLESIN=DSIN(ANGLE)
C
      EP1=DCMPLX(0.0D1,0.0D1)
```

```
      EP2=EP1
      EP3=EP1
      EPH1=EP1
      EPH2=EP1
      EPH3=EP1
C
      DO 130 J=1,NP
      RJ=RJA(J)
      RJ2=DSQRT(X(J)*X(J)+Y(J)*Y(J))
      IF(RJ2.LE.0.1E-30)THEN
      PSIJCOS=1.0
      PSIJSIN=0.0
      PSIJSIN2=0.0
      PSIJCOS2=1.0
      ELSE
      PSIJCOS=X(J)/RJ2
      PSIJSIN=Y(J)/RJ2
      PSIJSIN2=2.0*PSIJCOS*PSIJSIN
      PSIJCOS2=PSIJCOS*PSIJCOS-PSIJSIN*PSIJSIN
      END IF
      IF(RJ.LE.0.1E-30)THEN
      CHIJCOS=1.0
      CHIJSIN=0.0
      ELSE
      CHIJCOS=Z(J)/RJ
      CHIJSIN=RJ2/RJ
      END IF
      COSB=CHIJCOS*ANGLECOS + CHIJSIN*ANGLESIN*PSIJSIN
      RJ=RJ*COSB
      TEMP1=DCOS(RJ)
      TEMP2=-DSIN(RJ)
      EP6=DCMPLX(TEMP1,TEMP2)
      EPH6=EP6
      EP1=EP1+EP6*E(1,J)
      EP2=EP2+EP6*E(2,J)
      EP3=EP3+EP6*E(3,J)
      EPH1=EPH1+EPH6*EH(1,J)
      EPH2=EPH2+EPH6*EH(2,J)
130   EPH3=EPH3+EPH6*EH(3,J)
      THETA=ANGLECOS*EP2-ANGLESIN*EP3
      PHI=EP1
      TWIC=W(IC)*CHISIN*WIPPI2
      SCAHV(K)=SCAHV(K)+TWIC*THETA*DCONJG(THETA)
      SCAVV(K)=SCAVV(K)+TWIC*PHI*DCONJG(PHI)
      THETAH=ANGLECOS*EPH2-ANGLESIN*EPH3
```

```
      PHIH=EPH1
      SCAHH(K)=SCAHH(K)+TWIC*THETAH*DCONJG(THETAH)
      SCAVH(K)=SCAVH(K)+TWIC*PHIH*DCONJG(PHIH)
 135  CONTINUE
 140  CONTINUE
      QEXT=QEXT+WIPPI2*QEI
      QSCA=QSCA+WIPPI2*QSI
      QABS=QABS+WIPPI2*QAI
      QEXTH=QEXTH+WIPPI2*QEIH
      QSCAH=QSCAH+WIPPI2*QSIH
 150  CONTINUE
      QEXT= ALPHA/(3.*NP)*QEXT
      QABS= ALPHA/(3.*NP)*QABS
      QSCA= 0.5*ALPHA4/(27.*NP)*TEMPCEPS*QSCA
      QEXTH= ALPHA/(3.*NP)*QEXTH
      QSCAH= 0.5*ALPHA4/(27.*NP)*TEMPCEPS*QSCAH
C  INTENSITY FUNCTION CONTAINS ALPHA**6
 160  C=TEMPCEPS/9.*ALPHA6
C
      DO 170 K=1,NS
      SCAHH(K)=0.25*C*SCAHH(K)
      SCAVH(K)=0.25*C*SCAVH(K)
      SCAHV(K)=0.25*C*SCAHV(K)
 170  SCAVV(K)=0.25*C*SCAVV(K)
      RETURN
      END
C
C-------------------------------------------------------------------------
C---SUB: TRANS MAY BE USED TO TRANSFORM (X,Y,Z) INTO----------
C-------(X',Y',Z')-NEW COORDINATES AFTER ROTATING THE AXES----
C--------J.J. TUMA,ENGINEERING MATH HANDBOOK, P.61------------
C--------WJ=PSI, FIX Z-AXIS & ROTATE X-AXIS----------------------
C--------WK=CHI, FIX Y-AXIS & ROTATE Z-AXIS----------------------
C-------------------------------------------------------------------------
      SUBROUTINE TRANS(NP,CHI,PSI)
C
      INTEGER*4 MNP,I,NP
      parameter (mnp=100)
      REAL*8 CP,SP,CC,SC,CHI,PSI
      REAL*8 C(3,3),P(3)
      REAL*8 XO(mnp),YO(mnp),ZO(mnp)
C
      COMMON/L1/XO,YO,ZO
C
      cp=dcos(psi)
```

```
      sp=dsin(psi)
      cc=dcos(chi)
      sc=dsin(chi)
      C(1,1)=CP*CC
      C(1,2)=SP*CC
      C(1,3)=-SC
      C(2,1)=-SP
      C(2,2)=CP
      C(2,3)=0.0
      C(3,1)=CP*SC
      C(3,2)=SP*SC
      C(3,3)=CC
      DO 10 I=1,NP
      P(1)=XO(I)
      P(2)=YO(I)
      P(3)=ZO(I)
      XO(I)=0.
      YO(I)=0.
      ZO(I)=0.
C
      XO(I)=XO(I)+C(1,1)*P(1)
      XO(I)=XO(I)+C(1,2)*P(2)
      XO(I)=XO(I)+C(1,3)*P(3)
      YO(I)=YO(I)+C(2,1)*P(1)
      YO(I)=YO(I)+C(2,2)*P(2)
      YO(I)=YO(I)+C(2,3)*P(3)
      ZO(I)=ZO(I)+C(3,1)*P(1)
      ZO(I)=ZO(I)+C(3,2)*P(2)
      ZO(I)=ZO(I)+C(3,3)*P(3)
10    CONTINUE
      RETURN
      END
C-------------------------------------------------------------------------------
C---SUB: COORD TRANSFORMS (X',Y',Z') INTO MEASURING COORD.(X,Y,Z)--
C----- ROTATIONS:  WJ=PSI, FIX Z-AXIS AND ROTATE X-AXIS AND----------
C----------------WK=CHI, FIX Y-AXIS AND ROTATE Z-AXIS--------------------
C-------------------------------------------------------------------------------
      SUBROUTINE COORD(NP,ALPHA,CHI,PSI)
C
      INTEGER*4 MNP,NP,I
      parameter (mnp=100)
      REAL*8 CPSI,SPSI,CCHI,SCHI,ALPHA,CHI,PSI
      REAL*8 C(3,3),P(3)
      REAL*8 XO(mnp),YO(mnp),ZO(mnp)
      REAL*8 X(mnp),Y(mnp),Z(mnp)
```

```
C
      COMMON/L1/XO,YO,ZO
      COMMON/L2/X,Y,Z
      common/trans1/c
C
      cpsi=dcos(psi)
      spsi=dsin(psi)
      cchi=dcos(chi)
      schi=dsin(chi)
      C(1,1)=CPSI*CCHI
      C(1,2)=-SPSI
      C(1,3)=CPSI*SCHI
      C(2,1)=SPSi*CCHI
      C(2,2)=CPSI
      C(2,3)=SPSI*SCHI
      C(3,1)=-SCHI
      C(3,2)=0.
      C(3,3)=CCHI
      DO 10 I=1,NP
      P(1)=XO(I)
      P(2)=YO(I)
      P(3)=ZO(I)
      X(I)=0.
      Y(I)=0.
      Z(I)=0.
      X(I)=X(I)+2.*ALPHA*C(1,1)*P(1)
      X(I)=X(I)+2.*ALPHA*C(1,2)*P(2)
      X(I)=X(I)+2.*ALPHA*C(1,3)*P(3)
      Y(I)=Y(I)+2.*ALPHA*C(2,1)*P(1)
      Y(I)=Y(I)+2.*ALPHA*C(2,2)*P(2)
      Y(I)=Y(I)+2.*ALPHA*C(2,3)*P(3)
      Z(I)=Z(I)+2.*ALPHA*C(3,1)*P(1)
      Z(I)=Z(I)+2.*ALPHA*C(3,2)*P(2)
      Z(I)=Z(I)+2.*ALPHA*C(3,3)*P(3)
10    CONTINUE
      RETURN
      END

C-----------------------------------------------------------------
C---SUB: SOSYS1 establishes the matrix A for the internal field------
C--------in the structural coordinate system (x',y',z')-----------------
C-----------------------------------------------------------------
      SUBROUTINE SOSYS1(NP,ALPHA,EPSLON)
C
      INTEGER*4 MNP,MN3,NRANK,NROW0,NCOL0,NROWE,NROW,NCOL
```

```
      INTEGER*4 IR,I,J,NP,NC,NCOLDG
      parameter (mnp=100, mn3=mnp*3)
      REAL*8 ALPHA,ALPHA2,ALPHA3,D1,DX,DY,DZ,DJ,DJ2
      REAL*8 PSICOS,PSISIN,CHISIN,CHICOS,DJK
      REAL*8 X0(mnp),Y0(mnp),Z0(mnp)
      COMPLEX*16 EPSLON,A(mn3,mn3), T(3,3),C,D
      COMPLEX*16 EPS1,EPS2,CTEMP1,CTEMP2
      CHARACTER EFF*1,POL*1
C
      COMMON/JLA/A
      COMMON/L1/X0,Y0,Z0
      COMMON/C2/EFF
      COMMON/P2/POL
C
      PI=DACOS(-1.0D0)
      NRANK=3*NP
      ALPHA2=ALPHA*ALPHA
      ALPHA3=ALPHA*ALPHA*ALPHA
      EPS1=EPSLON-1.0
      EPS2=EPSLON+2.0
C
      IF (EFF.EQ.'F') THEN
      CTEMP1=DCMPLX(0.0D1,-1.0D0)
      C=ALPHA3*EPS1/(3.0*EPS2) * CTEMP1
      ELSE IF (EFF.EQ.'W') THEN
      CTEMP1=DCMPLX(0.0D1,1.0D0)
      C=ALPHA3*EPS1/(3.*EPS2) * CTEMP1
      ENDIF
C
      D1=2.0*ALPHA/3.0
      CTEMP1=DCMPLX(1.0D0,0.0D1)
      CTEMP2=DCMPLX(1.0D0,D1)
      D=CTEMP1-ALPHA2*EPS1/EPS2 * CTEMP2
      IF (EFF.EQ.'N') GO TO 55
      DO 10 I=1,NP
      NROW0=1+3*(I-1)
      NROWE=3*I
      DO 20 NROW=NROW0,NROWE
      DO 20 NCOL=NROW,NROWE
      A(NROW,NCOL)=(0.0,0.0)
      IF (NCOL.EQ.NROW)Then
            A(NROW,NCOL)=D
      endif
20    continue
      IF(I .EQ. NP) GOTO 10
```

```
      IR=I+1
      DO 30 J=IR,NP
        DX=X0(J)-X0(I)
        DY=Y0(J)-Y0(I)
        DZ=Z0(J)-Z0(I)
      DJ=DSQRT(DX*DX+DY*DY+DZ*DZ)
      DJ2=DSQRT(DX*DX+DY*DY)
      CHICOS=DZ/DJ
      CHISIN=DJ2/DJ
C
      IF (DJ2 .LE. 0.1E-30) THEN
      PSICOS=1.0
      PSISIN=0.0
      ELSE
      PSICOS=DX/DJ2
      PSISIN=DY/DJ2
      ENDIF
C
      DJK=DJ*2.0*ALPHA
      CALL TMATRX(DJK,CHICOS,CHISIN,PSICOS,PSISIN,T)
      NCOL0=3*(J-1)
      DO 40 NC=1,3
      DO 40 NROW=NROW0,NROWE
 40   A(NROW,NCOL0+NC)=C*T(NROW-NROW0+1,NC)
 30   CONTINUE
 10   CONTINUE
      DO 50 NROW=2,NRANK
      NCOLDG=NROW-1
      DO 50 NCOL=1,NCOLDG
 50   A(NROW,NCOL)=A(NCOL,NROW)
      CALL CBDECP(A,NRANK)
 55   continue
      RETURN
      END
C-------------------------------------------------------------------------------
C---SUB: SOSYS3 SOLVES THE INTERNAL FIELD IN THE (X',Y',Z') SYSTEM,--
C-----THEN TRANSFORMS IT INTO THE MEASURING COORDINATE----------
C-------------------------------------------------------------------------------
      SUBROUTINE SOSYS3(NP,EPSLON)
C
      INTEGER*4 MNP,MN3,NRANK,I,NP,NROW0,I1,I2,I3
      parameter (mnp=100, mn3=mnp*3)
      REAL*8 TEMP1,TEMP2
      real*8 T(3,3)
      REAL*8 X(mnp),Y(mnp),Z(mnp)
```

```
      COMPLEX*16 EPSLON,A(mn3,mn3),B(mn3),BH(mn3),C,D
      COMPLEX*16 ex, ey, ez, exH, EYH, EZH
      CHARACTER EFF*1
C
      COMMON/JL/B,BH
      COMMON/JLA/A
      COMMON/L2/X,Y,Z
      COMMON/C2/EFF
      common/trans1/T
C
      NRANK=3*NP
      DO 64 I=1,NP
         TEMP1=DCOS(Z(I))
         TEMP2=DSIN(Z(I))
         C=DCMPLX(TEMP1,TEMP2)
         NROW0=3*(I-1)
         BH(NROW0+1)=C*T(2,1)
         BH(NROW0+2)=C*T(2,2)
         BH(NROW0+3)=C*T(2,3)
         B(NROW0+1)=C*T(1,1)
         B(NROW0+2)=C*T(1,2)
      B(NROW0+3)=C*T(1,3)
 64   CONTINUE
      D=3./(EPSLON+2.)
C
      IF (EFF.EQ.'F') THEN
        DO 70 I=1,NRANK
        B(I)=B(I)*D
 70   BH(I)=BH(I)*D
        CALL CBSOLX(A,B,NRANK)
        CALL CBSOLX(A,BH,NRANK)
      ELSE IF(EFF.EQ.'W')THEN
        CALL MULT(NRANK)
        DO 76 I=1,NRANK
        B(I)=B(I)*D
 76   BH(I)=BH(I)*D
      ELSE IF(EFF.EQ.'N')THEN
        DO 78 I=1,NRANK
        B(I)=B(I)*D
 78   BH(I)=BH(I)*D
      ELSE
      STOP
      END IF
C
      DO 100 I=1,NP
```

```
      I1=3*(I-1)+1
      I2=I1+1
      I3=I2+1
      EX=B(I1)*T(1,1)+B(I2)*T(1,2)+B(I3)*T(1,3)
      EY=B(I1)*T(2,1)+B(I2)*T(2,2)+B(I3)*T(2,3)
      EZ=B(I1)*T(3,1)+B(I2)*T(3,2)+B(I3)*T(3,3)
      EXH=BH(I1)*T(1,1)+BH(I2)*T(1,2)+BH(I3)*T(1,3)
      EYH=BH(I1)*T(2,1)+BH(I2)*T(2,2)+BH(I3)*T(2,3)
      EZH=BH(I1)*T(3,1)+BH(I2)*T(3,2)+BH(I3)*T(3,3)
      B(I1)=EX
      B(I2)=EY
      B(I3)=EZ
      BH(I1)=EXH
      BH(I2)=EYH
      BH(I3)=EZH
100   CONTINUE
      RETURN
      END
C-------------------------------------------------------------------------------
C---SUB: MULT ----------------------------------------------------------------
C--------SOLVE THE INTERNAL FIELDS WHEN WEAK COUPLING IS CHOSEN---
C-------------------------------------------------------------------------------
      SUBROUTINE MULT(N)
C
      INTEGER*4 MNP,MN3,I,J,N
      parameter (mnp=100, mn3=mnp*3)
      COMPLEX*16 A(mn3,mn3),B(mn3),B1(mn3),BH(mn3)
C
      COMMON/JL/B,BH
      COMMON/JLA/A
C
      DO 10 I=1,N
        B1(I)=DCMPLX(0.0D1,0.0D1)
        DO 10 J=1,N
10    B1(I)=B1(I)+A(J,I)*B(J)
      DO 15 I=1,N
        B(I)=DCMPLX(0.0D1,0.0D1)
        DO 15 J=1,N
15    B(I)=B(I)+A(J,I)*BH(J)
      DO 20 I=1,N
        BH(I)=B(I)
20    B(I)=B1(I)
      RETURN
      END
C-------------------------------------------------------------------
```

```
C---SUB: TMATRX ----------------------------------------------
C--------CALCULATES MATRIX T(L,J)-----------------------------
C-----------------------------------------------------------------
      SUBROUTINE TMATRX(Z,CHICOS,CHISIN,PSICOS,PSISIN,T)
C
      REAL*8 S,C,Z1,Z2,Z,CC,SC,CP,SP,CHICOS,CHISIN,PSICOS
      REAL*8 PSISIN
      COMPLEX*16 T(3,3),H10,H12
C
      S=DSIN(Z)
      C=DCOS(Z)
      H10=DCMPLX(S,-C)/Z
      Z1=(3./Z/Z-1.)*S-3.*C/Z
      Z2=(1.-3./Z/Z)*C-3.*S/Z
      H12=DCMPLX(Z1,Z2)/Z
      CC=CHICOS
      SC=CHISIN
      CP=PSICOS
      SP=PSISIN
      t(1,1)=2.0*h10-h12*(1-3.0*sc*sc*cp*cp)
      t(1,2)=h12*3.0*sc*sc*sp*cp
      t(1,3)=h12*3.0*sc*cc*cp
      t(2,1)=t(1,2)
      t(2,2)=2.0*h10-h12*(1.0-3.0*sc*sc*sp*sp)
      t(2,3)=h12*3.0*sc*cc*sp
      t(3,1)=t(1,3)
      t(3,2)=t(2,3)
      t(3,3)=2.0*H10-h12*(1-3.0*cc*cc)
      RETURN
      END
C-----------------------------------------------------------------
C---S U B: CBDECP ----------------------------------------------
C----------CHOLESKY DECOMPOSITION :A=(L)(D)(U)---------
C-----------------------------------------------------------------
      SUBROUTINE CBDECP(A,N)
C
      INTEGER*4 MNP,MN3,I,I1,J,J1,K,K1,N
      parameter (mnp=100, mn3=mnp*3)
      COMPLEX*16  A(mn3,mn3), AIJ, AJJ
C
      DO 40 J=1,N
            J1=J-1
            IF (J1.LT.2) GO TO 25
            DO 20 I=2,J1
            I1=I-1
```

```
            AIJ=dcmplx(0.0D1,0.0D1)
            DO 10 K=1,I1
 10                AIJ=AIJ+A(K,I)*A(K,J)*A(K,K)
                   A(I,J)=(A(I,J)-AIJ)/A(I,I)
 20                A(J,I)=A(I,J)
 25                AJJ= dcmplx(0.0D1,0.0D1)
                   IF (J.EQ.1) GO TO 35
            DO  30 K1=1,J1
 30         AJJ=AJJ+ A(K1,J)*A(K1,J)*A(K1,K1)
            A(J,J)=A(J,J)-AJJ
 35         IF(A(J,J).EQ.0.) GO TO 50
 40    CONTINUE
       RETURN
 50    PRINT 55
 55    FORMAT(/  'A(J,J)  IS ZERO  PROGRAM STOP.')
       RETURN
       END
C-------------------------------------------------------------------
C---SUB: CBSOLX ---------------------------------------------
C--------FORWARD SUBSTITUTION-------------------------------
C--------(L)(D)(U)(X)=(B) WITH (D) CANNOT BE ZERO-----------
C--------LET (L)(Z)=(B), AND (D)(U)(X)=(Z)-----------------
C-------------------------------------------------------------------
       SUBROUTINE CBSOLX(A,B,N)
C
       INTEGER*4 MNP,MN3,I,N,I1,K,J
       parameter (mnp=100, mn3=mnp*3)
       COMPLEX*16  A(mn3,mn3),B(N)
C
       DO 70 I=2,N
       I1=I-1
       DO 60 K=1,I1
 60    B(I)=B(I)-A(K,I)*B(K)
 70    CONTINUE
C    DIVIDED BY DIAGONAL
C    (D)(Y)=(Z),  WHERE (Y) TO BE FOUND
       DO 72 I=1,N
 72    B(I)=B(I)/A(I,I)
C      BACKWARD SUBSTITUTION
C      (U)(X),   WHERE (X) IS FINAL SOLUTION
       DO 80 I = N-1,1,-1
       DO 75 J=I+1,N
 75    B(I)=B(I)-A(I,J)*B(J)
 80    CONTINUE
       RETURN
```

```
      END

C-----------------------------------------------------------------------
C---SUB: RANCOO GENERATES A RANDOM ORIENTATION---------
C-----------------------------------------------------------------------
      SUBROUTINE RANCOO(X,Y,Z)
C
      INTEGER*4 ISEED
      REAL*8 R(2),THETASIN,THETACOS,PHISIN,PHICOS
      REAL*8 X,Y,Z,PI,THETA,PHI,TEMP
C
      COMMON/VRN/ISEED
C
      PI=DACOS(-1.0D0)
      CALL VRAND(ISEED,TEMP,1,1)
      R(1)=TEMP
      R(1)=PI*R(1)
      R(1)=0.0D1+R(1)
      CALL VRAND(ISEED,TEMP,1,1)
      R(2)=TEMP
      R(2)=PI*R(2)
      R(2)=0.0D1+R(2)
      THETA=R(1)
      PHI=R(2)*2.
      THETASIN=DSIN(THETA)
      THETACOS=DCOS(THETA)
      PHISIN=DSIN(PHI)
      PHICOS=DCOS(PHI)
      X=THETASIN*PHICOS
      Y=THETASIN*PHISIN
      Z=THETACOS
      RETURN
      END
C-----------------------------------------------------------------------
C---SUB: RANDOM CREATES COORDINATES FOR EACH PARTICLE---
C--------REFERENCES: RANCOO, DSCAL, DADD, TRANS----------
C-----------------------------------------------------------------------
      SUBROUTINE RANDOM(NT,IS)
C
      INTEGER*4 NPCH(4),NBA(4),MNP,ISEED,IS
      INTEGER*4 NT,NP,NB,NACC,RN,I,L,N,NREMAIN,NCHAIN,ICK
      parameter (mnp=100)
      REAL*8 XX,YY,ZZ,XC,YC,ZC,XL,TEMP,X1,Y1,Z1,DI,DIST,D2
      REAL*8 PI,CHI,PSI,TEMP1,TEMP2,TEMP3
      REAL*8 X(mnp),Y(mnp),Z(mnp)
```

```
C
      COMMON/L1/X,Y,Z
      COMMON/RAN/XL
      COMMON/VRN/ISEED
C
      ISEED=IS
      PI=DACOS(-1.0D0)
C   NPCH=NUMBER OF PARTICLES/CHAIN
C   NBA=PARTICLE @ WHICH NEW CHAIN STARTS
      XX=0.
      YY=0.
      ZZ=0.
      XC=0.
      YC=0.
      ZC=0.
      XL=0.
      NP=0
      NACC=1
      NB=1
      X(1)=0.
      Y(1)=0.
      Z(1)=0.
      IF(NT .EQ. 1) RETURN
      CALL VRAND(ISEED,TEMP,1,1)
      TEMP=DFLOAT(NT-2)*TEMP
      TEMP=3.0D0+TEMP
      NPCH(1)=INT(TEMP)
      NREMAIN=NT-NPCH(1)
      IF(NREMAIN .EQ. 0) NCHAIN=1
      IF(NREMAIN .EQ. 0) GOTO 16
      IF(NREMAIN .LE. 4) THEN
       NPCH(2)=NREMAIN
       NCHAIN=2
       GOTO 15
      ELSE
       CALL VRAND(ISEED,TEMP,1,1)
       TEMP=DFLOAT(NREMAIN-2)*TEMP
       TEMP=3.0D0+TEMP
       NPCH(2)=INT(TEMP)
       NREMAIN=NREMAIN-NPCH(2)
       IF(NREMAIN .EQ. 0) NCHAIN=2
       IF(NREMAIN .EQ. 0) GOTO 15
       IF(NREMAIN .LE. 4) THEN
        NPCH(3)=NREMAIN
        NCHAIN=3
```

```
        GOTO 15
       ELSE
       CALL VRAND(ISEED,TEMP,1,1)
       TEMP=DFLOAT(NREMAIN-2)*TEMP
       TEMP=3.0D0+TEMP
       NPCH(3)=INT(TEMP)
       NPCH(4)=NREMAIN-NPCH(3)
       IF(NPCH(4) .EQ. 0) NCHAIN=3
       IF(NPCH(4) .NE. 0) NCHAIN=4
       ENDIF
      ENDIF
15    DO 14 I=1,NCHAIN-1
      CALL VRAND(ISEED,TEMP,1,1)
      TEMP=DFLOAT(NPCH(I)-2)*TEMP
      TEMP=2.0D0+TEMP
14    NBA(I)=INT(TEMP)
16    DO 20 L=1,NCHAIN
      ICK=1
      NP=NP+NPCH(L)
10    CALL RANCOO(X1,Y1,Z1)
      IF(ICK .EQ.1) THEN
      X1=X1+X(NB)
      Y1=Y1+Y(NB)
      Z1=Z1+Z(NB)
      ELSE
      X1=X1+X(NACC)
      Y1=Y1+Y(NACC)
      Z1=Z1+Z(NACC)
      ENDIF
      DO 25 N=1,NACC
      TEMP1=(X1-X(N))*(X1-X(N))
      TEMP2=(Y1-Y(N))*(Y1-Y(N))
      TEMP3=(Z1-Z(N))*(Z1-Z(N))
      DI=TEMP1+TEMP2+TEMP3
      IF((1.-DI) .GT. 1.E-5) GOTO 10
      DIST=DSQRT(DI)
      IF(DIST .GT. XL) XL=DIST
25    CONTINUE
      ICK=2
      NACC=NACC+1
      X(NACC)=X1
      Y(NACC)=Y1
      Z(NACC)=Z1
      IF(NACC .LT. NP) GOTO 10
20    NB=NP+NBA(L)-NPCH(L)
```

```
      DO 110 I=2,NP
      D2=DSQRT(X(I)*X(I)+Y(I)*Y(I)+Z(I)*Z(I))
      XC=XC+X(I)
      YC=YC+Y(I)
      ZC=ZC+Z(I)
      XX=XX+X(I)/D2
      YY=YY+Y(I)/D2
110   ZZ=ZZ+Z(I)/D2
      RN=NP-1
      XC=XC/NP
      YC=YC/NP
      ZC=ZC/NP
      XX=XX/RN
      YY=YY/RN
      ZZ=ZZ/RN
      CHI=DACOS(ZZ)
C
      IF(XX .GT. 0.) THEN
        PSI=DATAN(YY/XX)
      ELSE IF(XX .LT. 0.) THEN
        PSI=PSI+PI
      ELSE
         IF(YY .GT. 0.) THEN
              PSI=0.5*PI
         ELSE IF(YY .LT. 0.) THEN
              PSI=-0.5*PI
         ELSE
              PSI=0.
         ENDIF
      ENDIF
C
      DO 120 I=1,NP
      X(I)=X(I)-XC
      Y(I)=Y(I)-YC
120   Z(I)=Z(I)-ZC
      CALL TRANS(NP,CHI,PSI)
      RETURN
      END
C-------------------------------------------------------------------
C---SUB: STRAIT ---------------------------------------------------
C--------GENERATE STRAIGHT CHAIN GEOMETRY-----------
C-------------------------------------------------------------------
      SUBROUTINE STRAIT(NT)
      INTEGER*4 NT,NT2,I,MNP
      parameter (mnp=100)
```

```
      REAL*8 XL
      REAL*8 X(mnp),Y(mnp),Z(mnp)
C
      COMMON/L1/X,Y,Z
      COMMON/RAN/XL
C
      nt2=nt/2
      if(nt-2*nt2 .eq. 0)then
            do 140 i=1,nt2
            x(i)=0.0
            y(i)=0.0
            z(i)=-0.5+(i-nt2)*1.0
            x(i+nt2)=0.0
            y(i+nt2)=0.0
            z(i+nt2)=0.5+(i-1)*1.0
140     continue
      else
            do 142 i=1, nt2
            x(i)=0.0
            y(i)=0.0
            z(i)=-1.0+(i-nt2)*1.0
            x(i+nt2+1)=0.0
            y(i+nt2+1)=0.0
            z(i+nt2+1)=1.0+(i-1)*1.0
142     continue
            x(nt2+1)=0.0
            y(nt2+1)=0.0
            z(nt2+1)=0.0
      end if
      XL=NT
      RETURN
      END

C-------------------------------------------------------------------------
C---SUB: CLUSTR ---------------------------------------------------------
C--------GENERATES COORDINATES FOR CLUSTER WITH LESS THAN---
C--------30 PARTICLES-----------------------------------------------------
C-------------------------------------------------------------------------
      SUBROUTINE CLUSTR(NT)
      INTEGER*4 MNP,NT,I,J,RN
      parameter (mnp=100)
      REAL*8 DI,XL,XC,YC,ZC,XX,YY,ZZ,D2,CHI,PSI,PI
      REAL*8 TEMP1,TEMP2,TEMP3
      REAL*8 X(mnp),Y(mnp),Z(mnp)
C
```

```
      COMMON/L1/X,Y,Z
      COMMON/RAN/XL
C
      IF(NT.GT.30)THEN
       WRITE(6,*)'NUMBER OF PARTICLES IN THE CLUSTER EXCCEDED'
       STOP
      END IF
      PI=DACOS(-1.0D0)
      XX=0.
      YY=0.
      ZZ=0.
      XC=0.
      YC=0.
      ZC=0.
      XL=0.
      X(1)= 0.
      Y(1)= 0.
      Z(1)= 0.
      IF(NT .EQ. 1) RETURN
      IF(NT .LE. 12) THEN
      X(2)= 1.
      Y(2)= 0.
      Z(2)= 0.
      X(3)=  .5
      Y(3)= 0.86603
      Z(3)= 0.
      X(4)= 0.5
      Y(4)=  .28868
      Z(4)= 0.81650
      X(5)= 0.5
      Y(5)=  .28868
      Z(5)= -.81650
      X(6)= 1.33333
      Y(6)= 0.76980
      Z(6)=  .54433
      X(7)= -.33333
      Y(7)= 0.76980
      Z(7)=  .54433
      X(8)= -.33333
      Y(8)=  .76980
      Z(8)= -.54433
      X(9)= 1.33333
      Y(9)=  .76980
      Z(9)= -.54433
      X(10)= .44444
```

```
Y(10)=1.28301
Z(10)=-.90722
X(11)=1.18421
Y(11)=1.59531
Z(11)= 0.
X(12)= .55555
Y(12)=1.28301
Z(12)= .90722
ELSE
X(2)= 1.
Y(2)= 0.
Z(2)= 0.
X(3)=-1.
Y(3)= 0.
Z(3)= 0.
X(4)= 0.
Y(4)= 1.
Z(4)= 0.
X(5)= 0.
Y(5)=-1.
Z(5)= 0.
X(6)= 0.
Y(6)= 0.
Z(6)= 1.
X(7)= 0.
Y(7)= 0.
Z(7)=-1.
X(8)= .666666667
Y(8)= .666666667
Z(8)= .666666667
X(9)= -.666666667
Y(9)= -.666666667
Z(9)= .666666667
X(10)=-.666666667
Y(10)= .666666667
Z(10)=-.666666667
X(11)= .666666667
Y(11)=-.666666667
Z(11)=-.666666667
X(12)=-.666666667
Y(12)= .666666667
Z(12)= .666666667
X(13)= .666666667
Y(13)=-.666666667
Z(13)= .666666667
```

X(14)=.666666667
Y(14)=.666666667
Z(14)=-.666666667
X(15)=-.666666667
Y(15)=-.666666667
Z(15)=-.666666667
X(16)= 1.
Y(16)= 0.
Z(16)= 1.33333333
X(17)=-1.
Y(17)= 0.
Z(17)= 1.33333333
X(18)= 0.
Y(18)= 1.
Z(18)=-1.33333333
X(19)= 0.
Y(19)=-1.
Z(19)=-1.33333333
X(20)= 0.
Y(20)= 1.
Z(20)= 1.33333333
X(21)= 0.
Y(21)=-1.
Z(21)= 1.33333333
X(22)= 1.
Y(22)= 0.
Z(22)=-1.33333333
X(23)=-1.
Y(23)= 0.
Z(23)=-1.33333333
X(24)= 1.194
Y(24)= 1.194
Z(24)= 0.
X(25)=-1.194
Y(25)=-1.194
Z(25)= 0.
X(26)= 1.194
Y(26)=-1.194
Z(26)= 0.
X(27)=-1.194
Y(27)= 1.194
Z(27)= 0.
X(28)= 0.
Y(28)= 0.
Z(28)= 2.

```
      X(29)= 0.
      Y(29)= 0.
      Z(29)=-2.
      X(30)= 2.
      Y(30)= 0.
      Z(30)= 0.
      ENDIF
      DO 20 I=1,NT
      DO 20 J=I+1,NT
      TEMP1=(X(I)-X(J))*(X(I)-X(J))
      TEMP2=(Y(I)-Y(J))*(Y(I)-Y(J))
      TEMP3=(Z(I)-Z(J))*(Z(I)-Z(J))
      DI=DSQRT(TEMP1 + TEMP2 + TEMP3)
      IF(DI .GT. XL) XL=DI
20    CONTINUE
      DO 110 I=2,NT
      D2=DSQRT(X(I)*X(I)+Y(I)*Y(I)+Z(I)*Z(I))
      XC=XC+X(I)
      YC=YC+Y(I)
      ZC=ZC+Z(I)
      XX=XX+X(I)/D2
      YY=YY+Y(I)/D2
110   ZZ=ZZ+Z(I)/D2
      RN=NT-1
      XC=XC/NT
      YC=YC/NT
      ZC=ZC/NT
      XX=XX/RN
      YY=YY/RN
      ZZ=ZZ/RN
      CHI=DACOS(ZZ)
C
      IF(XX .GT.0.) THEN
       PSI=DATAN(YY/XX)
      ELSE IF(XX .LT. 0.) THEN
       PSI=PSI+PI
      ELSE
        IF(YY .GT. 0.) THEN
            PSI=0.5*PI
        ELSE IF(YY .LT. 0.) THEN
            PSI=-0.5*PI
        ELSE
            PSI=0.
        ENDIF
      ENDIF
```

```
C
      DO 120 I=1,NT
      X(I)=X(I)-XC
      Y(I)=Y(I)-YC
 120  Z(I)=Z(I)-ZC
      CALL TRANS(NT,CHI,PSI)
      RETURN
      END
C
C*************************************************************
C          RANDOM NUBER GENERATOR SUBROUTINE
C*************************************************************
C****** @(#)VRAND 5.1 10/11/89  Copyright (c) 1989 by FPS Computing
C
C  Copyright (c) 1989 by FPS Computing
C
C  Permission to use, copy, modify, and distribute this software,
C  FPSMath (TM), and its documentation for any purpose and without fee
C  is hereby granted, provided that the above copyright notice and this
C  permission notice appear in all copies of this software and its
C  supporting documentation, and that FPS Computing and FPSMath (TM) be
C  mentioned in all documentation and advertisement of any products
C  derived from or using this software. This software library may not
C  be renamed in any way and must be called FPSMath (TM). FPS Computing
C  makes no representations about the suitability of this software for
C  any purpose. It is provided AS IS without express or implied
C  warranty including any WARRANTY OF FITNESS FOR A PARTICULAR
PURPOSE
C  AND MERCHANTABILITY. The information contained in FPSMath (TM) is
C  subject to change without notice.
C
C  FPSMath and FPS Computing are Trademarks of Floating Point Systems,
C  Inc.
C
C-------------------------------------------------------------
C
C  V E C T O R   R A N D O M   N U M B E R
C
C  PURPOSE:
C       To fill a vector with random floating-point numbers
C       uniformly distributed in the interval [0.0, 1.0).
C
C  FORTRAN SYNOPSIS:
C       SUBROUTINE VRAND (IS, C, IC, N)
C       REAL*8       C(1)
```

```
C       INTEGER*4   IS, IC, N
C
C INPUT PARAMETERS:
C       IS      Integer         Scalar
C       Input random number seed.
C       IC      Integer         Scalar
C       Element stride for C.
C       N       Integer         Scalar
C       Element count.
C
C OUTPUT PARAMETERS:
C       C       Real    Vector
C       Output vector of random numbers.
C       IS      Integer Scalar
C       Output seed.
C
C DESCRIPTION:
C       Generates a sequence of pseudo-random floating-point numbers
C       uniformly distributed between 0.0 and 1.0.
C
C       The sequence is generated using a linear congruential
C       method based on the recursive formula:
C
C       IS <= a*IS + b, mod 2**26
C
C       a and b are constants; all arithmetic is done mod 2**26.
C       The starting value, IS, is called the seed; the last value
C       calculated is returned as the new seed.
C
C       VRAND normalizes the integers IS by dividing by 2**26, so
C       the seed for the call to VRAND can be any integer between 0
C       and 2**26 - 1.  The N resulting floating-point numbers are
C       returned in the vector C.
C
C       References:
C
C       Knuth, D.E., "The Art of Computer Programming: Seminumerical
C       Algorithms", Vol. 2, Addison-Wesley, 1969.
C
C EXAMPLE:
C       Input:
C
C       N = 5
C       IC = 1
C       IS = 0
```

```
C
C       Output:
C
C       IS = 6515839
C
C       C : 0.211  0.774  0.736  0.251  0.097
C
C-----------------------------------------------------------------------
C
        SUBROUTINE VRAND (IS, C, IC, N)
C
        REAL*8  C(1)
        INTEGER*4  IS, IC, N
C
C-----------------------------------------------------------------------
C
        INTEGER*4   CI
C       Index for C vector
        INTEGER*4   I
C       Loop index
        REAL*8      SIS
C       Hold seed value
C
C-----------------------------------------------------------------------
C
        REAL*8      A
        PARAMETER (A = 67081293.0D0)
C       Algorithm constant
        REAL*8      B
        PARAMETER (B = 14181771.0D0)
C       Algorithm constant
        REAL*8      T26
        PARAMETER (T26 = 0.67108864000000000D+008)
C       Constant DBLE(2**26)
C
C-----------------------------------------------------------------------
C
C  Verify parameter
C
        IF (N .LE. 0)  GOTO 9999
C
        CI = 1
        SIS = DBLE(IS)
C
        DO 10 I = 1, N
```

```
          SIS = SIS * A + B
          SIS = MOD(SIS, T26)
          C(CI) = (SIS / T26)
          CI = CI + IC
   10   CONTINUE
C
        IS = INT(SIS)
C
 9999   CONTINUE
        RETURN
        END
C*********************************************************************
C  END OF FILE
C*********************************************************************
```

VITA

Demetris Theodosios Venizelos was born in Latsia, Cyprus on August 30, 1963 to parents Theodosios and Evdokia. Demetris was exposed to the world of machining early in his life, through the family business. By the time he graduated from High School he was an experienced machinist. After serving in the Cyprus National Guard as a military policeman for 26 months, he enrolled at Louisiana State University in Baton Rouge. He received his B.Sc. in Mechanical Engineering in 1987 and his M.Sc. in Mechanical Engineering in 1989. In 1994, he received his Ph.D. from the same university. While at LSU, Demetris met his wife Gloria and they were married in the summer of 1993.

DOCTORAL EXAMINATION AND DISSERTATION REPORT

Candidate: Demetris T. Venizelos

Major Field: Mechanical Engineering

Title of Dissertation: A Study of the Radiative Properties of Agglomerated Flame Particulates Using Light Scattering

Approved:

Major Professor and Chairman

Dean of the Graduate School

EXAMINING COMMITTEE:

Date of Examination:

11/7/94